DOCTORAL THESIS BY

NATIONAL HIGHER SCHOOL
OF ADVANCED TECHNOLOGIES BRETAGNE

DOCTORAL SCHOOL NO. 648
Sciences for Engineering and Digital Technology
Specialization: Mechanics of Solids, Materials, Structures, and Surfaces

by

Mohamed DALY

Design and Optimization of Next-Generation Composite Materials through Additive Manufacturing: Towards Revolutionary Mechanical Performance.

Thesis presented and defended in Brest on Thursday, January 9, 2025
Research Unit: Dupuy de Lôme Research Institute - Sousse Mechanics Laboratory

Pre-defense Reviewers:

Anas Buguecha	Professor - National Engineering School of Sfax, Sfax, Tunisia.
Laurent Dala	Professor - University of Northumbria, Newcastle, United Kingdom.

Composition of the Jury:

President:	First Name Last Name	Position and Institution
Examiners:	Francisco Chinesta,	Professor, ENSAM, Paris, France.
	Daniela Placha	Professor, VSB-TUO, Ostrava, Czech Republic.
	Mourad Nachtane	MCF, HDR, UM6P, Benguerir, Morocco.
Thesis Director:	Mostapha Tarfaoui	Professor, ENSTA Bretagne, Brest, France.
Co-thesis Director:	Chokri Bouraoui	Professor, ENISO, Sousse, Tunisia.
Co-supervisors:	Manel Chihi	Doctor, ENISO, Sousse, Tunisia.

Guest:
Farhat Zemzemi MCF, HDR, ENISO, Sousse, Tunisia.

Table of Contents

Table of Contents ... **1**
List of Figures ... **5**
List of Tables ... **9**
Nomenclature ... **10**
General introduction ... **12**
Chapter 1 State of the art: 3D printing and composite materials ... **17**
1. 1 Introduction ... 18
1. 2 Definition of a Composite Material ... 20
1. 3 Compositions of a Composite Material ... 21
1.3.1 Matrix ... 21
1.3.1.1 Polymer matrix ... 21
1.3.1.2 Metal matrix ... 23
1.3.1.3 Ceramic Matrix ... 25
1.3.2 Reinforcements ... 27
1.3.2.1 Continuous fibers ... 27
1.3.2.2 Discontinuous fibers ... 28
1.3.2.3 Particles ... 30
1.3.2.4 Fabrics ... 32
1.3.3 Nanofillers ... 33
1.3.3.1 Carbon Nanotubes (CNT) ... 33
1.3.3.2 Metallic Nanoparticles ... 35
1.3.3.3 Ceramic Nanoparticles ... 36
1. 4 3D Printing ... 37
1.4.1 Definition of 3D Printing ... 37
1.4.2 3D printing processes ... 37
1.4.2.1 Fused Deposition Modeling (FDM) ... 37
1.4.2.2 Selective Laser Sintering (SLS) ... 38
1.4.2.3 Selective Laser Melting (SLM) ... 39
1.4.2.4 Stereolithography (SLA) ... 39
1. 5 Application sectors of printed composites ... 40
1.5.1 Automobile sector ... 40
1.5.2 Aerospace sector ... 42
1.5.3 Medical sector ... 44
1. 6 Composite Materials and Damage Scenarios ... 45
1.6.1 Delamination ... 45
1.6.2 Cracking ... 47

1.6.3 Fatigue 48
1. 7 Conclusion 49
Chapter 2 Materials for 3D-printing 50
2. 1 Introduction 51
2. 2 Acrylonitrile butadiene styrene (ABS) 51
2.2.1 Printing parameters 51
2.2.2 Mechanical Properties 52
2. 3 Carbon fiber-Polyethylene Terephthalate Glycol (CF-PETG) 53
2.3.1 Mechanical properties and printing parameters 53
2.3.2 Differential scanning calorimetry analysis (DSC) 54
2.3.3 Scanning Electron Microscopy analysis (SEM) 55
2.3.4 Structural design 57
2.3.4.1 Tensile samples 57
2.3.4.2 Compression samples 59
2. 4 Aerosil/Polycarbonate 61
2.4.1 Properties of Aerosil/Polycarbonate 61
2.4.2 Production of ceramic nanofiller-filled masterbatch 62
2.4.3 Production of coils for additive manufacturing and printing parameters 63
2.4.4 Nanoscopic analysis (SEM) 65
2.4.4.1 Sample preparation 65
2.4.4.2 Scanning electron microscope (zoom ×35) 66
2.4.4.3 Scanning electron microscope (Zoom ×50) 66
2.4.4.4 Scanning electron microscope (zoom ×1500) 67
2. 5 Conclusion 68
Chapter 3 Experimental study 70
3. 1 Introduction 71
3. 2 Study of the tensile behavior of 3D-printed CF-PETG composites. 71
3.2.1 Structural design of the sample 72
3.2.2 Repeatability test 73
3.2.3 Result 74
3.2.4 Mechanisms of damage 75
3. 3 Study of the dynamic compression behavior of 3D-printed CF-PETG composites 77
3.3.1 Split Hopkinson Pressure Bars 77
3.3.2 Repeatability of tests for various impact pressures 78
3.3.3 Result and discussion of the Dynamic behavior 79
3.3.4 Damage Mechanisms 83
3. 4 Study of the temperature-dependent compression behavior of Aerosil/polycarbonate composites 85

3.4.1 Static compression test 85
3.4.2 Test reproducibility 86
3.4.3 Effect of nanoceramic particles on material behavior 87
3.4.4 Effect of temperature on material behavior 90
3.4.5 Analysis of elastic and plastic properties 92
3.4.6 Effect of temperature on the imprint produced between the trays and the sample 94
3. 5 Conclusion 96
Chapter 4 Numerical study 97
4. 1 Introduction 98
4. 2 Abaqus/Digimat modeling of FDM technology and the effect of printing parameters on the tensile strength of ABS parts 99
4.2.1 Recap of experimental study 99
4.2.2 FEA: Constitutive mechanical and thermal models 101
4.2.2.1 Mechanical analysis 101
4.2.2.2 Thermal analysis 103
4.2.3 Implementation of the Numerical Study 104
4.2.4 Finite Element Model 107
4.2.4.1 First modeling: Abaqus 107
4.2.4.2 Second modeling: Abaqus/Digimat coupling 108
4.2.5 Effect of printing speed on residual stresses 111
4.2.6 Effect of Printing Speed on the deflection 111
4.2.7 Parametric study of 3D printing 114
4.2.7.1 Effect of discretization method: Layer-by-layer vs Filament 118
4.2.7.2 Effect of the printing direction 120
4.2.7.3 Effects of 3D printing on the geometry of the part 122
4.2.8 Cost of printing 122
4. 3 Study of the tensile behavior of 3D-printed CF-PETG composites 123
4.3.1 Finite element Model of tensile tests 123
4.3.2 Finite element analysis results 124
4.3.3 3D printing modeling 130
4.3.3.1 Effect of 3D printing on the geometry of the part 131
4.3.4 Parametric study of 3D printing 132
4.3.5 Abaqus/Digimat coupling for efficient numerical modeling 138
4. 4 Dynamic compression behavior of 3D-printed CF-PETG composites 140
4.4.1 Finite element model 140
4.4.2 Meshing and limit condition 141
4.4.3 Results and Discussion 143
4.4.3.1 Results of variations in Von Mises stresses, plasticity, and displacements 143

4.4.3.2 Comparison and validation: test vs. simulation 146
4. 5 Static compression modeling of Aerosil/polycarbonate composites 158
4.5.1 Homogenization cycle 158
4.5.2 Nanocharge effect after Aerosil/ Polycarbonate homogenization 160
4.5.3 Representation of the elementary volume of the composite 161
4.5.4 Position of the nanoceramic relative to the matrix 162
4. 6 Conclusion 166
General conclusion 168
References 170
Publications 180

List of Figures

Figure 1. 1: Classification of Matrix and Reinforcement Types in Composite Materials. 20
Figure 1. 2: Formation and Structure of Composite Materials. 21
Figure 1. 3: Schematic of filament winding process [29]. 22
Figure 1. 4: Extrusion Apparatus for Fabricating Polymer Matrix Composites Used in 3D Printing [30]. 22
Figure 1. 5: Diagrammatic schematic for injection molding of powder [37]. 24
Figure 1. 6: An example of a standard SLM procedure [38]. 24
Figure 1. 7: Ceramics 3D printing process diagram [43]. 26
Figure 1. 8: Visualization of Continuous Fiber Distributions. 27
Figure 1. 9: Visualization of discontinuous fibers Distributions. 29
Figure 1. 10: Unidirectional prepreg laminates with short fibers are used to create aligned staple-fiber composite [55]. 30
Figure 1. 11: Example of particles distribution in a matrix [58]. 31
Figure 1. 12: Mono-axial fabric [59]. 32
Figure 1. 13: One axis fabric (a) with the fiber direction at 0°, and two stacked 0° and 90° single-axis fabric layers (b) [59]. 32
Figure 1. 14: Overarching factors should be considered while creating a highly electrically and mechanically performing nanocomposite [60]. 33
Figure 1. 15: Carbon nanotubes with one and more walls [61]. 34
Figure 1. 16: Various kinds of nanomaterials based on metals [68]. 35
Figure 1. 17: The effect of ceramic nanoparticles on material behavior after printing [74]. 37
Figure 1. 18: Schematic view of the FDM technology [9]. 38
Figure 1. 19: Schematic view of the SLS technology [84]. 39
Figure 1. 20: Principle of the SLM process [85]. 39
Figure 1. 21: Schematic diagram of the stereolithography process [88]. 40
Figure 1. 22: (a) A functional alternator bracket printed using SLS nylon, (b) A complex, functional ducting design printed in SLS nylon [90]. 41
Figure 1. 23: 3D Printing Technology in aerospace industry. 43
Figure 1. 24: Liquid oxygen flange [97]. 44
Figure 1. 25: Applications of polymer 3D printing in implant dentistry [98]. 44
Figure 1. 26: A prosthetic utilizing a 3D printed socket [99]. 45
Figure 1. 27: Micrograph taken by the fracture interface microscope following the flexural test [101]. 46
Figure 1. 28: Fiber-matrix debonding [102]. 47
Figure 1. 29: Damage after the (a) First contact; and (b) complete impact energy transfer [106]. 47
Figure 1. 30: Mechanism fatigue failure [109]. 48
Figure 1. 31: Variables that impact the fatigue life of composite materials [109]. 49

Figure 2. 1: DSC analysis. 54
Figure 2. 2: Scanning Electron Microscopy (SEM) analysis of CF-PETG for different filling ratios. 56
Figure 2. 3: 3D printing system and the difference between the two infill patterns. 58
Figure 2. 4: Fused filament fabrication (FFF) process. 60
Figure 2. 5: Honeycomb-Patterned PETG Composites: Examining Varied Configurations with Short Carbon Fibers. 60
Figure 2. 6: Production of ceramic nanofiller-filled masterbatch in an internal mixer. 63
Figure 2. 7: Production of coils for additive manufacturing. 64
Figure 2. 8: Sample preparation. 65
Figure 2. 9: Scanning electron microscope (zoom ×35). 66
Figure 2. 10: Scanning electron microscope (zoom ×50). 67

Figure 2. 11: Scanning electron microscope (zoom ×1500)..... 68

Figure 3. 1: INSTRON 5969 tensile machine. 71
Figure 3. 2: Tensile test specimens. 72
Figure 3. 3: Examples of test reproducibility, NIDA, and RECT patterns..... 73
Figure 3. 4: Force-Displacement curves..... 74
Figure 3. 5: Variation of the maximum force as a function of filling rate for the two patterns: Rectilinear and Honeycomb. 75
Figure 3. 6: Breakage of the specimens after the tensile test. 76
Figure 3. 7: Description of the concept of thermomechanical behavior. 76
Figure 3. 8: SHPB device: schematic representation of the experimental procedure. 78
Figure 3. 9: Tests repeatability, Nida, P = 1.7 bar..... 79
Figure 3. 10: True Stress vs. True Strain at different impact pressure for the Nida filler. 81
Figure 3. 11: Dynamic behavior, CF-PETG at 1.4 bars for the Nida filler. 81
Figure 3. 12: Dynamic behavior, CF-PETG at 1.7 bars. 82
Figure 3. 13: Dynamic behavior, CF-PETG at 2 bars. 82
Figure 3. 14: Dynamic behavior, CF-PETG at 2.4 bars. 83
Figure 3. 15: Images captured by a high-speed camera during tests with various impact pressures. .. 84
Figure 3. 16: Test equipment for compression testing. 85
Figure 3. 17: Test reproducibility..... 87
Figure 3. 18: Effect of weight percentage and temperature. 89
Figure 3. 19: Nanoparticle-dependent variation in Young's modulus at ambient temperature. 90
Figure 3. 20: The effect of temperature on material behavior..... 91
Figure 3. 21: Analysis of elastic and plastic properties: the characteristic curve..... 92
Figure 3. 22: Variation of Final Elastic Load with Temperature for Different Aerosil Percentage..... 93
Figure 3. 23: Variation of Final Plastic Load with Temperature for Different Aerosil Percentage. 93
Figure 3. 24: Variation of densification modulus with temperature. 94

Figure 4. 1: Geometry and dimensions of the tensile specimens [110]..... 100
Figure 4. 2: Characterisation of the mechanical properties of FDM-ABS specime (a) Printed tensile specimen and (b) tensile testing configuration [110]. 100
Figure 4. 3: Representative True stress vs. True strain curves for the manufactured tensile specimens with different printing speeds..... 101
Figure 4. 4: Kinetics of a coupled Abaqus/Digimat computation..... 105
Figure 4. 5: Coupling procedure between Abaqus and Digimat. 106
Figure 4. 6: Mapped manufacturing data visualized on the structural model, filament orientation (eigenvector)..... 107
Figure 4. 7: Specimen mesh C3D8R..... 107
Figure 4. 8: Stress-Strain curve for a printing speed of 10 mm/s..... 108
Figure 4. 9: Work sequences in Digimat-AM. 109
Figure 4. 10: Superposition of the mesh between Abaqus and Digimat. 109
Figure 4. 11: Stress-Strain curves for a printing speed of 10 mm/s. 110
Figure 4. 12: Stress-Strain curve determined numerically for 4 printing speeds. 110
Figure 4. 13: Residual stresses at the end of the manufacturing process. 112
Figure 4. 14: Deflection at the end of the manufacturing..... 113
Figure 4. 15: Technique for scanning many layers of an ASTM-D638 part (type IV)..... 114
Figure 4. 16: A few frames for 3D printing of polymer composites using layer deposit FDM process: temperature variation..... 116
Figure 4. 17: Profile of temperature and Von Mises stress utilizing the layer deposit technique at various points of the ABS thickness..... 117
Figure 4. 18: Layer-by-layer vs Filament discretisation. 118

Figure 4. 19: Comparison of the temperature profile for two printing techniques. 119
Figure 4. 20: Variation of the stress concentration and the temperature for two processes. 120
Figure 4. 21: Printing direction. 121
Figure 4. 22: Curves determined numerically for printing direction 45/-45, 0/90, 60/-60. 121
Figure 4. 23: Warping of ABS specimen. 122
Figure 4. 24: Printing cost for an ABS specimen. 123
Figure 4. 25: Boundary conditions. 124
Figure 4. 26: Mesh type: C3D10. 124
Figure 4. 27: Fracture zone of the specimen. 126
Figure 4. 28: Variation of the Von Mises stress for each type of specimen. 127
Figure 4. 29: Force versus displacement for different filling patterns. 129
Figure 4. 30: Meshing of the specimen in Digimat. 130
Figure 4. 31: Effect of 3D printing on the part's geometry, 100% filling. 132
Figure 4. 32: Reference points for the study of temperature distribution. 133
Figure 4. 33: Temperature variation at different layers of the specimen. 134
Figure 4. 34: Variation of temperature, deflection, and stress in different layers of the 3D-printed composite. 136
Figure 4. 35: Variation of the temperature and deflection vs. Printing time. 138
Figure 4. 36: Variation of the temperature and Von Mises stress vs. Printing time. 138
Figure 4. 37: Coupling procedure between Abaqus and Digimat. 139
Figure 4. 38: Force vs. Displacement curve, NIDA-75%. 140
Figure 4. 39: Example of a honeycomb test specimen with 20% fill (13×13×13 mm3). 141
Figure 4. 40: Numerical model of the SHPB system. 142
Figure 4. 41: The honeycombs' orientation about the direction of compression. 143
Figure 4. 42: Maximum Von Mises stress, plasticity, and displacement values for the honeycomb pattern with a 20% fill ratio, 1.4 bar. 144
Figure 4. 43: Maximum Von Mises stress, plasticity, and displacement values for the honeycomb pattern with a 20% fill ratio, 1.7 bar. 144
Figure 4. 44: Maximum Von Mises stress, plasticity, and displacement values for the honeycomb pattern with a 75% fill ratio, 1.7 bar. 145
Figure 4. 45: Variation of Von Mises stresses for different filling ratios 50%, 75%, and 100%, 2.4 bar. 146
Figure 4. 46: Variation of the incident signal for filling rates from 20% to 100% at 1.4 bar pressure: test vs. simulation. 147
Figure 4. 47: Variation of the transmitted signal for filling rates from 20% to 100% at 1.4 bar pressure: test vs. simulation. 148
Figure 4. 48: Variation of the incident velocity for filling rates from 20% to 100% at 1.4 bar pressure: test vs. simulation. 149
Figure 4. 49: Variation of the transmitted velocity for filling rates from 20% to 100% at 1.4 bar pressure: test vs. simulation. 150
Figure 4. 50: Variation of the incident load for filling rates from 20% to 100% at 1.4 bar pressure: test vs. simulation. 151
Figure 4. 51: Variation of the incident signal for filling rates from 20% to 100% at 1.7 bar pressure: test vs. simulation. 152
Figure 4. 52: Variation of the transmitted signal for filling rates from 20% to 100% at 1.7 bar pressure: test vs. simulation. 153
Figure 4. 53: Variation of the incident velocity for filling rates from 20% to 100% at 1.7 bar pressure: test vs. simulation. 154
Figure 4. 54: Variation of the incident signal for filling rates from 20% to 100% at 2.0 bar pressure: test vs. simulation. 155
Figure 4. 55: Variation of the transmitted signal for filling rates from 20% to 100% at 2.0 bar pressure: test vs. simulation. 156

Figure 4. 56: Variation of the incident signal for filling rates from 20% to 100% at 2.4 bar pressure: test vs. simulation. 157
Figure 4. 57: Variation of the transmitted signal for filling rates for Nida filler from 20% to 100% at 2.4 bar pressure: test vs. simulation..... 158
Figure 4. 58: Mean-field homogenization cycle..... 159
Figure 4. 59: Multistep & Multilevel homogenization for multiphase inclusions 160
Figure 4. 60: Illustration of the Uniaxial_1 loading. 161
Figure 4. 61: Nanocharge effect after Polycarbonate/Aerosil homogenization for 6% loading, uniaxial deformation in direction 11 161
Figure 4. 62: Position of the nanoceramic relative to the matrix in the XY plane. 163
Figure 4. 63: Gamma and Rho variation as a function of relative weight for Aerosil 1%. 164

List of Tables

Table 1. 1: An Overview of the Mechanical Performance Findings for Polymer Matrix Materials and Reinforcements..... 23
Table 1. 2: An Overview of the Mechanical Performance Findings for metal Matrix Materials and Reinforcements..... 25
Table 1. 3: An Overview of the Mechanical Performance Findings for ceramic Matrix Materials and Reinforcements..... 26
Table 1. 4: Summary of Mechanical Performance Results for Continous Fibers with Various Matrix. 28
Table 1. 5: Inclusion forms available. 31
Table 1. 6: Properties of Composite Materials with Carbon Nanotube Reinforcements. 34
Table 1. 7: A summary of the characteristics of polymer matrices that incorporate nanoparticles based on metals. 36
Table 1. 8: Benefits of additive manufacturing. 42

Table 2. 1: Constant building parameters for manufacturing the test specimens. 52
Table 2. 2: Mechanical Properties of ABS material. 52
Table 2. 3: Mechanical properties of CF-PETG. 53
Table 2. 4: Printing parameters for CF-PETG composite material. 54
Table 2. 5: (A) Print Properties of CF/PETG and (B) Print statistics. 59
Table 2. 6: Specifics of the tested parts' 3D printing. 60
Table 2. 7: The characteristics of polycarbonate. 61
Table 2. 8: Properties of Aerosil 300. 62
Table 2. 9: Printing parameters. 65

Table 3. 1: The effect of temperature on the imprint produced between the trays and the sample. 95

Table 4. 1: Constant building parameters for manufacturing the test specimens [110]. 100
Table 4. 2: Average Tensile properties of the tested FDM-ABS specimens [110]. 101
Table 4. 3: ABS properties for a printing speed of 10 mm/s. 108
Table 4. 4: Printing parameters. 130
Table 4. 5: Information on printed test specimens. 131
Table 4. 6: Mesh information on each fill rate. 141
Table 4. 7: Mesh information on each bar. 143
Table 4. 8: Limit condition applied to the striker. 143
Table 4. 9: The representation of the elementary volume of the composite (Aerosil/polycarbonate) with meshing for various nanoceramic levels. 162
Table 4. 10: Variation of Von Mises stresses and elastic Strain as a function of nanofiller ratio. 165

Nomenclature

ABS: Acrylonitrile butadiene styrene

AM: Additive manufacturing

FDM: Fused deposition modelling

PLA: Polylactic acid

PETG: Polyethylene Terephthalate Glycol

PEKK: Polyetherketoneketone

CF: Carbon fibre

DIC: Digital image correlation

Digimat-RP: Reinforced Plastics Analysis

Digimat AM: Additive manufacturing Analysis

FEA: Finite Element Analysis

CNT: Carbon nanotubes

RP: Rapid Prototyping

SFF: Solid-Freeform (SFF)

FFF: Fused Filament Fabrication

SLS: Selective Laser Sintering

ASTM: American Society for Testing and Materials

FEM: Finite Element Modeling

DSC: Differential Scanning Calorimetry

Tg: Glass Transition Temperature

SHPB: Split Hopkinson Pressure Bar

CFRP: Carbon Fiber Reinforced Polymer

GNPs: Graphene nanoplatelets

DGEBA: Diglycidyl Ether of Bisphenol A

SEM: Scanning Electron Microscopy

SLA: Stereolithography

MM: Multi-material

TP: Thermoplastic polymers

QC: Quasicrystal

GB: Glass bead

PEI: Polyétherimide

PEEK: Polyetheretherketone

SLM: Selective Laser Melting

CGF: Continuous glass fiber

EP: Epoxy

DFCs: Discontinuous fiber composites

Gf: Glass fiber

SiC: Silicon carbide

Al: Aluminium

3DP: 3D Printing

General introduction

3D printing, also referred to as additive manufacturing, is a cutting-edge technology revolutionizing the production of goods. This is not a novel concept, but it has gained popularity recently because of several patents expiring, equipment becoming smaller, and processing power increases. The market for additive manufacturing is predicted to develop at a compound annual growth rate (CAGR) of 31.4% between 2018 and 2025, reaching a value of USD 76,900 million. By then, it is anticipated that 51% of the 3D printing market will be accounted for by the aerospace, automotive, and medical sectors. Because 3D printing can quickly and precisely create complicated shapes, it is becoming an indispensable tool in the automotive, medical, aerospace, and naval industries. Like every other manufacturing equipment, 3D printing has benefits and drawbacks. Among its benefits is the ability to quickly, precisely, and frequently create intricate forms for less money than with more conventional methods. But it also has drawbacks, like parts warping and distortion after cooling, and a production rate that is frequently lower than traditional methods. It's crucial to remember that 3D printing employs various materials, including metals, polymers, and composites. It also uses several printing techniques, including stereolithography (SLA), selective laser melting, Fused Deposition Modeling (FDM), and Selective Laser Sintering (SLS). Even while 3D printing has been extensively studied, especially in creating novel materials, there are still a lot of unanswered questions.

The main topics of this thesis are the study of the behavior of printed composite materials at high and low temperatures, as well as dynamic and static testing. Numerical modeling of 3D printing is also included. Extensive experiments and numerical modeling have been conducted to comprehend how 3D printing works and how printing settings affect the behavior of composite materials. The goal is to improve printing by adjusting input parameters to minimize the pieces' warping, deflection, and residual stresses. We have experience with various materials, including thermoplastics like ABS and composites made of thermoplastics such as CF-PETG. A new generation of composites reinforced with nanoceramics has also been designed and produced using the FDM method. We looked at how various filler types and filling rates affected the behavior of the materials.

This thesis project aims to create novel materials that can be used to print multi-material (MM) components with various functionalities. These materials will be based on thermoplastic polymers (TP) modified with nano-additives and fibers. The primary goal of the proposed effort is to create a three-dimensional representation of the materials' microstructure using 3D

printing. The main discussion topics will be the progressive formation and evolution of phases at various scales. The four primary components of the strategy will be microstructure, qualities, treatment, materials, and methods. The research and comprehension of the mechanisms relating process, microstructure, and properties of a composite or nanocomposite made via 3D printing is another goal of this work. We'll try to assess how the created procedure affected the final material's three-dimensional architecture. This serves two purposes: first, it will improve our fundamental comprehension of the critical elements of additive manufacturing; second, it will give us more control over the properties of these materials so that we can think about using them in particular applications. Because of their great strength and heat resistance, high-temperature thermoplastics like PEKK, PETG, PC, and ABS have grown in popularity in sectors like aerospace, automotive, oil & gas, and medicine. An experimental and numerical investigation will be carried out to strengthen PEKK and PETG with carbon microfibers at varying filling densities (20%, 50%, 75%, and 100%) and samples created with 3D printing technology. These materials will be thoroughly characterized using several experimental techniques (static, dynamic) in various environmental settings (temperature, humidity). This study aims to measure the impact of filler shape, such as rectilinear or honeycomb, and filling rate, ranging from 20% to 100%, on the mechanical behavior and damage kinetics.

In-depth discussion of composite materials and their uses is provided in four major chapters of this thesis report: a bibliographic study, offering a comprehensive review of current knowledge on composite materials, their compositions, their application sectors (automotive, aeronautics, medical, naval), damage mechanisms, 3D printing processes, and recycling methods; a detailed analysis of the specific properties and application modes of three composite materials – Acrylonitrile Butadiene Styrene (ABS), Carbon Fiber / Polyethylene Terephthalate Glycol-modified (CF-PETG), and Aerosil/Polycarbonate – including mechanical, thermal, chemical, microscopic analyses, and differential calorimetry; an experimental study describing the methods used to characterize these materials, such as microindentation, simple tension, and static and dynamic compression tests, with a focus on sample design, test reproducibility, and damage mechanisms; and a numerical study detailing the modeling of tensile and compressive behaviors of CF-PETG and Aerosil/Polycarbonate composites using Abaqus and Digimat software, examining the effects of 3D printing parameters, the synergy between simulations and experiments, and the impact of nanofillers on mechanical properties. A synopsis of the primary findings concludes each chapter and sets the reader up for the following one.

Manuscript organization

Chapter 1: Building on earlier work, the first part of this paper is devoted to thoroughly examining the literature to clearly define composite materials and their processing in the context of 3D printing. It starts with a clear explanation of a composite material and then delves deeply into examining its constituent parts. The many forms of reinforcement, including continuous and discontinuous fibers, are covered in this analysis. The matrices utilized in composites—categorized as polymers, metals, and ceramics—are examined in the following section. 3D printing and the methods of 3D printing applied to composites are then defined. The chapter discusses the many forms of fatigue and delamination affecting printed composite materials.

Chapter 2: The second chapter's structure was chosen to provide a comprehensive overview of all the materials worked with throughout the thesis period. Following the thesis requirements and the need to work on thermoplastics and 3D-printed composite materials, the chapter begins with a numerical study of the thermoplastic material ABS. This initial step was undertaken to improve proficiency with the tools required for numerical analysis.
Subsequently, the focus was placed on 3D-printed thermoplastic composites, specifically CF-PETG, a thermoplastic PETG matrix reinforced with carbon fibers. This material was investigated experimentally and numerically, with tensile and dynamic compression tests conducted. In-depth analyses, such as Scanning Electron Microscopy (SEM) and Differential Scanning Calorimetry (DSC), were also performed to understand the material's properties better.
Finally, polycarbonate reinforced with ceramic nanoparticles, specifically Aerosil, was examined to observe the effect of nanoparticles on the material's behavior. This material was analyzed at the nanoscale to identify nanoparticle dispersion within the matrix better. Static compression tests under varying temperatures were then conducted, along with a numerical study focusing on the homogeneity of both materials.

Chapter 3: During this thesis period, a variety of experimental tests were employed. Different tests were performed on various materials depending on the task's utility and order. Tensile tests, dynamic compression tests, and static compression tests with temperature variations were used in this work. To determine the mechanical characteristics of CF-PETG, the tensile test was first performed, allowing a computer model with finite elements to be created. Following this,

dynamic compression was conducted on the same material to determine its dynamic properties and observe its behavior under dynamic conditions. Data from Hopkinson bars were used to create a numerical model. For static compression testing, the Aerosil/polycarbonate composite material was examined to determine its behavior under compression and how it changes at high and low temperatures. Additionally, the effect of ceramic nanofillers on the mechanical properties of the material was observed.

Chapter 4: Our ability to work on and validate several tests on a wide range of materials has been made possible by the advancement of numerical tools and the coupling of multiple numerical modeling softwares.

Following a review of the work referred in literature and their experimental findings on ABS 3D printing, the focus in the first section of this chapter was placed on the numerical modeling of these results. Initially, the effect of printing speeds (10, 30, 50, and 70 mm/s) on the tensile and fracture properties of ABS samples produced using the FDM method was numerically investigated. It was observed that print speed directly influences material behavior, as higher speeds increase the likelihood of over-extrusion, spinning, and other material defects. Moreover, elevated print speeds can result in dimensional issues such as bending and distortion, underscoring the importance of carefully adjusting the print speed for optimal results. Using Abaqus and Digimat software and a parametric study, the experimental results obtained in the literature were numerically enhanced after validating the numerical model. This modeling enabled the evaluation of residual stresses, deflection, warpage, and the mechanical behavior resulting from various 3D printing parameters, such as printing speed, direction, and discretization (layer-by-layer or filament). During the costing phase, the printing installation costs were estimated, considering the cost of the printing substrate (ABS). Several data points were required for this estimation, including the material's cost, the part's mass, and the substrate's mass.

The mechanical behavior of a thermoplastic polymer reinforced with carbon fibers (CF-PETG) produced with FFF technology was examined in the second section. Two filling patterns, rectilinear (RECT) and honeycomb (NIDA), were subjected to static tensile tests at various filling ratios (20%, 50%, 75%, and 100%). Two numerical techniques have been devised to approximate natural manufacturing and loading conditions. The first assumes that the printed part is flawless and uses the Abaqus calculation code. The second aspect of our work is unique since it involves numerical modeling. Specifically, we have created a method that combines Abaqus with Digimat while accounting for the influence of printing factors on material

behavior. By considering the impact of coupling between two computer codes and printing parameters on the quality of FEM predictions, this work offers significant opportunities for the correct prediction of the behavior of printed structures under various printing conditions.

This third section's primary goal was investigating how fill density affects the dynamic properties of 3D-printed parts. A composite material reinforced with short carbon fibers, polyethylene terephthalate glycol (CF-PETG), was selected due to its exceptional mechanical, physical, thermal, and energy-absorbing qualities. The goal of this research is to evaluate the dynamic behavior of CF-PETG produced by the fused filament fabrication (FFF) process using a numerical investigation.

Using the Digimat software modules, a numerical analysis was performed in the last section to represent the elementary volume, compute the mean field, and homogenize the Aerosil/PC material. This technique allows for the examination of the different matrix and reinforcement parameters, providing a comprehensive picture of the composite material's performance.

CHAPITRE 1

State of the art: 3D Printing and composite materials

Table of content

1. 1 Introduction 18
1. 2 Definition of a Composite Material 20
1. 3 Compositions of a Composite Material 21
1.3.1 Matrix 21
1.3.1.1 Polymer matrix 21
1.3.1.2 Metal matrix 23
1.3.1.3 Ceramic Matrix 25
1.3.2 Reinforcements 27
1.3.2.1 Continuous fibers 27
1.3.2.2 Discontinuous fibers 28
1.3.2.3 Particles 30
1.3.2.4 Fabrics 32
1.3.3 Nanofillers 33
1.3.3.1 Carbon Nanotubes (CNT) 33
1.3.3.2 Metallic Nanoparticles 35
1.3.3.3 Ceramic Nanoparticles 36
1. 4 3D Printing 37
1.4.1 Definition of 3D Printing 37
1.4.2 3D printing processes 37
1.4.2.1 Fused Deposition Modeling (FDM) 37
1.4.2.2 Selective Laser Sintering (SLS) 38
1.4.2.3 Selective Laser Melting (SLM) 39
1.4.2.4 Stereolithography (SLA) 39
1. 5 Application sectors of printed composites 40
1.5.1 Automobile sector 40
1.5.2 Aerospace sector 42
1.5.3 Medical sector 44
1. 6 Composite Materials and Damage Scenarios 45
1.6.1 Delamination 45
1.6.2 Cracking 47
1.6.3 Fatigue 48
1. 7 Conclusion 49

1. 1 Introduction

3D printing, also known as additive manufacturing (AM), rapid prototyping (RP), or solid-freeform (SFF) [1], [2], is a process of mixing materials to make products from 3D model data, generally layer by layer, initially proposed by Charles Hull in 1986 [3]. This approach achieves adequate geometric precision while reducing wastage by mixing materials with construction products.

Composites are frequently printed in three dimensions using fused deposition modeling (FDM) or fused filament fabrication (FFF) [4], [5], [6]. Polymer is melted in a vertical nozzle, deposited in layers on a horizontal build bed, cooled, and solidified [7], [8], [9]. As a result, the machined pieces' mechanical characteristics, shape, and size are significantly altered. In addition, the growth of temperature gradients and residual stresses are strongly influenced by experimental variables such as nozzle velocity and temperature, nozzle dimension, chamber temperature, polymer viscosity, printed layer and filament diameters, and bed temperature [10].

Materials are an essential element of 3D printing technology because they must match the stiffness, and strength needs of the additive manufacturing technique. Polymers are ideal for additive manufacturing. Their low cost and low density distinguish them. Thermoplastic materials most widely used are acrylonitrile butadiene styrene (ABS), polylactic acid (PLA), polyether ether ketone (PEEK), and, more recently, Polyethylene Tetra Glycol (PETG) [11], [12], and PolyEtherKetoneKetone (PEKK) [13]. However, PETG copolymer, including an amorphous microstructure, balances the durability and strength of ABS with the biocompatibility, ease of printing, and recyclability of PLA [12]. Furthermore, PETG has shown outstanding qualities such as flexibility, chemical and impact resistance, ductility, toughness, thermoformability [14], [15], and UV and weather resistance [16], [17], [18]. As a result, PETG has emerged as an excellent alternative for 3D-printed polymeric components in specialized and innovative industries such as autos, biotechnology, and robotics [19]. Furthermore, the behavior of 3D-printed PETG polymers may be improved by adding reinforcement such as carbon fiber [20], glass fiber [21], carbon nanotubes [22], etc. Nonetheless, carbon fiber-reinforced thermoplastic composites are the most commonly employed because of their excellent specific density, strength-to-weight ratio, recyclability, and simplicity of manufacture with lower material and manufacturing costs [23], [24].

Several researchers investigated the mechanical characteristics of 3D printed materials and the impact of printing settings on the FDM manufacturing process. Es-Said et al. [25] examine the effect of layer orientation on the mechanical properties of rapid prototyped samples. The samples were fabricated using a selective laser sintering (SLS) process and tested using tensile

and flexural tests. The results show that the layer orientation significantly impacts the mechanical properties of the samples. The results indicate that samples with the layer orientation perpendicular to the loading direction had higher tensile and flexural strengths than those with the layer orientation at an angle. The results also showed that samples with the layer orientation parallel to the loading direction had the lowest tensile and flexural strengths. The findings suggest layer orientation should be considered when designing rapid prototyping parts and components. Through experimental design and analysis, Ahn et al. [26] revealed that process characteristics like air gap and raster orientation significantly affect the tensile strength of FDM manufactured parts compared to other parameters like raster width, model temperature, and colors. In terms of tensile and flexural strength, manufactured parts have anisotropic qualities based on build orientation. They found that the measured tensile strengths of injection molded FDM ABS were between 65 and 72 percent of the tested strength of the standard Criss-cross raster [45°/−45°] and Cross raster [0°/90°] with −0.003 air gap. The FDM material's compressive strength was more significant than its tensile strength, and the build direction had little effect.

Researchers have created numerous novel composite materials in recent years. These inventions result from ongoing efforts to enhance the qualities of materials already in use and cater to the particular requirements of many sectors. A new Al-based composite reinforced by nano-sized Al91Fe4Cr5 quasicrystal (QC) on Al substrate by SLM was reported by Kang et al. [27]. This composite material was created by combining Al65Cu20Fe10Cr5 QC particles with pure aluminum. The result was nearly negligible material waste while producing pieces with intricate forms and fine microstructures. The partially melted QC particle showed better hardness (8.59 GPa) than the other structure in the composite (4.58 GPa or 3.37 GPa), according to the instrumented indentation test. Pavon et al. [28] investigated various polycaprolactone-based composites containing rosin gum and beeswax, two natural additions. The bed and extrusion temperatures of every composition were set during the 3D printing procedure. The outcomes demonstrated that combining beeswax and rosin gum provided a higher tensile strength than either additive alone, enabling 3D printing. However, the material's ductility increased with beeswax, making it challenging to prepare for 3D printing.

In this bibliographic chapter, composite materials will be defined, and their constituent parts will be discussed. The sectors where these materials might be used will also be examined, considering the difficulties associated with their use, particularly in damage and recyclability. Key terms will be introduced first, followed by a discussion on the various elements of composite materials: reinforcements, nanofillers, and matrices. The primary application areas

where composites are utilized, and their impact will then be explored. The various types of damage these materials can sustain will be analysed next. Finally, recycling techniques and 3D printing technologies used with composites will be reviewed, concluding with a discussion of the potential future of these novel materials.

1. 2 Definition of a Composite Material

A composite material is designed for specific applications and comprises two or more constituents (***Figure 1. 1***) with different mechanical, thermal, and chemical properties. The first constituent, the matrix, is generally of three types: polymer, ceramic, or metal. The role of the matrix is to bind the other components of the composite, serving as the base of the composite material. The second constituent is the reinforcement, which aims to strengthen the material. Reinforcements, such as fibers, inclusions, particles, etc., are integrated into the matrix. There are three types of composite materials: polymer matrix, metal matrix, and ceramic matrix composites. Generally, composite materials are lighter than other materials and have higher mechanical strength and good corrosion resistance. Therefore, they are widely used and highly developed for various applications in several industries, such as aerospace, automotive, medical, and construction. ***Figure 1. 2*** shows the microstructure of a composite material, highlighting the presence of the two constituents: the matrix and the reinforcement.

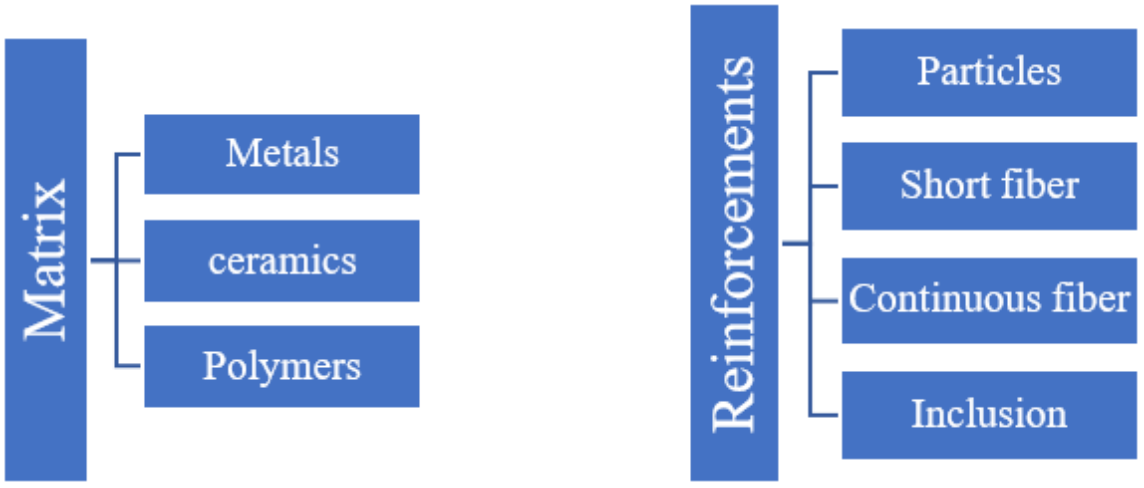


Figure 1. 1: Classification of Matrix and Reinforcement Types in Composite Materials.

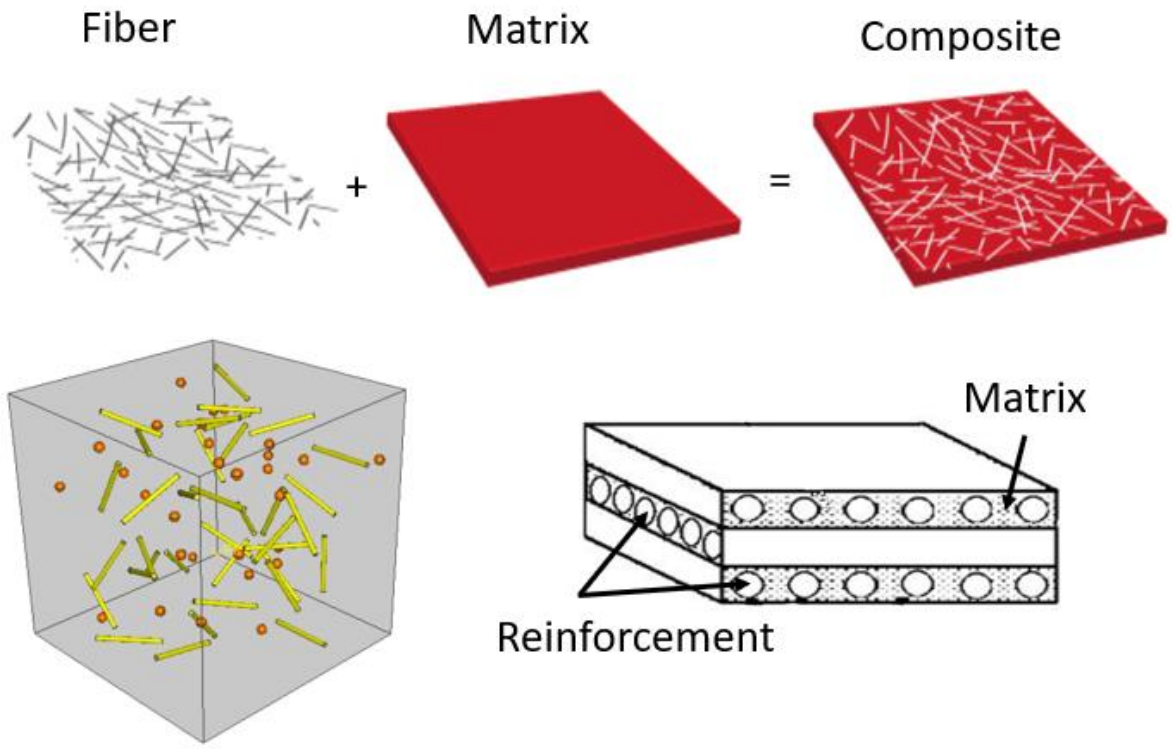


Figure 1. 2: Formation and Structure of Composite Materials.

1. 3 Compositions of a Composite Material

1.3.1 Matrix

Matrices play a significant role in a composite material, whether it is for mechanical, thermal, or chemical properties. The matrix fulfills several functions, including load transfer to ensure a uniform stress distribution throughout the composite, resistance to cracks, and prevention of crack propagation. The matrix also protects the fibers integrated into the composite against environmental factors such as moisture, chemicals, and UV rays, which could otherwise degrade the fibers and compromise the composite's performance.

1.3.1.1 Polymer matrix

Two primary categories comprise polymer matrices. First, thermoplastics cool down and solidify, then melt when heated. Second, during hardening, thermosets go through an irreversible chemical reaction. Polymer matrices are used in a wide range of applications because of their unique qualities, including flexibility, resistance to corrosion, and mechanical strength. Polymers can be made using various methods, such as filament winding (***Figure 1. 3***), injection molding, infusion, and extrusion (***Figure 1. 4***). They are extensively employed in

the building, aerospace, and automotive industries. shows the importance and role of polymer matrices when reinforced with various materials.

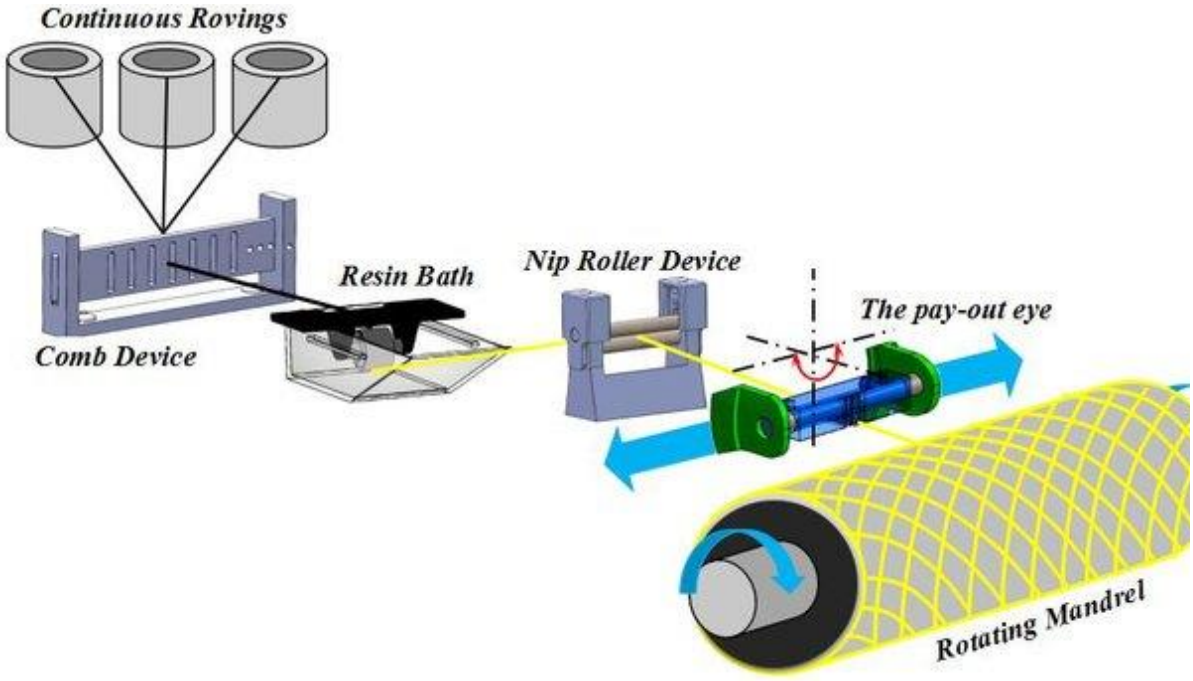


Figure 1. 3: Schematic of filament winding process [29].

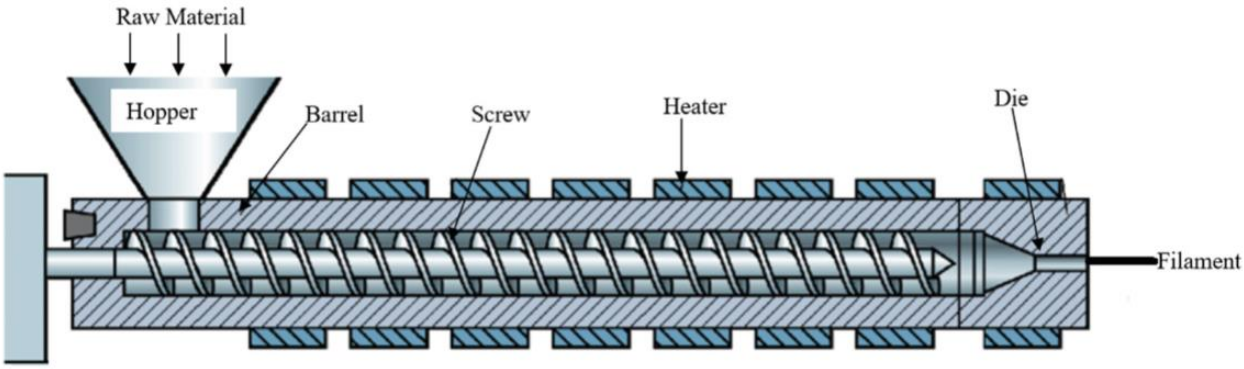


Figure 1. 4: Extrusion Apparatus for Fabricating Polymer Matrix Composites Used in 3D Printing [30].

Table 1. 1: An Overview of the Mechanical Performance Findings for Polymer Matrix Materials and Reinforcements.

Matrix Material	Reinforcements	Findings	Authors
PLA	Carbon fiber	Increased mechanical strength and better material extrusion.	[30]
ABS	Plastic Fiber	Enhanced resilience against abrasion.	[31]
PETG	Carbon fiber	The honeycomb pattern improves strength, stiffness, tensile resistance, and structural integrity.	[32]
PEKK	Carbon fiber	The outcomes demonstrated that fillings with varying densities and higher densities were more economical than solid samples.	[33]
PA12	Glass bead	The printed part PA12-CB/GB had an outstanding mechanical performance.	[34]
PEI	Carbon black	According to the results, the blade printed using PEI-CB performs well mechanically.	[35]
PEEK	Carbon fiber	breaking strength and strain first decline, then rise as the strain rate increases.	[36]

1.3.1.2 Metal matrix

A metallic matrix can be defined as being enveloped by reinforcement charges. Thanks to this crucial role, it is used widely across various industries. Among the properties of the metallic matrix are thermal and electrical conductivity, which are necessary for applications requiring efficient thermal dissipation. Additionally, the ductility in metal matrix composites allows for impact-resistant materials without easily cracking. The most commonly used materials are aluminum, due to its good thermal and electrical conductivity; magnesium, due to its low density; and titanium because it retains good mechanical properties at high temperatures. Powder injection ***Figure 1. 5*** and SLM (Selective Laser Melting) ***Figure 1. 6*** are the most

frequently employed to identify a metal matrix. Metal powder is injected into a mold using a powder injection technique to create the required metal matrix. A laser selectively melts layers of metal powder during the SLM process.

Previous research on metal matrix composites with different kinds of reinforcements is shown in ***Table 1. 2***.

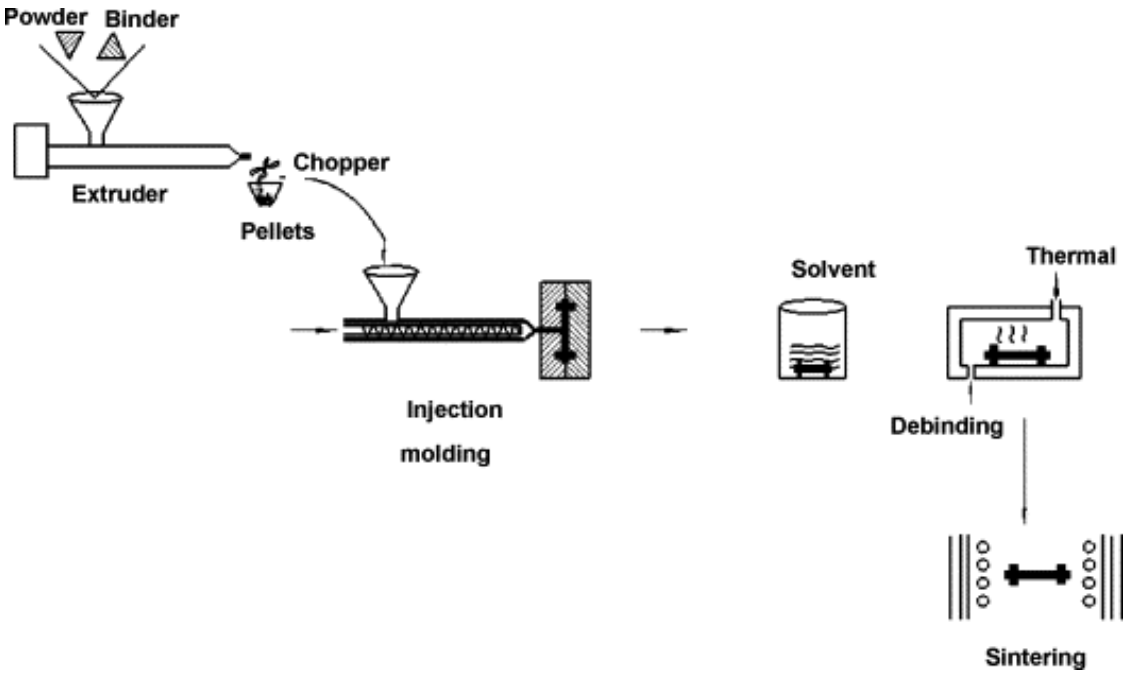


Figure 1. 5: Diagrammatic schematic for powder injection molding [37].

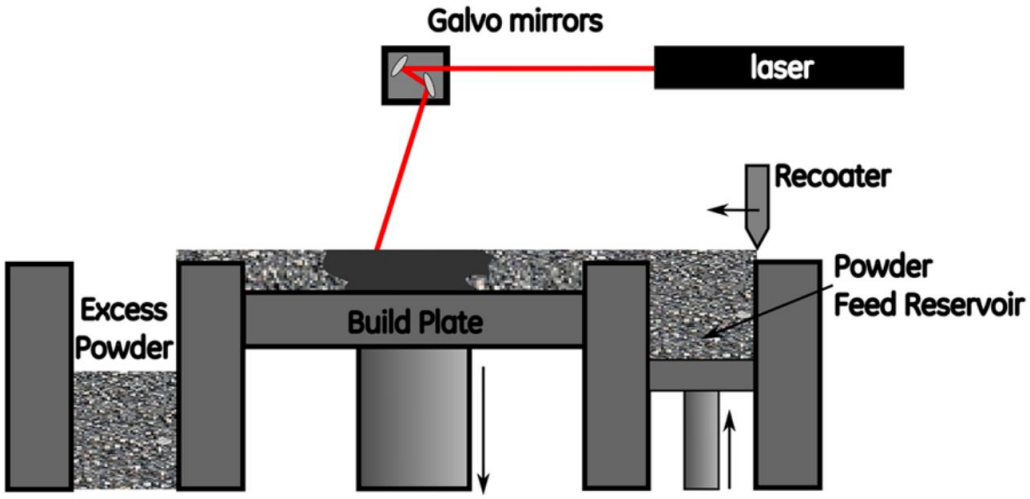


Figure 1. 6: An example of a standard SLM procedure [38].

Table 1. 2: An Overview of the Mechanical Performance Findings for Metal Matrix Materials and Reinforcements.

Matrix Material	Reinforcements	Findings	Authors
Aluminium	Titanium Carbide	The matrix material's low yield point and high strength of the particles accelerate debonding along the matrix-particle interface, thereby suppressing in-particle cracking.	[39]
Copper	Chromium Carbide	The most significant influence on energy demand was a 52.71 % reinforcement ratio, followed by a 24.26 % feed rate and a cutting speed (12.85%).	[40]
Magnesium	boron carbide	The reinforcement's morphological characteristics during the matrix phase determine the composite's characteristics.	[41]
Nickel	monocrystalline oxide fibers	Using internal crystallization-produced single-crystal eutectic oxide fibers to reinforce nickel-based matrices limits the strength of the fiber/matrix interface.	[42]

1.3.1.3 Ceramic Matrix

Ceramic matrices offer high-temperature resistance and good corrosion resistance. These materials can be reinforced with fibers or particles and are used in applications requiring heat resistance, such as aerospace engine manufacturing.

Among the most commonly used techniques for manufacturing ceramic matrix materials are sintering and the ceramization of organic precursors. The most commonly used ceramic matrices are alumina and zirconia due to their strong corrosion resistance and excellent thermal insulation properties. **Figure 1. 7** depicts the steps involved in 3D printing. A powder-spreading roller usually applies the powder uniformly onto the build platform. A liquid binder is applied to the powder layer using a printing head. The powder's particles come together whenever the liquid binder is added. Following the completion of the first layer, the build platform is lowered, a second layer of powder is applied over the first, and a second layer of binder is applied over

the freshly created surface layer [43]. **Table 1. *3*** shows a variety of ceramic materials used as ceramic materials used as matrices in composite materials. Early researchers used these materials and found promising results, especially for mechanical properties.

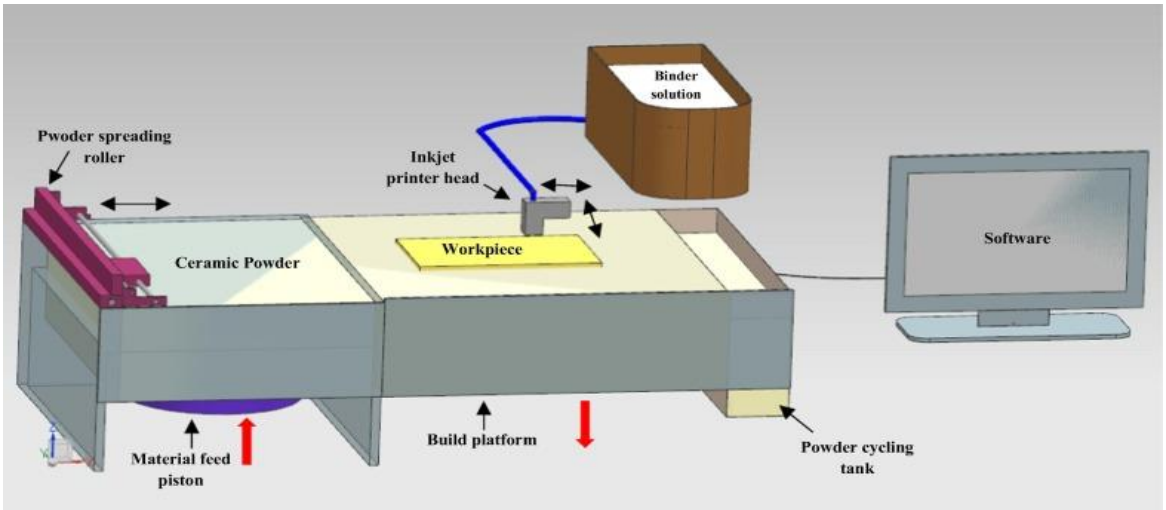


Figure 1. 7: Ceramics 3D printing process diagram [43].

Table 1. 3: An Overview of the Mechanical Performance Findings for Ceramic Matrix Materials and Reinforcements.

Matrix Material	Reinforcements	Findings	Authors
silicon carbide oxygen	silicon carbide	Non-reinforced parts shrink by 42%, compared to 37% for ceramic composites.	[44]
silicon-boron-nitrogen carbide	silicon nitride	For sintered printed composite, flexural strength increased to 183 MPa at 1200 °C.	[45]
silicon carbide	silicon carbide whiskers	The 3D networks showed impressive flexural and compressive strengths of 33.2 ± 5.2 MPa and 30.6 ± 4.3 MPa, respectively, with a porosity of about 62%.	[46]
Wollastonite	whisker-shaped hydroxyapatite	The mechanical properties improved with the addition of more hydroxyapatite trichites, reaching a high of 20% of the total weight before declining with the addition of additional hydroxyapatite trichites.	[47]

1.3.2 Reinforcements

Reinforcements are structural elements implemented into the matrix to enhance the mechanical properties and stability of the final composite material. The purpose of using reinforcements is also to select materials that meet industrial requirements, such as hardness and lightweight properties, which are highly demanded, especially in the naval, aerospace, and automotive industries. There are several types of reinforcements, including continuous fibers, discontinuous fibers, particles, and fabrics.

1.3.2.1 Continuous fibers

In contrast to conventional materials, continuous fibers are added to a polymer matrix to create robust and stiff materials. Consequently, remarkable mechanical qualities are provided by this combination of continuous fibers. Continuous fibers can be manufactured of glass, aramid, carbon, etc. Since continuous fibers are lighter than other reinforcements and have a higher specific strength and modulus than other materials, they are frequently utilized in the automotive, aerospace, and aeronautics industries. Continuous fiber 3D printing development has ushered in a new age of creating intricate, high-performing, reasonably priced composite constructions [48].

A summary of earlier study findings regarding the mechanical performance of continuous fibers with various matrices is shown in ***Table 1. 4***. These researchers found that the stability and light weight of continuous fibers positively affect the mechanical properties of composites

An illustration of continuous fiber distribution in a matrix is shown *in* ***Figure 1. 8***.

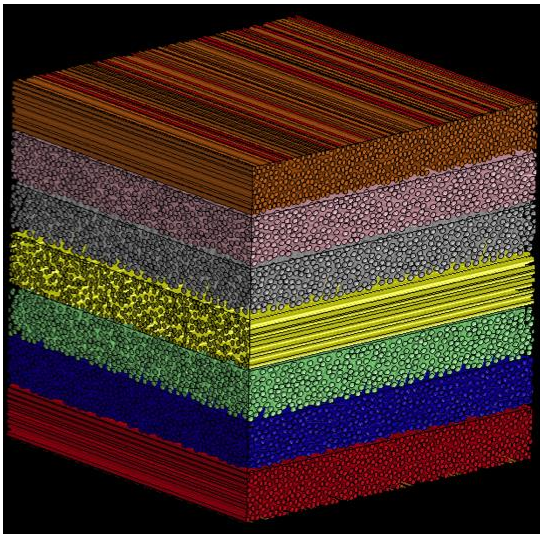


Figure 1. 8: Visualization of Continuous Fiber Distributions.

Table 1. 4: Summary of Mechanical Performance Results for Continous Fibers with Various Matrix.

Matrix Material	Reinforcements	Findings	Authors
Epoxy	Continuous glass fiber	Tensile strength and tensile modulus of 272.51 ± 5.12 MPa and 8.01 ± 0.45 GPa, respectively, were demonstrated by 3D printed CGF/EP samples with a 43 ± 3 weight percent fiber content.	[49]
Polyamide	Continuous Kevlar fiber	With fiber volume fractions of 4.04, 8.08, and 10.1%, respectively, the experimentally determined elastic modulus was 1767.2, 6920, and 9001.2 MPa.	[50]
Acrylonitrile-butadiene-styrene	Continuous carbon fiber	The findings demonstrated that the flexural and tensile strengths of these 10% continuous carbon fiber samples had increased to 127 and 147 MPa, respectively.	[51]
Polypropylene	Continuous glass fiber	The polypropylene concentration strongly impacts tensile, flexural, and impact strengths, although compressive strength is less affected by polypropylene concentration.	[52]

1.3.2.2 Discontinuous fibers

One of the most popular types of reinforcement in composite materials is discontinuous fibers. They are brief and might point in a particular direction or at random (***Figure 1. 9***). They cannot be orientated in multiple directions, in contrast to continuous fibers. Present-day discontinuous fibers are primarily made of glass, carbon, and aramid. The fact that discontinuous fibers are less expensive than continuous fibers is one of their benefits. It should be mentioned that the composite material has isotropic qualities—that is, the mechanical properties are the same in all directions—when discontinuous fibers are randomly arranged.

Jasmina et al. [53] examined and assessed several matrix and fiber variables and the various mechanical characteristics of a discontinuous composite reinforced with short fibers. They concluded that, compared to the traditional composites that contained particle fillers, the fiber composite made of millimeter-scale discontinuous glass fibers with a semi-IPN matrix demonstrated superior tolerance to crack propagation (fracture toughness).

The mode I intra-laminar fracture and size effect of discontinuous fiber composites (DFCs) as a function of structural thickness was studied experimentally and numerically by Seunghyun et al. [54] For a wafer size of 50 × 8 mm and a structural thickness of 4.1, 3.32.2, and 1.1 mm, respectively, Gf and cf were computed. The results showed that cf = ± 3.69 0.51 mm, 8.67 1.3 ± 7 mm, 3.63 0.9 ± 7 mm, and 1.78 0.30 ± mm, while Gf = ± 49.54 9.57 N/mm, 63.47 14.16 ± N/mm, 40.32 14.9 ± 8 N/mm, and 34.55 9.50 ± N/mm. The aforementioned findings unambiguously demonstrate that thickness has a noteworthy impact on the material's fracture characteristics.

Lorent et al. [55] researched highly aligned staple fiber composites to characterize the extensibility of composite material and attain good performance attributes with the ease of creating short fiber composites (***Figure 1. 10***). They discovered that the extensibility temperature range moved upward when the strain rate rose.

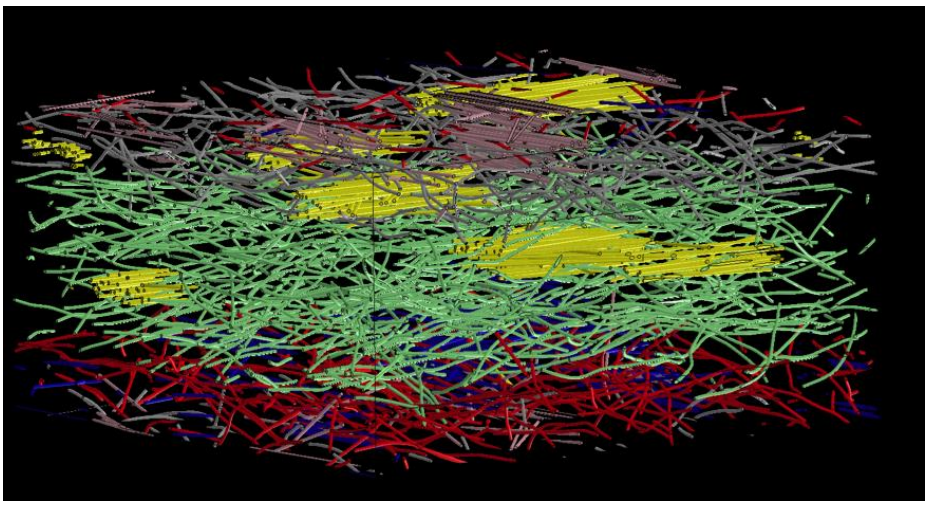


Figure 1. 9: Visualization of discontinuous fibers Distributions.

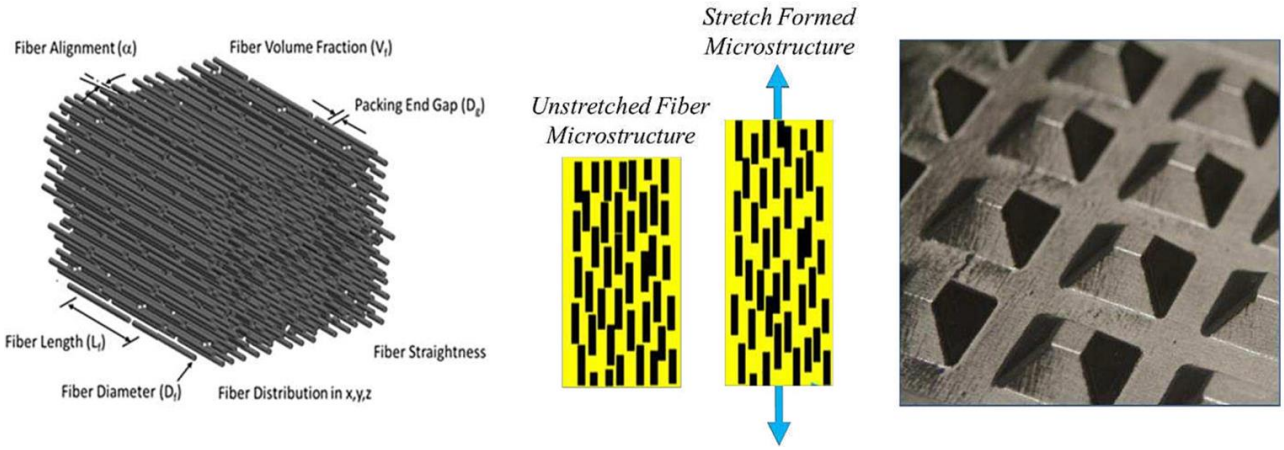


Figure 1. 10: Unidirectional prepreg laminates with short fibers are used to create aligned staple-fiber composite [55].

1.3.2.3 Particles

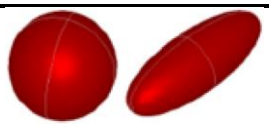
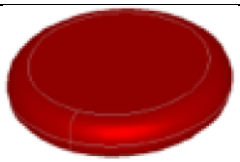
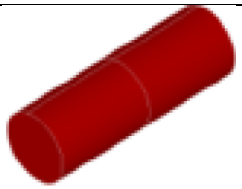
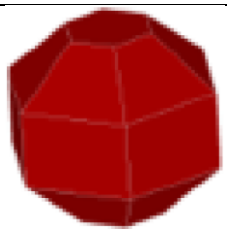
Particles are among the reinforcements used in composite materials (***Figure 1. 11)***. They are used less frequently than fibers, but this does not diminish their crucial role in specific composites. Among these roles are weight reduction, improvement in mechanical and thermal properties, and an increase in wear resistance due to their shape, which stabilizes easily within the matrix. The most commonly used particles as reinforcements are ceramic.

Table 1. 5 includes the various inclusion shapes, along with the relevant pictures. The red 3D models clearly and distinctly represent each shape, including the ellipsoid, spherocylinder, platelet, cylinder, prism, and icosahedron.

Dilek et al. [56] numerically investigated the effective heat conductivity of aluminum-filled high-density polyethylene composites as a function of filler content. They discovered that the heat flux lines are directed towards the inclusions because aluminum has a substantially higher thermal conductivity (204 W/mK) than high-density polyethylene (0.543 W/mK).

Flom et al. [57] produced discontinuous SiC/Al composites with varying sizes of SiC particles to investigate particle size's impact on the fracture mechanism. They discovered that SiC fracture starts to predominate in the composite reinforced with SiC particles 20 μm and larger. Because the SiC and Al matrices have different thermal expansion coefficients, the SiC generates a high density of dislocations at the SiC/Al contacts, which impacts the matrix.

Table 1. 5: Inclusion forms available.

Shape	Illustration
Ellipsoid	
Sphero-cylinder	
Platelet	
Cylinder	
Prism	
lcosahedron	

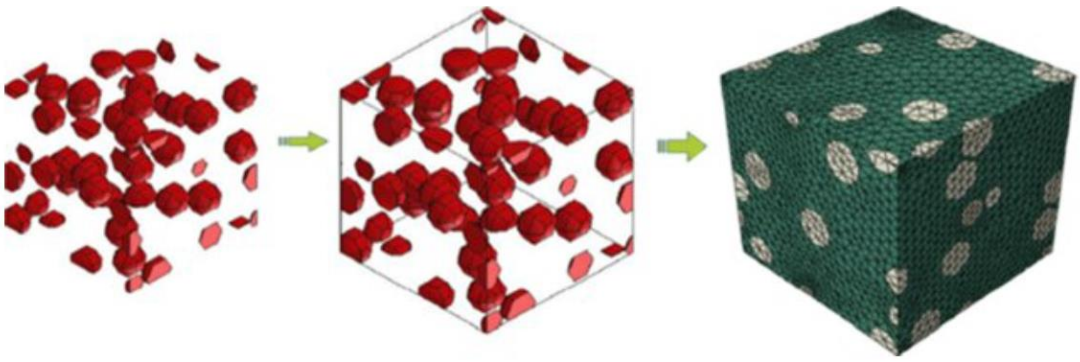


Figure 1. 11: Example of particles distribution in a matrix [58].

1.3.2.4 Fabrics

Reinforcements made of fabric can also improve a material's mechanical qualities. Fabric reinforcements come in four different varieties. The most often used textiles are unidirectional. The fibers of bidirectional fabrics are entwined in both directions (0°/90°). The fibers of multiaxial fabrics are orientated at 45°, 0°, and 90°. Lastly, the fibers of triaxial fabrics are orientated in three different directions: 0°, 60°, and -60°. Fabrics' effects on stiffness and strength enable the construction of sturdy, lightweight structures.

Goutianos et al. [59] created high-performance natural fiber composite systems using continuous textile reinforcements like textiles for structural purposes. Tests were conducted on various fabric types (***Figure 1. 12***), including biaxial woven, unidirectional, and non-crimp materials (***Figure 1. 13***). They discovered that low-twist yarns cannot be utilized in procedures like pultrusion or textile manufacture since they show inferior strength when evaluated dry in air. However, as the amount of twist increases, the mechanical qualities of the impregnated yarns deteriorate.

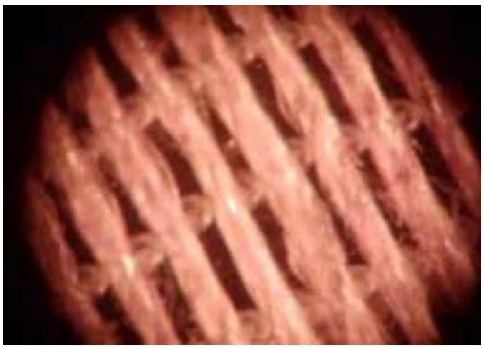
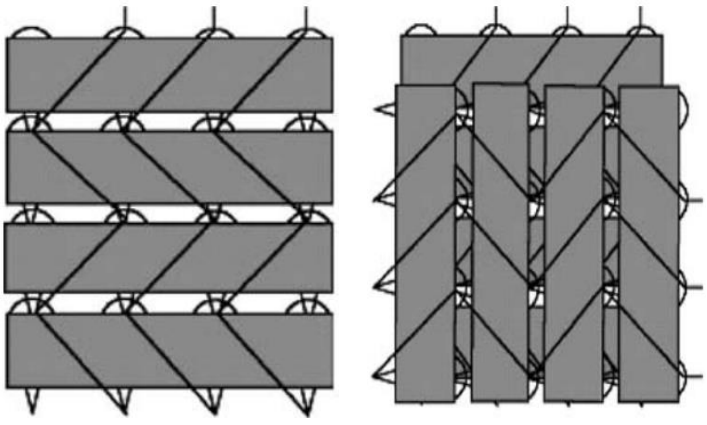


Figure 1. 12: Mono-axial fabric [59].



(a) *(b)*

Figure 1. 13: One axis fabric (a) with the fiber direction at 0°, and two stacked 0° and 90° single-axis fabric layers (b) [59].

1.3.3 Nanofillers

Nanofillers are nanometric-scale particles used in composite materials to enhance mechanical qualities. They have three main functions: mechanical reinforcement, enhanced thermal characteristics, and weight reduction. One benefit is the simplicity of adding nanofillers to the matrix, which provides excellent and robust structural stability.

Figure 1. 14 shows that careful design in three stages is required to produce polymer nanocomposites with high electrical and mechanical properties: building robust, conductive nanofiller networks, a suitable polymer matrix, and well-designed interfaces between the two components [60].

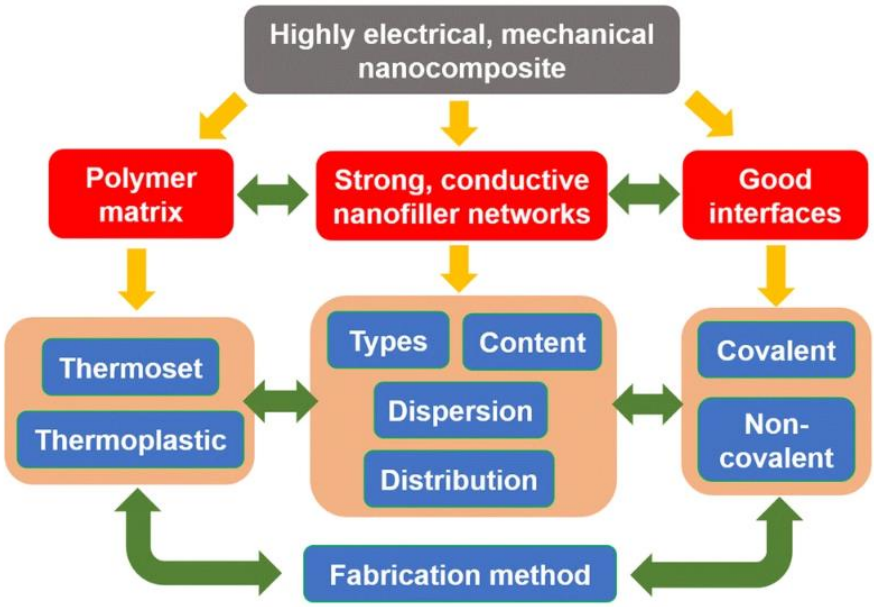


Figure 1. 14: Overarching factors should be considered while creating a highly electrically and mechanically performing nanocomposite [60].

1.3.3.1 Carbon Nanotubes (CNT)

Carbon nanotubes (CNTs) are a noteworthy advancement in nanostructures. Scientists are very interested in carbon nanotubes (CNTs) because of their unique qualities (***Table 1. 6***). Because of their remarkable mechanical, physical, and electrical qualities as well as their unique geometrical features—namely, their small diameter and high aspect ratio—carbon nanotubes have a plethora of potential technological uses. Research has demonstrated that composite materials' mechanical, thermal, and electrical properties can be significantly improved by dispersing a small percentage of nanotubes by weight throughout the matrix [61].

Figure 1. 15 depicts examples of single-walled (left) and multi-walled (right) carbon nanotubes.

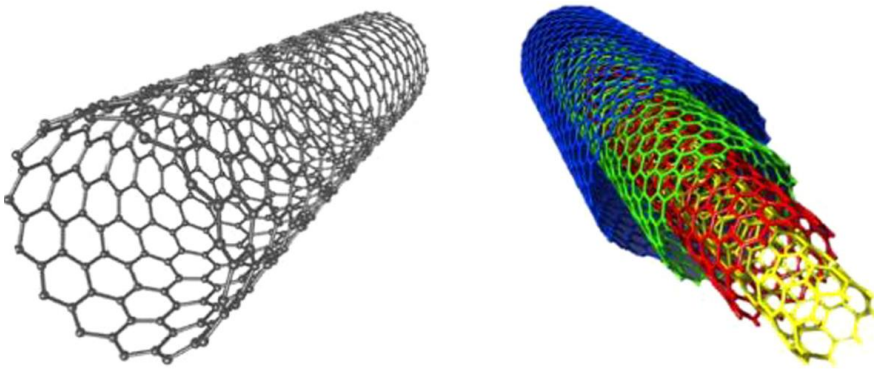


Figure 1. 15: Carbon nanotubes with one and more walls [61].

Table 1. 6: Properties of Composite Materials with Carbon Nanotube Reinforcements.

Matrix Material	**Reinforce -ments**	**Findings**	**Authors**
Aluminium	CNT	Compared to pure aluminum, improvements of up to 50% in tensile strength and 23% in stiffness were noted.	[62]
Cooper		For the composite material, including 1 vol.% CNT in the copper matrix, a +7% increase in thermal conductivity is demonstrated.	[63]
Epoxy		The improvement in tensile strength for crude CNT, carboxylated CNT, octadecyl amide-functionalized CNT, and hydroxylated CNT was 7.2%, 11.2%, 11.4%, and 14.2%, respectively, with a CNT loading of 0.5% by weight.	[64]
Glass		Experimental results show that the panel's surface temperature increases gradually with heating time, suggesting that CNT-based composite panels have good heating capability.	[65]
Aluminum-carbide		Because of the strong adhesion between the nanofillers and the matrix, increasing the interphase thickness between the CNTs and the Al matrix raises the nanocomposite Young's modulus.	[66]

1.3.3.2 Metallic Nanoparticles

Because of their solid electrical and optical characteristics and ease of production, metal nanoparticles are widely used in mechanics, biology, physics, and nanoscale scientific studies. These beneficial properties result from the particle's small size and material composition [67]. ***Figure 1. 16*** shows that nanomaterials, crucial to many materials' science applications, often exist in a few primary forms. The pure form of metal-based nanoparticles, commonly called metal nanoparticles, such as silver, copper, gold, titanium, platinum, etc., is included in the first category of nanomaterials. Metal oxide nanoparticles, such as titanium dioxide, silver oxide, zinc oxide, etc., constitute another class of nanomaterials [68].

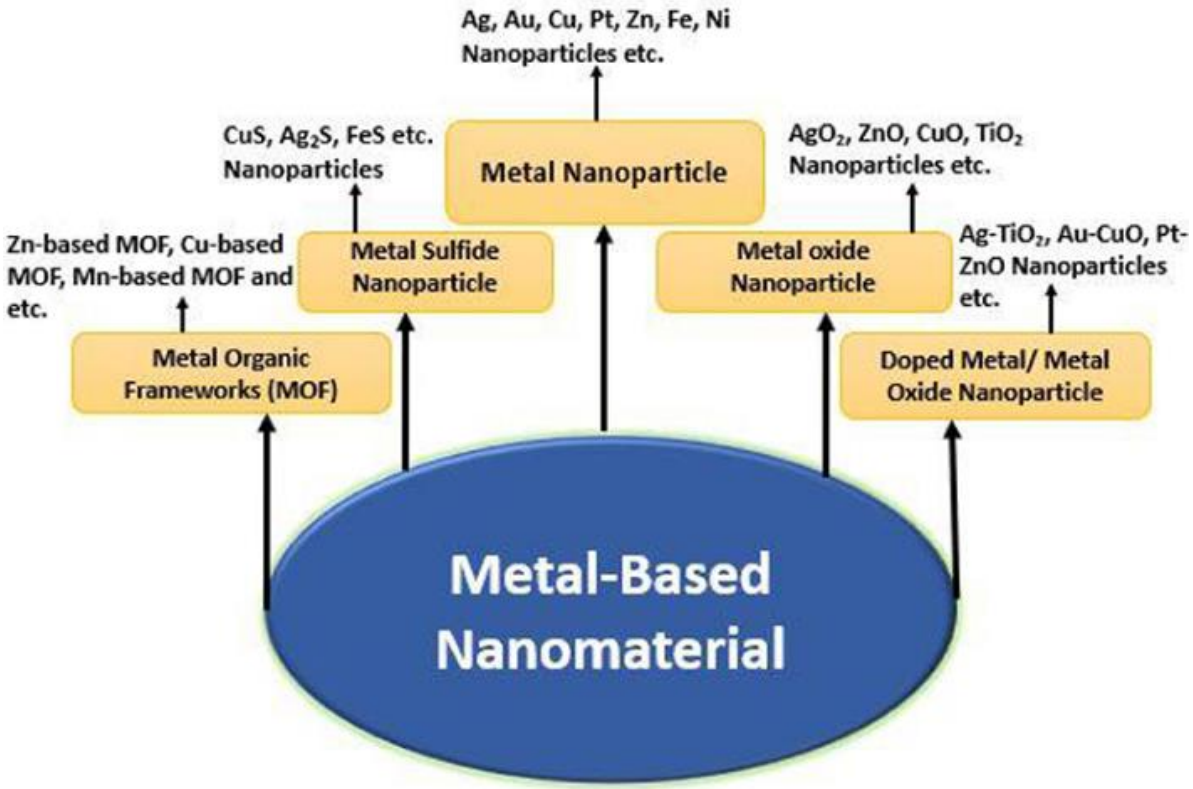


Figure 1. 16: Various kinds of nanomaterials based on metals [68].

Table 1.*7* presents previous work on metal nanoparticles in composites with different matrices.

Table 1. 7: A summary of the characteristics of polymer matrices that incorporate nanoparticles based on metals.

Matrix Material	Reinforcements	Findings	Authors
Acrylic resin	Silver	Including silver nanoparticles enhances the samples' mechanical and physical characteristics; they become noticeably more robust and more rigid than the virgin matrix.	[69]
Resin	Iron oxide	At 8–12 GHz, the permittivity of the passive and active inks was 2.25 and 2.73 F/m, correspondingly.	[70]
PLA	Zinc oxide	increased crystallinity in the nanocomposite, brought about by the 3D printing procedure and the presence of ZnO nanofibers.	[71]
PLGA	Titanium	The mechanical, thermal, and adhesion properties were enhanced by including titanium nanoparticles.	[72]

1.3.3.3 Ceramic Nanoparticles

Outstanding mechanical strength and hardness, high chemical and thermal stability, and excellent optical, electrical, and magnetic performance are just a few of ceramics' special qualities [72]. Because of their hardness and brittleness, ceramics are quite challenging to process in 3D printing. Cracking rarely produces 3D-printed products with good surface quality and dimensional precision [73]. However, to improve the mechanical properties of 3D-printed polymeric nanocomposites, ceramic nanoparticles have been employed as nanofillers in 3D printing.

To assess the influence of ceramic nanoparticles on material behavior and mechanical characteristics, Pragnya et al. looked at the effects of nanoparticle densifiers added to the printing medium on the mechanical performance of ceramics created by binder jetting. Samples of alumina were produced by suspending filler particles, which had an average size of 40 μm, and nanoparticles, which had an average size of 50 nm, at a variable concentration of 0–15 weight percent in the printing medium. They found that the mechanical and physical

characteristics of the samples were significantly affected by the presence of nanoparticles, as evidenced by an increase in the relative density of the samples of around 30% [74].

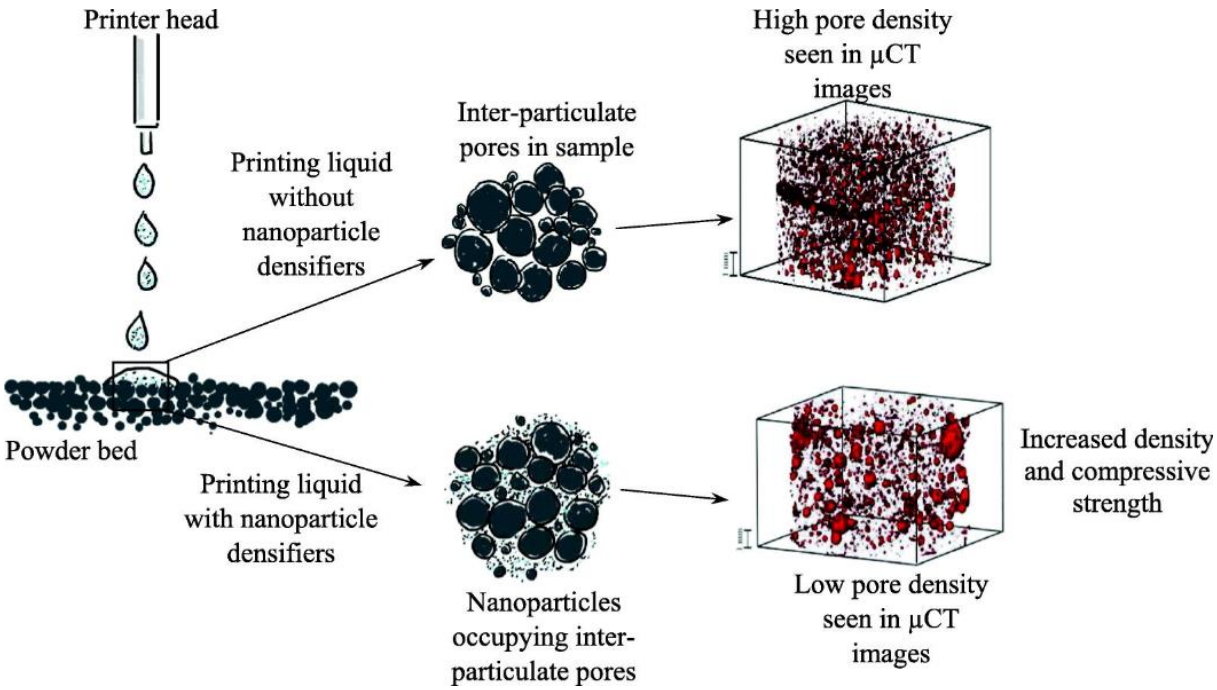


Figure 1. 17: The effect of ceramic nanoparticles on material behavior after printing [74].

1. 4 3D Printing

1.4.1 Definition of 3D Printing

The rapidly developing digital manufacturing process [75], known as additive manufacturing (AM) or 3D printing, entails constructing a three-dimensional object by superimposing layers [76]. Today, 3D printing is required in most industries [77]. Due to its many benefits, trustworthy outcomes, design, materials, and manufacturing techniques, 3D printing now plays a significant role in the aircraft and aerospace industry [78]. AM makes it possible to quickly have functioning parts with complex shapes, increasing reliability and lowering costs. AM can also create pieces with a lattice structure, which reduces an aircraft's weight and improves fuel economy [79]. Airbus has decreased the number of parts for a hydraulic tank from 126 elements to a single 3D printed portion, which is one of the accomplishments of 3D printing [80].

1.4.2 3D printing processes

1.4.2.1 Fused Deposition Modeling (FDM)

The fused deposition model (FDM), also known as fused filament fabrication (FFF), allows manufacturing products with complex geometry using mainly polymer or composite filaments.

Figure 1. 18 shows a schematic representation of the FDM technique. The printed material filament is loaded into the 3D printer's extruder. The filament is heated and melted to form liquid plastic. Then, following the instructions generated by cutting software using the generated FDM g-code, the 3D printer begins depositing the molten material layers layer by layer [81], [82]. After each layer has been completed, the print platform will be slightly reduced (layer height) and repeated for the next layer. This process repeats until all layers are printed and the model is completed.

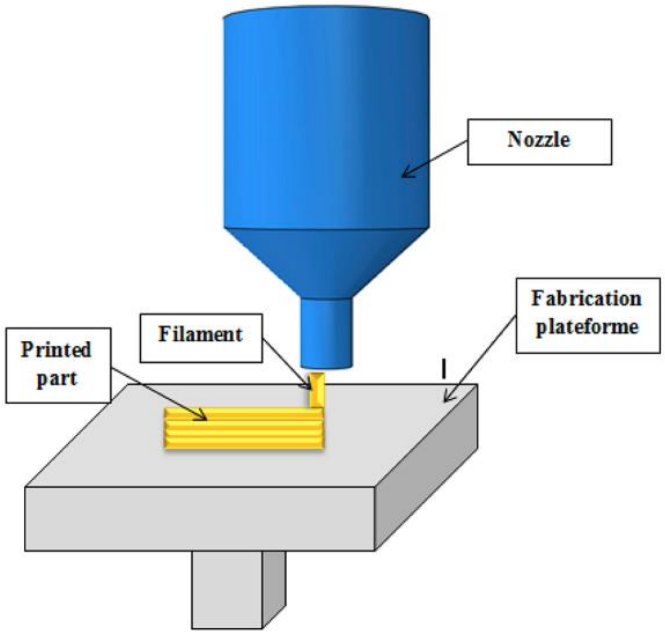


Figure 1. 18: Schematic view of the FDM technology [9].

1.4.2.2 Selective Laser Sintering (SLS)

Using laser energy to heat powder particles selectively ***Figure 1. 19***, Selective Laser Sintering (SLS) is a powder bed melting technique that produces partial melting of the powder, melting of the particles, and solidification of the melted material into a three-dimensional structure that complies with computer-aided design. It produces solid oral dosage forms of different sizes and shapes in a single step with great precision, eliminating the need for different excipients and solvents. Reprocessing and recycling raw materials is an additional advantage. SLS enables the manipulation of multiple process parameters, including feed bed temperature, print bed temperature, laser power, and layer thickness, to produce objects with regulated compactness, porosity, and internal architectures [83].

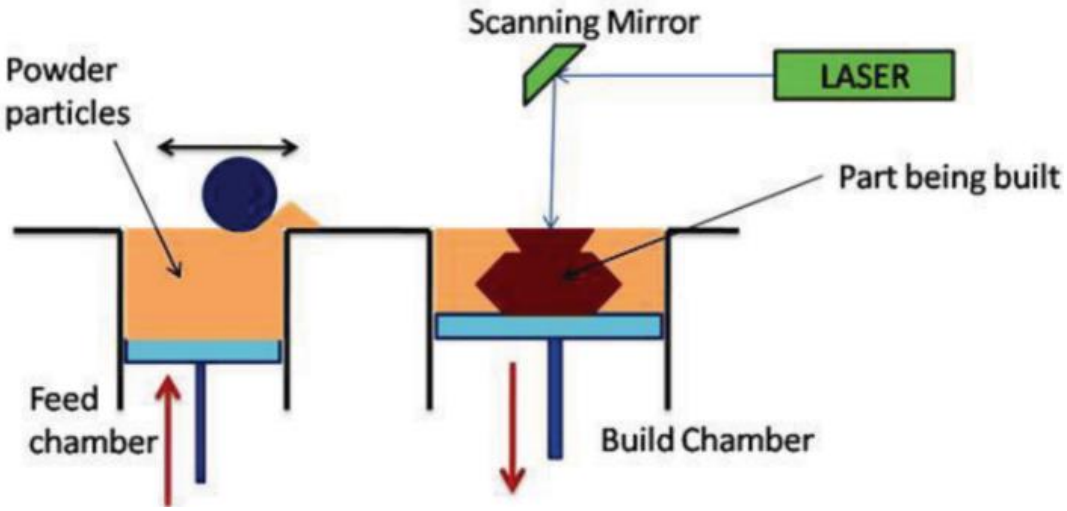


Figure 1. 19: Schematic view of the SLS technology [84].

1.4.2.3 Selective Laser Melting (SLM)

The SLM process is among the best choices for producing printed metal parts. This process melts metal powders to create dense parts. The printing process begins with preparing a fine layer spread on the build platform. Then, a high-power laser selectively melts the powder. After the stratification step, the platform slightly descends, and a new layer is spread. This cycle repeats the same way, layer by layer until the final part is produced.

SLM technology has overcome the challenges posed by intricate metal part manufacturing processes. ***Figure 1. 20*** depicts the SLM technology's processing flow [85].

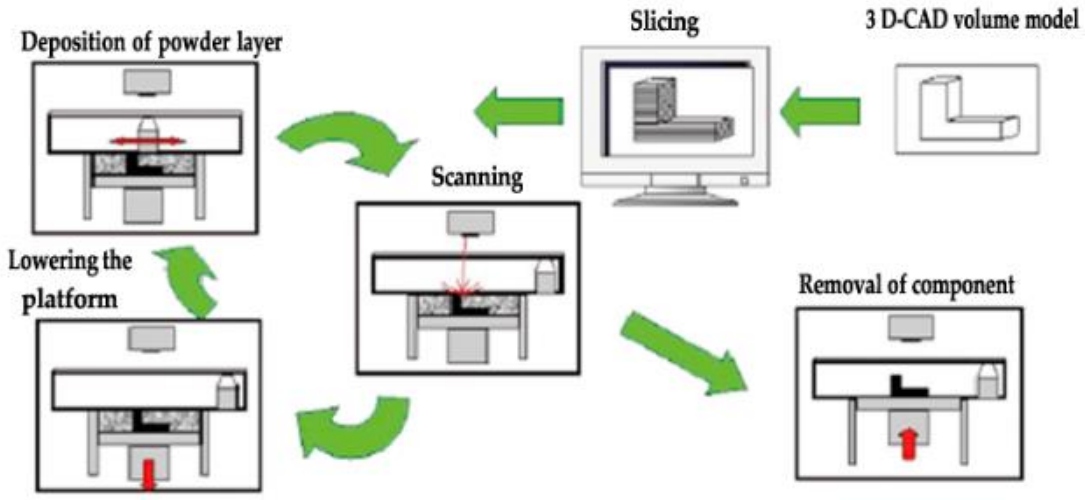


Figure 1. 20: Principle of the SLM process [85].

1.4.2.4 Stereolithography (SLA)

Stereolithography (SLA) is an additive manufacturing (3D printing) technique that uses a laser to harden a photosensitive resin, layer by layer, to create solid objects (***Figure 1. 21***). The

stereolithography apparatus (SLA), an early-adopted vat-based AM technology, uses photopolymerization to operate on the 3D printing process, solidifying photocurable resin by light absorption-triggered photopolymerization [86]. Photopolymerization uses light rays to spread a chain polymerization process that causes pre-existing macromolecules to become photo-crosslinked [87]. Another element or substance that creates covalent or ionic bonds between polymer chains is called a crosslinker. Photopolymerization causes a pattern within the resin layer to solidify and hold successive layers together.

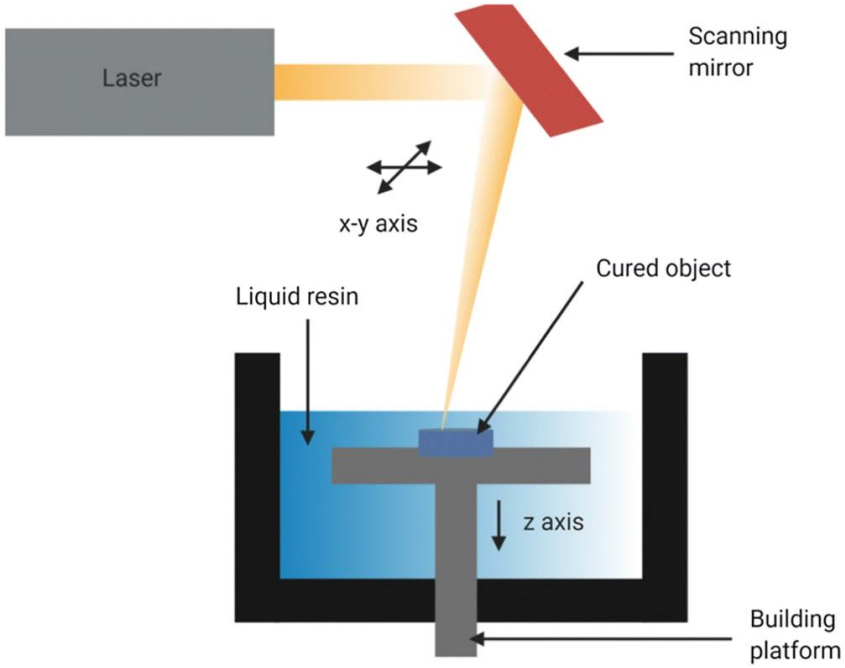


Figure 1. 21: Schematic diagram of the stereolithography process [88].

1. 5 Application sectors of printed composites

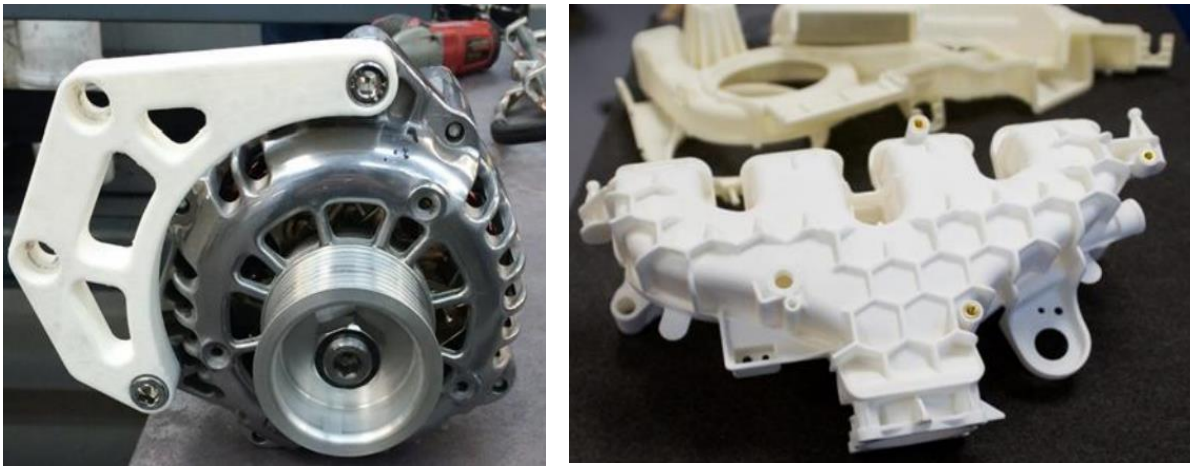
1.5.1 Automobile sector

The automotive industry is notable for its intense competition, making time-to-market reduction a critical factor. AM is a sustainable option that allows for flexible manufacturing of certain items with cost and timing constraints under control [89]. In the automobile sector, 3DP technology has produced fantastic shapes, making lighter, more intricate designs possible at the lowest possible cost. This saves designers from undergoing intricate and varied production operations to adjust. These 3D-printed parts include seat frames, armrest covers, instrument panels, and bonnet decorations [90].

A sophisticated, useful conduit support printed in SLS nylon is depicted in ***Figure 1. 22*** (a). The AM industry is known for its ability to produce intricate, lightweight brackets quickly—

overnight. Engineers can quickly move from a design on a computer to assembly in a short amount of time thanks to additive manufacturing (AM), which makes it possible to build organic shapes and designs and requires very little operator participation.

Figure 1. 22 (b) illustrates the design of a complex and practical SLS nylon duct. SLS technology can create low-volume, non-structural ducts, such as environmental control systems for aerospace and motor racing, enabling the design of highly optimized, highly detailed, one-piece structures [90].



(a) *(b)*

Figure 1. 22: (a) A functional alternator bracket printed using SLS nylon, (b) A complex, functional ducting design printed in SLS nylon [90].

For the automotive industry, additive manufacturing has numerous benefits over traditional manufacturing. Some of the benefits of additive manufacturing are listed in **Table 1. *8***.

Table 1. 9: Benefits of additive manufacturing.

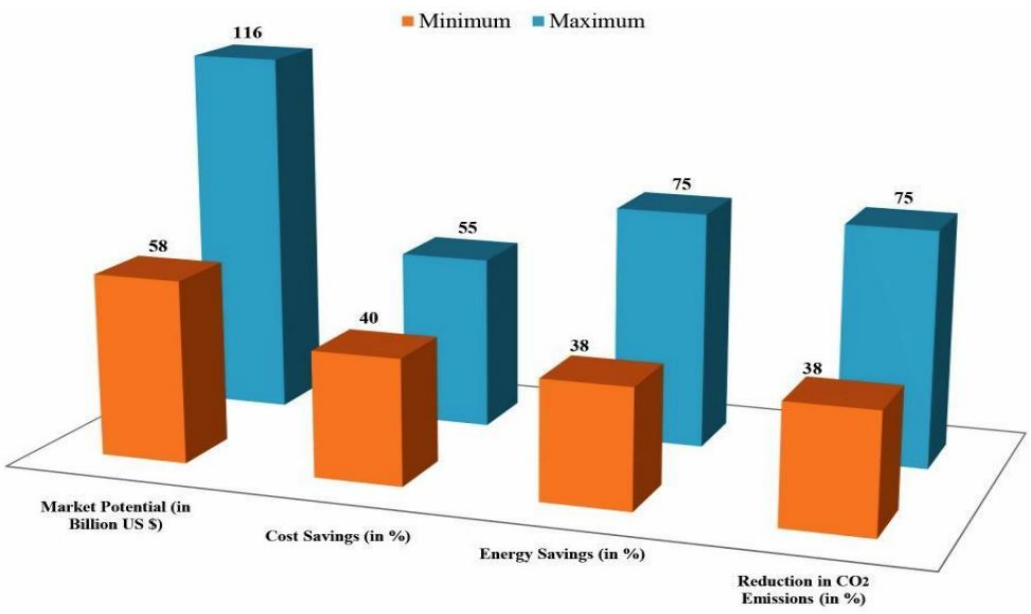
Benefits	Demonstration
Flexibility	Traditional manufacturing techniques limit product form and structure, hindering the manufacture of complex parts. Additive manufacturing offers unparalleled design flexibility by creating layers and realizing internal channels and features [91].
Rapid Prototyping	Additive manufacturing allows for the production of prototypes without the need for advanced tooling, thereby reducing production costs and time [92].
Decreased Material Expenditure	With a more excellent purchase-to-volume ratio, the subtractive method is frequently utilized in conventional manufacturing. Conversely, additive manufacturing produces little waste and has an excellent purchase-to-volume ratio [93].
Minimal Weight	Thanks to lattice structures, hollow sections, and topology optimization, additive manufacturing may create lightweight goods. The process of examining internal and external structures in light of performance requirements is known as topology optimization [94].

1.5.2 Aerospace sector

Manufacturing aerospace parts requires well-defined criteria, especially given the sector's sensitivity, ***Figure 1. 23***. Consequently, aerospace parts must be lightweight, durable, and precise. Therefore, 3D printing is among the top choices for producing parts dedicated to aerospace. 3D printing is equipped to produce products with a low density/quality ratio. Aircraft have a long lifespan, which can extend up to 30 years. The possession of long-lasting components incurs considerable expenses in terms of inventory. However, 3D printing allows for the assembly of components on demand, thus reducing maintenance time [95]. Although the aerospace sector has not yet fully embraced 3DP technology, Figure 1.23b shows the market for 3DP technology and its advantages by 2025.



(a) Examples of 3D Printed Rockets



(b) Impacts of 3D Printing Technology on the Aircraft Sector by 2025 [96]

Figure 1. 23: 3D Printing Technology in aerospace industry.

3D printers enable exceptional internal flow patterns that would be almost impossible to achieve using traditional manufacturing techniques. The image on the right of ***Figure 1. 24*** is a 3D-printed part, while the one on the left represents the original product. There are variations

between the two. The inner "fins" are brazed on the left. They are only printed on the right as part of the 3D assembly process. This component will function the same as the original once it has been certified for flight [97].



Figure 1. 24: Liquid oxygen flange [97].

1.5.3 Medical sector

3D printing and the continuous evolution of composite materials play a crucial role in the medical sector. Among the advantages of using 3D printing in the medical field is the customization, which allows for printing orthoses or prostheses tailored to patients' needs. Additionally, the reliability of producing complex-shaped products, which would be difficult to achieve with older techniques, is a significant benefit. It is important to emphasize that the materials used must be biocompatible.

Since 2000, static implant-guided surgery workflows have used AM-guided surgical templates. The most popular AM technology in implant dentistry is SLA [98]. Planning software determines the physical placement of a metal implant sleeve over the guide following production, ***Figure 1. 25***.



Figure 1. 25: Applications of polymer 3D printing in implant dentistry [98].

An additional illustration of printing in the medical domain is a prosthesis manufactured at Masanga Hospital with an Ultimaker S5 (***Figure 1. 26***). FDM was the 3D printing method employed. Cura, a free 3D printer cutting program, was used to import virtual 3D models and convert them into printable files before printing. The print parameters for the socket were 0.8 mm print core, 100% fill, 0.2 mm layer thickness, and 45 mm/s print speed [99].



Figure 1. 26: A prosthetic utilizing a 3D printed socket [99].

1. 6 Composite Materials and Damage Scenarios

In recent years, composite materials have played an increasingly important role in the global industry, thanks to rapid growth and steady development, driven in particular by the diversity of applications (aeronautics, automotive, naval, etc.). Nevertheless, composite materials give a disastrous image when they are used with poorly studied properties and mechanical characteristics that do not meet requirements, leading to problems of damage and sudden breakage.

1.6.1 Delamination

Poor bonding between layers during 3D printing is caused by several factors, such as printing parameters, the nature of the materials used, the printer, etc. The separation between the layers occurs under mechanical stress. One solution to avoid delamination is optimizing the printing parameters, especially the temperature and cooling parameters, to ensure good bonding or adhesion between the layers. To detect and characterize delamination, one can use non-

destructive testing, microscopy, and mechanical testing to evaluate the delamination resistance of the printed parts [100].

Nabeel et al. [101] assessed specimen fracture on a continuous thermoplastic composite specimen reinforced with carbon fibers by performing a 3-point bending test, ***Figure 1. 27***. They discovered that, rather than fracture or fracture in the composite component, delamination occurred towards the sides of the applied force between the layers as the CCFRTC specimen bent during the test under the influence of the applied load. Large standard deviation values were also seen during the test, along with sudden failure and a sharp decline in the stress value. Poor interfacial bonding between the layers of the 3D-printed composite may cause these oscillations [101].

Le et al. demonstrated a three-dimensional (3D) discrete element simulation of damage and crack propagation in composite materials. It addresses ply-to-ply delamination, fiber rupture, matrix cracking, and fiber/matrix debonding (Figure 1. 28) [102].

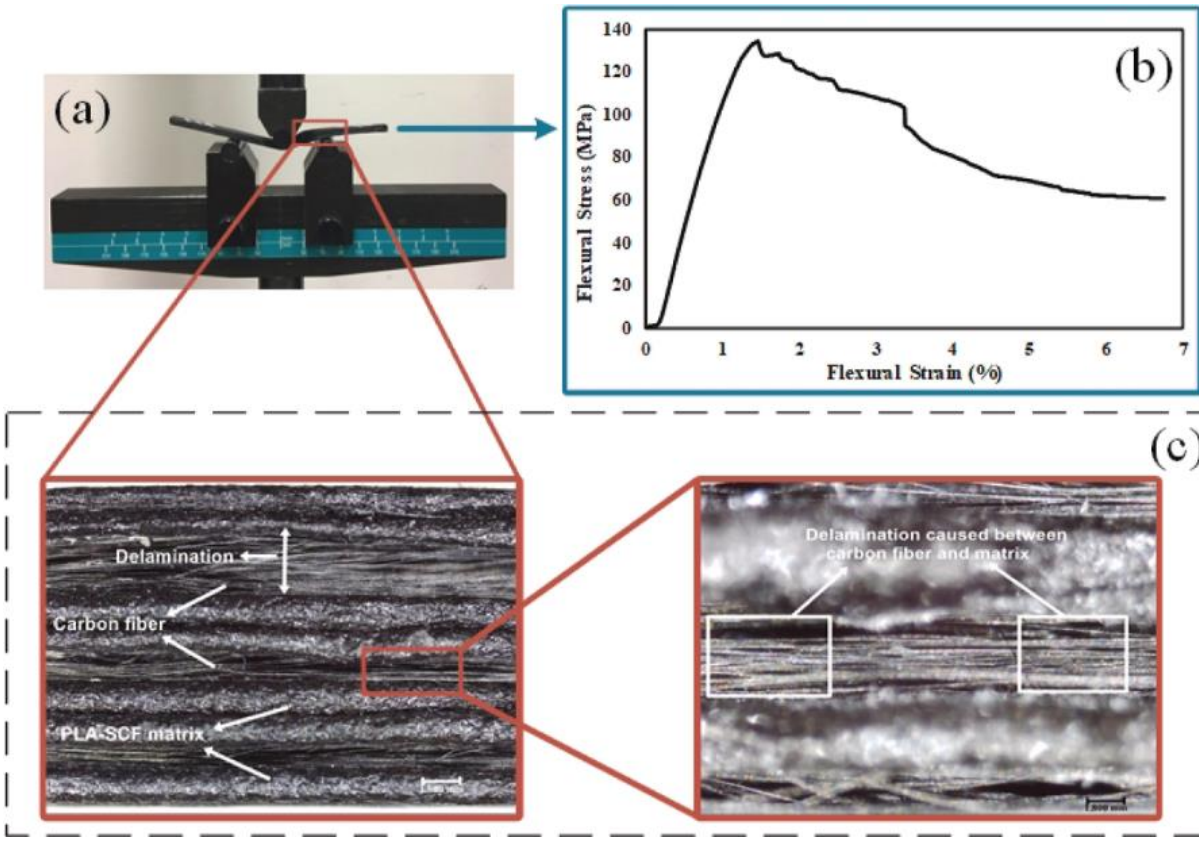


Figure 1. 27: Micrograph taken by the fracture interface microscope following the flexural test [101].

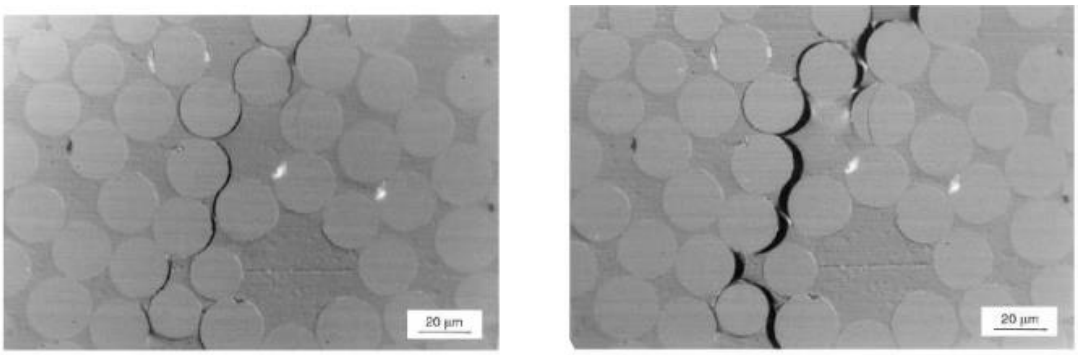


Figure 1. 28: Fiber-matrix debonding [102].

1.6.2 Cracking

The distribution and volume percentage of the reinforcements significantly impact the mechanical characteristics of composites reinforced with fibers and particles [103], [104]. Particle-reinforced metal matrix composites, such as SiC particle-reinforced aluminum, exhibit crack growth strongly influenced by the matrix's properties and the reinforcement's microstructure [105].

A finite element analysis of matrix cracking in a laminated composite material was performed by Shi et al. [106] from the point of initial contact to complete rebound. Since matrix cracking at a 90° angle is the primary damage mode anticipated in crack-induced delamination, an impact energy of 7.35 J was selected to replicate the damage evolution process in the cross-ply laminate. They discovered that, at 90°, matrix cracking initially appears in the lower ply, with a few cracks being seen in the central plies, ***Figure 1. 29*** [106].

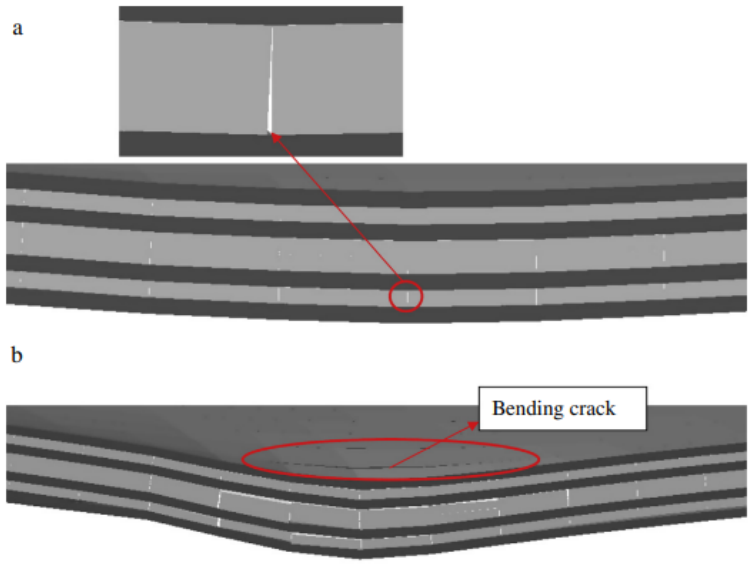


Figure 1. 29: Damage after the (a) First contact; and (b) complete impact energy transfer [106].

1.6.3 Fatigue

The potential for utilizing additively created parts as final products in various sectors has increased with the development of 3D printing technology. However, when fatigue loading is applied, the manufactured parts are highly prone to failure because of their layer-by-layer construction [107]. The fatigue mechanism can be defined in three actions. The first is initiating cracks, which can form due to porosity between layers. Then, the propagation of cracks is caused by the effect of applied load cycles on the part. Finally, the final failure occurs when the cracks reach a significant critical size (***Figure 1. 30***). Among the factors affecting fatigue are the composite architecture (fiber/matrix), forming processes, specimen condition, and printing parameters, ***Figure 1. 31***.

Emmanuel and colleagues assessed the mechanical characteristics of continuous carbon fiber composites manufactured using additive manufacturing. They discovered that fatigue testing at 70% of their ultimate strength for 200,000 cycles shows that woven carbon fiber composites are superior to unidirectional (non-woven) carbon fiber composites [108].

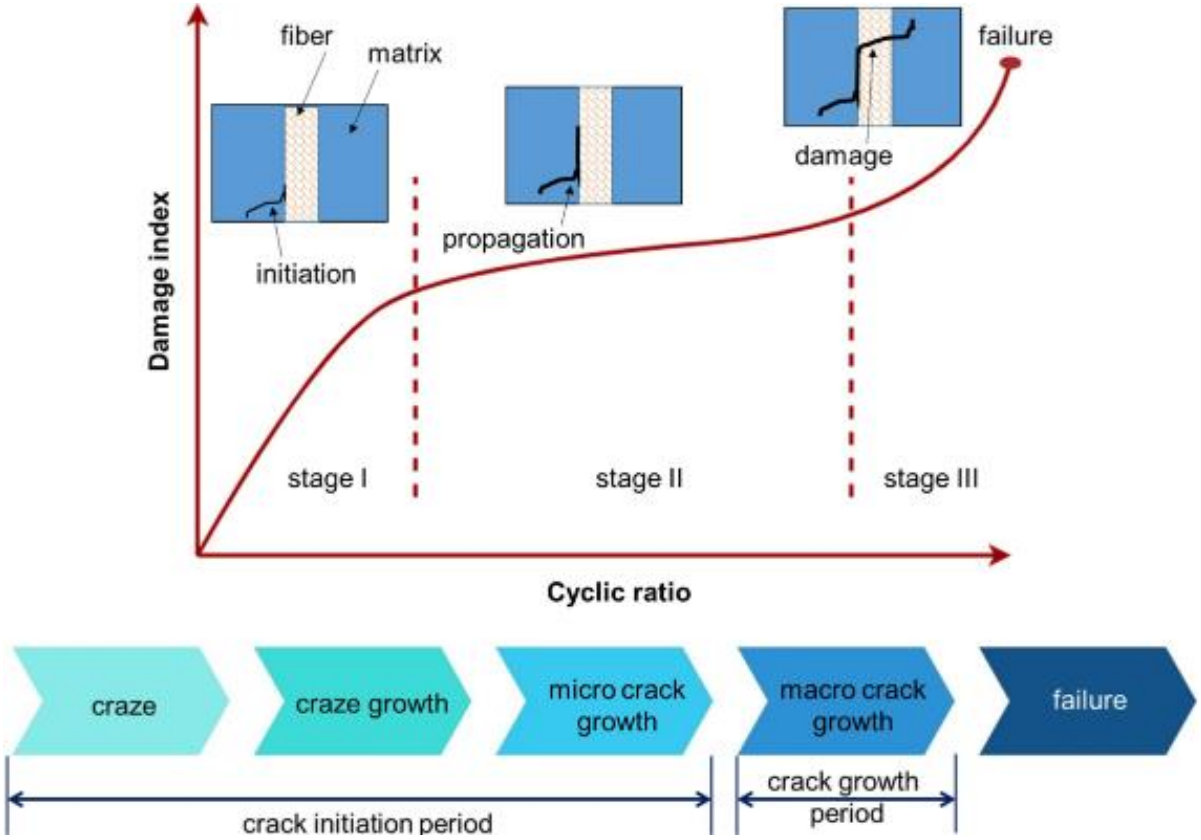


Figure 1. 30: Mechanism fatigue failure [109].

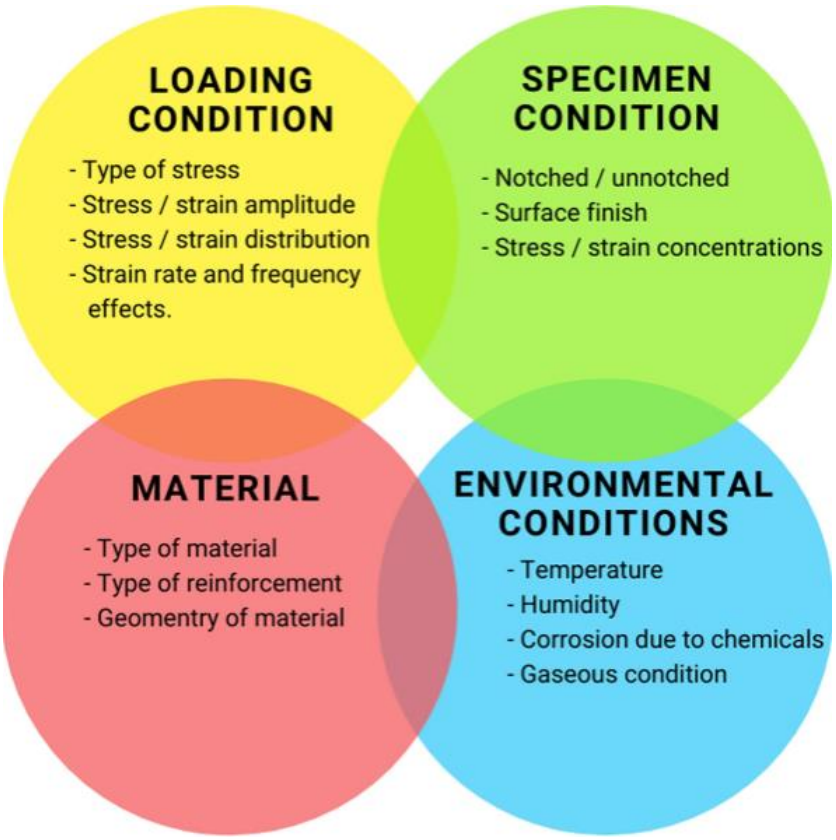


Figure 1. 31: Variables that impact the fatigue life of composite materials [109].

1. 7 Conclusion

This first chapter has established the theoretical framework for comprehending composite materials and how they fit into contemporary manufacturing processes, especially 3D printing. The definition, content, and types of matrices, nanofillers, and reinforcements used in the production of composite materials were examined. Emphasis was placed on the various industrial applications of these materials, particularly their growing importance in key industries such as automotive, aerospace, and medical sectors. Additionally, the degradation mechanisms that may impact the longevity of composites were discussed, along with the different additive manufacturing methods that utilize these materials. In the following chapter, we will delve deeper into the specific materials used for 3D printing, focusing on their properties, classifications, and suitability for various applications. This exploration will provide a foundation for understanding how these materials are selected and optimized in additive manufacturing processes.

CHAPITRE

2 Materials for 3D-Printing

Table of content

2. 1 Introduction 51
2. 2 Acrylonitrile butadiene styrene (ABS) 51
2.2.1 Printing parameters 51
2.2.2 Mechanical Properties 52
2. 3 Carbon fiber-Polyethylene Terephthalate Glycol (CF-PETG) 53
2.3.1 Mechanical properties and printing parameters 53
2.3.2 Differential scanning calorimetry analysis (DSC) 54
2.3.3 Scanning Electron Microscopy analysis (SEM) 55
2.3.4 Structural design 57
2.3.4.1 Tensile samples 57
2.3.4.2 Compression samples 59
2. 4 Aerosil/Polycarbonate 61
2.4.1 Properties of Aerosil/Polycarbonate 61
2.4.2 Production of ceramic nanofiller-filled masterbatch 62
2.4.3 Production of coils for additive manufacturing and printing parameters 63
2.4.4 Nanoscopic analysis (SEM) 65
2.4.4.1 Sample preparation 65
2.4.4.2 Scanning electron microscope (zoom ×35) 66
2.4.4.3 Scanning electron microscope (Zoom ×50) 66
2.4.4.4 Scanning electron microscope (zoom ×1500) 67
2. 5 Conclusion 68

2. 1 Introduction

The second chapter provides a comprehensive summary of all the resources used to complete the thesis. The numerical analysis of the thermoplastic material ABS was initiated by the thesis requirements and the necessity of working on thermoplastics and 3D-printed composite materials. This initial phase aimed to develop proficiency with the tools required for numerical analysis.

Following this, the focus was on 3D-printed thermoplastic composites, specifically CF-PETG, a thermoplastic PETG matrix reinforced with carbon fibers. Tensile and dynamic compression tests were conducted as part of this material's experimental and numerical investigation. In-depth analyses, including Differential Scanning Calorimetry (DSC) and Scanning Electron Microscopy (SEM), were also performed to explore the material's properties further.

The polycarbonate material reinforced with ceramic nanoparticles, specifically Aerosil, was then analyzed to observe the effect of the nanoparticles on the material’s behavior. Nanoscale investigations were carried out to understand the dispersion of nanoparticles within the matrix. Additionally, static compression tests were conducted at varying temperatures alongside a numerical study to evaluate the homogeneity of both materials.

2. 2 Acrylonitrile butadiene styrene (ABS)

2.2.1 Printing parameters

In this section, we worked with FDM-ABS samples produced by Parham et al. [110] using an Umbriel 300x 3D printer. To obtain the best possible sample quality with the fewest manufacturing defects, the printing system's resolution was adjusted to 300 µm. A numerical analysis of the ABS material was carried out to validate Parham et al.'s experimental results. Fused Deposition Modeling (FDM), based on material extrusion and operates by extruding molten polymer on a printer bed platform, is a widely used additive manufacturing process. This process is carried out layer by layer until the entire model is produced. The parameters of the FDM process mainly control the quality of the finished pieces. ***Table 2. 1*** lists the consistent construction characteristics used to create test specimens for tensile and fracture investigations. For ABS-FDM products, the 45/-45° weft angle has been used for this work since it can increase mechanical and fracture strength. The ABS filament data sheet was used to choose the nozzle and bed temperatures [110].

Table 2. 1: Constant building parameters for manufacturing the test specimens.

Building parameters	**Value**
Filament diameter (mm)	1.75
Infill density (%)	100
Nozzle diameter (mm)	0.4
Nozzle temperature (°C)	235
Bed temperature (°C)	140
Raster angle (deg)	45/-45

2.2.2 Mechanical Properties

The mechanical properties of ABS are similar to those used by many researchers. ***Table 2. 2*** presents the mechanical properties of ABS used in this work. The tensile strength ranges from 18 to 50 MPa, while the elongation at break varies between 40 and 90%. Due to these high mechanical properties, ABS is in high demand in many industries. ABS also changes its behavior under the effect of temperature, as it belongs to the thermoplastic family. The heat deflection temperature of ABS is around 95 to 105°C.

Table 2. 2: Mechanical Properties of ABS material.

Property	**Value**
Tensile Strength (MPa)	18-50
Elongation at Break (%)	40-90
Tensile Modulus (GPa)	1.2 - 3.2
Flexural Strength (MPa)	40-100
Flexural Modulus (GPa)	1.7 - 3.2
Notched Izod (J/m)	1-3
Impact Strength (J/m)	4-20
Heat Deflection Temperature (°C)	95-105

2. 3 Carbon fiber-Polyethylene Terephthalate Glycol (CF-PETG)

2.3.1 Mechanical properties and printing parameters

For the second material, we'll be employing CF-PETG composite material made by the Fused Filament Fabrication (FFF) method of 3D printing. CF-PETG is a highly sought-after material in various industries due to its exceptional mechanical properties [111], [112], [113]. In numerous medical fields, including tissue engineering, dentistry, optometry, vascular health, cardiology, orthopedics, neurology, gynecology, and surgery, PETG has proven to be a feasible biomaterial [114].

Compared to ordinary PETG, CF-PETG is perfect for producing structural parts for industries including robotics, aerospace, automotive, and drones, where higher mechanical strength and rigidity are needed [115].

It is the perfect option for applications where strength and resistance are crucial because it is lightweight and incredibly durable [116], [117], [118]. Combining carbon fiber reinforcement with PETG thermoplastic matrix provides excellent stiffness, impact resistance, and dimensional stability [119]. CF-PETG exhibits a high strength-to-weight ratio (***Table 2. 3***), making it suitable for structural integrity applications without compromising weight limitations. Its distinct makeup enables improved load-bearing capacity and deformation resistance. CF-PETG has excellent mechanical resistance, allowing it to be used in various conditions. The printing parameters for CF-PETG have been established and are displayed in ***Table 2. 4***.

Table 2. 3: Mechanical properties of CF-PETG.

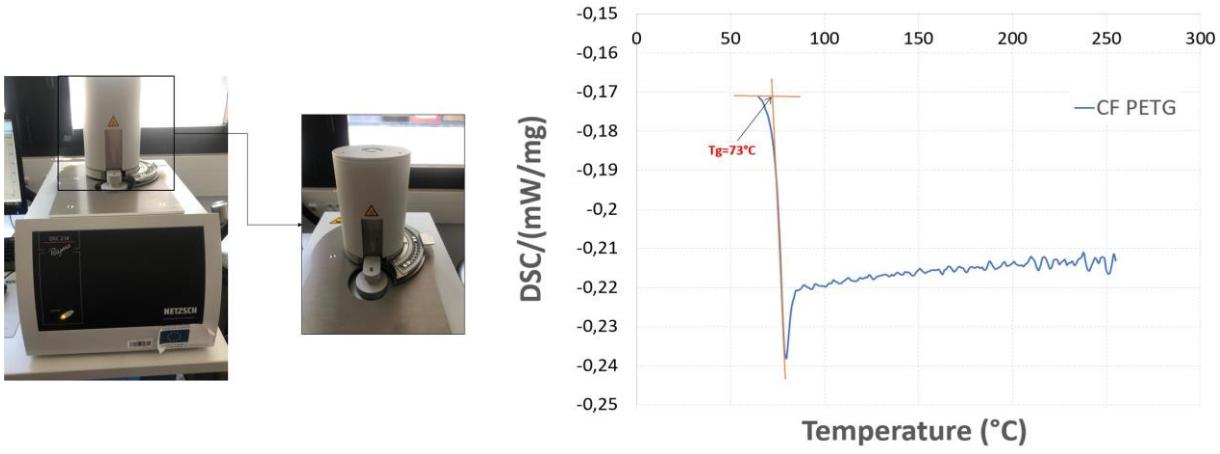
Parameters	**Value**
Density	1.0
Tensile modulus	4700 (MPa)
Flexural modulus	3800 (MPa)
Elongation at break	2 (%)
Stress at breakup	42 (MPa)
Charpy	20 (kJ/m²)

Table 2. 4: Printing parameters for CF-PETG composite material.

Parameters	Value
Extrusion temperature	220 (°C)
Plate temperature	90 (°C)
Nozzle diameter	0.3 (mm)
Printing speed	70 (mm/s)
Filament diameter	1.75 (mm)

2.3.2 Differential scanning calorimetry analysis (DSC)

A thermal analysis technique called differential scanning calorimetry (DSC) was used to investigate the thermal properties of CF-PETG. It measures the differences in heat transfer between a reference control and an analytical sample. With the calorimetric analysis that DSC offers, it is possible to determine composites' glass transition temperature (Tg). The glass transition temperature is when an amorphous polymer changes from a complex (glassy) state to a soft (rubbery) one or vice versa. Tg directly correlates with the material's strength and capabilities in a given end-use application. The curve obtained from the thermal analysis is displayed in ***Figure 2. 1***, and it is evident that the Tg of CF-PETG is 73°C.



(a) DSC 214 Polyma *(b) Determination of Tg (°C)*

Figure 2. 1: DSC analysis.

2.3.3 Scanning Electron Microscopy analysis (SEM)

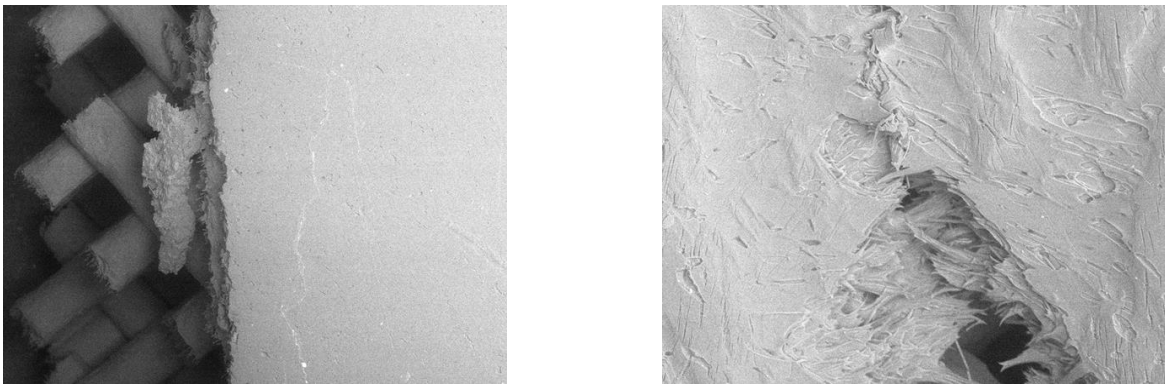
Figure 2. 2 shows the results of the scanning electron microscopy (SEM) study. First, as shown in the figure, the material's surface morphology is uniform (***Figure 2. 2*** *(c)*). This uniformity proposes a homogeneous distribution of material components at the surface size to ensure continuous mechanical and aesthetic features across the material.

Looking more closely at ***Figure 2. 2*** (c) and (d), we see that the carbon fibers are dispersed uniformly throughout the PETG matrix. This result is especially significant since it shows that the fibers have been successfully integrated throughout the material, preventing areas of discontinuity or concentration that would compromise the overall structure.

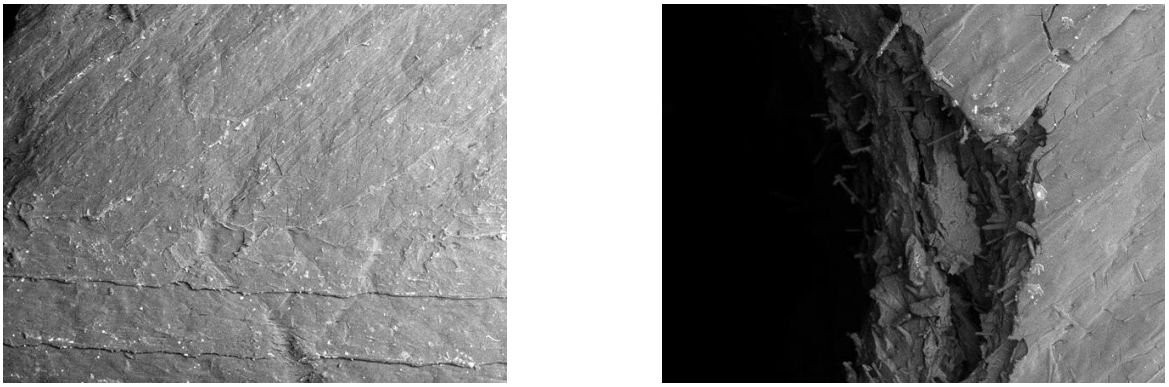
In addition, it's essential to recognize that the fibers in 3D have a random direction (***Figure 2. 2*** (c)). This random dispersion reinforces the material isotropically and uniformly in all directions. This quality is crucial for guaranteeing balanced mechanical performance in all directions, which is frequently a top priority in the design of composite materials.



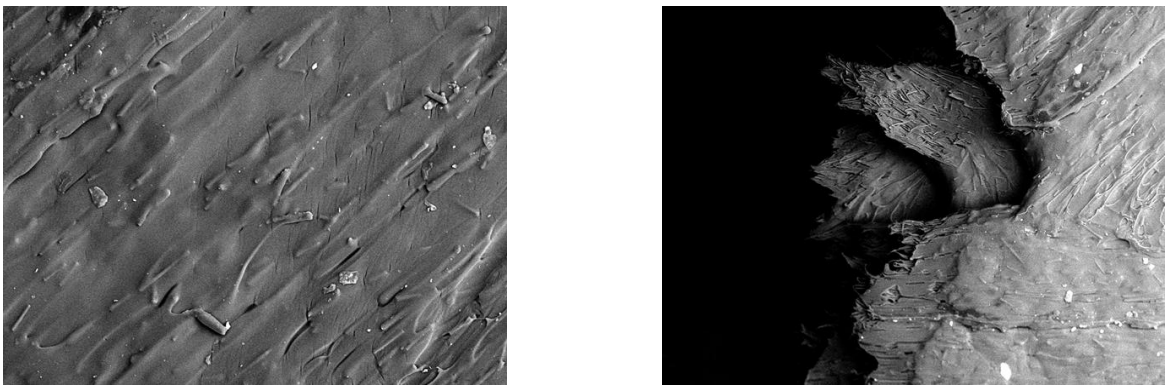
(a) 20% Honeycomb



(b) 50% Straight



(c) 75% Honeycomb



(d) 75% Straight

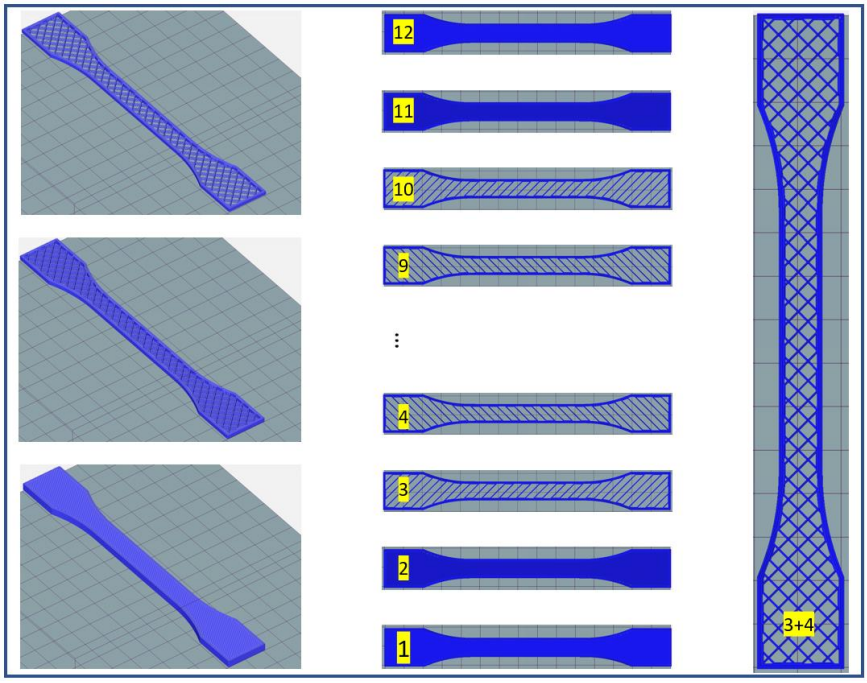
Figure 2. 2: Scanning Electron Microscopy (SEM) analysis of CF-PETG for different filling ratios.

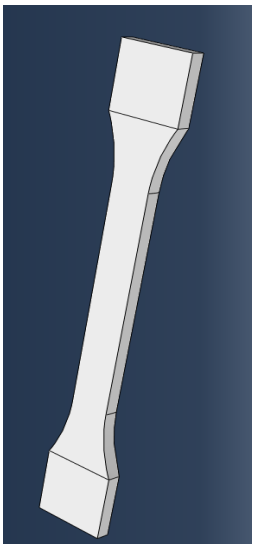
2.3.4 Structural design

2.3.4.1 Tensile samples

The samples presented in this study were manufactured using the FDM procedure. ***Figure 2. 3*** shows the operating diagram of the FDM system and the printing system used in our study to print the samples. ***Table 2. 5 (a)*** summarizes the printing characteristics of all samples. Two different CF/PETG composite configurations, Nida and Rectilinear, were experimentally tested. The FDM process created specimens 151.8 mm long, 4 mm thick, and 21.8 mm wide. The fill density is modified during specimen fabrication to better understand the mechanical properties. All specimens used to test the effect of fill densities were manufactured with NIDA and REC fill patterns, with fill densities of 20%, 50%, 75%, and 100%, ***Figure 2. 3.***

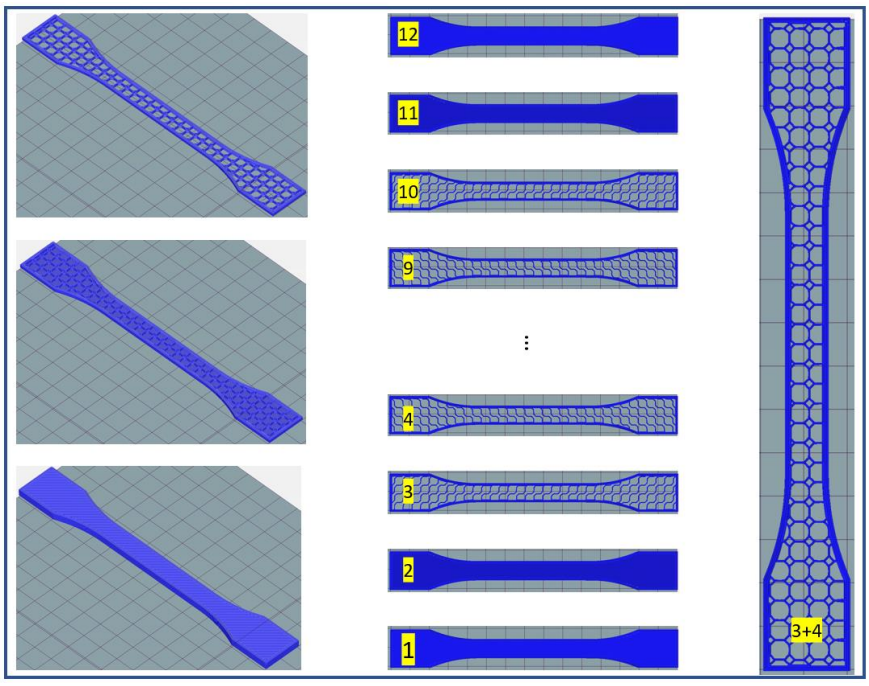
When selecting the filler, each print job's specifications must be considered. Saving money and time without compromising material durability is the fundamental justification for printing less than 100% filler. ***Table 2. 5 (b)*** shows the total number of parts printed and a comparison of the different filler densities in terms of time and material required for printing.





Abaqus View

(a) Printing rectilinear pattern, 20%





Sample

(b) Printing Nida pattern, 20%

Figure 2. 3: 3D printing system and the difference between the two infill patterns.

Table 2. 5: (A) Print Properties of CF/PETG and (B) Print statistics.

(A)			**Print Properties of CF/PETG**		
Extrusion temperature			395	(°C)	
Plate temperature			165	(°C)	
Nozzle			0.5	(mm)	
Print speed			40	(mm/s)	
Layer thickness			0.3	(mm)	
(B)		**Number of layers**	**Total rows**	**Filament required (mm)**	**Print Time**
Rectilinear	20%	12	11140	871	0h40mn36s
	50%	12	12369	1064	0h47mn01s
	75%	12	12369	1272	0h47mn01s
Honeycomb	20%	12	12832	882	0h41mn04s
	50%	12	35752	1226	0h54mn06s
	75%	12	35752	1515	0h54mn06s
	100%	12	15875	1438	1h03mn21s

2.3.4.2 Compression samples

The sample's appearance is shown in ***Figure 2. 4***. Four different CF-PETG composite topologies were the subject of experimental research. The FFF method created 13 × 13 × 13 mm cubic samples. During sample fabrication, the fill density was changed to examine mechanical properties. The controller for the 3D printer received the G-code file. As shown in ***Figure 2. 5***, all specimens that investigated the fill density effect were made using the same honeycomb infill structure, with fill densities of 20%, 50%, 75%, and 100%, respectively. The selection of infill should correspond to the demands of a particular printing task. Lower infill percentages are typically used to cut expenses and speed up printing. ***Table 2. 6*** shows the total number of printed pieces and contrasts the costs and printing times for various infill densities, illustrating the variances in the amount of material needed and printing time.

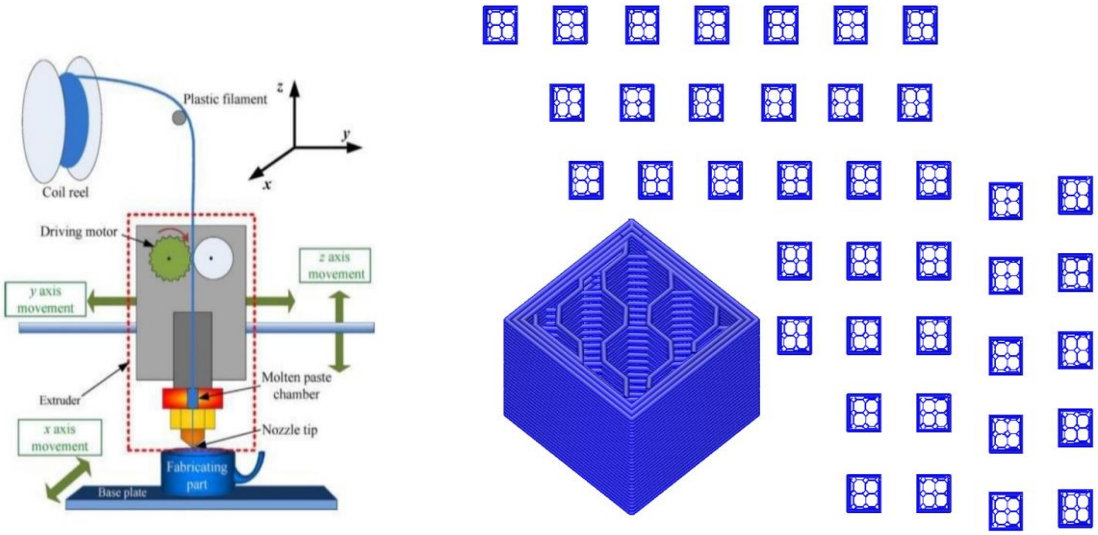
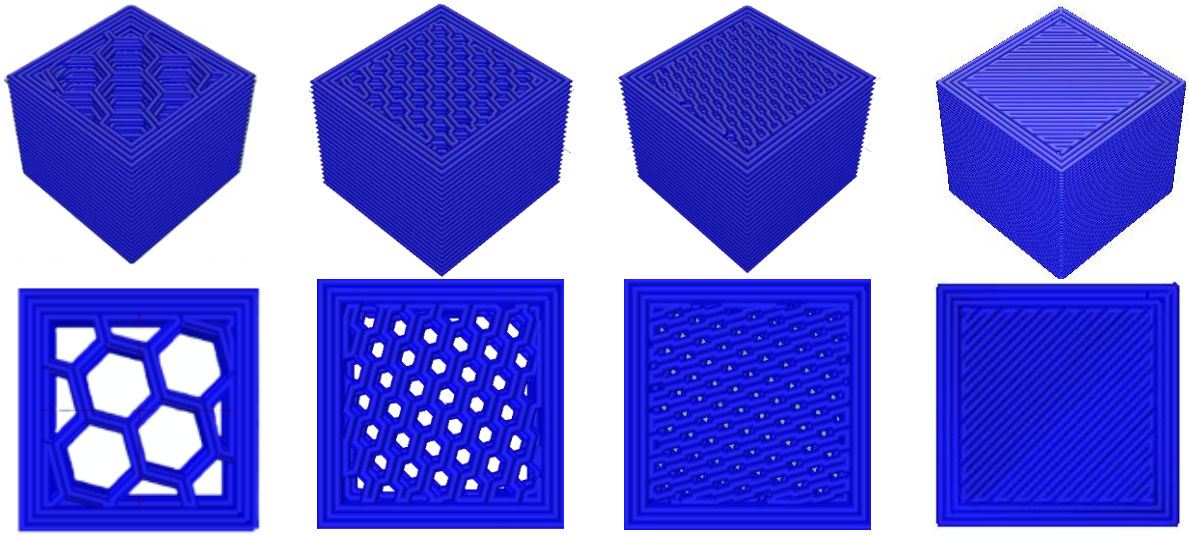


Figure 2. 4: Fused filament fabrication (FFF) process.



(a) 20% *(b) 50%* *(c) 75%* *(d) 100%*

Figure 2. 5: Honeycomb-Patterned PETG Composites: Examining Varied Configurations with Short Carbon Fibers.

Table 2. 6: Specifics of the tested parts' 3D printing.

Infill densities	Number of specimens	Number of layers	Total number of lines	Filament required (mm)	Extruder (mm)	Printing time
20%	40	48	323041	11974	8386	8h:52m:48s
50%	40	48	571921	17007	13419	12h:2m:48s
75%	40	48	600348	22083	16799	13h:41m:21s
100%	40	48	409521	18402	14815	13h:41m:56s

2. 4 Aerosil/Polycarbonate

2.4.1 Properties of Aerosil/Polycarbonate

The polymer matrix, polycarbonate (PC), a thermoplastic known to offer protection against ballistic impact, will be the third material used [120], [121]. This material exhibits remarkable impact and puncture resistance because of its substantial work hardening and extraordinarily high yield strength and ductility [122]. The fillers' presence further enhances the material's resistance to impacts [123], [124]. We are particularly interested in Aerosil 300, a silica grade with a large specific surface area and well-known for its tiny particle size [125], [126]. This distinctive feature of Aerosil 300 sets it apart from other silica grades and emphasizes its value in various applications [127]. Because of its small particle size, it is more easily dissolved and interacts with surrounding components more successfully, giving the finished products desirable qualities. Aerosil 300's sizeable specific surface area has the potential to improve performance and functionality in a variety of industries, from coatings and composites to medicinal formulations. ***Table 2. 7*** shows polycarbonate's mechanical, thermal, and electrical properties.

Table 2. 7: The characteristics of polycarbonate.

Proprieties		**Values**
Mechanical	Density $(g/cm3)$	1.2
	Tensile strength Rm (MPa)	70
	Resilience (KJ/m^2)	20
	Young Modulus (MPa)	2250
	Elongation at break (%)	50
Thermal	Glass transition T° $(°C)$	148
	Coefficient of expansion $(mm/°C)$	$6.5 * 10^{-5}$
	T° of merger $(°C)$	220
	Thermal conductivity $(W/°C.m)$	0.21
Electric	Dielectric constant at 1 MHz	2.9
	Dielectric resistance $(KV.mm^{-1})$	15-67

Polycarbonate is a lightweight, resilient material with a mechanical density of 1.2 g/cm^3, a Young's modulus of 2250 MPa, and a tensile strength of 70 MPa. Its high thermal melting point, glass transition temperature, low thermal conductivity, and low expansion coefficient make it ideal for dimensional accuracy and energy efficiency.

Table 2. 8: Properties of Aerosil 300.

Proprieties	**Values**
Specific surface (m²/g)	300
PH	3.7–4.7
Acid resistance	Excellent
Diameters of elementary particles (nm)	12
Tensile strength (N/mm²)	1.25
Elongation at break (%)	530
Resilience (%)	42

2.4.2 Production of ceramic nanofiller-filled masterbatch

The masterbatch loaded with ceramic nanofillers in the internal mixer must be precise and well-planned. To achieve thermal homogeneity, the polycarbonate is first heated to 125°C for 16 hours in an oven. The filler is also exposed to this temperature at the same time. For ideal mixing conditions, the inside mixer is heated to 280°C. The creation of a masterbatch containing ceramic nanofillers in an internal mixer is depicted in ***Figure 2. 6***.

The polycarbonate and fillers are precisely weighed when the components achieve the proper temperature. The fillers are added to the mixer at 20 tr/min speed after adding the polycarbonate. The mixture is then kept at this speed for two minutes before being accelerated to 50 tr/min for three minutes to promote uniform dispersion of the nanofillers in the polymer matrix. After thoroughly mixing and collecting the material, the mixer is thoroughly cleaned to prevent contamination. After precisely incorporating ceramic nanofillers, the material is ground to the appropriate particle size and prepared for use in producing end products with improved qualities.



(a) Internal mixer



(b) Inside the internal mixer



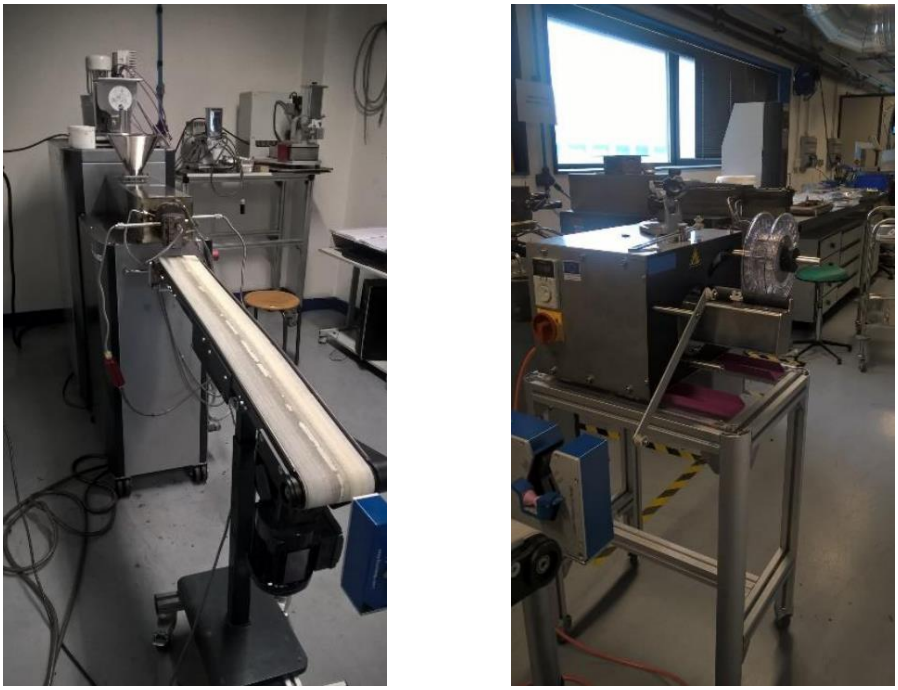


(c) Internal mixer containing polycarbonate filled with ceramic nanofillers

Figure 2. 6: Production of ceramic nanofiller-filled masterbatch in an internal mixer.

2.4.3 Production of coils for additive manufacturing and printing parameters

Figure 2. 7 shows how to produce coils (polycarbonate + Aerosil 300) for additive manufacturing. Interestingly, early process parallels exist between the stages needed to produce coils for additive manufacturing and pellets for conventional injection molding. The initial stage in both situations is to oven-process the polycarbonate and masterbatch for 16 hours at 125°C. This stage guarantees the mixture is as homogenized as possible before being processed further. Next, in both scenarios, the single-screw extruder is heated to 280°C as part of the ongoing process. The extruder settings, which revolve at a speed of 40 tr/min, must be exact to guarantee the final product's quality.



(a) Coil manufacturing equipment



(b) Granules



(c) Coils (PC +2% AEROSIL 300)

Figure 2. 7: Production of coils for additive manufacturing.

After this shared step, the two processes differ. After feeding the PC + masterbatch combination into the extruder hopper, a rod is produced at the extruder output, ready for standard injection. In contrast, the finished rod is transported on a conveyor belt during the coil manufacturing process for additive manufacturing before it goes through the winding process.

We started producing the specimens for the compression tests after successfully obtaining the required material, polycarbonate reinforced with Aerosil nanoparticles at concentrations of 1%, 2%, and 4%. These cube-shaped, 13×13×13 mm^3 specimens were made with the Fused Deposition Modeling (FDM) additive manufacturing technique. ***Table 2. 9*** lists the printing parameters that were employed.

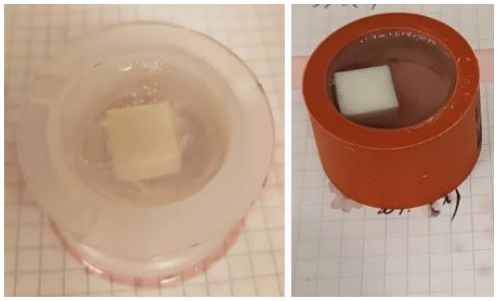
Table 2. 9: Printing parameters.

Parameters	Values
Layer height (mm)	0.2
Layer width (mm)	0.4
Filling wt.% (%)	100
Nozzle temperature (°C)	270
Chamber temperature (°C)	110

2.4.4 Nanoscopic analysis (SEM)

2.4.4.1 Sample preparation

Before the nanoscopic analysis, a well-defined sample preparation and polishing cycle was followed to ensure optimal results. The first step in this cycle involved embedding the samples to provide protection and ensure precision. Embedding also facilitated safer and more practical handling of the samples. Following this, the polishing stage ensured that no foreign material contaminated the sample's surface and that all samples were flat and mirror-polished. In the final step, a metalized coating was applied to the sample's surface to improve contrast and allow for more precise observation of nanoscopic details. ***Figure 2. 8*** presents the three steps before the nanoscopic analysis attack.



(a) Coating



(b) Polishing

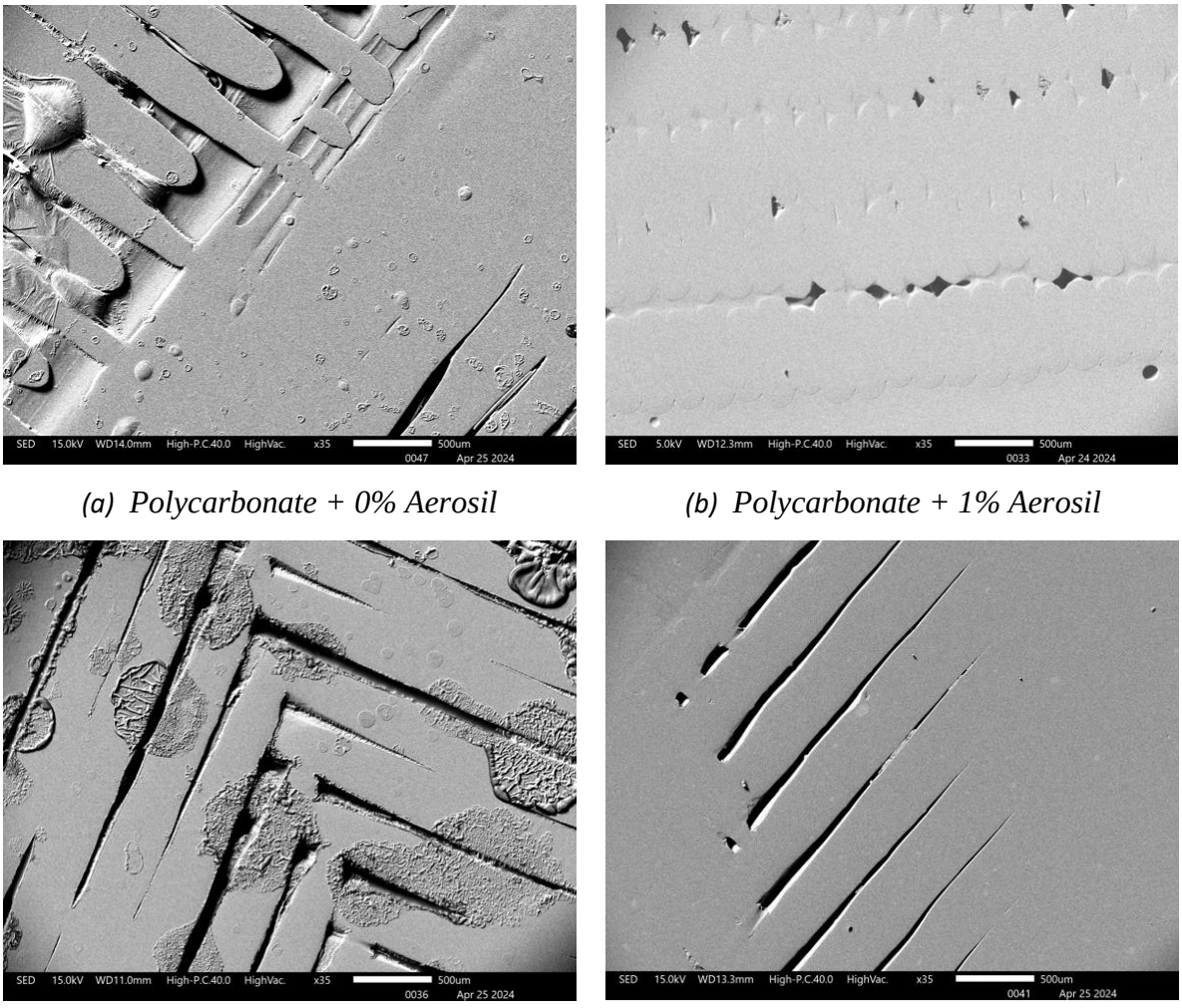


Metallic coating

Figure 2. 8: Sample preparation.

2.4.4.2 Scanning electron microscope (zoom ×35)

Thanks to a 35x magnification from the SEM (***Figure 2. 9***), the surface of the printed parts and the printing lines are visible. Voids are observed between these lines, a phenomenon explained by crossing lines during the printing process. Thus, it can be said that with a 35x magnification, voids are always present between the printing lines, and this can be optimized by adjusting the printing parameters. It's important to note that the voids between the lines directly influence the material's behavior.



(a) Polycarbonate + 0% Aerosil *(b) Polycarbonate + 1% Aerosil*

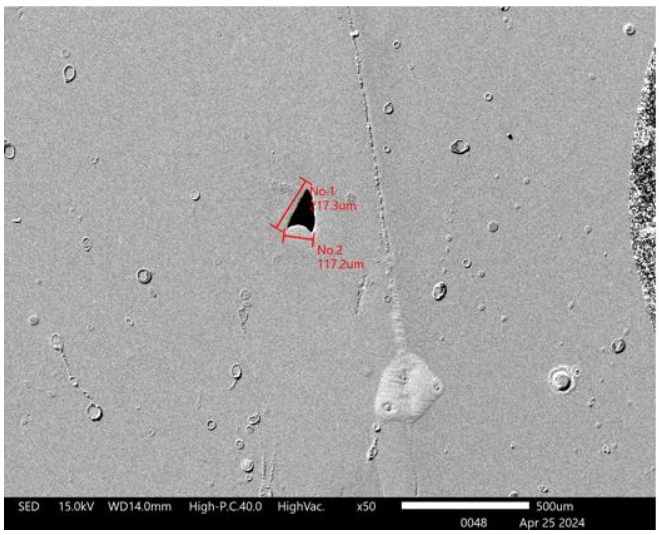
(c) Polycarbonate + 2% Aerosil *(d) Polycarbonate + 4% Aerosil*

Figure 2. 9: Scanning electron microscope (zoom ×35).

2.4.4.3 Scanning electron microscope (Zoom ×50)

After a ×50 magnification with the SEM (***Figure 2. 10)***, we could distinguish the voids in the sample. We also noticed the presence of other voids beyond those located between the printing lines. These voids significantly impact the samples' fracture and the material's maximum

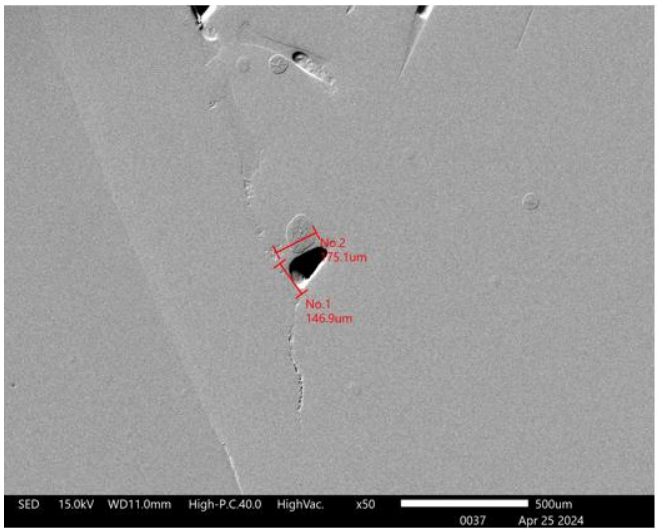
strength. Thus, these images give us an idea of the different types of voids in the sample. It is, therefore, essential to optimize the printing parameters to minimize the formation of these voids as much as possible.



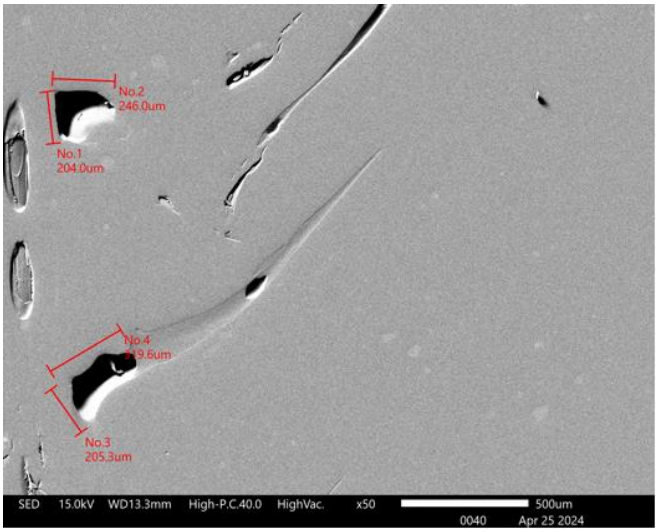
(a) Polycarbonate + 0% Aerosil



(b) Polycarbonate + 1% Aerosil



(c) Polycarbonate + 2% Aerosil



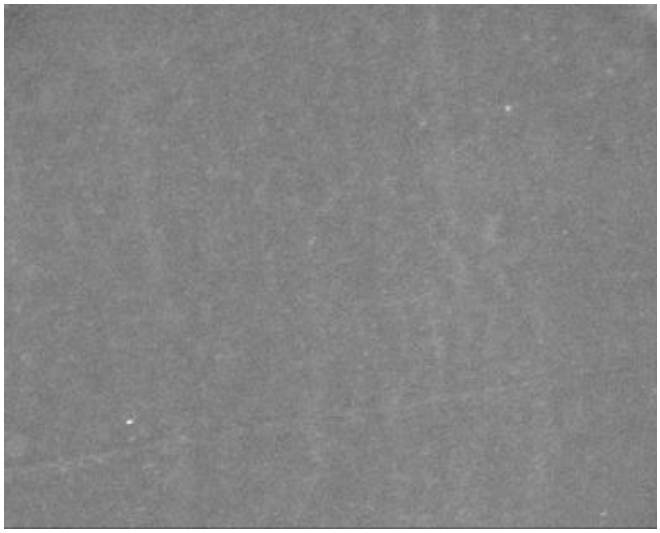
(d) Polycarbonate + 4% Aerosil

Figure 2. 10: Scanning electron microscope (zoom ×50).

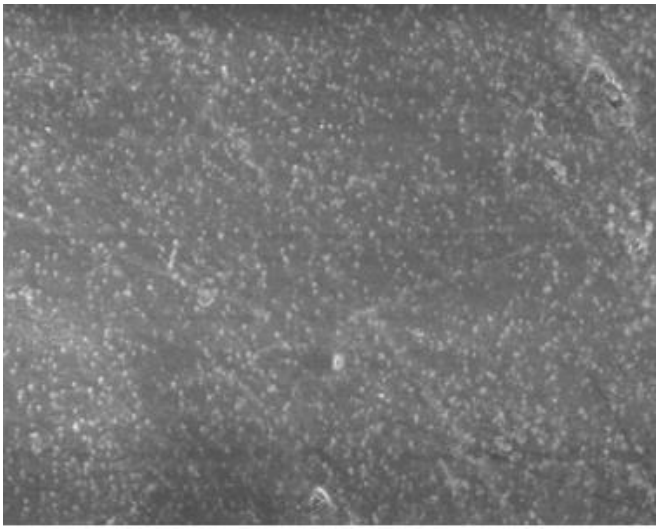
2.4.4.4 Scanning electron microscope (zoom ×1500)

To observe the distribution of nanofillers, a scanning electron microscope (SEM) was used to visualize the Aerosil nanoparticles at a magnification of x1500 (***Figure 2. 11***). The distribution of the nanofillers as a function of the Aerosil content in the matrix is clearly observable. This analysis, along with the accompanying figures, provides us with an idea of the nature of the

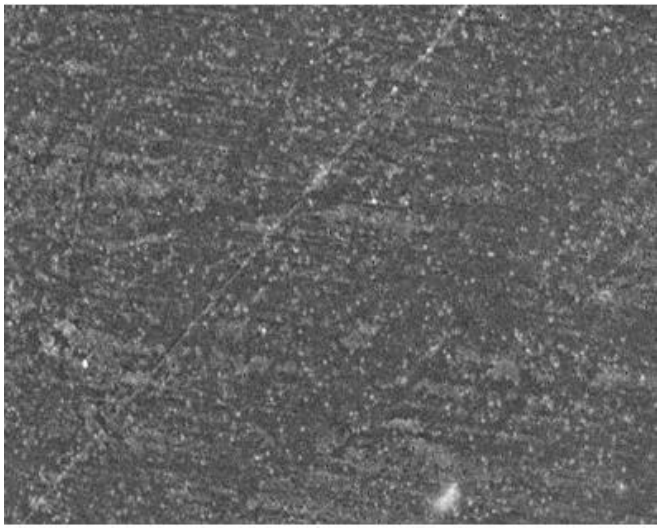
distribution, which appears to be random in three dimensions (Random 3D). This means that the nanoparticles are dispersed homogeneously throughout the matrix.



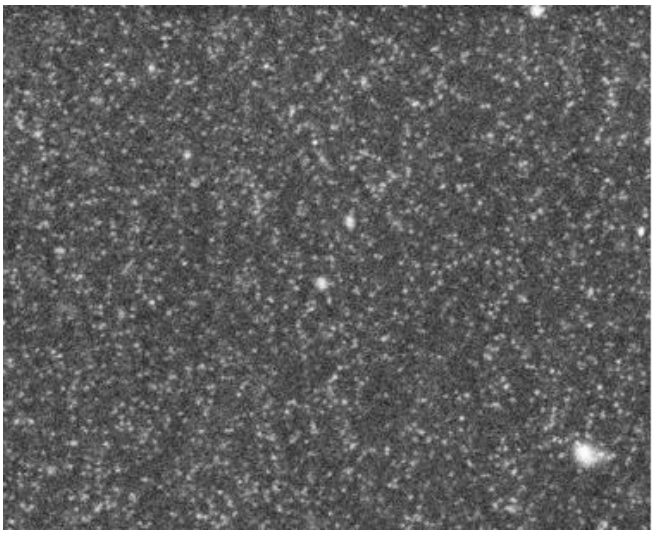
(a) Polycarbonate + 0% Aerosil



(b) Polycarbonate + 1% Aerosil



(c) Polycarbonate + 2% Aerosil



(d) Polycarbonate + 4% Aerosil

Figure 2. 11: Scanning electron microscope (zoom ×1500).

2. 5 Conclusion

This second chapter accurately described and listed the materials used throughout the thesis. These materials, which vary in mechanical and chemical properties and printing parameters, were introduced. ABS, a thermoplastic material, was initially described, and its properties were later utilized in numerical studies. A detailed description of CF-PETG followed, in which reinforcement was added to the thermoplastic matrix. Lastly, a new generation of composite

materials was developed. These materials' manufacturing and printing methods were also clearly defined, along with how nanoparticles were incorporated into the matrix at different percentages.

After presenting the different materials that were the focus of this thesis, it is now essential to delve into their experimental characterization. The following chapter will address the methods and techniques used to assess their mechanical and thermal properties, providing a comprehensive understanding of their behavior under various conditions.

CHAPITRE 3

Experimental study

Table of content

3. 1 Introduction 71
3. 2 Study of the tensile behavior of 3D-printed CF-PETG composites. 71
3.2.1 Structural design of the sample 72
3.2.2 Repeatability test 73
3.2.3 Result 74
3.2.4 Mechanisms of damage 75
3. 3 Study of the dynamic compression behavior of 3D-printed CF-PETG composites 77
3.3.1 Split Hopkinson Pressure Bars 77
3.3.2 Repeatability of tests for various impact pressures 78
3.3.3 Result and discussion of the Dynamic behavior 79
3.3.4 Damage Mechanisms 83
3. 4 Study of the temperature-dependent compression behavior of Aerosil/polycarbonate composites 85
3.4.1 Static compression test 85
3.4.2 Test reproducibility 86
3.4.3 Effect of nanoceramic particles on material behavior 87
3.4.4 Effect of temperature on material behavior 90
3.4.5 Analysis of elastic and plastic properties 92
3.4.6 Effect of temperature on the imprint produced between the trays and the sample 94
3. 5 Conclusion 96

3. 1 Introduction

During the thesis period, several types of experimental tests were conducted. Different tests were required for various materials, depending on the task's sequence and utility. Static and dynamic tests, such as tensile and compression tests with temperature variation, were employed. The tensile test for CF-PETG was initially performed to identify the material's mechanical properties, subsequently allowing for the development of a finite element numerical model. Dynamic compression tests were then conducted on the same material to obtain its dynamic properties and examine its behavior under dynamic conditions. Hopkinson bars provided the necessary data for developing the numerical model. Lastly, the Aerosil/polycarbonate composite material was subjected to a static compression test under varying temperatures to identify its compression behavior and how it evolved at high and low temperatures while observing the effect of ceramic nanofillers on its mechanical properties.

3. 2 Study of the tensile behavior of 3D-printed CF-PETG composites.

The tensile test is one of the most often used mechanical characterization techniques. It enables the determination of multiple standardized quantities used in structural calculations, such as Young modulus, fracture stress, maximum stress, yield points, etc. The INSTRON 5969 is employed as a tensile test machine for 3D-printed specimens (***Figure 3. 1***). It comprises two tensile bits between which the specimen is placed after being marked by four points. Samples were loaded with a displacement speed of 2 mm/min.



Figure 3. 1: INSTRON 5969 tensile machine.

All tests are performed at ambient temperature and repeated three to five times on different tests of the same shade to ensure repeatable results. The tensile tests are conducted on dumbbell-shaped specimens under static tensile tests for both honeycomb (NIDA) and rectilinear (RECT) fill patterns at different infill densities (20%, 50%, 75%, and 100%).

3.2.1 Structural design of the sample

For the structure of the specimens, we worked on dumbbell-shaped specimens with different infill rates (20%, 50%, 75%, and 100%) and different types of infill patterns (honeycomb and rectilinear) (***Figure 3. 2***) to study the effect of each on the material's behavior. We chose these patterns because they are widely used in industries and research laboratories. Our goal is to analyze the variation in the behavior of CF-PETG based on these infill patterns.

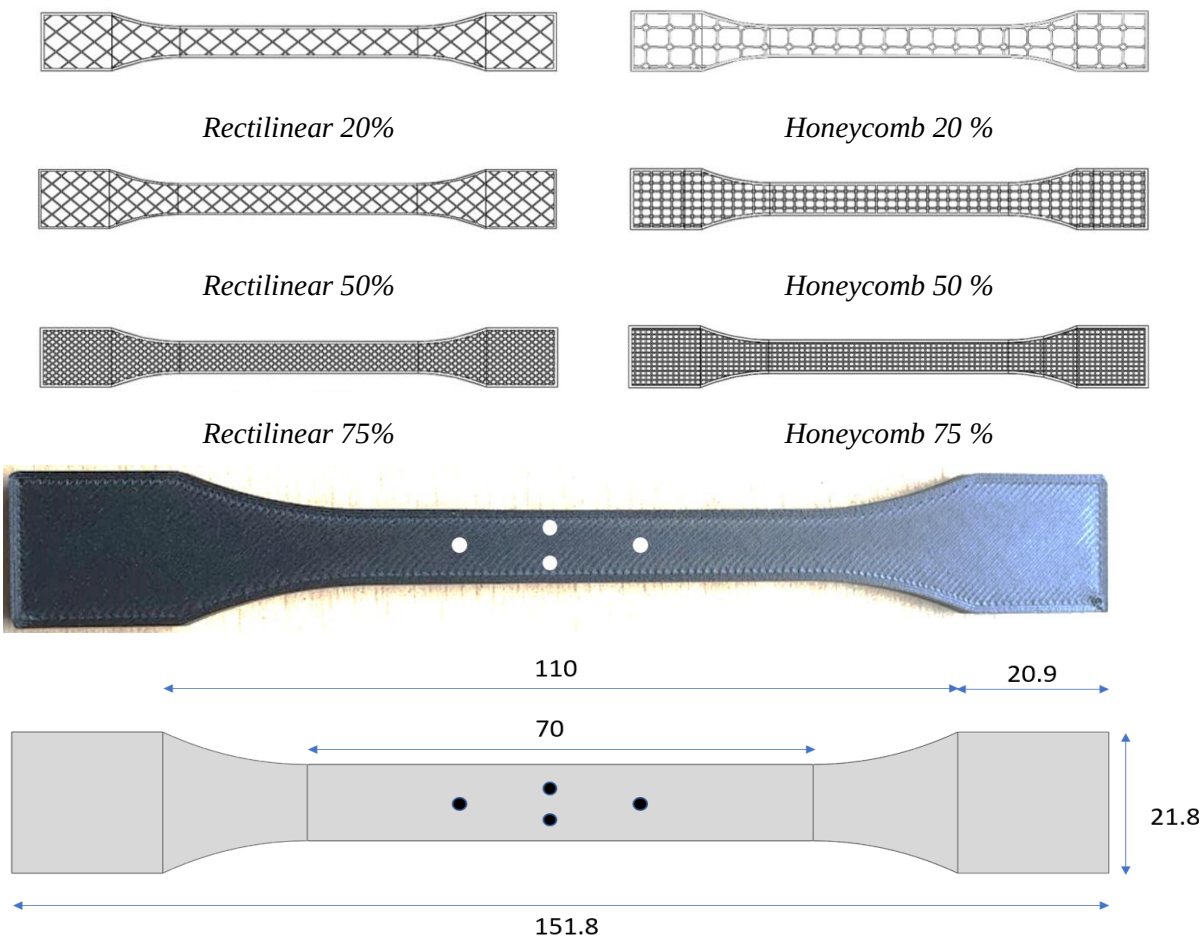
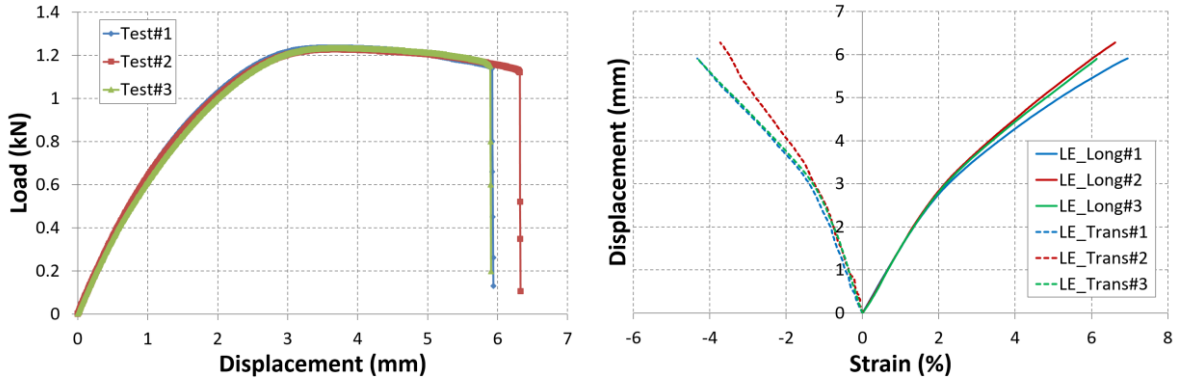


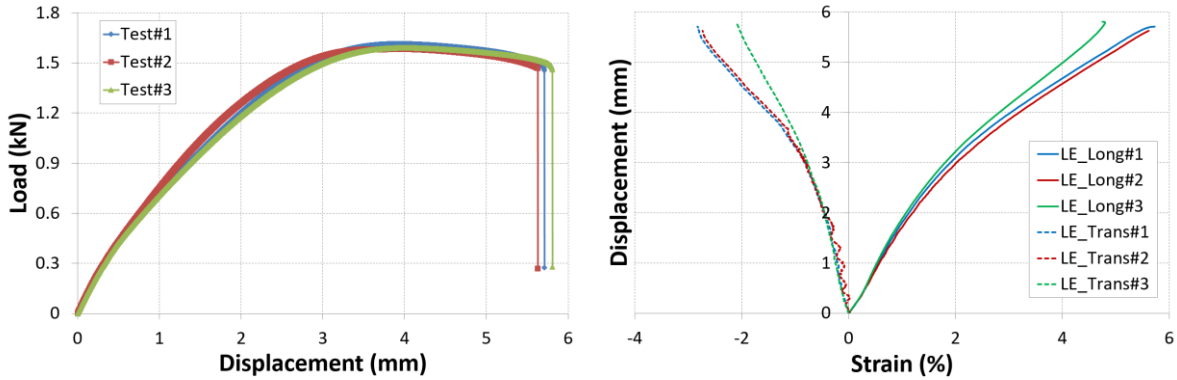
Figure 3. 2: Tensile test specimens.

3.2.2 Repeatability test

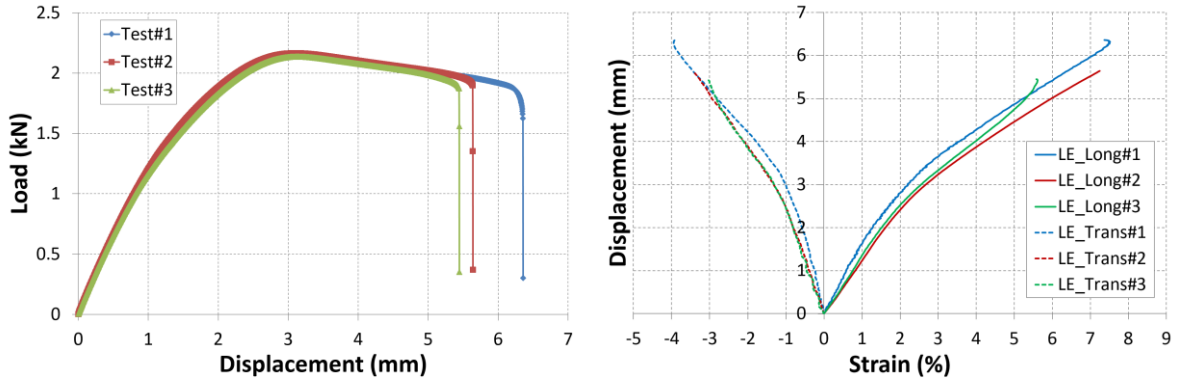
The repeatability of the tests must be guaranteed for a qualitative and quantitative study. For this reason, the tests were conducted three times for each filling ratio (20 %, 50%, 75%, and 100%) and filler type (rectilinear and honeycomb) to ensure the experimental tests were repeatable. ***Figure 3. 3*** shows an example of the repeatability tests for a 50% and 100% filling ratio for the different honeycomb and rectilinear fillers. ***Figure 3. 3*** shows force vs. displacement curves obtained for different CF/PETG filling densities with a honeycomb filling pattern (NIDA) and a rectilinear filling pattern (REC). A representative and reproducible force variation with displacement for CF/PETG filling densities was observed.



(a) 50% RECT



(b) 50% NIDA

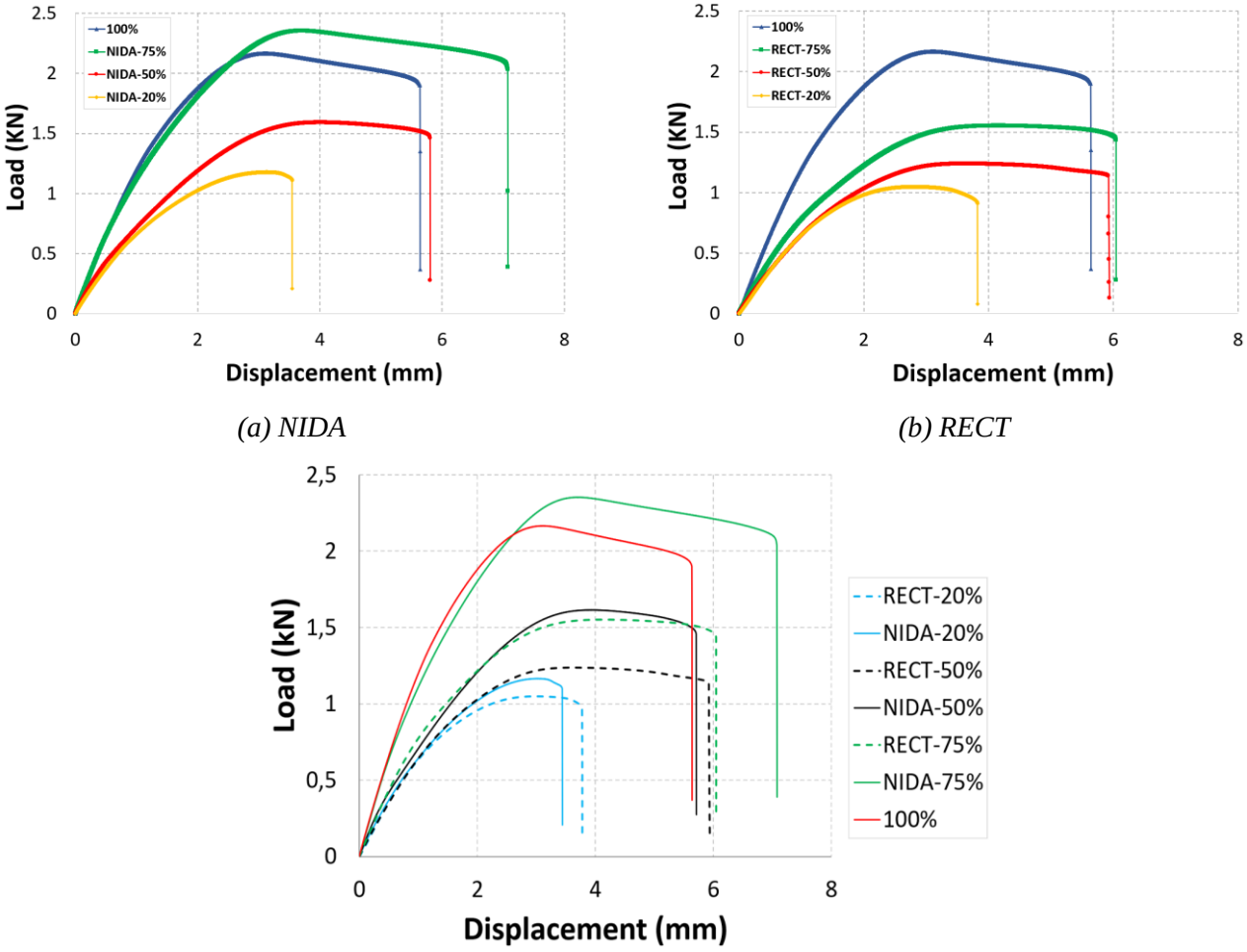


(c) 100%

Figure 3. 3: Examples of test reproducibility, NIDA, and RECT patterns.

3.2.3 Result

A tensile test was conducted on dumbbell-shaped specimens to verify the mechanical behavior of PETG polymer reinforced with short carbon fibers produced using the FFF process. Through the experimental campaign, the material was completely characterized by recording parameters such as displacement, load, and longitudinal and transverse deformations. The experimental results indicated that the mechanical behavior of each specimen was elastoplastic, as shown in ***Figure 3. 4***. Load-displacement curves were plotted to analyze the impact of different filling patterns at various infill densities on the material behavior.



(a) NIDA *(b) RECT*

(c) NIDA vs RECT

Figure 3. 4: Force-Displacement curves.

The variation of peak force about fill rate for the rectilinear and honeycomb patterns was presented in ***Figure 3. 5*** to facilitate the analysis. The honeycomb pattern demonstrated greater strength and stiffness compared to the rectilinear pattern. Additionally, with an increase in fill ratio, the maximum force for static tensile strength also increased. According to ***Figure 3. 5,***

the honeycomb pattern with a 75% fill rate exhibited the best mechanical performance, surpassing the fully filled specimen (100% fill rate). Due to its unique structural properties, the honeycomb pattern offered superior strength and stiffness over the rectilinear pattern in FFF (Fused Filament Fabrication) 3D printing technology.

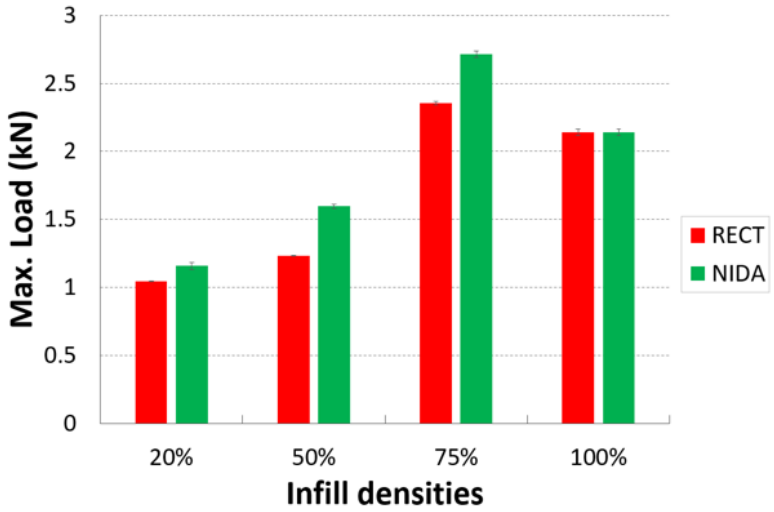


Figure 3. 5: Variation of the maximum force as a function of filling rate for the two patterns: Rectilinear and Honeycomb.

3.2.4 Mechanisms of damage

Figure 3. 6 shows two representative tested samples from each set after a fracture. Most thermoplastic material fractures are ductile because the reorientation and stretching of the thread-like macromolecules allow for considerable material deformation.

However, the breakage occurred in different sections of the tested samples at the end of the tensile test. The filler type, the filling density, and printing parameters may be the main factors influencing the zone where the sample breaks. For example, ***Figure 3. 6*** (a) shows the breakage zone of the 20%-Honeycomb specimens. The fracture locations for the two specimens are not the same; the fracture for the first specimen happens in the middle of the fictive portion, whereas the fracture for the second specimen occurs at the extremity of the fictive part. Both specimens, however, exhibit the same type of filling pattern and density. As a result, only the 3D printing procedure determines the position of the specimens' breaking. For instance, the shrinking of the part is caused by progressive cooling between the extrusion/sintering temperature and the ambient temperature. Warpage also affects total specimen failure; it occurs when thermoplastics expand slightly and contract while cooling. A thermal reaction occurs due to the higher extrusion temperature, causing the plastic to shrink during cooling, ***Figure 3. 7***.

(a) NIDA CF-PETG *(b) RECT CF-PETG*

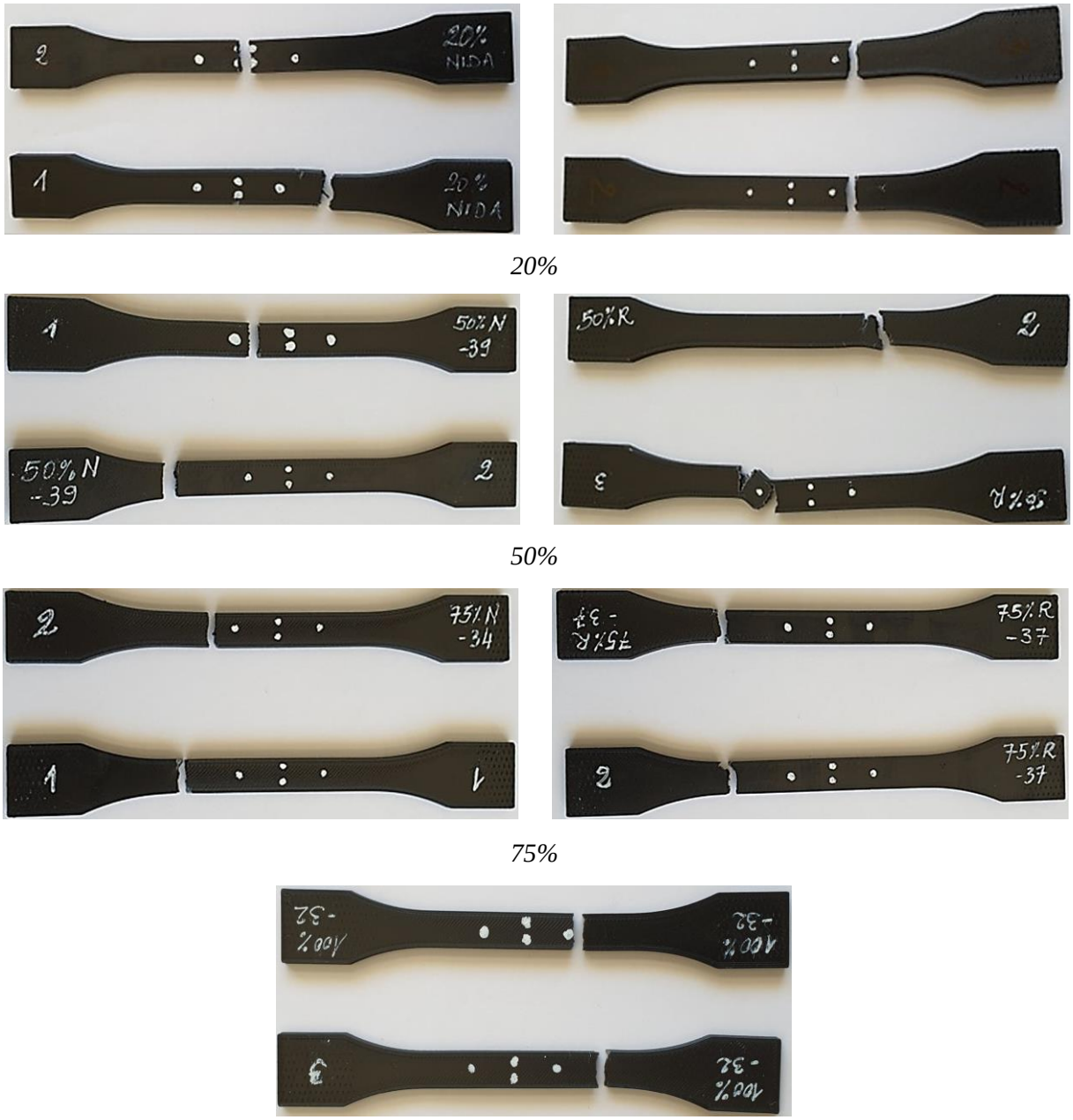


Figure 3. 6: Breakage of the specimens after the tensile test.

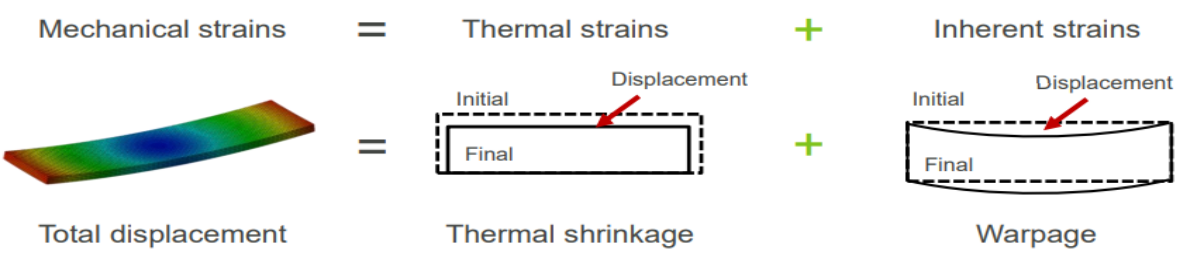


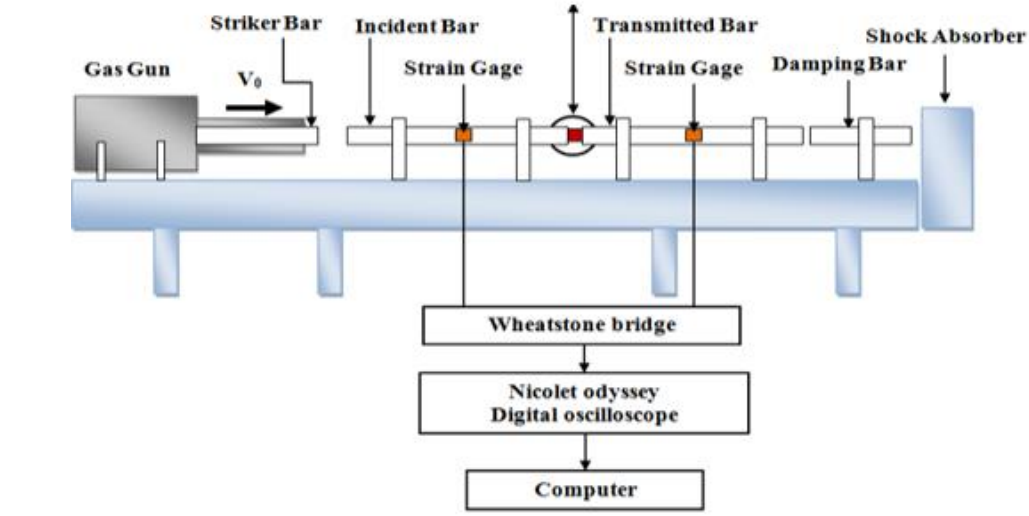
Figure 3. 7: Description of the concept of thermomechanical behavior.

3. 3 Study of the dynamic compression behavior of 3D-printed CF-PETG composites

3.3.1 Split Hopkinson Pressure Bars

Using the Hopkinson bar system (SHPB), the in-plane dynamic compressive behavior of CF-PETG 3D printed composite specimens was investigated at various strain rates ranging from 10^2 s^{-1} to 10^4 s^{-1}, ***Figure 3. 8***. The striker, input (incident), and output (transmission) bars of the SHPB apparatus are all composed of 20 mm-diameter high-strength Maraging steel. Each specimen was positioned between the incident and transmission bars without other attachments to evaluate the composite materials' dynamic response. This strategy is intended to stop measurement distortions brought on by additional interfaces. The striker bar was used to apply load parallel to the layer plane at predetermined impact pressures. The input bar was subjected to four impact velocity through the striker launched at four impact pressures: 1.4 bar, 1.7 bar, 2 bar, and 2.4 bar. The CF-PETG samples behaved in various ways, from elastic-plastic reaction to initial damage to catastrophic failure. Using a gas cannon mechanism with a maximum pressure of 6 bar, the striker bar's velocity was controlled, and an incident wave (I(t)) of compressive strain was induced. This pulse traversed the entire input bar. Due to the impedance mismatch of the composite material, some waves were reflected when they reached the specimen's surface (reflected wave = R(t)). The remaining portion (transmitted wave T(t)) continued to travel through the specimen and transmission bar until it reached the far end.

Additionally, a cutting-edge high-speed camera (FASTCAM) was incorporated into the experimental design to track the deformation and damage under high strain rates of CF-PETG specimens. The camera was set to capture at a frame rate of 33000 frames per second (fps/s) with a resolution of 896 × 496 pixels. A dynamic strain indicator amplified strain pulses detected by strain gauges placed in the middle of each bar. A rapid Fourier transformation technique from Maple Software was used to post-process the wave signals after capturing them using a digital oscilloscope. The study aims to understand the dynamic behavior of the CF-PETG composite made by 3D printing. This understanding involves the evaluation of the various dynamic parameters and their evolution as a function of time and deformation speed. Additionally, the study aims to investigate experimentally and numerically the compressive behavior of 3D-printed PETG composites with different infill densities.





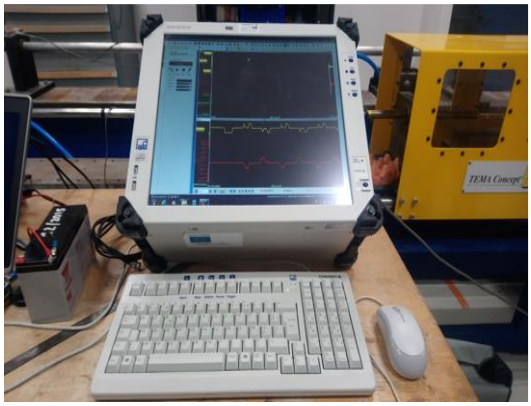
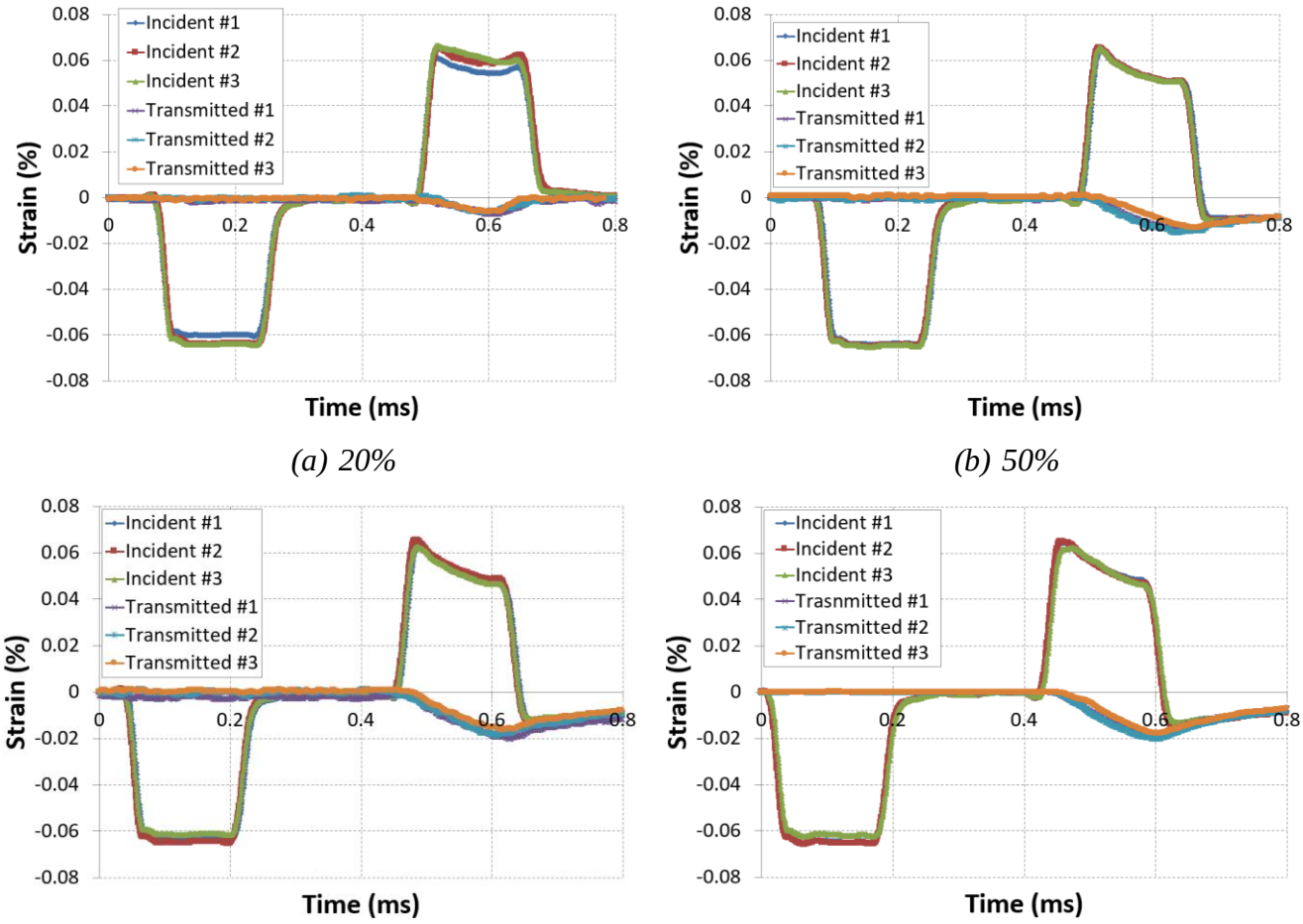


Figure 3. 8: SHPB device: schematic representation of the experimental procedure.

3.3.2 Repeatability of tests for various impact pressures

Before performing Hopkinson bar dynamic compression testing, it is essential to ensure the consistency and repeatability of the tests in a dynamic environment. To achieve this, three distinct series of experiments involving various impact pressures (1.4, 1.7, 2.0, and 2.4 bar) while retaining the same incident wave intensity were performed on each specimen. These tests were conducted using CF-PETG filling densities ranging from 20% to 100%. In the context of a pressure of 1.7 bar, ***Figure 3. 9*** shows the substantial representation of repeated deformation over time for a particular CF-PETG filling density (20% to 100%).



(a) 20% *(b) 50%*

(c) 75% *(d) 100%*

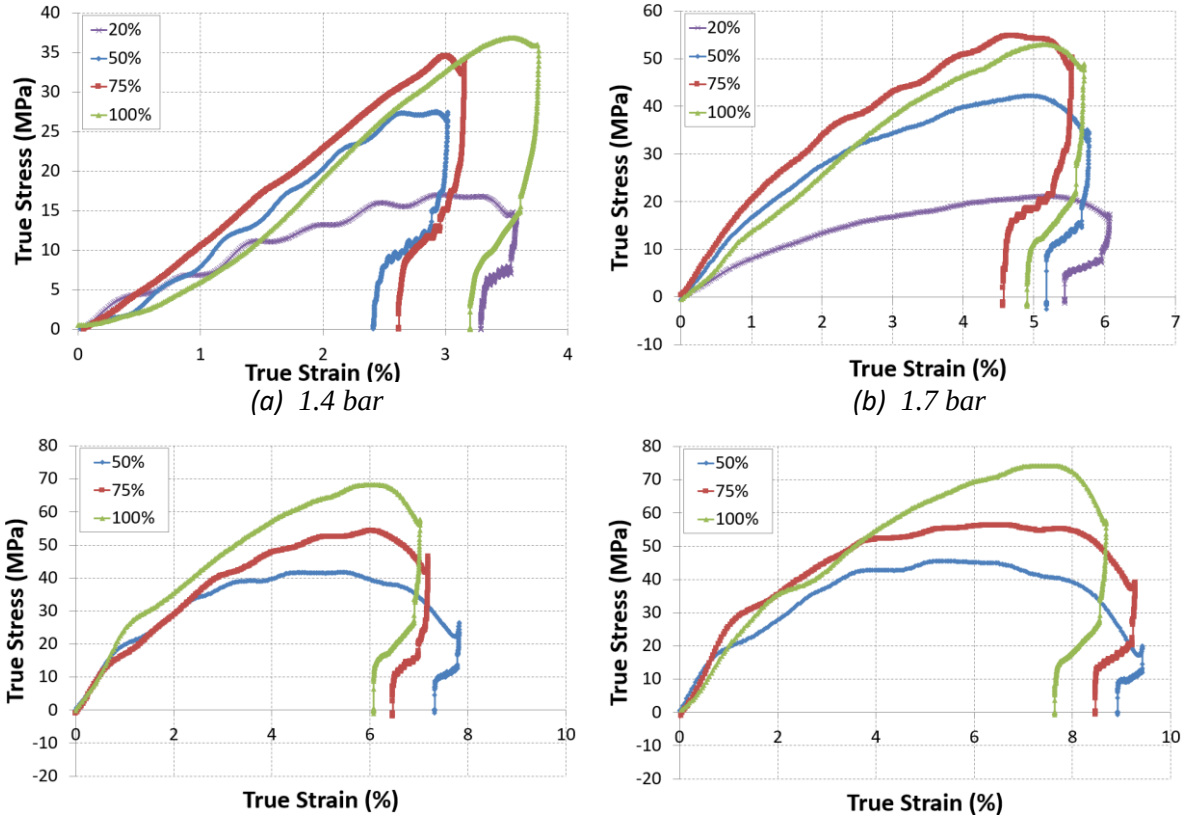
Figure 3. 9: Tests repeatability, Nida, P = 1.7 bar.

3.3.3 Result and discussion of the Dynamic behavior

The experimental results of compression tests carried out on the SHPB device at different filling densities are described in this section. Various dynamic parameters are illustrated in ***Figure 3. 10*** to ***Figure 3. 14***. These graphs show that the various emotional factors expand with increasing impact pressure. All samples show comparable compression trends for different impact pressures for the four filling densities (20%, 50%, 75%, and 100%). On the other hand, the transmitted signal is often weaker, with considerable attenuation appearing at lower filling ratios. In addition, the amplitude of reflected and incident signals is equal, indicating the material's ability to dampen and absorb dynamic stresses. The strain rate, on the other hand, increases sharply until it reaches a maximum value and is inversely related to impact pressure. It then decreases and finally becomes close to zero for different impact pressures. Negative strain rates are visible at all impact pressures, indicating elastic recovery of the specimens. It has been established that all analyses for different filling densities refer to unscathed scenarios.

About the load curves, it is first demonstrated that equilibrium is present in these curves at both ends of the specimen, fulfilling the primary premise of a legitimate SHPB experiment. Since the incident velocity is independent of the inherent characteristics of the samples, it is simple to see why it remains nearly constant for all filling ratios. However, a fascinating dynamic about transmitted velocity appears. Surprisingly, the sample with 100% filling consistently reaches the maximum amplitude, followed by the model with 75% filling and the piece with 50% filling. By highlighting a minor connection between the degree of filling and velocity transmission, this amplitude hierarchy helps us better understand the mechanics underlying the dynamic compression of these samples.

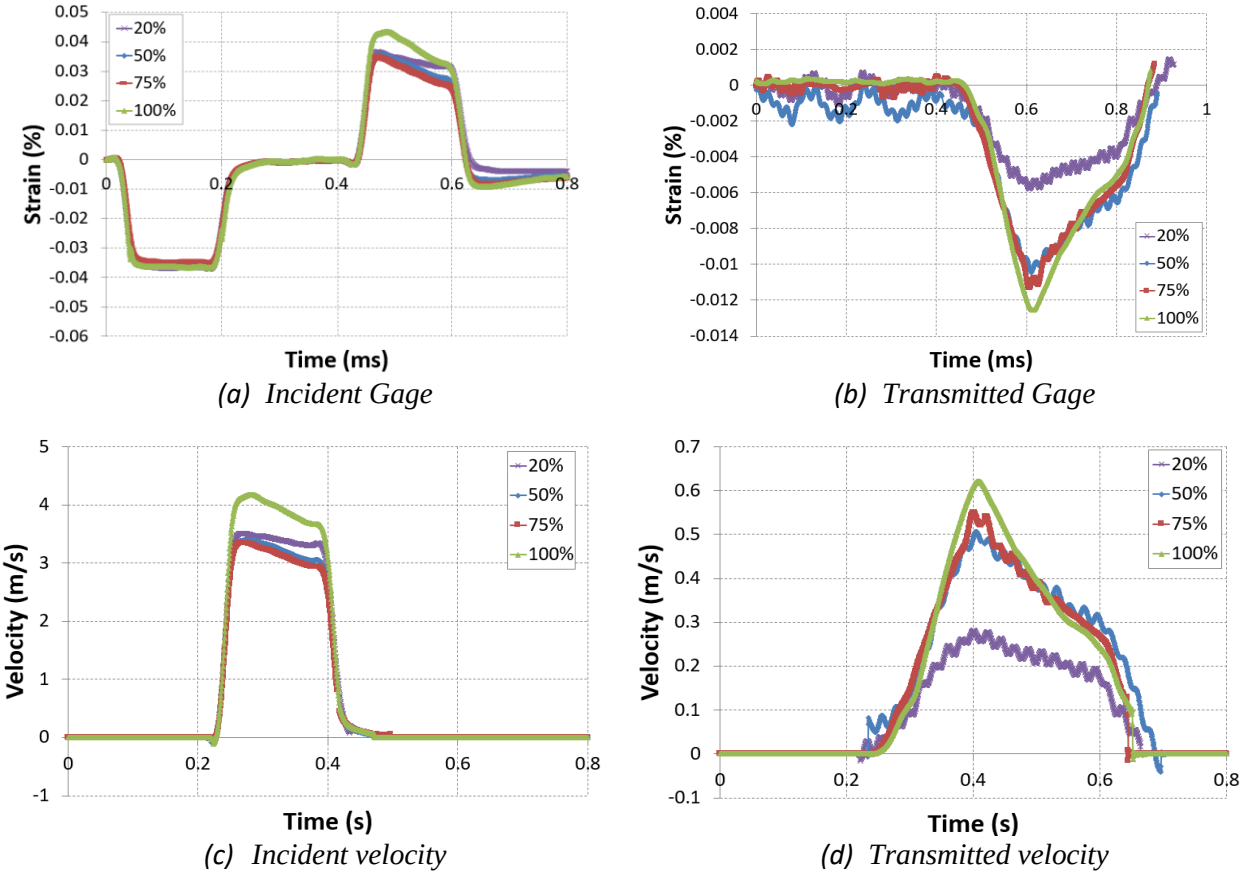
Figure 3. 10 presents stress-strain data from dynamic compressive testing carried out at various impact pressures, using varied infill patterns and densities, to better understand how the strain rate impacts the mechanical properties of CF-PETG composites. The results show that the compressive properties of 3D-printed CF-PETG are sensitive to the applied strain rate. Notably, the early linear section of the curves considerably increased in prominence as the strain rate increased and the stress steadily increased. This finding points to a rate-dependent behavior and a stiffening property that may be connected to the higher applied pressure and higher energy consumption of specimens under high strain rate loading. Therefore, increasing elastic strain recovery, lowering plastic deformation, attenuating the macro-damage, higher filling densities, or, more specifically, the honeycomb pattern can improve the stress-strain performance of CF-PETG composites under each pressure. This illustrates how vital the fill pattern and density are in determining the dynamic behavior of a 3D-printed sample.



(a) 1.4 bar *(b) 1.7 bar*

(c) 2 bars *(d) 2.4 bars*

Figure 3. 10: True Stress vs. True Strain at different impact pressure for the Nida filler.



(a) Incident Gage *(b) Transmitted Gage*

(c) Incident velocity *(d) Transmitted velocity*

Figure 3. 11: Dynamic behavior, CF-PETG at 1.4 bars for the Nida filler.

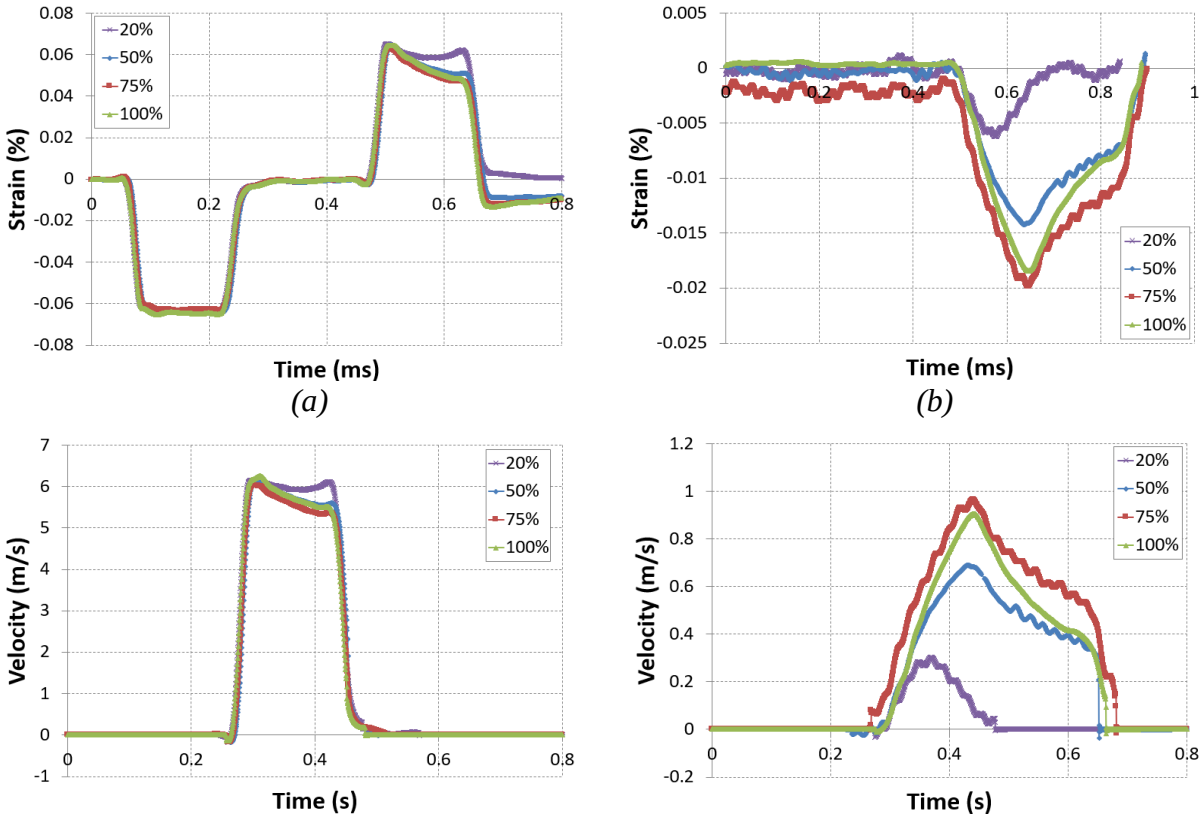


Figure 3. 12: Dynamic behavior, CF-PETG at 1.7 bars.

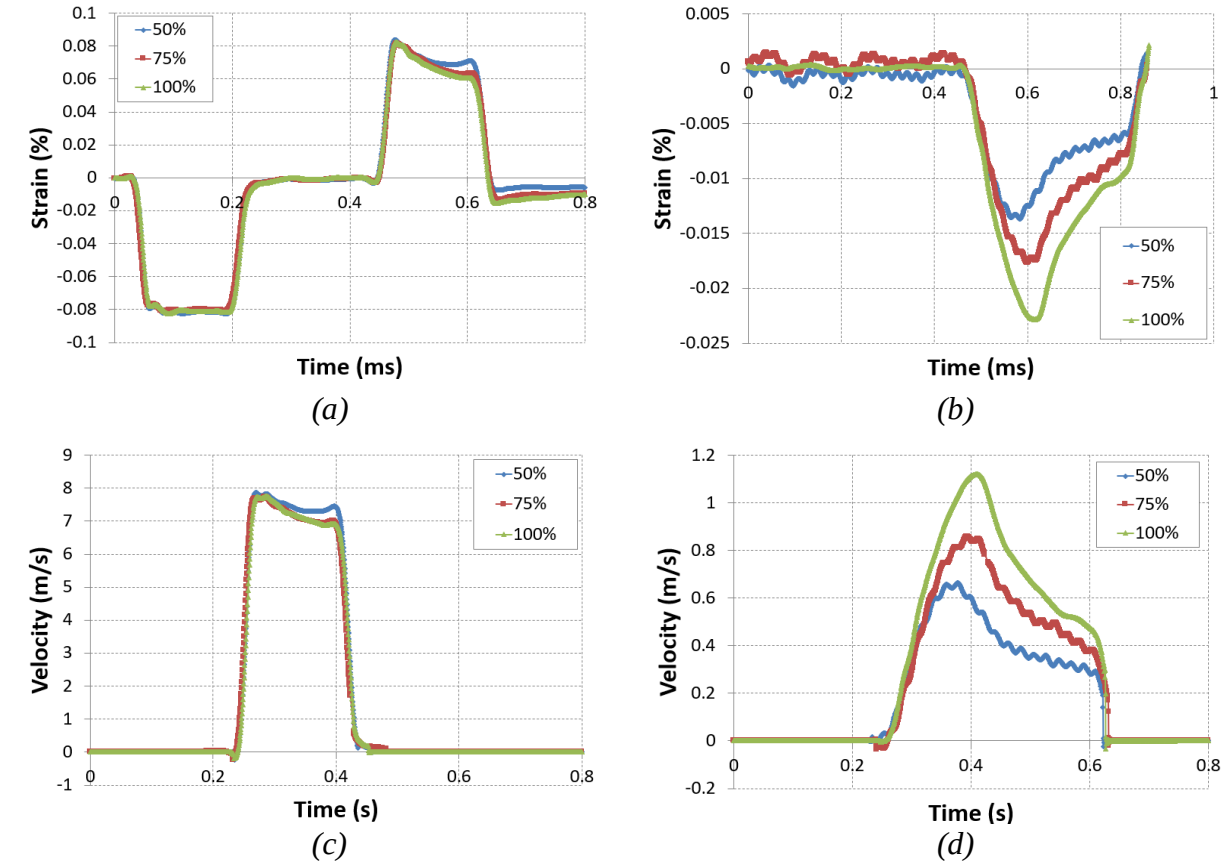


Figure 3. 13: Dynamic behavior, CF-PETG at 2 bars.

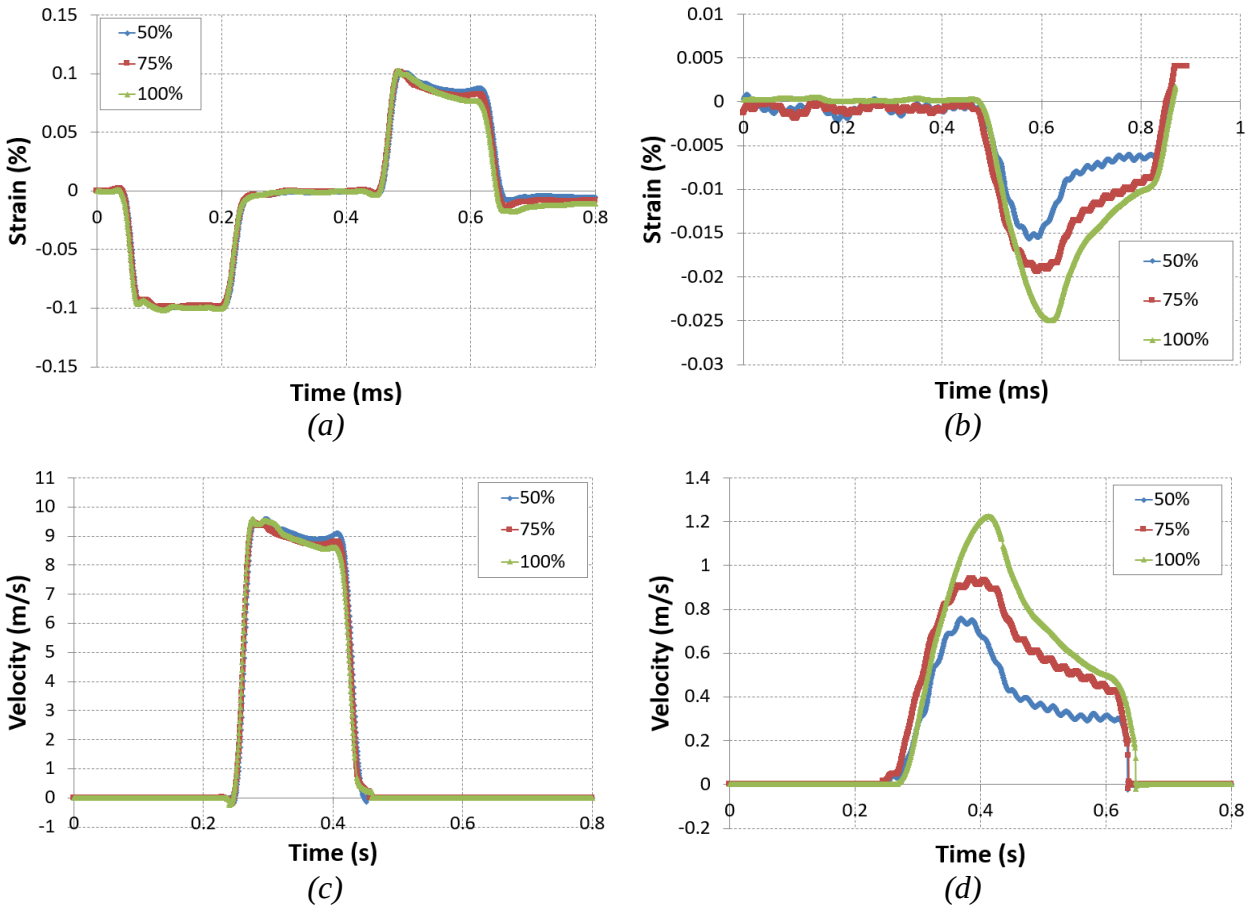


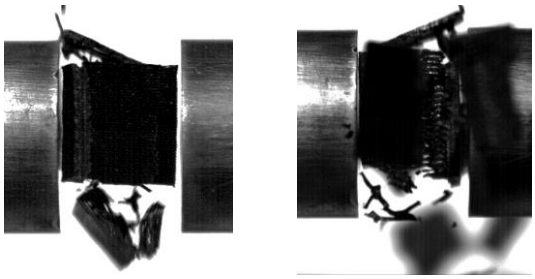
Figure 3. 14: Dynamic behavior, CF-PETG at 2.4 bars.

3.3.4 Damage Mechanisms

Monitoring and studying the damage behavior of composites is crucial for technologically sophisticated industries using composite materials. This work used high-speed camera images to explore the deformation, failure mechanism, and damage modes of 3D-printed CF-PETG composites during in-plane dynamic compression testing. The final state after impact is shown in ***Figure 3. 15*** for samples with 20%, 50%, and 75% honeycomb patterns evaluated at various impact pressures. Even at modest impact pressures, such as 1.4 and 1.7 bar, the 3D-printed CF-PETG composite sample with a 20% infill density of the honeycomb infill pattern displayed macro damage and final fracture. As demonstrated in ***Figure 3. 15*** (b), created from high-speed camera photos, samples with a 50% infill density of the honeycomb infill pattern showed macro damage at 2 bar impact pressure.

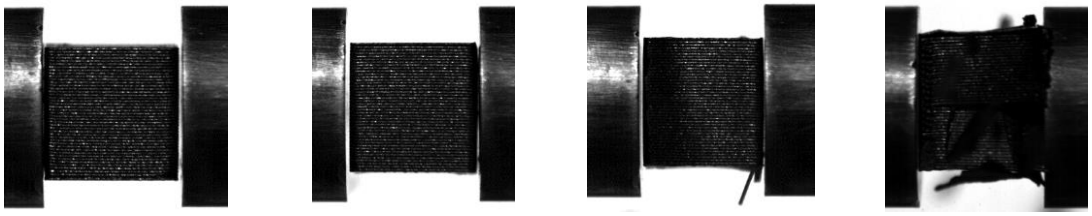
The study showed that utilizing a honeycomb design has improved the final damage performance of the 3D printed samples, regardless of the infill density at each impact pressure. In addition, samples revealed less crack and delamination propagation between the layers,

demonstrating that the honeycomb pattern had lessened overall macro damage and strengthened the bonds between different layers. The samples' high-speed images matched precisely with what was previously understood about their mechanical behavior.



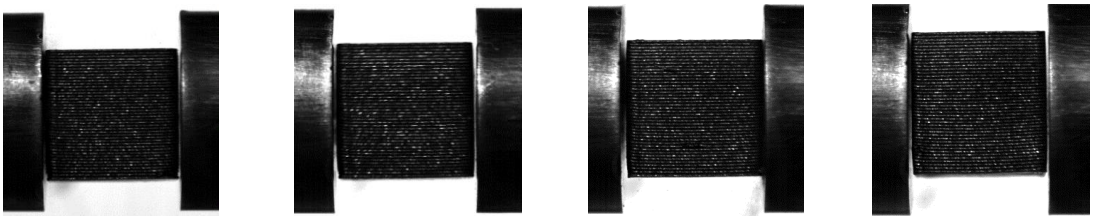
P=1.4 bars *P=1.7 bars*

(a) *20%-HON*



P=1.4 bars *P=1.7 bars* *P=2 bars* *P=2.4 bars*

(b) *50%-HON*



P=1.4 bars *P=1.7 bars* *P=2 bars* *P=2.4 bars*

(c) *75%-HON*

Figure 3. 15: Images captured by a high-speed camera during tests with various impact pressures.

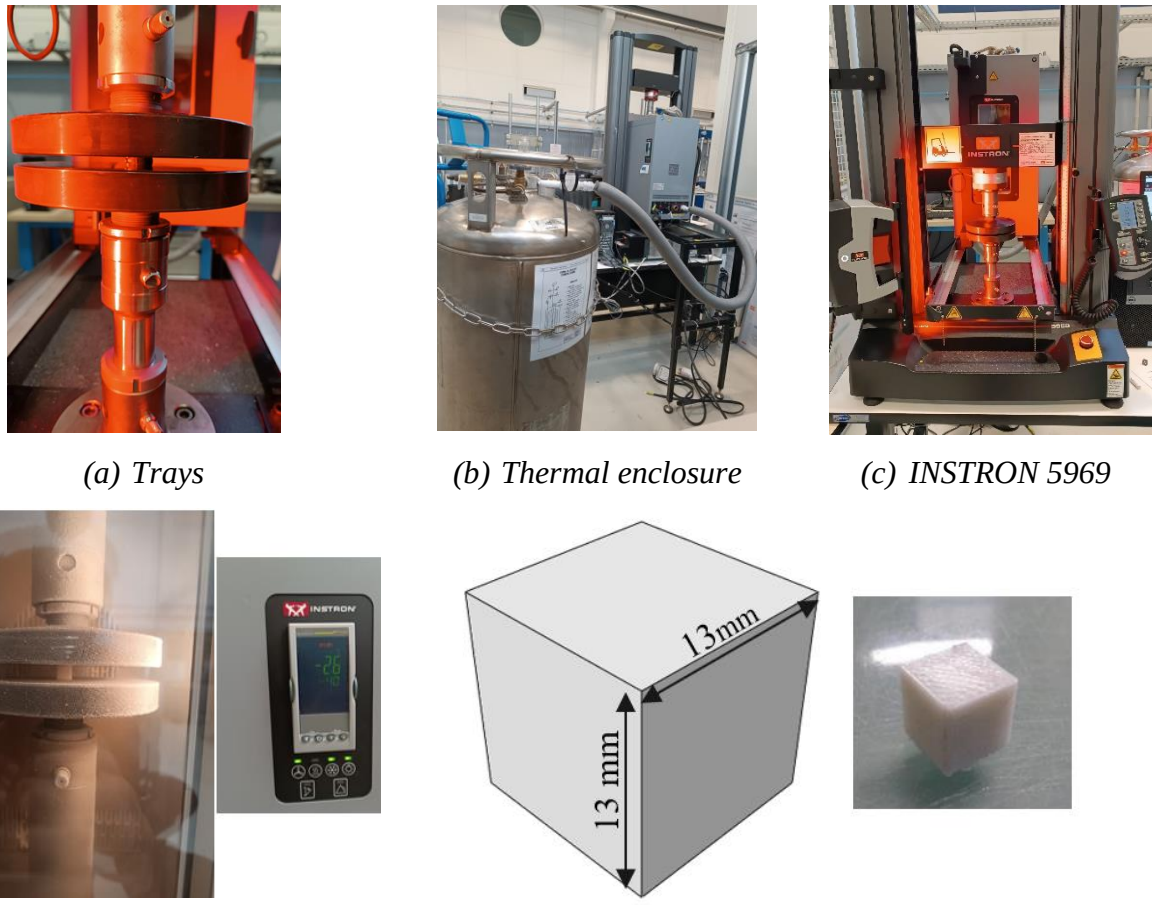
This study showed that the honeycomb pattern's hexagonal hollow cells significantly reduced the macro damage at each impact pressure while improving the dynamic properties of the CF-PETG composites. Impact energy absorption during the impact was visible in samples that showed no damage but increased shrinkage or a drop-in sample volume. This suggests that models with honeycomb infill designs could attenuate or absorb the impact energy because of their hollow construction. The hexagonal cell walls bend in a honeycomb manner. The walls of the strain lines turn in a rectilinear shape; however, they capture the impact energy and release

it as strain energy. When the point exceeds the material's predefined limit or threshold, the link between the adjacent layers is broken, and the final fracture happens.

3. 4 Study of the temperature-dependent compression behavior of Aerosil/polycarbonate composites

3.4.1 Static compression test

Static compression tests under the effect of temperature were carried out on the INSTRON 5969 machine to analyze the material's behavior (PC+Aerosil) under various thermal conditions, ***Figure 3. 16***. A series of tests were carried out at temperatures ranging from -90°C to 80°C, with specific points at -40°C, 23°C, 40°C, 60°C, and 80°C. An electric oven integrated into the INSTRON machine was used for positive temperatures, enabling precise thermal environment control. A nitrogen-filled thermal chamber was used for negative temperatures (-40 °C, -90°C), ***Figure 3. 16*** (b). Thermal regulation was ensured by a display on the machine, allowing the temperature to vary according to the experiment's needs, ***Figure 3. 16*** (d).



(a) Trays *(b) Thermal enclosure* *(c) INSTRON 5969*

(d) Temperature display *(e) Sample*

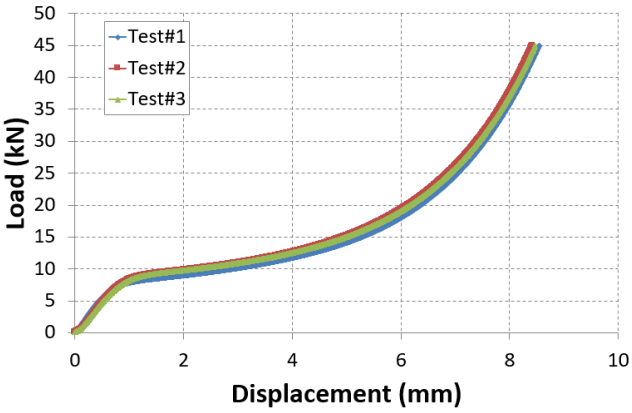
Figure 3. 16: Test equipment for compression testing.

The sample, cubic test tubes with dimensions of 13x13x13 mm, were carefully selected for the experiments, ***Figure 3. 16*** (e). The choice of working with small cubes was deliberate to ensure complete homogenization of the temperature inside the cube. To this end, a holding time of 30 minutes was rigorously applied for each test to ensure thermal homogenization in both the oven and the nitrogen chamber. This meticulous approach aimed to create optimal conditions for observations and measurements, minimizing temperature variations within the sample, thus ensuring reliable and reproducible results.

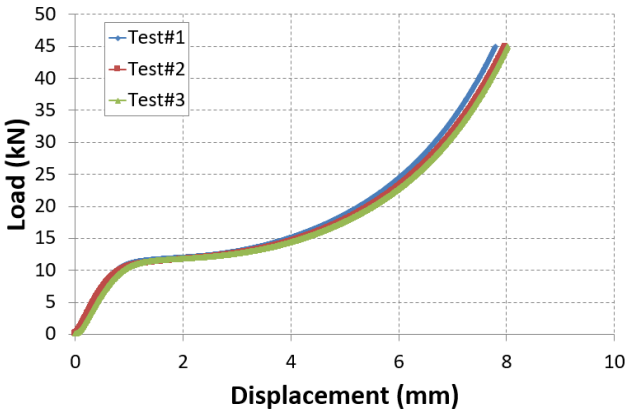
3.4.2 Test reproducibility

Guaranteeing test repeatability ensures the quality and reliability of both qualitative and quantitative studies. With this in mind, each test was meticulously carried out at least three times for each Aerosil proportion (1%, 2%, and 4%) and each temperature range (-90°, -40°, 23°, 40°, 60°, 80°). This meticulous approach was adopted to verify and confirm the consistency of the experimental results.

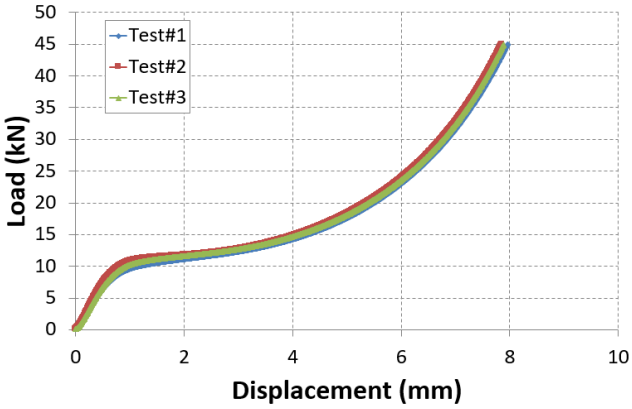
Figure 3. 17 illustrates the reproducibility test for selected compression tests, showing remarkable consistency between the data. The curves are almost perfectly superimposed, testifying to the excellent reproducibility of the tests and the quality of produced materials. This observation naturally raises the question of test reliability. In the light of these results, it seems legitimate to assert that the tests are highly reliable. The remarkable consistency between measurements suggests consistency in test conditions and precision in the results obtained, thus reinforcing confidence in the validity of the conclusions drawn from these compression tests.



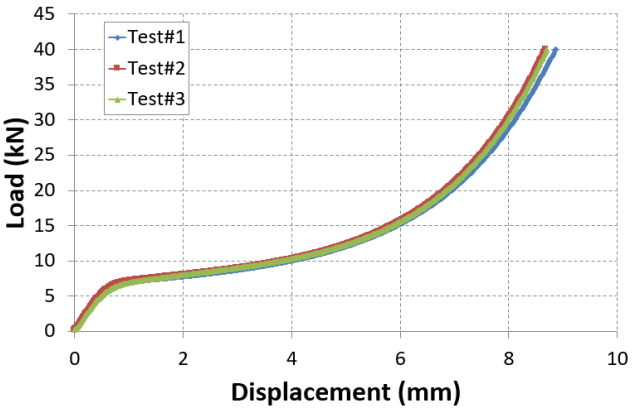
(a) PC+ 0% d'Aerosil, 23°



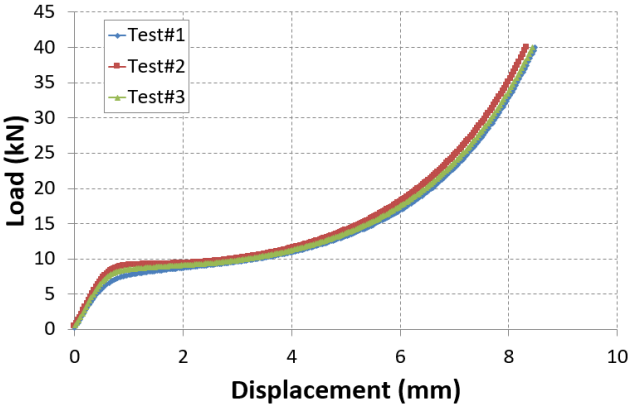
(b) PC+ 2% d'Aerosil, 23°



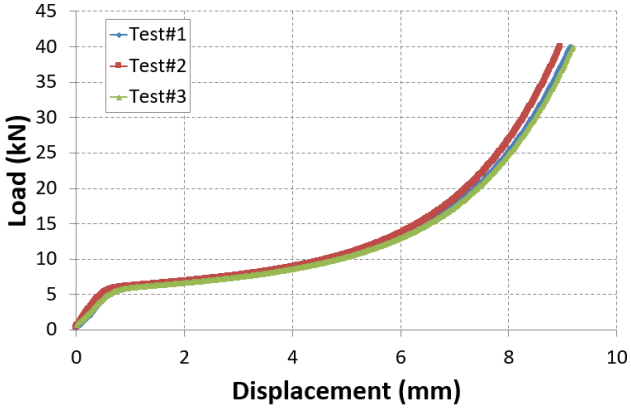
(c) PC+ 4% d'Aerosil, 23°



(d) PC+0% d'Aerosil, 60°



(e) PC+ 1% d'Aerosil, 60°



(f) PC+0% d'Aerosil, 80°

Figure 3. 17: Test reproducibility.

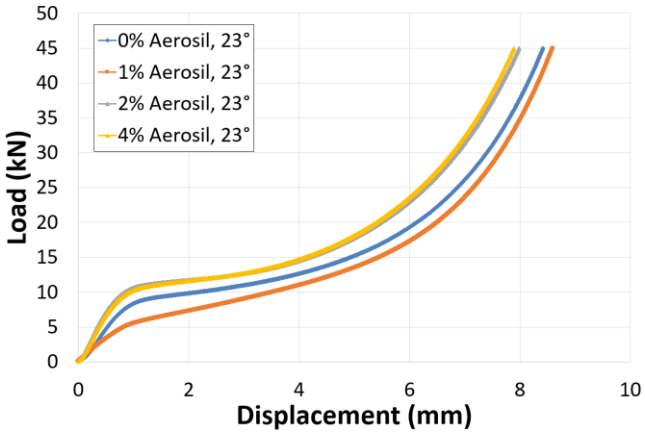
3.4.3 Effect of nanoceramic particles on material behavior

For each test, a specific temperature is maintained in the chamber while the nanoparticle wt.% is varied. At a temperature of -40°C, ***Figure 3. 18*** (e), the elastic part was at its maximum, with a significant difference between nanoparticle wt.%. In particular, the 2% wt.% showed minimal

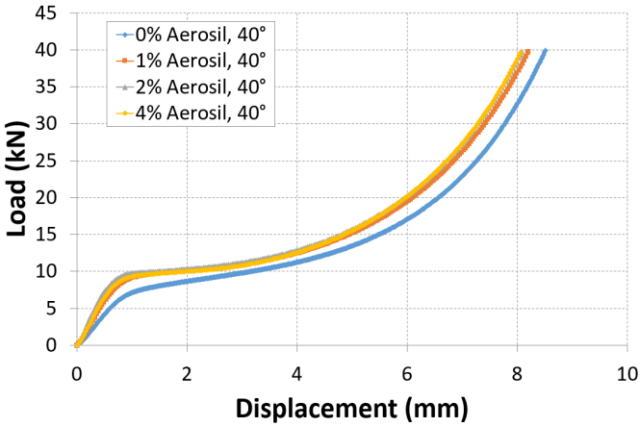
elasticity at this temperature. At a temperature of -90°C, ***Figure 3. 18*** (f), the curves corresponding to the 2 and 4 wt.% were practically merged, suggesting similar behavior for these two configurations.

In contrast, the 0% and 1% curves remained constant at this temperature. At a temperature of 40°C, the compression tests revealed exciting trends in the behavior of composite materials as a function of nanoparticle content. The curves corresponding to 1wt.%, 2wt.%, and 4wt.% nanoparticle contents showed marked similarities, virtually merging, ***Figure 3. 18*** (b). However, the curve associated with the neat polycarbonate (0wt.%) was distinguished by different characteristics. In particular, it exhibited a lower elastic portion than the other nanoceramic wt.%. This observation suggests that adding nanoparticles to the composite at 1wt.%, 2wt.%, and 4wt.% leads to similar mechanical behaviors at this temperature.

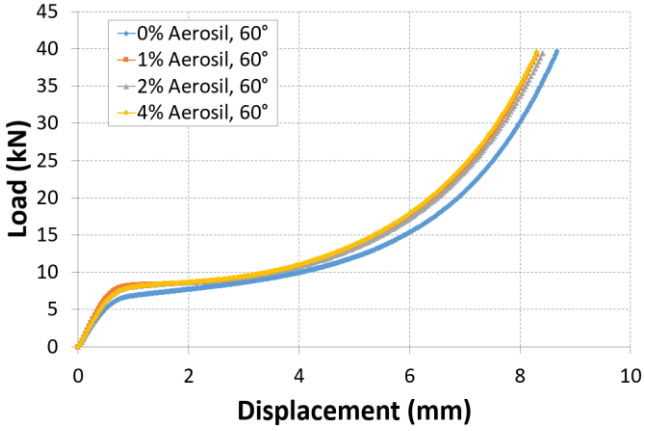
Figure 3. 19 shows the variation of Young's modulus as a function of nanofiller at ambient temperature. Incorporating nanofibers in the filled Aerosil at percentages ranging from 1 to 4% induces a linear progression in its mechanical behavior, as described by the mathematical model y=40x+1290. This gradual increase in nanofibers in the polycarbonate considerably enhances its mechanical properties, with a significant improvement of 10%.



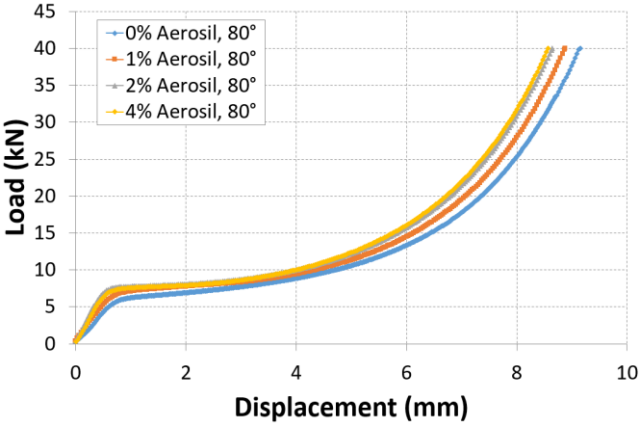
(a) Nanoceramic wt.% variation, 23°C



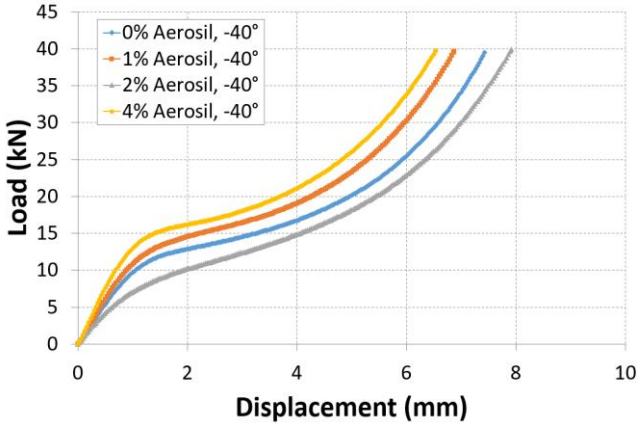
(b) Nanoceramic wt.% variation, 40°C



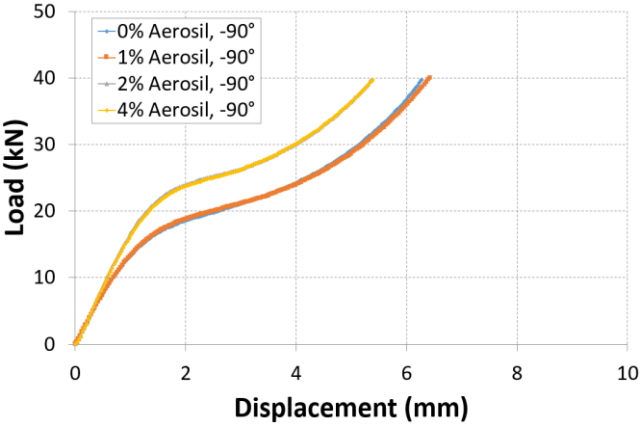
(c) Nanoceramic wt.% variation, 60°C



(d) Nanoceramic wt.% variation, 80°C



(e) Nanoceramic wt.% variation, -40°C



(f) Nanoceramic wt.% variation, -90°C

Figure 3. 18: Effect of weight percentage and temperature.

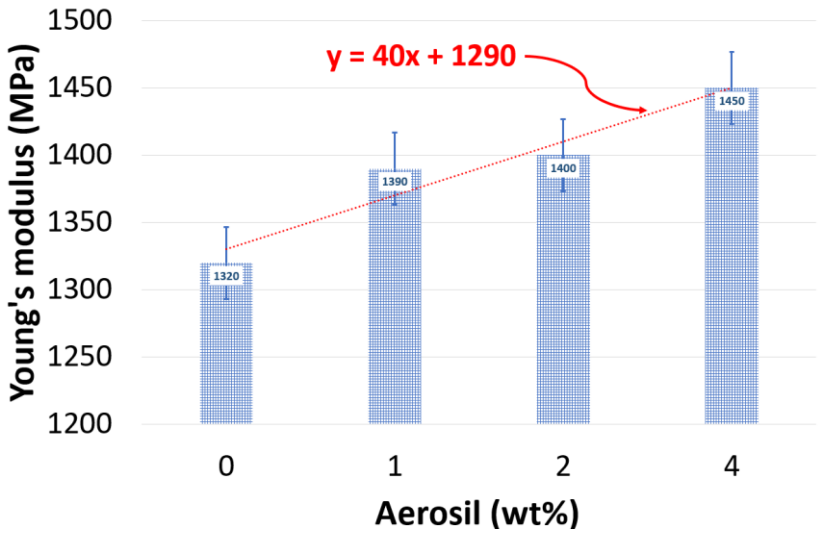
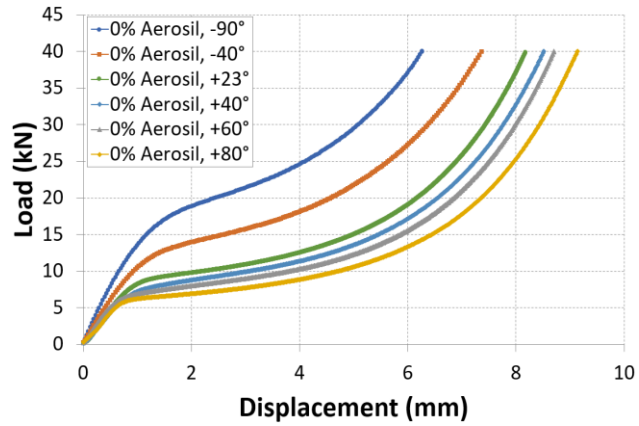


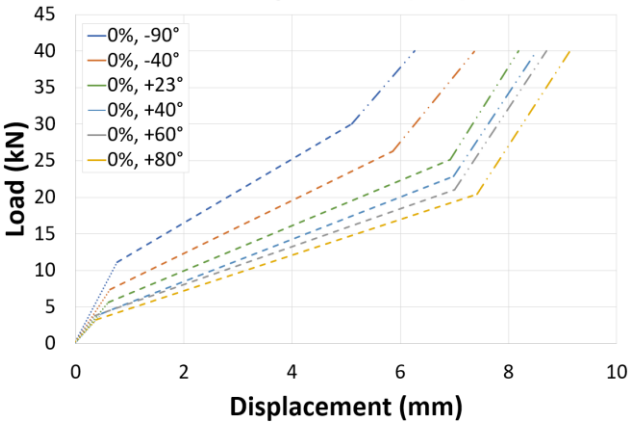
Figure 3. 19: Nanoparticle-dependent variation in Young's modulus at ambient temperature.

3.4.4 Effect of temperature on material behavior

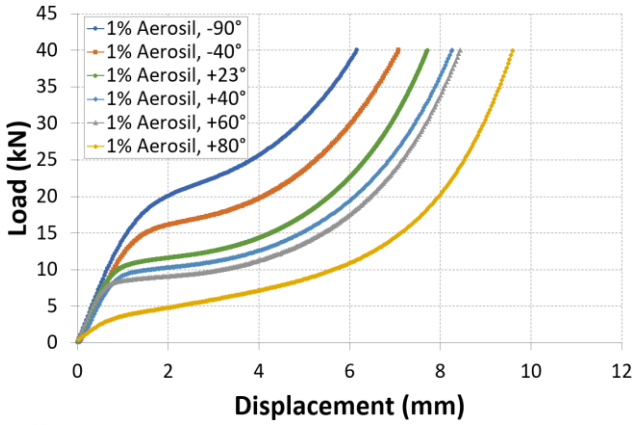
By analyzing the different nanoparticles' weight percentages present in the material, it was observed that increasing temperature leads to a decrease in the elastic portion of the material while the buckling portion increases. An exciting trend emerges from these observations: the elastic part reaches its maximum at -90°C, underlining maximum resilience to icy conditions. Conversely, the elastic part is minimal at 80°C, reducing the material's flexibility at high temperatures.

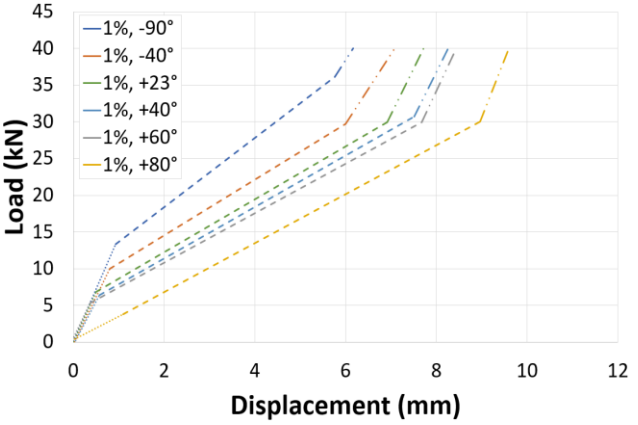
The three plateaus of the compression curve change as the temperature rises, as seen in ***Figure 3. 20***. ***Figure 3. 20*** (a), for example, the end of the elastic part corresponds to a value of 11.14 kN for a temperature of -90°C. In contrast, the end of the elastic part for a temperature of 80°C corresponds to a value of 3.24 kN. The elastic part varies with temperature; with increasing temperature, the elastic part decreases. The same holds for the nanoparticles percentage of 4% in ***Figure 3. 20*** (d); at -90°C, the elastic part equals 14.91 kN, while at 80°C, it equals 2.91 kN. Furthermore, we discovered that buckling plateaus also rise when temperature rises. This phenomenon can be attributed to the material's malleability above room temperature.



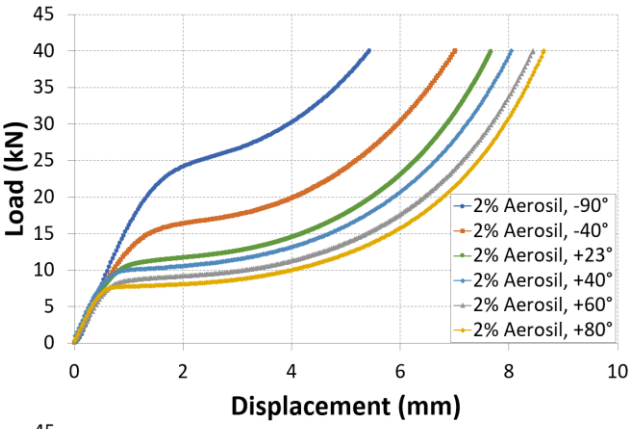


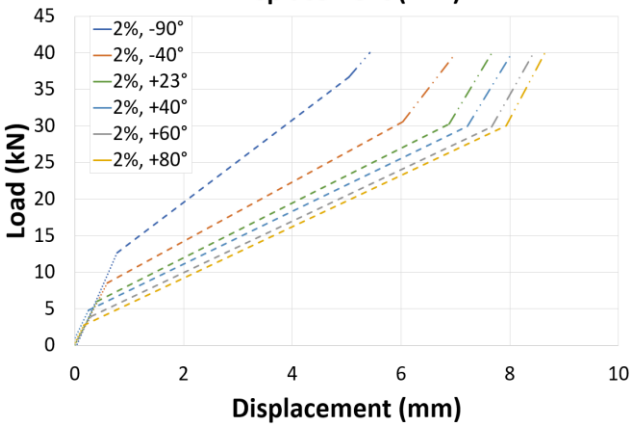
(a) 0wt.% Nanoceramic content



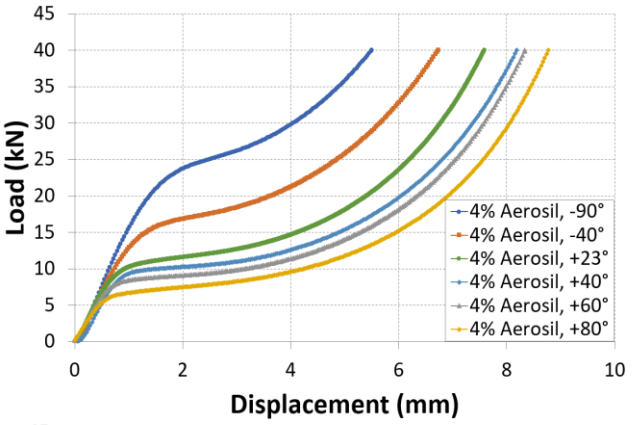


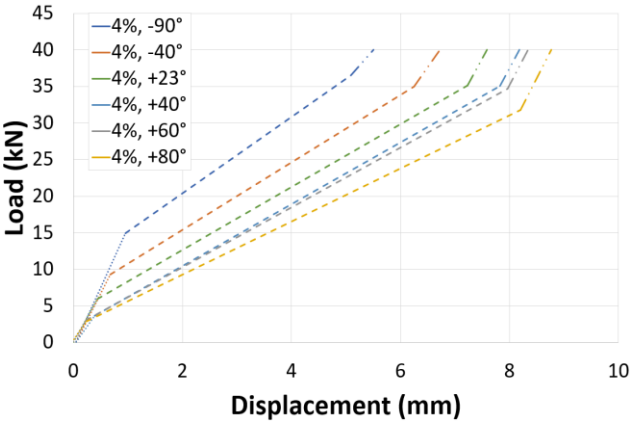
(b) 1wt.% Nanoceramic content





(c) 2wt.% Nanoceramic content





(d) 4wt.% Nanoceramic content

Figure 3. 20: The effect of temperature on material behavior.

3.4.5 Analysis of elastic and plastic properties

Figure 3. 21 depicts a typical characteristic curve for analyzing elastic and plastic properties, illustrating the elastic modulus, the buckling modulus, and the densification modulus.

Figure 3. 22 and ***Figure 3. 23*** show two diagrams illustrating the variation of the two plateaus; the elastic and plastic plateau, during the compression test. For each test, we have chosen to consider the end of the elastic part, the plastic part, or the rubbery plateau to study the effect of nanoparticle content and temperature on these plateaus in a compression curve. ***Figure 3. 22*** shows that the elastic part remains almost identical for a temperature of 80°C, with a slight difference between nanoparticle contents of 0wt.%, 1wt.%, 2wt.%, and 4wt.%. This allows us to say that working at a temperature of 80°C to increase elasticity does not require the material to be reinforced with Aerosil. On the other hand, at a temperature of -90°C, the elastic part is more significant, with a reinforcement wt.% of 4wt.%. This means that working at -90°C requires the polycarbonate to be reinforced with 4wt.% Aerosil to obtain good elasticity. For a temperature of 40°C, a 1wt.% reinforcement is sufficient to obtain suitable material elasticity.

The diagram shown in ***Figure 3. 23*** illustrates the variation of the buckling plateau as a function of temperature and Aerosil reinforcement. At -90 °C and -40°C, adding Aerosil reinforcement plays a significant role in improving plasticity. By increasing the nanoparticle content, plasticity also increases. On the other hand, at -90°C, adding 1wt.%, 2wt.%, and 4wt.% of reinforcement gives almost the same plasticity. At room temperature (23°C), 4wt.% Aerosil gives good plasticity compared with the other percentages. In addition, 1wt.% and 2wt.% give similar plasticity.

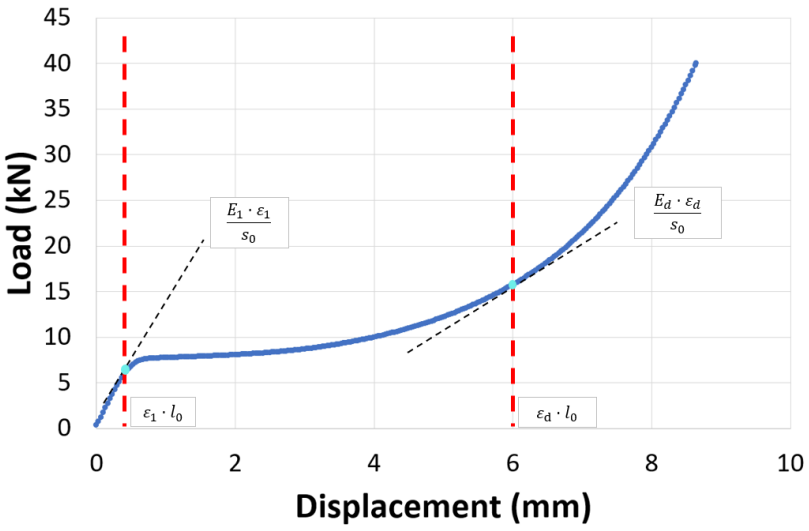


Figure 3. 21: Analysis of elastic and plastic properties: the characteristic curve.

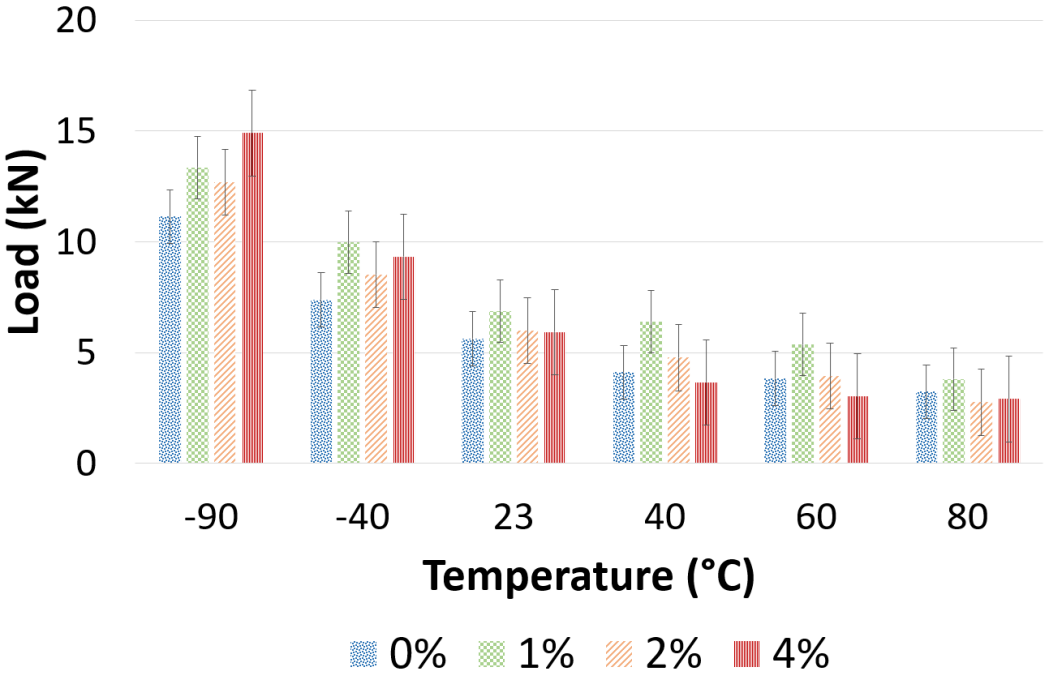


Figure 3. 22: Variation of Final Elastic Load with Temperature for Different Aerosil Percentage.

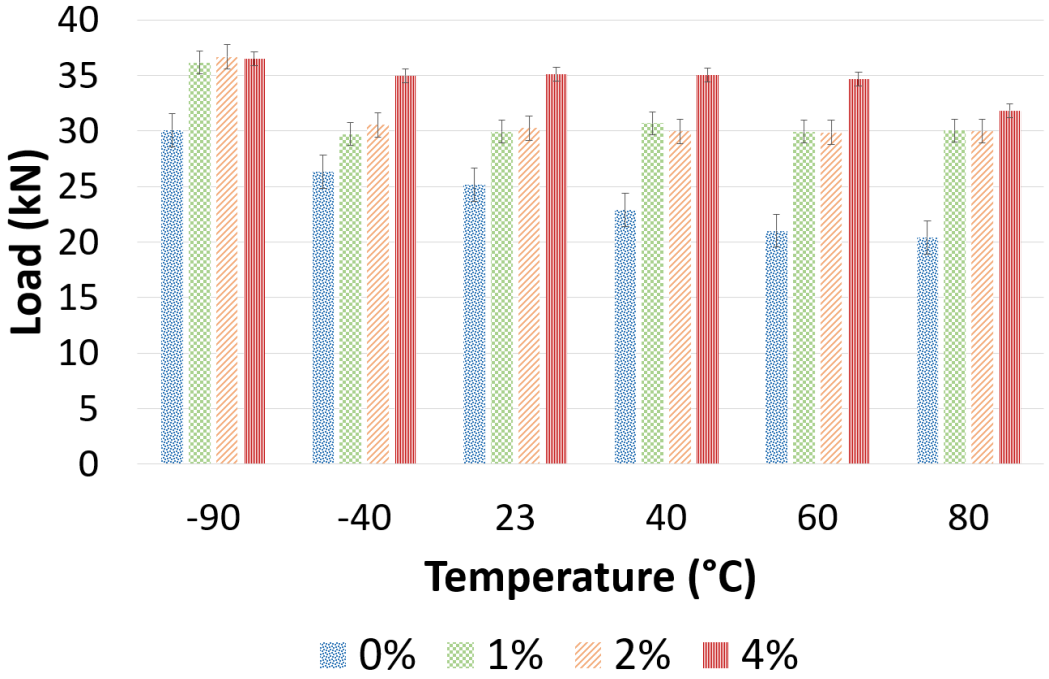


Figure 3. 23: Variation of Final Plastic Load with Temperature for Different Aerosil Percentage.

Figure 3. 24 illustrates the variation of densification modulus as a nanoparticle content and temperature function. A decrease in densification modulus is observed with increasing

temperature, as shown by decreasing linear mathematical equations. Remarkably, the densification modulus reaches its minimum at 0% nanoparticle content, characterized by the linear equation y = -11.23x + 183, while it reaches its maximum at 4wt.% nanofiller content, defined by the decreasing linear equation y = -4.11x + 219. Furthermore, the densification modulus is highest at -90°C for all nanofiller wt.%, while it is minimal at 80°C. This observation can be explained by the fact that, with increasing temperature, the material loses stiffness and becomes more malleable, decreasing the densification modulus.

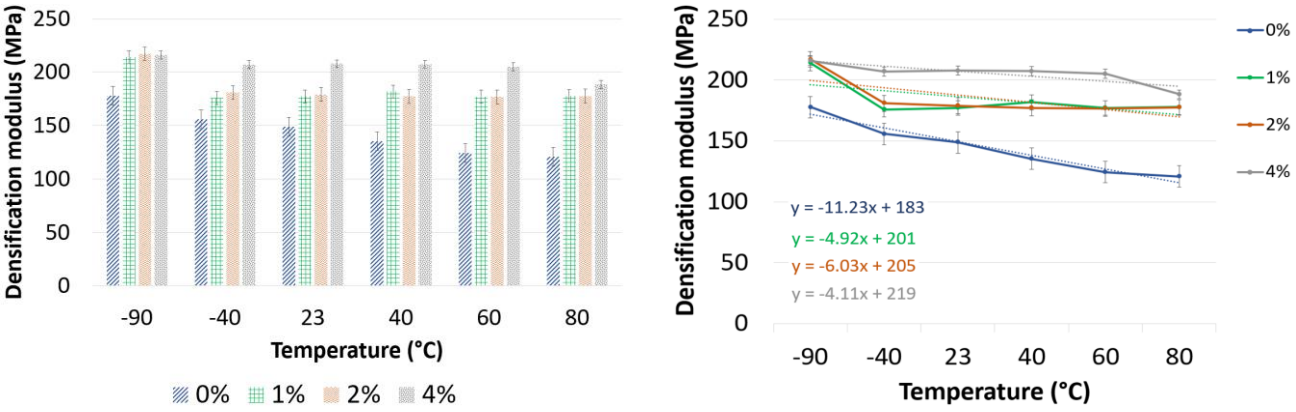
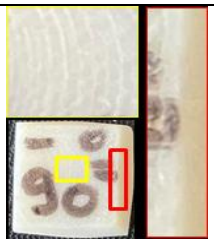
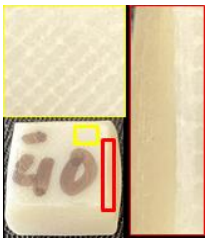
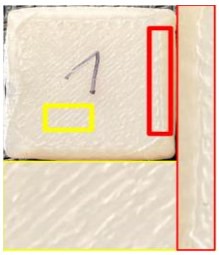
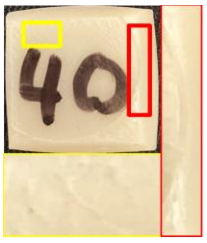
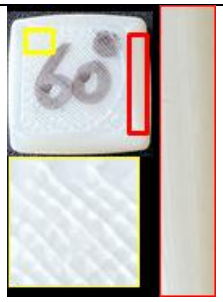
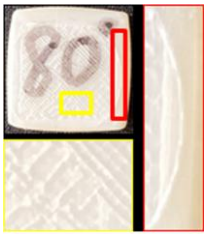


Figure 3. 24: Variation of densification modulus with temperature.

3.4.6 Effect of temperature on the imprint produced between the trays and the sample

Table 3. 1 shows the effect of temperature on the imprint produced between the trays and the sample. After each test, temperature variations significantly affect the impression left by the compression platens on the FDM-printed composite samples. At room temperature (23°C), the impression reveals inclined lines corresponding to the 45° printing direction, albeit slightly blurred, suggesting some fusion between the material layers. As the temperature rises to 60°C, this impression becomes sharper, clearly highlighting the material threads used in the FDM process, indicating better adhesion between the layers. On the other hand, at -90°C, the indentation has a uniform configuration, similar to that of circular compression plates, suggesting possible embrittlement of the material at extremely low temperatures.

Table 3. 1: The effect of temperature on the imprint produced between the trays and the sample.

Temperature (°C)	trays/sample	imprint
-90		
-40		
23		
40		
60		
80		

3. 5 Conclusion

For the first part, the tensile test on the CF-PETG concluded that a 75% honeycomb infill provides higher mechanical strength than a 100% infill. Regarding the dynamic tests on the Hopkinson bars, it was revealed that as the impact pressure increased, various dynamic parameters also increased, indicating a clear relationship between impact pressure and dynamic response. Interestingly, all samples showed similar compression trends for the impact pressures and infill densities. Notably, the material demonstrated its ability to dampen and absorb dynamic stresses, as evidenced by the equal amplitudes of the reflected and incident signals. The load curves showed a balance at both ends of the specimen, thus meeting the fundamental criteria for a valid SHPB experiment.

As for the third test, the study of static compression under the effect of temperature on Aerosil/polycarbonate revealed significant changes in the elasticity of composite materials at extreme temperatures, such as -90°C and 40°C, with notable variations between different levels of nanofillers. Incorporating Aerosil 300 into the polycarbonate matrix at concentrations ranging from 1% to 4% by weight significantly improved the material's mechanical properties. The following chapter will shift to the numerical study to complement and further understand the experimental results obtained. This approach will allow for the modeling of the mechanical behavior of the tested materials under various conditions, providing validation for the experimental observations through simulation.

CHAPITRE 4

Numerical study

Table of content

4. 1 Introduction 98
4. 2 Abaqus/Digimat modeling of FDM technology and the effect of printing parameters on the tensile strength of ABS parts 99
4.2.1 Recap of experimental study 99
4.2.2 FEA: Constitutive mechanical and thermal models 101
4.2.2.1 Mechanical analysis 101
4.2.2.2 Thermal analysis 103
4.2.3 Implementation of the Numerical Study 104
4.2.4 Finite Element Model 107
4.2.4.1 First modeling: Abaqus 107
4.2.4.2 Second modeling: Abaqus/Digimat coupling 108
4.2.5 Effect of printing speed on residual stresses 111
4.2.6 Effect of Printing Speed on the deflection 111
4.2.7 Parametric study of 3D printing 114
4.2.7.1 Effect of discretization method: Layer-by-layer vs Filament 118
4.2.7.2 Effect of the printing direction 120
4.2.7.3 Effects of 3D printing on the geometry of the part 122
4.2.8 Cost of printing 122
4. 3 Study of the tensile behavior of 3D-printed CF-PETG composites 123
4.3.1 Finite element Model of tensile tests 123
4.3.2 Finite element analysis results 124
4.3.3 3D printing modeling 130
4.3.3.1 Effect of 3D printing on the geometry of the part 131
4.3.4 Parametric study of 3D printing 132
4.3.5 Abaqus/Digimat coupling for efficient numerical modeling 138
4. 4 Dynamic compression behavior of 3D-printed CF-PETG composites 140
4.4.1 Finite element model 140
4.4.2 Meshing and limit condition 141
4.4.3 Results and Discussion 143
4.4.3.1 Results of variations in Von Mises stresses, plasticity, and displacements 143
4.4.3.2 Comparison and validation: test vs. simulation 146
4. 5 Static compression modeling of Aerosil/polycarbonate composites 158
4.5.1 Homogenization cycle 158
4.5.2 Nanocharge effect after Aerosil/ Polycarbonate homogenization 160
4.5.3 Representation of the elementary volume of the composite 161
4.5.4 Position of the nanoceramic relative to the matrix 162
4. 6 Conclusion 166

4. 1 Introduction

Thanks to the evolution of numerical tools and the coupling of several numerical modeling software, we have succeeded in developing and validating several tests on numerous materials. In the first part of this chapter, after reviewing the work and experimental results obtained by Parham et al. [110] on ABS 3D printing, we concentrated on their numerical modeling. First, we numerically investigated the effect of printing speed (10, 30, 50, and 70 mm/s) on the tensile and fracture behavior of ABS samples produced by the FDM technique. Print speed has a direct effect on material behavior. The higher the print speed, the greater the risk of over-extrusion, spinning, and other problems with the material. In addition, higher print speeds can lead to distortion, bending, and other dimensional problems. It is, therefore, essential to adjust the printing speed appropriately to obtain the best possible result with the material. After validating the numerical model, we numerically enhanced the results obtained experimentally by Parham et al. [110] using Abaqus and Digimat software and a parametric study. The latter enabled us to quantify the effect of 3D printing parameters such as printing speed, printing direction, and chosen discretization (layer by layer or filament) on residual stresses, deflection, warpage, and resulting mechanical behavior. The cost of the current printing installation was estimated during the costing process. The price of the printing substrate (ABS) must be considered. Several data are therefore required, including the material's cost, the portion's mass, and the substrate's mass. In the second part, we investigated the mechanical behavior of a carbon-fiber-reinforced thermoplastic polymer (CF-PETG) manufactured using FFF technology. Static tensile tests were carried out on two filling patterns, honeycomb (NIDA) and rectilinear (RECT), at different filling ratios (20%, 50%, 75%, and 100%). Two numerical approaches have been developed to approximate natural manufacturing and loading conditions. Using the Abaqus calculation code, the first assumes that the printed part is perfect. The second is the originality of our work, which lies in numerical modeling, where we have developed a technique that couples Abaqus/Digimat, considering the impact of printing parameters on material behavior. This work offers significant prospects for the accurate prediction of the behavior of printed structures under different printing conditions by considering the effects of coupling between two computer codes and printing factors on the accuracy of FEM predictions.

The main objective of the third part was to explore the influence of fill density on the dynamic characteristics of 3D-printed components. Polyethylene terephthalate glycol (CF-PETG), a composite material reinforced with short carbon fibers, was chosen for its outstanding mechanical, physical, thermal, and energy absorption properties. This research focuses on a

numerical study to characterize the dynamic behavior of CF-PETG manufactured using the fused filament fabrication (FFF) technique.

In the last part, the Digimat software modules were used, and numerical analysis was carried out to homogenize the Aerosil/PC material, calculate the mean field, and represent the elementary volume. This method makes it possible to study the various parameters of the matrix and reinforcement, giving a global view of the composite material's performance.

4. 2 Abaqus/Digimat modeling of FDM technology and the effect of printing parameters on the tensile strength of ABS parts

The effect of printing speed on the tensile strength of acrylonitrile butadiene styrene (ABS) samples fabricated using the fused deposition modeling (FDM) process is addressed in this research. The mechanical performance of FDM-ABS products was evaluated using four different printing speeds (10, 30, 50, and 70 mm/s). A numerical model was developed to simulate the experimental campaign by coupling two computational codes, Abaqus and Digimat. In addition, this work attempts to investigate the impacts of printing parameters on ASTM D638 ABS specimens. A 3D thermomechanical model was implemented to simulate the printing process and evaluate the printed part quality by analyzing residual stress, temperature gradient, and warpage. Several parts printed in Digimat were analyzed and compared numerically. The parametric study allowed us to quantify the effect of 3D printing parameters such as printing speed, printing direction, and the chosen discretization (layer by layer or filament) on residual stresses, deflection, warpage, and resulting mechanical behavior.

4.2.1 Recap of experimental study

Parham et al. employed a 3D printing method, particularly fused deposition modeling (FDM), to create ABS specimens at various printing speeds (10, 30, 50, and 70 mm/s). To choose the suitable/optimal speed for the 3D printing of this material, they studied the effect of printing speed (10, 30, 50, and 70 mm/s) on the behavior law of ABS. The geometry and dimensions of the tensile specimens are shown in ***Figure 4. 1***. ***Table 4. 1*** shows the printing parameters used in this study.

Tensile tests were conducted using a SATAM STM-150 universal testing machine at a displacement speed of 1 mm/min, and the displacement and deformation were measured using the digital image correlation (DIC) technique, ***Figure 4. 2***.

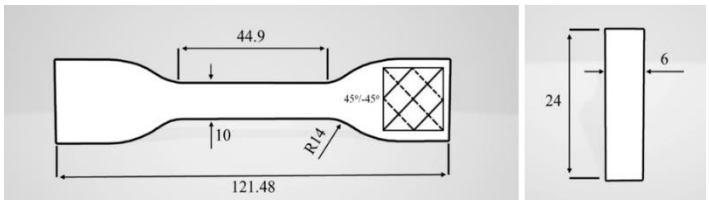


Figure 4. 1: Geometry and dimensions of the tensile specimens [110].



Figure 4. 2: Characterisation of the mechanical properties of FDM-ABS specime (a) Printed tensile specimen and (b) tensile testing configuration [110].

Table 4. 1: Constant building parameters for manufacturing the test specimens [110].

Building parameters	**Value**
Filament diameter (mm)	1.75
Infill density (%)	100
Nozzle diameter (mm)	0.4
Nozzle temperature (°C)	235
Bed temperature (°C)	140
Raster angle (deg)	45/-45

The stress-strain curves for ABS parts printed using the FDM technique at various printing speeds are shown in ***Figure 4. 3*** . At a printing speed of 10 mm/s, the specimen with the greatest tensile strength was produced. The specimen made at a speed of 30 mm/s has the lowest value in elongation at failure, while the specimen made at a speed of 70 mm/s exhibits the maximum value. ***Table 4. 2*** summarises the properties of ABS thermoplastic as determined by a tensile

test, where E stands for the Young modulus, ν is the Poisson's ratio, σ_y is the yield strength, σ_u is the ultimate strength, $\varepsilon_{elastic}$ is the elastic deformation and $\varepsilon_{plastic}$ is the plastic deformation.

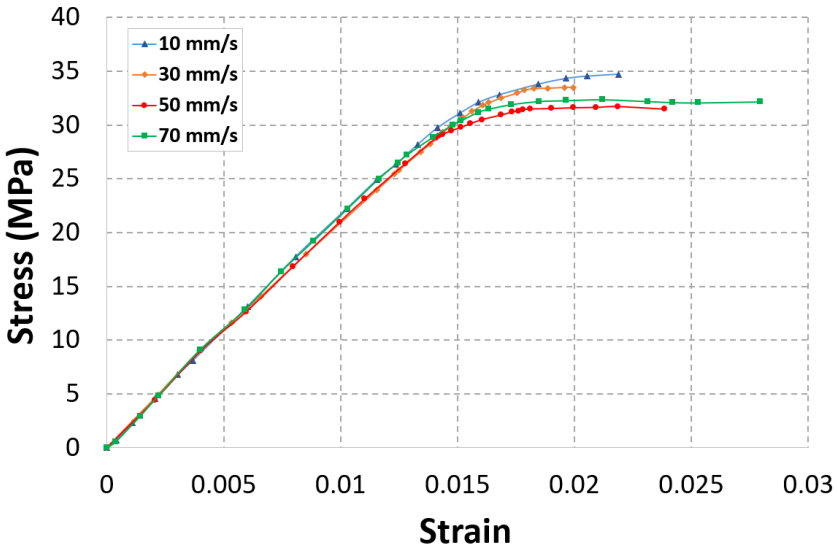


Figure 4. 3: Representative True stress vs. True strain curves for the manufactured tensile specimens with different printing speeds.

Table 4. 2: Average Tensile properties of the tested FDM-ABS specimens [110].

Printing speed (mm/s)	E (MPa)	ν	$\sigma_y(MPa)$	$\sigma_u(MPa)$	$\varepsilon_{elastic}$	$\varepsilon_{plastic}$
10	2321	0.34	32.8	34.15	0.017	0.005
30	2276	0.35	32.2	34.02	0.016	0.004
50	2357	0.34	31.8	32.9	0.015	0.006
70	2218	0.35	31.2	31.98	0.017	0.010

4.2.2 FEA: Constitutive mechanical and thermal models

4.2.2.1 Mechanical analysis

The constitutive equation that determines the mechanical behavior of FDM printed parts must be defined to use the FEA model to forecast the thermomechanical behavior of those parts. Hooke's law, which establishes the correlation between stress and strain, describes the linear elasticity of polymers. This relationship is described as follows in 3D:

$$\begin{pmatrix}\varepsilon_{11}\\ \varepsilon_{22}\\ \varepsilon_{33}\\ \gamma_{12}\\ \gamma_{23}\\ \gamma_{31}\end{pmatrix} = \begin{pmatrix}S_{11} & S_{12} & S_{13} & S_{14} & S_{15} & S_{16}\\ & S_{22} & S_{23} & S_{24} & S_{25} & S_{26}\\ & & S_{33} & S_{34} & S_{35} & S_{36}\\ & & & S_{44} & S_{45} & S_{46}\\ & Sym & & & S_{55} & S_{56}\\ & & & & & S_{66}\end{pmatrix} \cdot \begin{pmatrix}\sigma_{11}\\ \sigma_{22}\\ \sigma_{33}\\ \tau_{12}\\ \tau_{23}\\ \tau_{31}\end{pmatrix} \quad (1)$$

where ε is the deformation, γ is the shearing strain, τ is the shearing stress, and σ is the normal stress. By using the standard engineering constants, Eq. (1) expresses the constitutive law in terms of Young's modulus, Poisson's ratio, and shear modulus:

$$\begin{pmatrix}\varepsilon_{11}\\ \varepsilon_{22}\\ \varepsilon_{33}\\ \gamma_{12}\\ \gamma_{23}\\ \gamma_{31}\end{pmatrix} = \begin{pmatrix}1/E_{11} & -\vartheta_{12}/E_{11} & -\vartheta_{13}/E_{11} & 0 & 0 & 0\\ & 1/E_{22} & -\vartheta_{23}/E_{22} & 0 & 0 & 0\\ & & 1/E_{33} & 0 & 0 & 0\\ & & & 1/G_{23} & 0 & 0\\ & Sym & & & 1/G_{13} & 0\\ & & & & & 1/G_{12}\end{pmatrix} \cdot \begin{pmatrix}\sigma_{11}\\ \sigma_{22}\\ \sigma_{33}\\ \tau_{12}\\ \tau_{23}\\ \tau_{31}\end{pmatrix} \quad (2)$$

By inverting the stiffness matrix, the compliance matrix is created, and we are left with:

$$\begin{pmatrix}\sigma_{11}\\ \sigma_{22}\\ \sigma_{33}\\ \tau_{12}\\ \tau_{23}\\ \tau_{31}\end{pmatrix} = \begin{pmatrix}C_{11} & C_{12} & C_{13} & C_{14} & C_{15} & C_{16}\\ & C_{22} & C_{23} & C_{24} & C_{25} & C_{26}\\ & & C_{33} & C_{34} & C_{35} & C_{36}\\ & & & C_{44} & C_{45} & C_{46}\\ & Sym & & & C_{55} & C_{56}\\ & & & & & C_{66}\end{pmatrix} \cdot \begin{pmatrix}\varepsilon_{11}\\ \varepsilon_{22}\\ \varepsilon_{33}\\ \gamma_{12}\\ \gamma_{23}\\ \gamma_{31}\end{pmatrix} \quad (3)$$

Where

$$C_{11} = \frac{(S_{22} \cdot S_{33} - S_{23}^2)}{S}, C_{22} = \frac{(S_{11} \cdot S_{33} - S_{13}^2)}{S}, C_{33} = \frac{(S_{11} \cdot S_{22} - S_{12}^2)}{S} \quad (4)$$

$$C_{12} = \frac{(S_{23} \cdot S_{13} - S_{12} \cdot S_{33})}{S}, C_{13} = \frac{(S_{12} \cdot S_{23} - S_{22} \cdot S_{13})}{S}, C_{23} = \frac{(S_{12} \cdot S_{13} - S_{11} \cdot S_{23})}{S} \quad (5)$$

$$C_{44} = \frac{1}{S_{44}}, C_{55} = \frac{1}{S_{55}}, C_{66} = \frac{1}{S_{66}} \quad (6)$$

$$S = S_{11}S_{22}S_{33} + 2S_{12}S_{23}S_{13} - S_{13}^2S_{22} - S_{23}^2S_{11} - S_{13}^2S_{33} \quad (7)$$

In the case of polymers, the substance is thought to exhibit anisotropic behaviour, and the stress-strain behaviour can be expressed using the following Cartesian coordinates:

$$\varepsilon_{11} = \frac{1}{E}[\sigma_{11}\vartheta(\sigma_{22} + \sigma_{33})] + \alpha_e \Delta T \quad (8)$$

$$\varepsilon_{22} = \frac{1}{E}[\sigma_{22}\vartheta(\sigma_{11} + \sigma_{33})] + \alpha_e \Delta T \quad (9)$$

$$\varepsilon_{33} = \frac{1}{E}[\sigma_{33}\vartheta(\sigma_{11} + \sigma_{22})] + \alpha_e \Delta T \quad (10)$$

$$\varepsilon_{xy} = \frac{1+\vartheta}{E}\sigma_{xy}, \varepsilon_{xz} = \frac{1+\vartheta}{E}\sigma_{xz}, \varepsilon_{yz} = \frac{1+\vartheta}{E}\sigma_{yz} \quad (11)$$

where α_e is the coefficient of thermal expansion. The thermal stain can be found as:

$$\varepsilon_{th} = \alpha_e \Delta T \quad (12)$$

The real stress and the Von Mises Stress can be determined as follows:

$$\sigma_{eff} = \sqrt{\sigma_{11}^2 + \sigma_{22}^2 + \sigma_{33}^2} + 2\vartheta(\sigma_{11}\sigma_{22} + \sigma_{11}\sigma_{33} + \sigma_{22}\sigma_{33}) \quad (13)$$

$$\sigma_{\text{Mises}} = \sqrt{\frac{1}{2}[(\sigma_{11}^2 - \sigma_{22}^2)^2 + (\sigma_{22}^2 - \sigma_{33}^2)^2 + (\sigma_{33}^2 - \sigma_{11}^2)^2]} \quad (14)$$

4.2.2.2 Thermal analysis

Digimat 2022.1 offers the option of applying indirect sequentially coupled thermomechanical analysis for stress and heat analysis. Heat transfer is considered in the numerical model to determine the temperature profile and variation during the printing process. The heat transfer's governing partial differential equation is:

$$\rho C_p \frac{\partial T}{\partial t} = k\left(\frac{\partial^2 T}{\partial x^2} + \frac{\partial^2 T}{\partial y^2} + \frac{\partial^2 T}{\partial z^2}\right) \quad (15)$$

ρ, C_p, and k are the polymer's density, specific heat capacity, and thermal conductivity, respectively. The energy that the phase solidification requires is about equal to:

$$H = \int \rho C_p(T) dT \quad (16)$$

A newly deposited layer at temperature Tm cools with the chamber temperature Tc. The underlying layers are reheated by conduction during the printing process, and their temperature exceeds Tg. The thickness of the part was printed in the z-direction with a constant chamber temperature of Tc. In this direction, the evolution of the temperature T (z, t) for each position at time t satisfies the following heat equation:

$$\rho C_p \frac{\partial T}{\partial t} = k \frac{\partial^2 T}{\partial z^2} \tag{17}$$

This equation has the following solution

$$T = T_{\mathrm{c}} + \frac{H}{\rho C_{\mathrm{p}}} \frac{1}{\sqrt{\pi \varphi t}} \exp\left(-\frac{Z^2}{4\varphi t}\right) \tag{18}$$

Where the polymer's thermal diffusivity is given by the formula $\varphi = \frac{k}{\rho C_p}$.

The thermal energy of the layer can be calculated as follows if the FDM portion has a suitably high dimension and a thickness h that is higher than the layer thickness Δh:

$$H = \rho C_{\mathrm{p}} \Delta h (T_{\mathrm{m}} - T_{\mathrm{c}}) \tag{19}$$

Additionally, the temperature variation across the part's thickness can be determined as:

$$T = T_{\mathrm{c}} + (T_{\mathrm{m}} - T_{\mathrm{c}}) \frac{\Delta h}{\sqrt{\pi \varphi t}} \exp\left(-\frac{Z^2}{4\varphi t}\right) \tag{20}$$

The temperature fluctuation at the Z position can be calculated using Eq. 20. For instance, to determine the layer where the temperature Tg (T = Tg) is reached at a specific time t, we have:

$$Z = 2\sqrt{\varphi t} \sqrt{\ln\left(\frac{\Delta h}{\sqrt{\pi \varphi}} \frac{T_{\mathrm{m}} - T_{\mathrm{c}}}{T_{\mathrm{g}} - T_{\mathrm{c}}}\right) - \ln \sqrt{t}} \tag{21}$$

4.2.3 Implementation of the Numerical Study

A numerical model has been developed to simulate the experimental results reported by Parham et al.[110]. ***Figure 4. 4*** shows that the model validating method is based on alternating between the two numerical simulation programs, Abaqus and Digimat. The combination of Abaqus and Digimat offers various advantages, including the accuracy of the results due to the mesh's

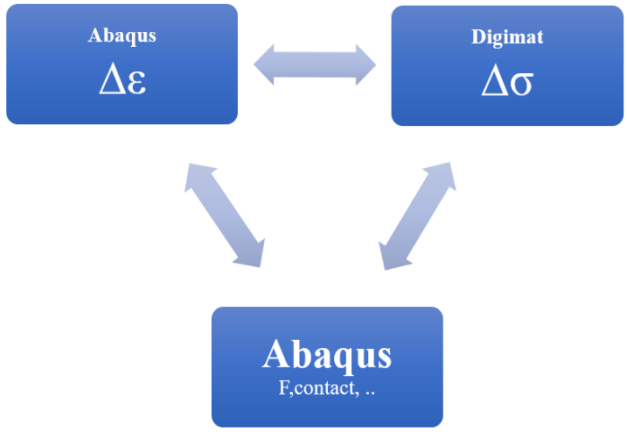
superposition between the two models and a significant set of developments related to the printed specimen.



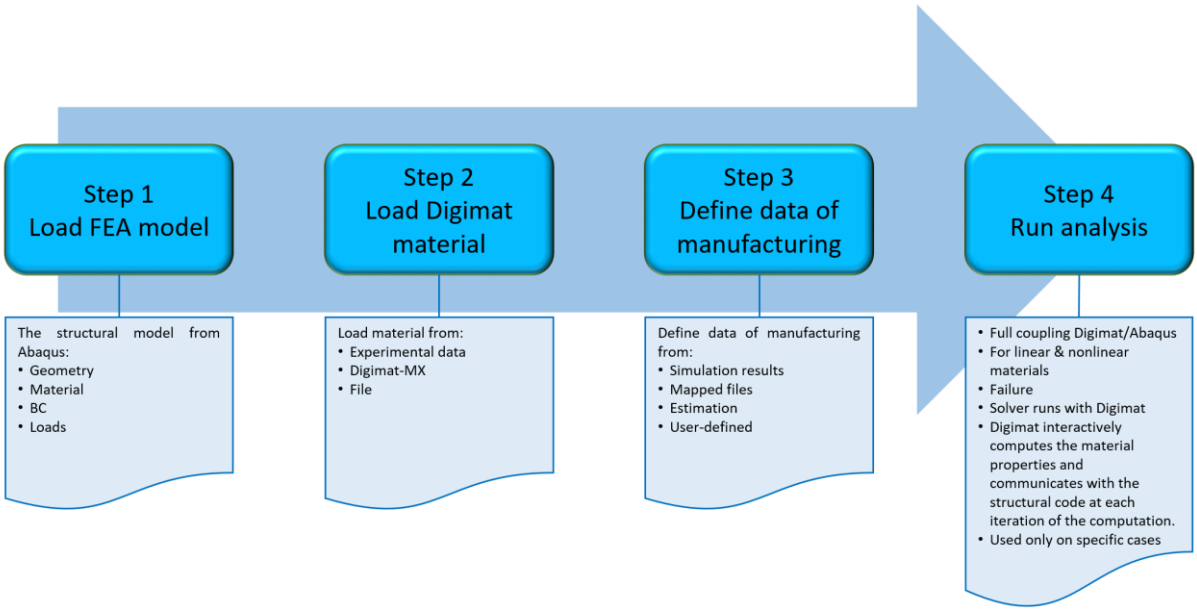
Figure 4. 4: Kinetics of a coupled Abaqus/Digimat computation.

At each integration point, Abaqus' role is to determine the strain increment under different contact types, boundary conditions, and loads before handing off to Digimat to determine the stress increment on each element. Then it will give a hand back to Abaqus to continue calculation (loads, contacts, etc.). Moreover, for the next step, Abaqus will compute the strain increment so that Digimat will use all the information recorded at the integration points (orientation tensor, residual stresses...), ***Figure 4. 5***a. ***Figure 4. 5***b shows the different steps to carry out a calculation by coupling Abaqus/Digimat.

One of the crucial points of this Abaqus/Digimat coupling is the consideration of the implementation process (effect of 3D printing: deflection, residual stress, warping) on the mechanical performance of the structure. ***Figure 4. 6*** shows the mapped manufacturing data visualized on the structural model.



(a)



(b)

Figure 4. 5: Coupling procedure between Abaqus and Digimat.

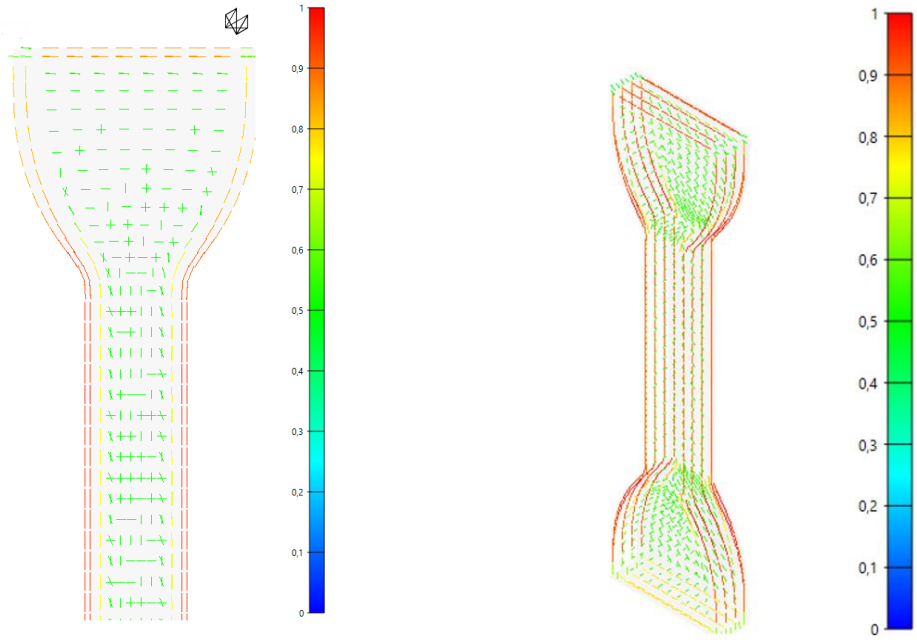


Figure 4. 6: Mapped manufacturing data visualized on the structural model, filament orientation (eigenvector).

4.2.4 Finite Element Model

4.2.4.1 First modeling: Abaqus

The initial part of the model validation process was the creation of an ASTM-D638 specimen in the simulation program Abaqus, using a C3D8R mesh with a 0.5 mm cell size (a total of 94913 nodes and 84768 linear hexahedral elements of type C3D8R) (***Figure 4. 7***). Then the curve corresponding to a printing speed of 10 mm/s was fitted to identify the elastic and plastic properties of ABS, which were estimated from the experimental results, ***Table 4. 3***. After that, the boundary conditions were inserted, and our model was meshed.

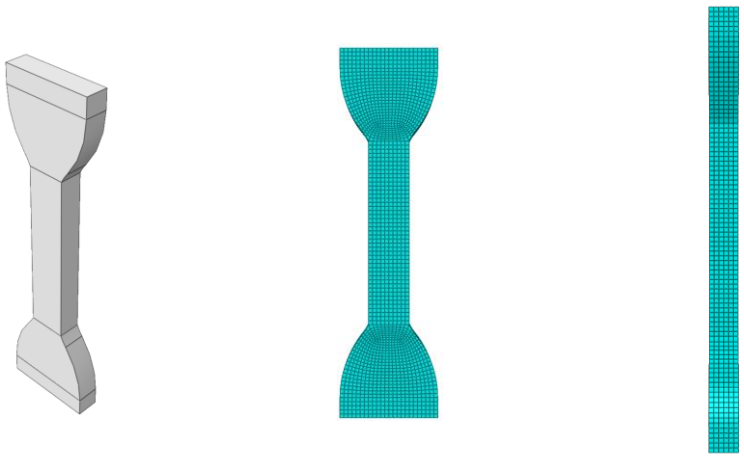


Figure 4. 7: Specimen mesh C3D8R.

Table 4. 3: ABS properties for a printing speed of 10 mm/s.

Properties of ABS	Value
Young's modulus (MPa)	2180
Yield strength (MPA)	24
Poisson ratio	0.3

Figure 4. ***8*** shows the stress-strain curve for a first printing speed of 10 mm/s. A good correlation between the experimental and numerical results can be noted.

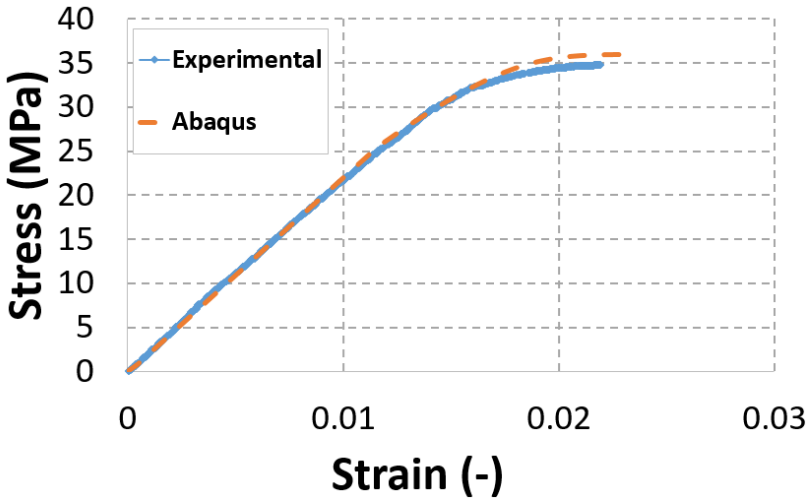


Figure 4. 8: Stress-Strain curve for a printing speed of 10 mm/s.

4.2.4.2 Second modeling: Abaqus/Digimat coupling

Digimat software is the second approach for simulating the material's response under tensile loading for the printing speed of 10 mm/s. The coupling between Abaqus and Digimat, mentioned in ***Figure 4. 5***, was used. The first step is to work on Digimat-AM, where all the printing parameters, including the nozzle and bed temperatures and the manufacturing process, have been entered, ***Table 4. 2***.

The G-code file must also be inserted, which includes details on the filling density, filler type, filament and nozzle diameters, printing speed, and printing density. To get the Gcode file, we used the software Slic3r, inserting all the parameters into the windows of Slic3r. Finally, the specimen has meshed. ***Figure 4. 9*** depicts the workflow for Digimat-AM.

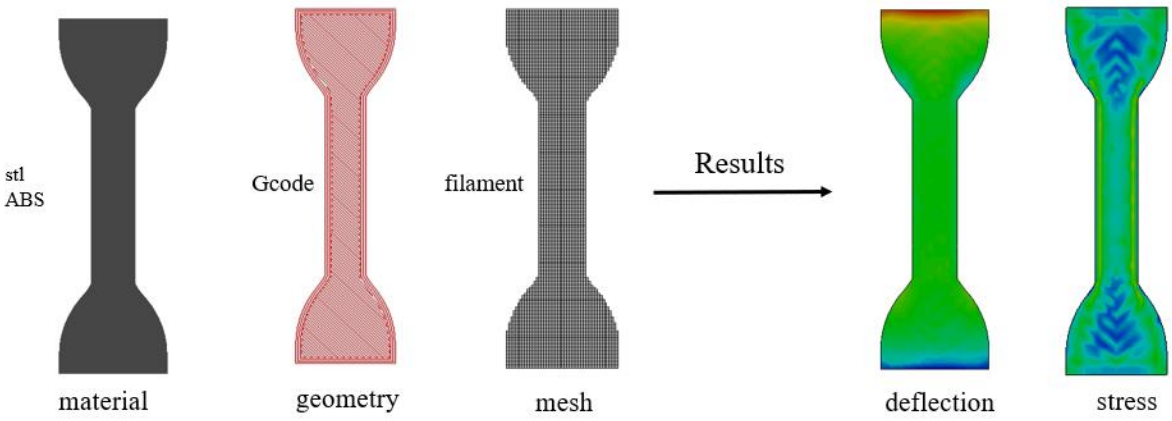


Figure 4. 9: Work sequences in Digimat-AM.

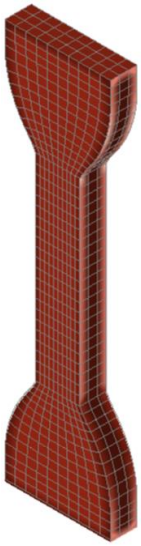


Figure 4. 10: Superposition of the mesh between Abaqus and Digimat.

Digimat-RP and the superposition of the mesh between Abaqus and Digimat-AM (***Figure 4. 10***) and considering the results found in Digimat-AM (residual stresses, deflection, undeformed mesh, temperature), we obtained the curve shown in ***Figure 4. 11***.

Furthermore, the curve determined by this approach and the experimental data are compared, and a good correlation was found. This curve will be used as a reference to establish the curves for the printing speeds of 30, 50, and 70 mm/s.

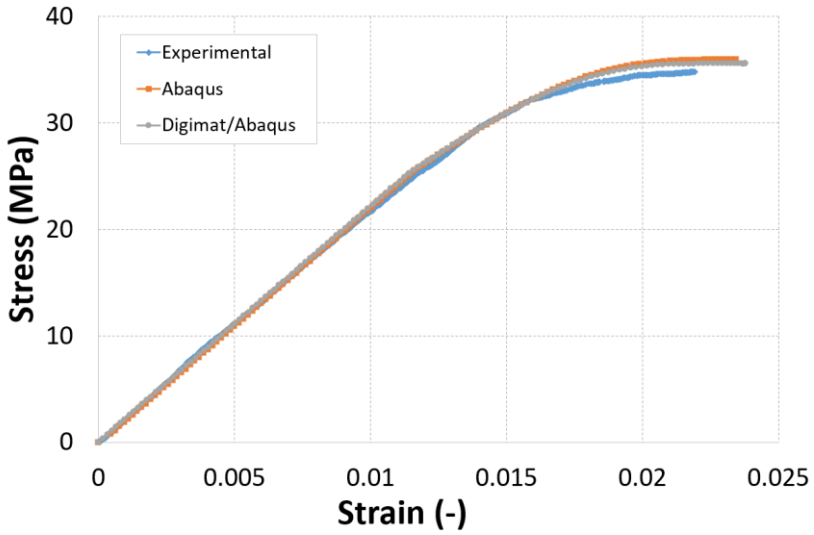


Figure 4. 11: Stress-Strain curves for a printing speed of 10 mm/s.

It is essential to validate the working sequence using different printing speeds, including 30, 50, and 70 mm/s, to confirm this approach after evaluating the mechanical behavior of ABS for a printing speed of 10 mm/s using the Digimat/Abaqus coupling technique. Therefore, a comparison with the experimental data has been built to validate the numerical models developed in this study. ***Figure 4. 12*** displays the stress-strain curves determined experimentally and numerically for printing rates of 10, 30, 50, and 70 mm/s. Generally, we can state a good correlation between the numerical simulations and the experimental results. We can thus conclude that the models predict the mechanical behavior of the tested composites for the different printing speeds.

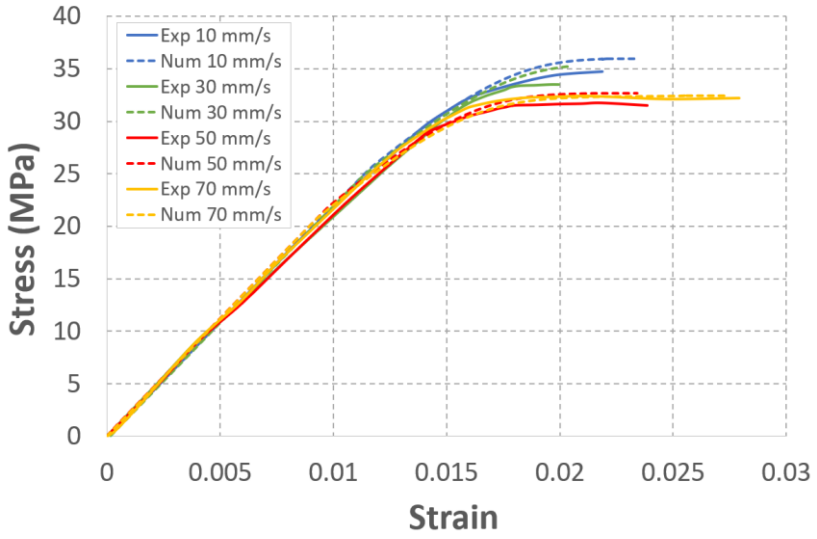


Figure 4. 12: Stress-Strain curve determined numerically for 4 printing speeds.

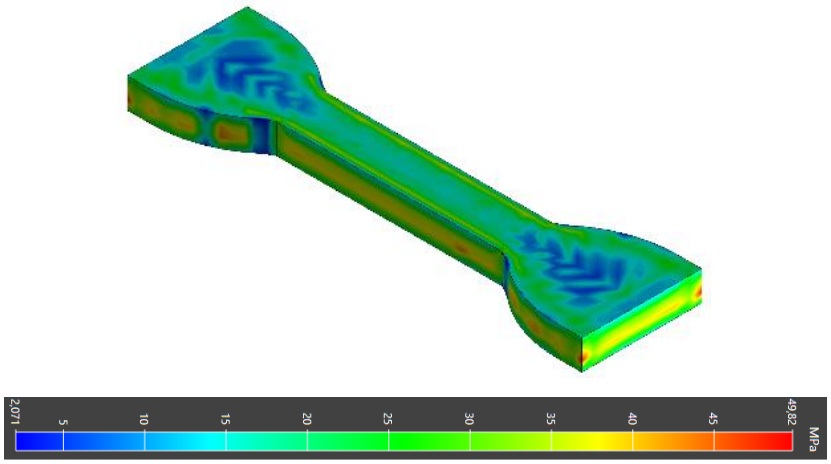
4.2.5 Effect of printing speed on residual stresses

Residual stresses introduced during the 3D printing process significantly affect the mechanical characteristics and dimensional accuracy of additive manufacturing items [128]. Therefore, the last layer of the print, where residual stresses accumulate (at the end of the manufacturing process), was selected to adequately investigate the effect of printing speed on the residual stresses and deflection induced by the FDM process and to measure the residual stresses precisely.

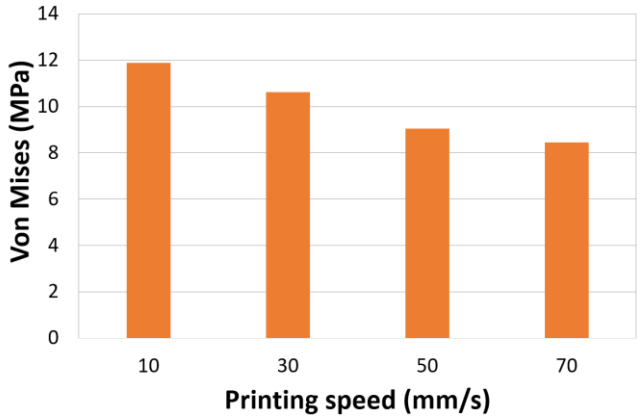
Figure 4. 13 shows the evolution of stresses as a function of printing time. The residual stresses were less important as the printing speed increased, and the maximum value of 11.87 MPa was reached with a speed of 10 mm/s. Conversely, the lowest residual stresses, with a value of 8.46 MPa, were observed at 70 mm/s.

4.2.6 Effect of Printing Speed on the deflection

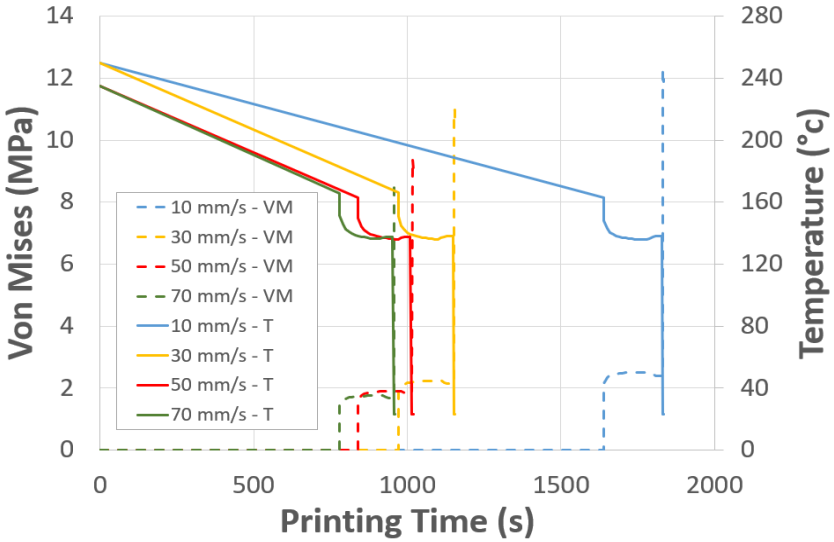
Figure 4. 14 displays the deflection and temperature evolution as a function of printing speed and time, respectively. Figure 14b showed that the deflection interval for printing at 10 and 30 mm/s was nearly identical [0.91, 0.93 mm] and that the deflection values for printing at 50 and 70 mm/s were extremely comparable [about 0.87 mm]. As a result, the deflection reduces as printing speed increases, which can be explained by the fact that at higher printing speeds, defects (such as voids and gaps) can cause a reduction in the part's strength.



(a) Residual stresses field (V=10mm/s)

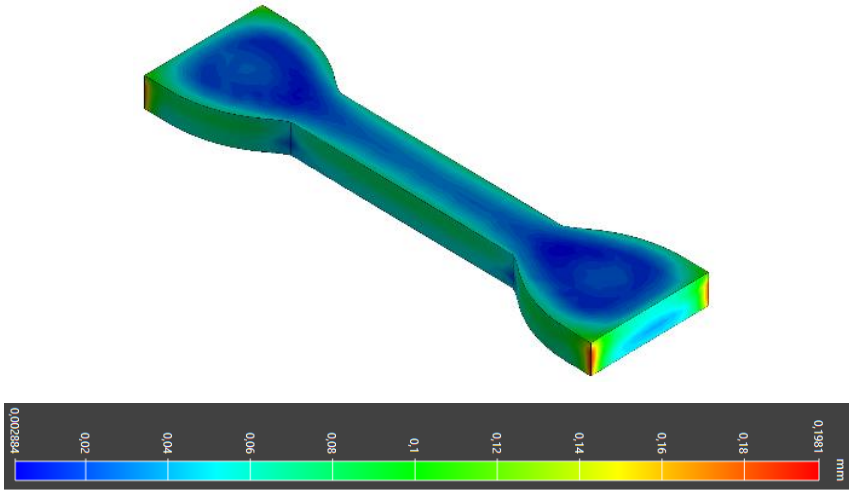


(b) Von Mises vs Printing speed

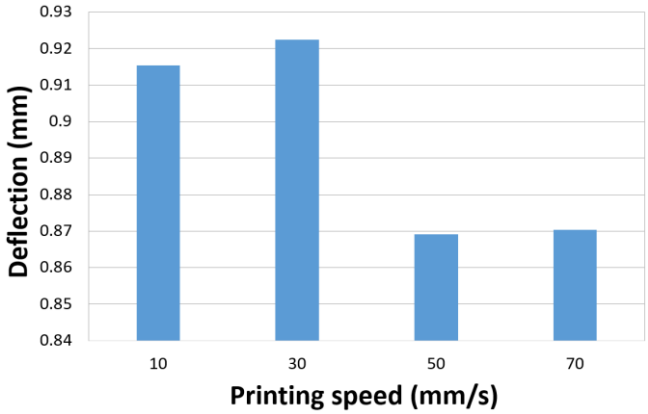


(c) Von Mises and Temperature vs Printing Time

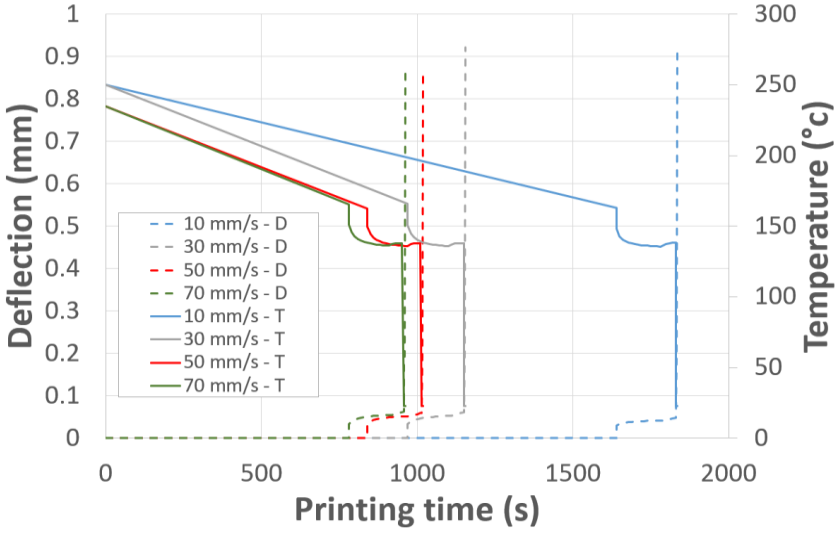
Figure 4. 13: Residual stresses at the end of the manufacturing process.



(a) Deflection field (V=10mm/s)



(b) Deflection vs Printing speed



(c) Deflection and Temperature vs Printing Time

Figure 4. 14: Deflection at the end of the manufacturing.

4.2.7 Parametric study of 3D printing

The specimen's temperature and Von Mises stress variations were recorded at several sample locations. Most previous research has focused on considering temperature as the most critical parameter influencing the mechanical behavior of polymers when designing industrial parts during the additive manufacturing process [129]. In this part, two distinct configurations of the FDM process, the filament deposit FDM process, and the layered deposit FDM method, are evaluated regarding temperature evolution and stress field during manufacturing the ASTM D638 specimen. ***Figure 4. 15*** shows that the characteristics were examined in various parts. Several frames from a simulation of the deposit layer process, which consists of the first layer, the sixth layer, and the twelfth layer, are shown in ***Figure 4. 16***.

Additionally, the temperature of the part is depicted in this picture at various points during the printing process. For instance, the top layer section is always the hottest and eventually cools down since the second layer is hotter than the first.

Depiction of this occurrence makes it easier to understand. When printing the part, the temperature field in the three specified layers follows three phases:

- The printing phase is where a sharp drop in temperature is noted (from 250°C to 140°C).
- The holding phase is where the temperature remains stable with very small decreases.
- The cooling phase reaches the final temperature of 23°C.

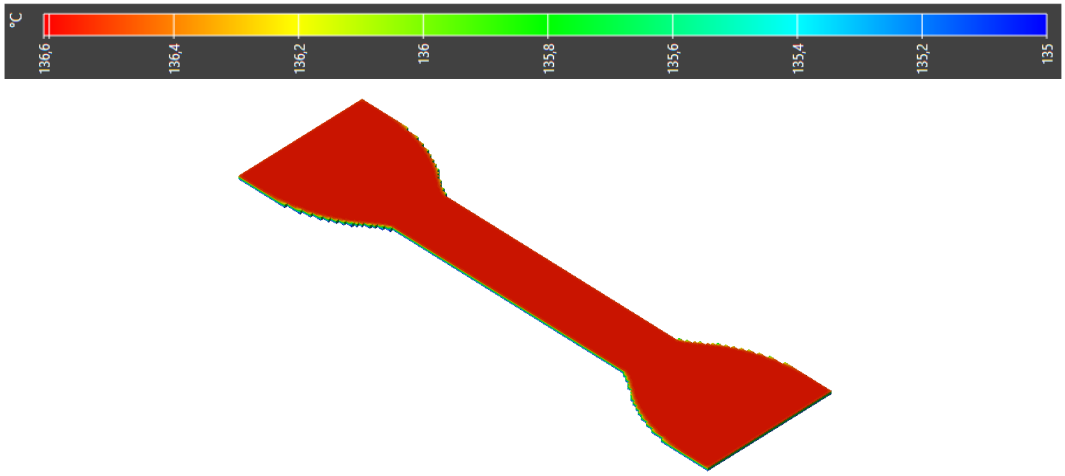


Figure 4. 15: Technique for scanning many layers of an ASTM-D638 part (type IV).

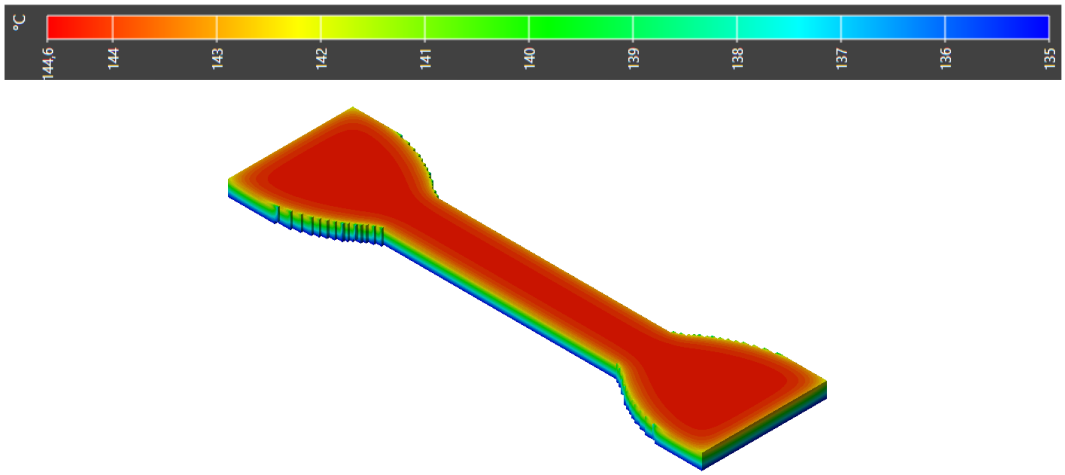
Figure 4. 16 shows the structure of the different printed layers and how the temperature changes for different thicknesses of ABS. The top surface of the first layer is where the hottest zone is located, with maximum temperatures of about 136.6 °C. However, the temperature of the bottom surface drops to that of the bed. In the first layer's case, the polymer thickness examination reveals a minimal temperature difference between 135 and 136.6 °C. When the top layer is printed, the adjacent layer is reheated, which assumes the adhesion between layers and modifies the temperature gradient and the polymer's crystallinity process. The surface temperature rises when comparing the 6th layer to the 1st layer, creating a significant gradient of 135 to 140°C. The printing process proceeds, and at 1830 seconds, the 12th layer, which

corresponds to the overall thickness of the polymer, starts. At this moment, the element gradually cools down.

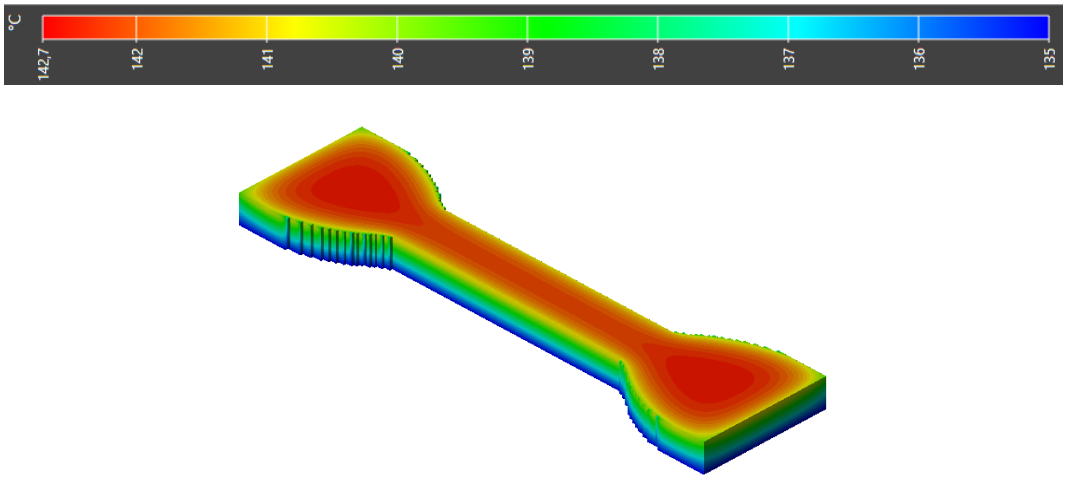
Figure 4. 17 depicts the temperature and Von Mises stress changes that occurred throughout the printing process in three zones of the ABS thickness: zone 1 (first layer), zone 2 (sixth layer), and zone 3 (12th layer). However, as the portion solidifies, the stress concentration rises and peaks at t = 1830 seconds (***Figure 4. 17****c*). The layer's temperature stabilizes at about 137°C, at t = 830 s, while the stress grows quickly.



(a) Layer deposit process, 1st Layer

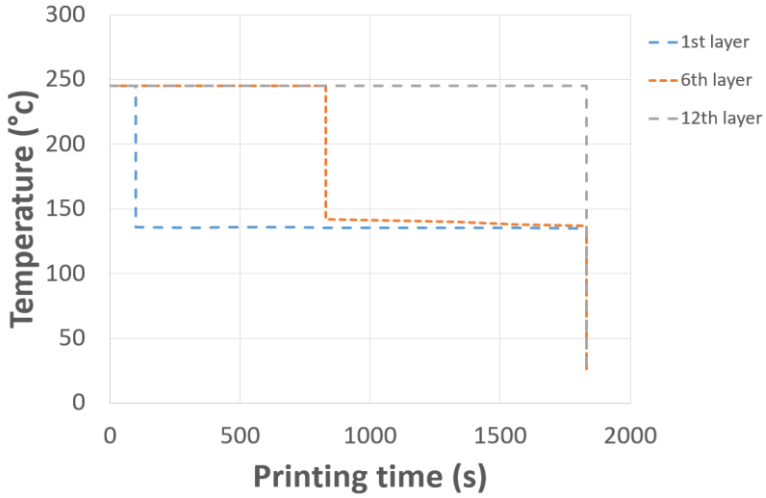


(b) Layer deposit process, 6th Layer

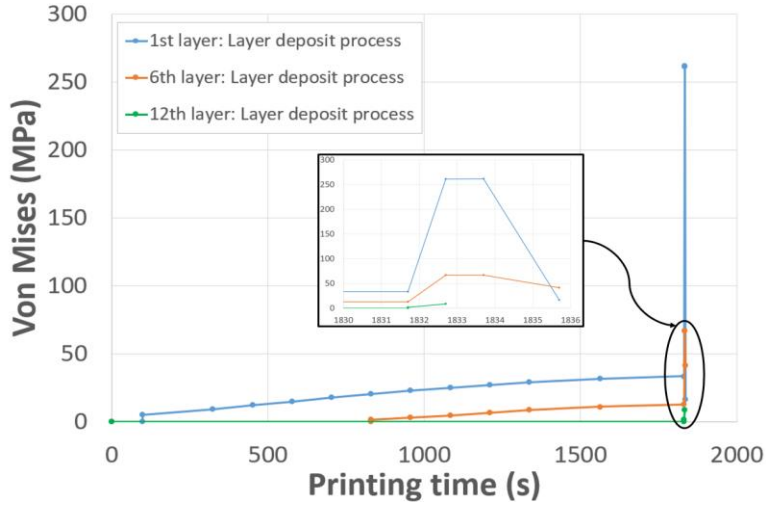


(c) Layer deposit process, 12th layer

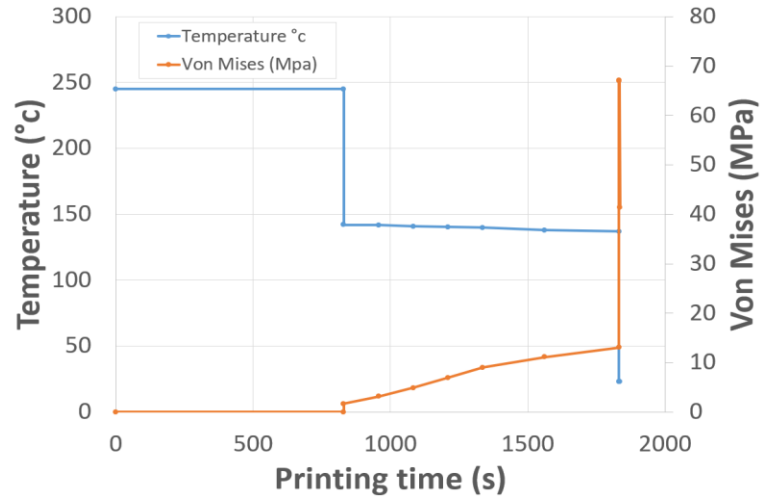
Figure 4. 16: A few frames for 3D printing of polymer composites using layer deposit FDM process: temperature variation.



(a) Variation of the temperature



(b) Variation of the Von Mises stress

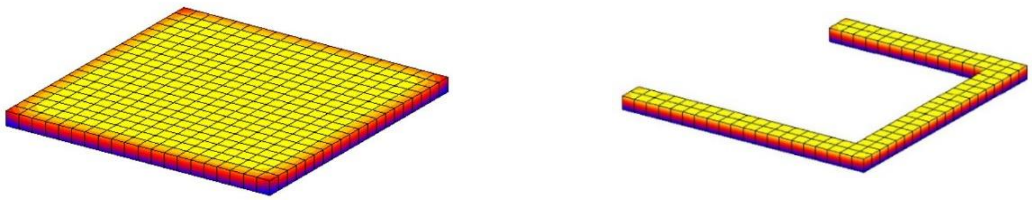


(c) Variation of the temperature and Von Mises stress vs printing time

Figure 4. 17: Profile of temperature and Von Mises stress utilizing the layer deposit technique at various points of the ABS thickness.

4.2.7.1 Effect of discretization method: Layer-by-layer vs Filament

The evolution of stress and temperature for the two discretizations layer-by-layer and filament are examined in this section for a printing speed of 10 mm/s, as shown in ***Figure 4. 18***.



(a) Layer-by-layer discretization *(b) Filament discretization*

Figure 4. 18: Layer-by-layer vs Filament discretisation.

To assess the impact of the discretization method (layer by layer and filament) used to simulate the 3D printing process on the final printed part, the temperature and stress fields as a function of printing time were compared and presented in ***Figure 4. 19*** and ***Figure 4. 20***. These results show that as the layer (filament) is printed, the top of the bottom layer is reheated, which generates temperature variations that affect the part's deformation. Using the layer deposition method, the temperature of the specimen remained relatively constant throughout the printed layers and was nearly similar to the platform fabrication temperature (23°C), whereas, using the filament deposition method (FDM), the temperature varies within the same layer and has a significant effect on the part distortion. Compared to the other layers, the temperature of the first layer drops dramatically and quickly. ***Figure 4. 20***b shows that the 6th layer experienced the most significant stress, roughly 37.08 MPa.

This concentration was caused by the temperature difference between the printed layers and the platform construction process (reheating phenomenon). Moreover, the stress variation is almost identical for both studied processes and increases as the part solidifies. The solidification phase starts at the beginning of the cooling phase when the temperature is below the glass transition temperature, and the residual stress significantly decreases.

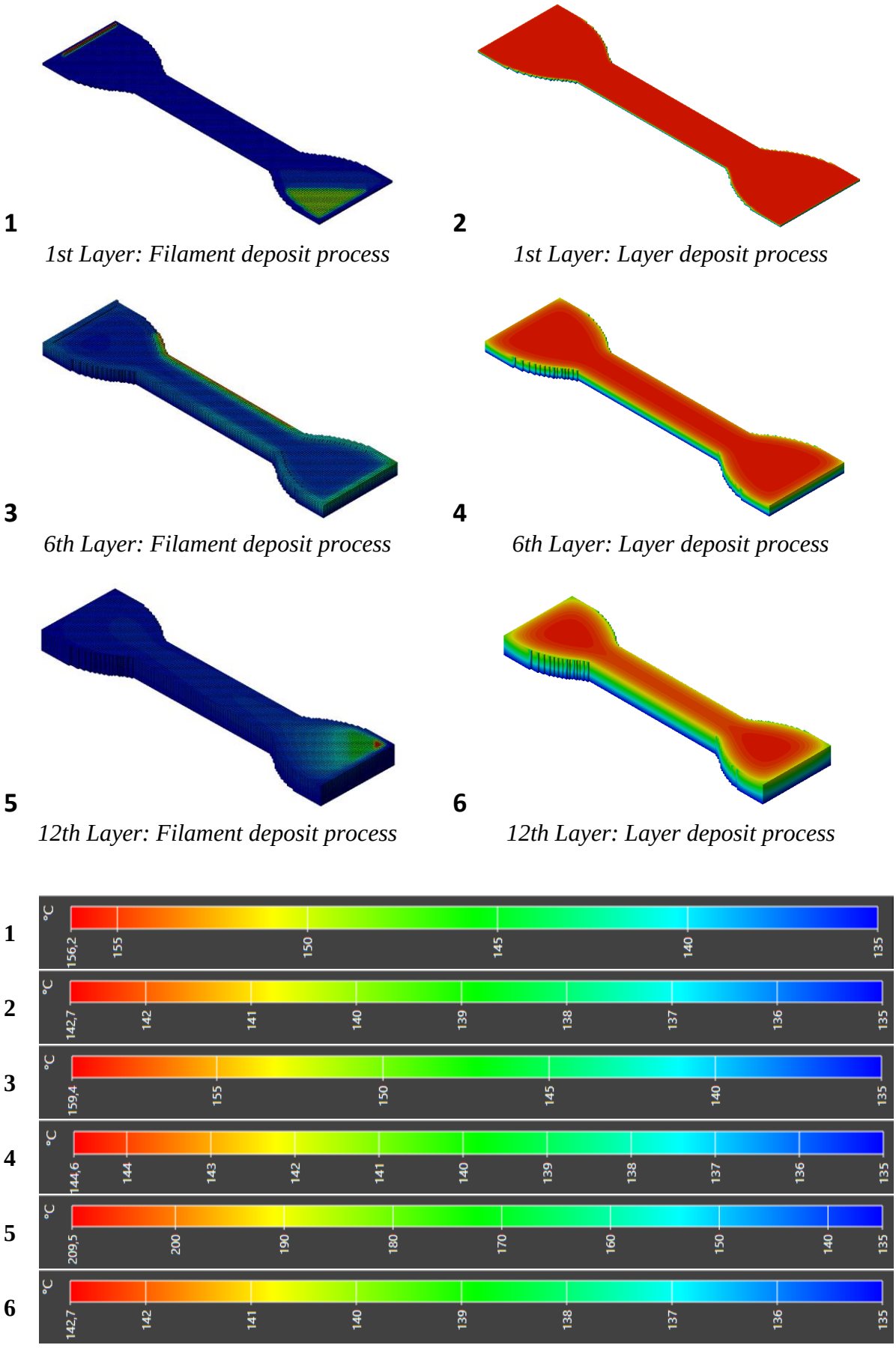
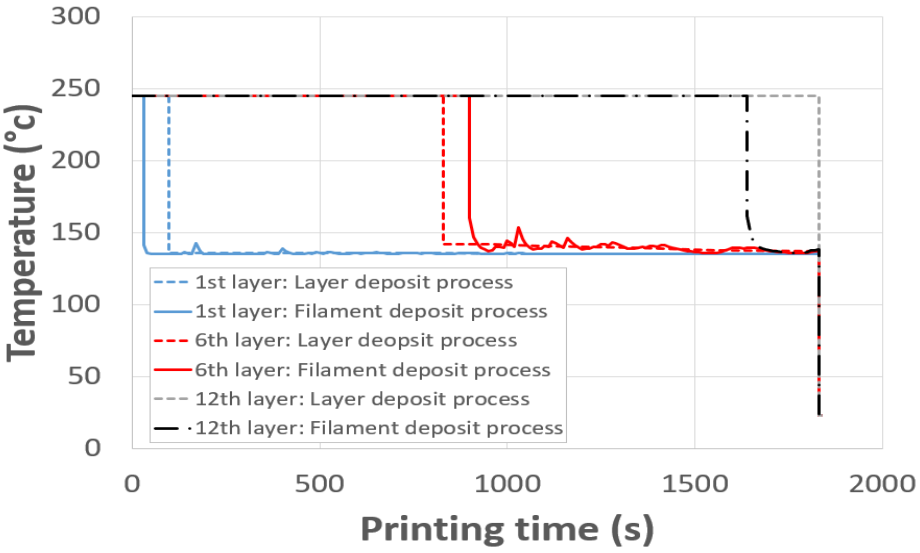
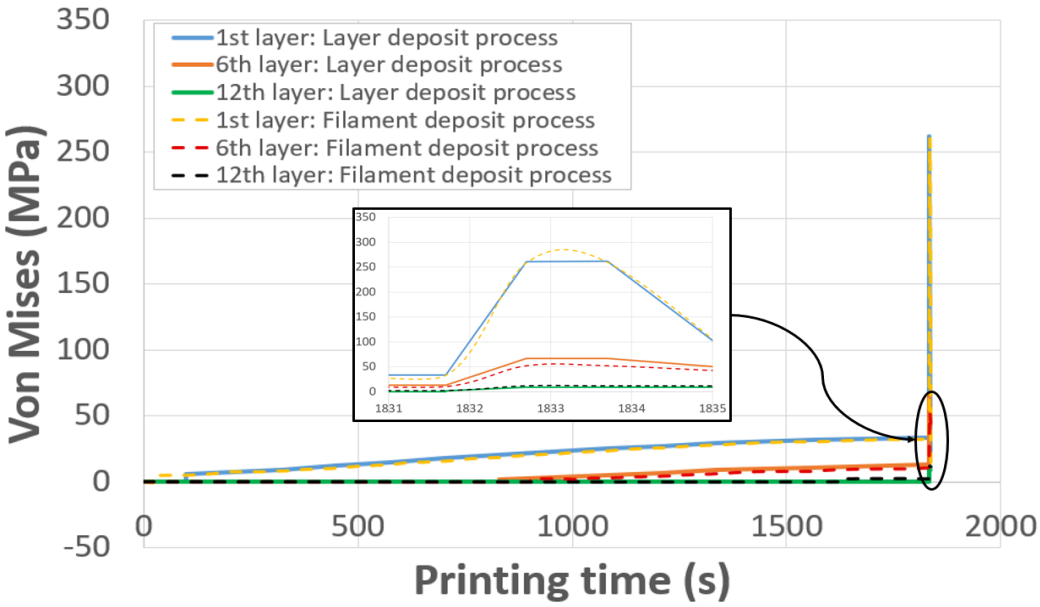


Figure 4. 19: Comparison of the temperature profile for two printing techniques.



(a) Variation of the temperature



(b) Variation of the Von Mises Stress

Figure 4. 20: Variation of the stress concentration and the temperature for two processes.

4.2.7.2 Effect of the printing direction

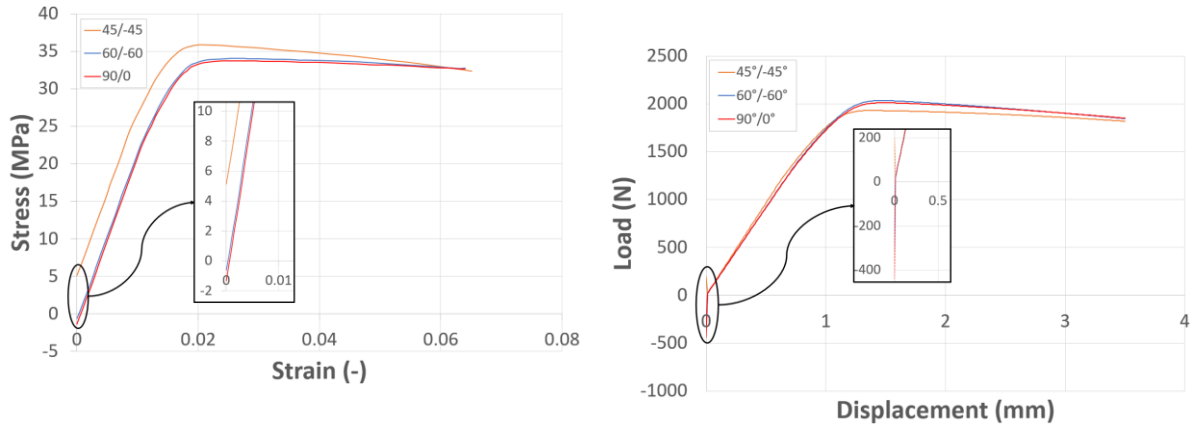
Studying how the printing direction affects the mechanical behavior of the considered material (ABS) in the narrow part of the tested specimen is crucial. This part has been the focus of several studies [130], [131]. Experimental research on the tensile properties of PLA specimens produced in 3D using FDM was carried out by Cristina et al. [132]. The main mechanical properties of size (various thicknesses) and spatial orientation (0°, 45°, and 90°) were examined. They found that spatial orientation has more of an effect on tensile strength than Young's modulus. This section examines three printing orientations (45/-45, 0/90, and 60/-60) using the

coupling between Abaqus and Digimat software ***Figure 4. 21***. The printing direction 45/-45 demonstrates the maximum stress of 35.84 MPa and the highest deformation of 6.5% in the narrow region of the specimen when compared to the other two orientations, ***Figure 4. 22***a. As an illustration, the curve for the 45/-45 printing direction starts with a stress value of 5.11 MPa, reflected by the stresses that accumulate in each layer as they cool on top of one another. This curve demonstrates how the printing process affects the initial state of the specimen (i.e. after the sample is fully printed and before the tensile test). The dynamics of stress accumulation also depend on the preheating of the support plate. ***Figure 4. 22***b depicts the Load versus displacement over the specimen. The residual stresses (impression effect) are also observable from the start of our tensile test.



(a) 45°/-45° *(b) 60°/-60°* *(c) 0°/90°*

Figure 4. 21: Printing direction.



(a) Stress-strain curve in the narrow part of the specimen *(b) Force-displacement curve in the whole test specimen*

Figure 4. 22: Curves determined numerically for printing direction 45/-45, 0/90, 60/-60.

4.2.7.3 Effects of 3D printing on the geometry of the part

Warping is the most important phenomenon that occurs after the piece is printed [133], and it occurs when thermoplastics such as the ABS expand slightly and then, during cooling, retract. Due to the higher extrusion temperature, a thermal reaction occurs, resulting in the plastic shrinking during cooling.

Figure 4. 23 shows the part's warpage after printing. The warpage is significant in the sample's sharp corners. Therefore, it is possible to conclude that the corners are more susceptible to warping than the central part.

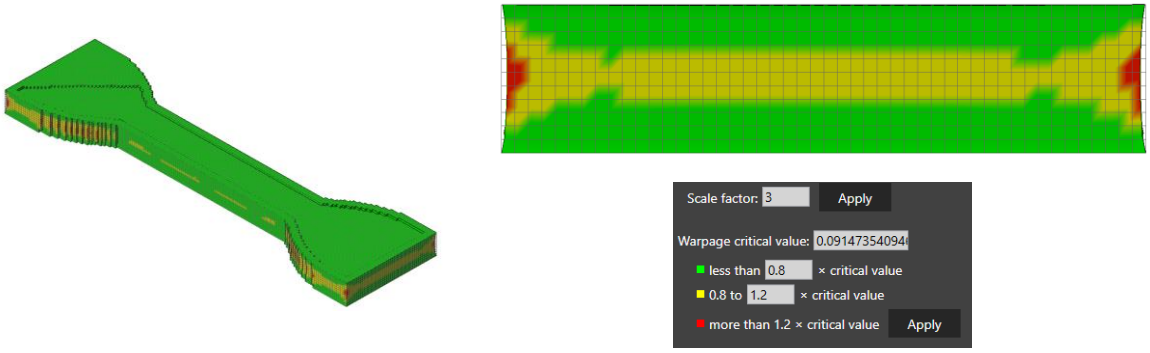


Figure 4. 23: Warping of ABS specimen.

4.2.8 Cost of printing

The cost of printing an ABS specimen may be assessed following these observations. Depending on machine, material, or labor, various expenses can be accounted for by considering the part number's impact on the total package. An estimation of the costs for the current print configuration may be done during the costing process. Finally, the cost of the material used for printing (ABS) must be considered. Therefore, several inputs are needed, such as the material's price, the part's mass, and the support's mass.

When calculating the depreciation cost of the printing machine, it is possible to take into consideration the total service time of the printer in the plan as well as the operating time of the printer for each batch, which includes setup time, warm-up time, printing time, cooling time, and removal/cleaning time. It is also possible to account for the cost of electricity used during the printing process, which can be calculated using electricity and the printer's power during preheating, printing, and cooling. The prices of printing a single ABS specimen of type ASTM-

D638 are summarised in detail in the table and graphic in ***Figure 4. 24***. When compared to raw materials and printing equipment, it should be highlighted that labor and electric energy costs are the most important. ***Figure 4. 24*** depicts curves that can estimate the costs and time required to print one or more samples (one by one).

Type of cost	**cost**
Material cost	0.98 €
Machine cost	1.74 €
Labor cost	5.30 €
Post-processing cost	0.60 €
Energy cost	3.30 €
Additional costs	0.68 €
Total	**12.59 €**

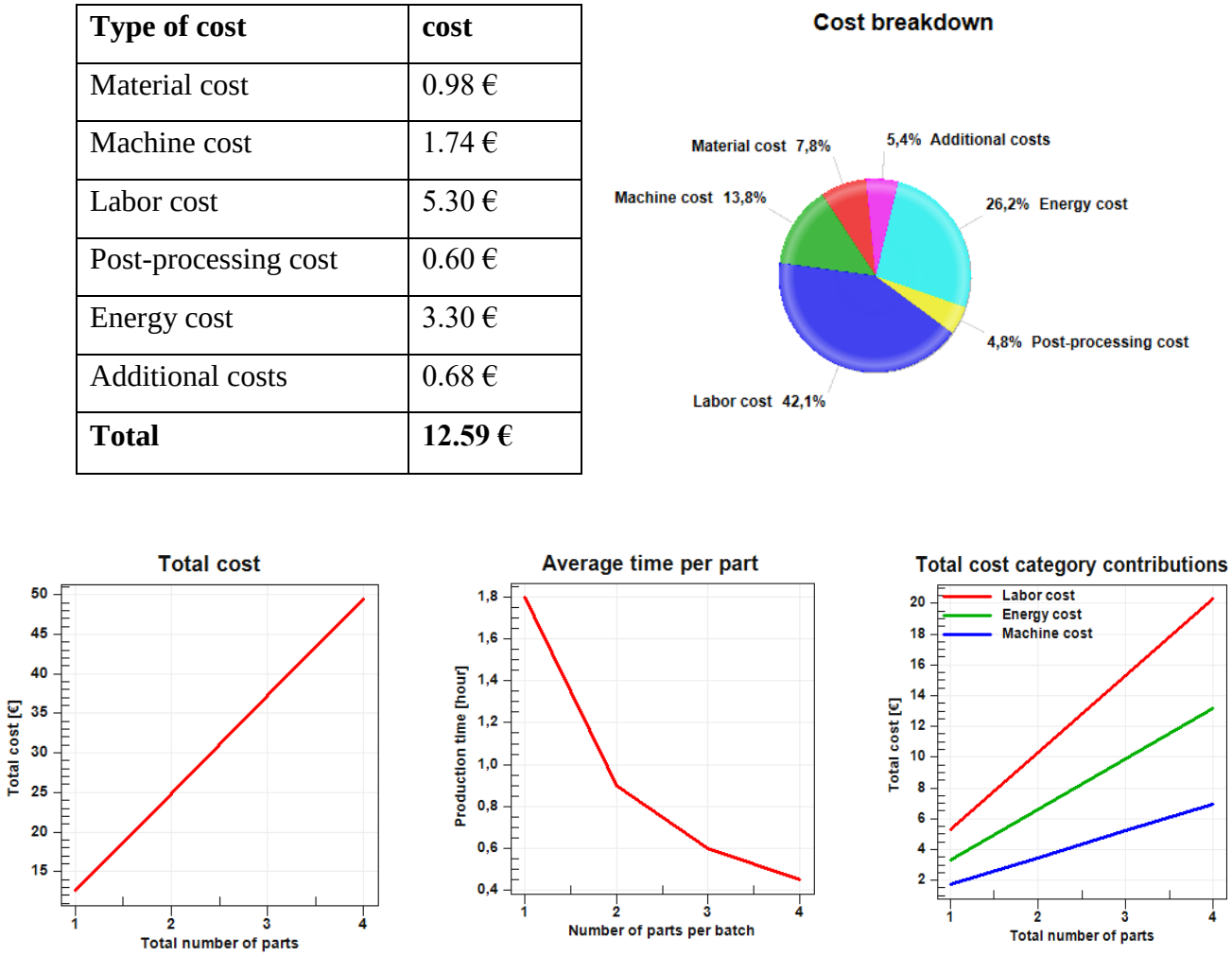


Figure 4. 24: Printing cost for an ABS specimen.

4. 3 Study of the tensile behavior of 3D-printed CF-PETG composites

4.3.1 Finite element Model of tensile tests

This section presents a finite element model of tensile tests performed on 3D-printed CF-PETG composite samples with dumbbell-shaped geometry and a fixed boundary condition at one end. The model simulates the load-displacement curves obtained from the tensile test experiments. A detailed description of the model's material properties, boundary conditions, and load settings is provided. The model is also used to explore the effects of various parameters on tensile

strength, such as pattern (NIDA vs. RECT) and fill densities (20%, 50%, 75%, and 100%). Finally, the model is used to guide the test specimen's design, helping to maximize the tensile strength of 3D-printed materials, ***Figure 4. 25***.

As illustrated in ***Figure 4. 26***, the mesh for the models under consideration is a volume element of tetrahedral quadratic type and a reduced integration C3D10. This arrangement has the advantage of keeping the computation reasonable while maintaining the precision of the results.

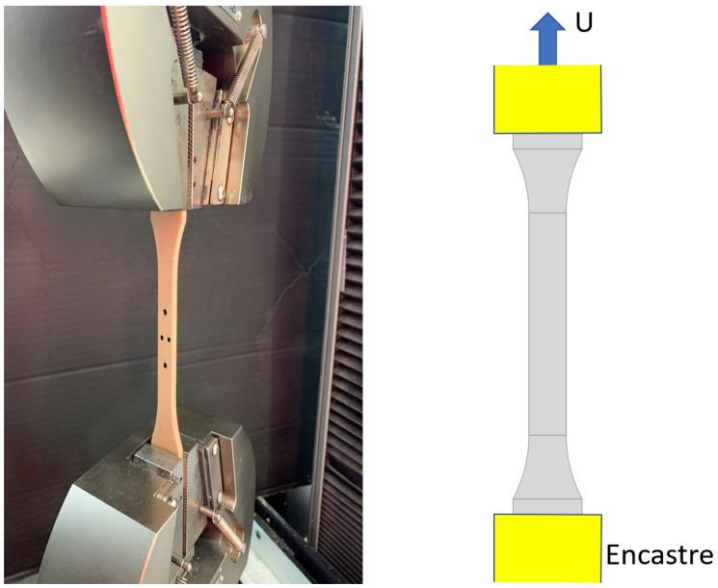


Figure 4. 25: Boundary conditions.

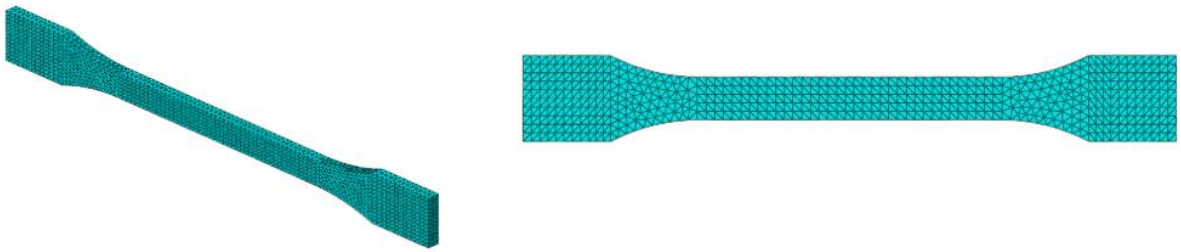


Figure 4. 26: Mesh type: C3D10.

4.3.2 Finite element analysis results

Figure 4. 27 depicts the numerical simulation results on the Abaqus/Implicit code for the variation of plastic elongation in each specimen, which is the failure zone. The specimen's plastic deformation is induced by the accumulation of strain energy, which causes material damage and rupture because the material's yield strength is exceeded. Plastic deformation is a

process in which a material undergoes permanent deformation under stress, ***Figure 4. 28***, leading to the initiation of damage and, ultimately, rupture of the specimen due to the dislocation motion and generation of defects within the material's microstructure.

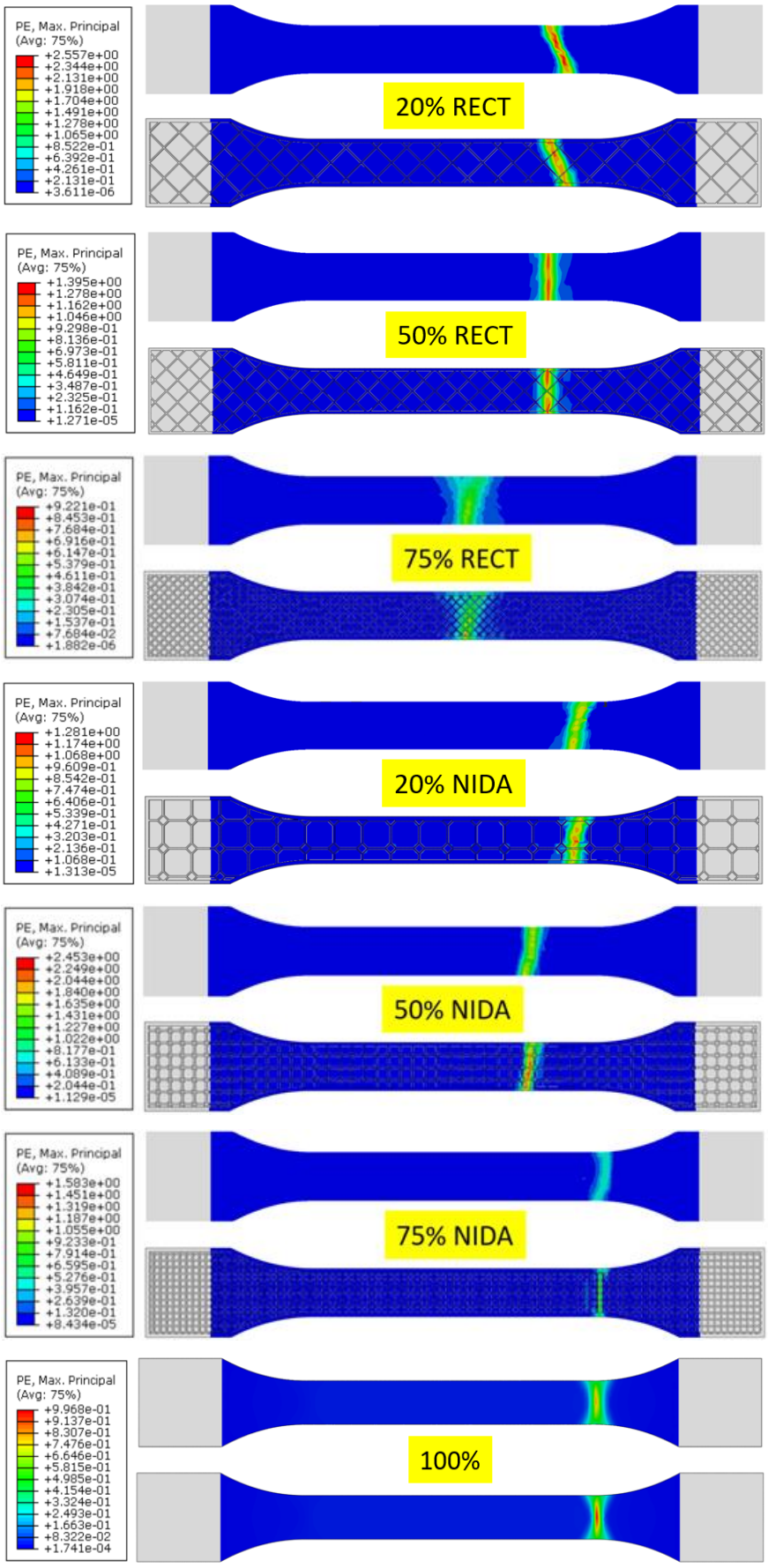
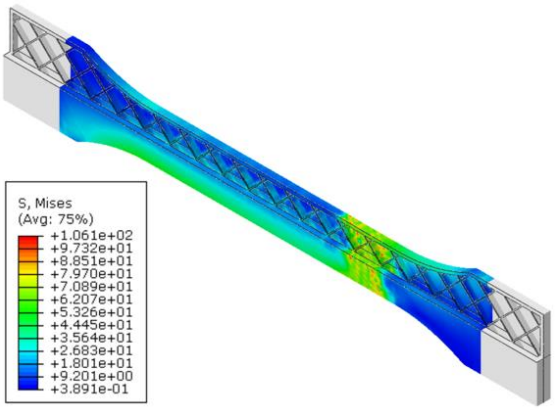
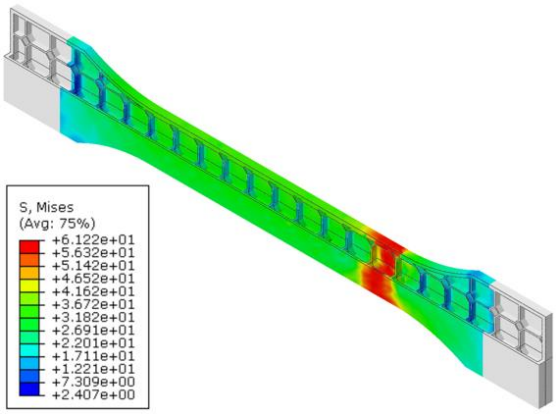


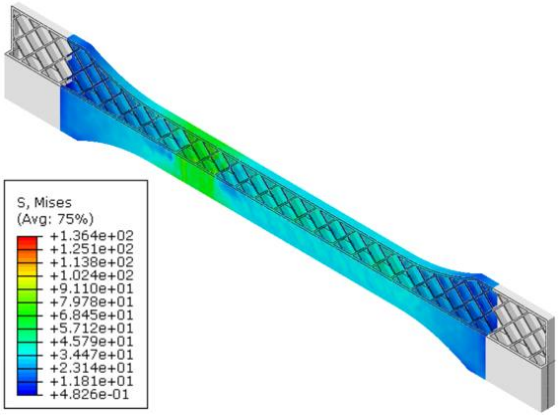
Figure 4. 27: Fracture zone of the specimen.



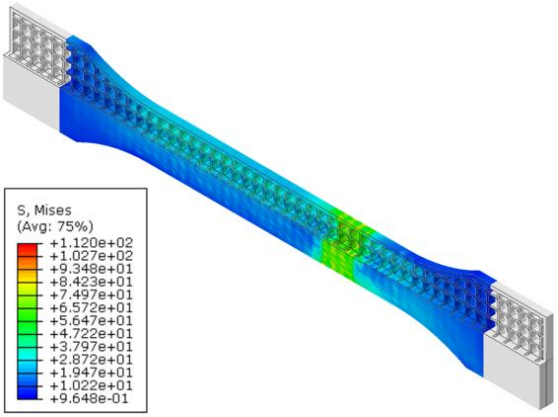
RECT 20%



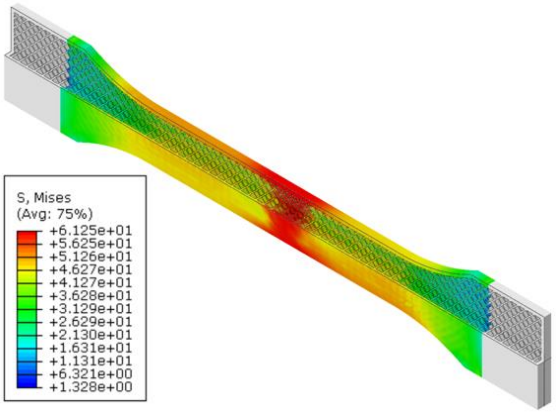
NIDA 20%



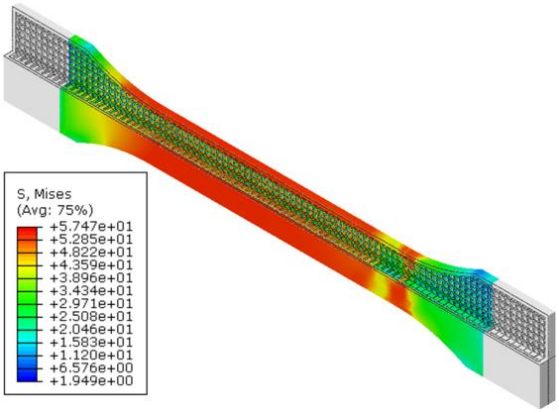
RECT 50%



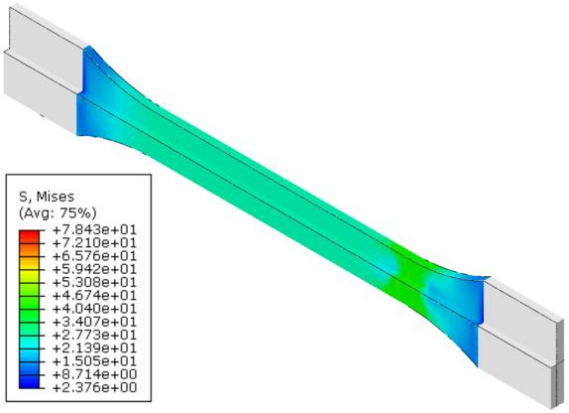
NIDA 50%



RECT 75%



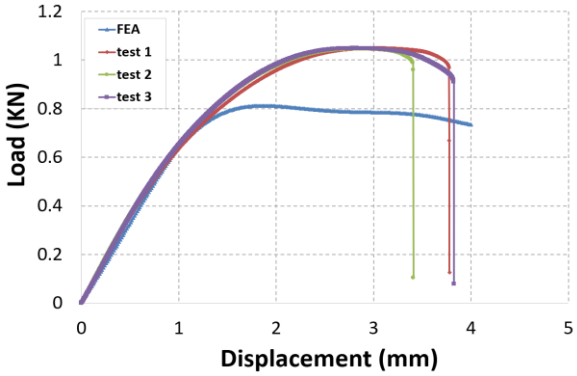
NIDA 75%



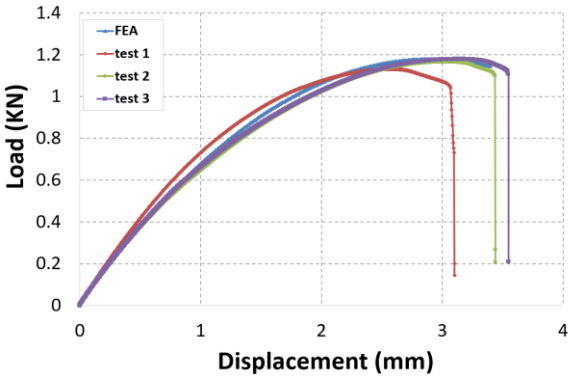
Filling 100%

Figure 4. 28: Variation of the Von Mises stress for each type of specimen.

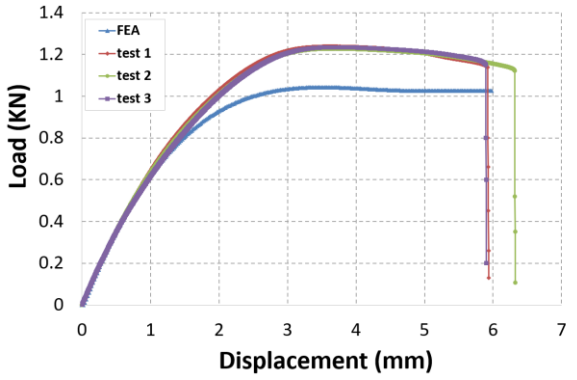
Figure 4. 29 depicts the numerical and experimental comparison of force versus displacement curves for honeycomb and rectilinear fill rates. The comparison between experimental and numerical results indicates a reasonably good correlation. However, further improvements are required to enhance the accuracy of the numerical simulations and achieve a more precise agreement with the experimental measurements. The difference between the numerical and experimental results can be explained by the numerical work process applied to the finite element software. Indeed, in modeling with Abaqus, the test sample is considered a perfect part and does not consider the effect of the printing process. The latter significantly affects the final properties of the sample as many features and defects appear during the printing process, such as warpage, shrinkage, and residual stresses.



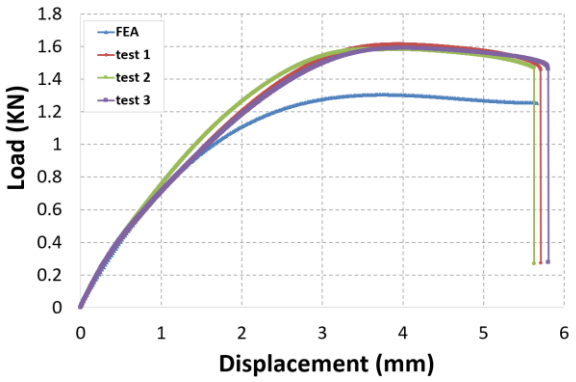
RECT 20%



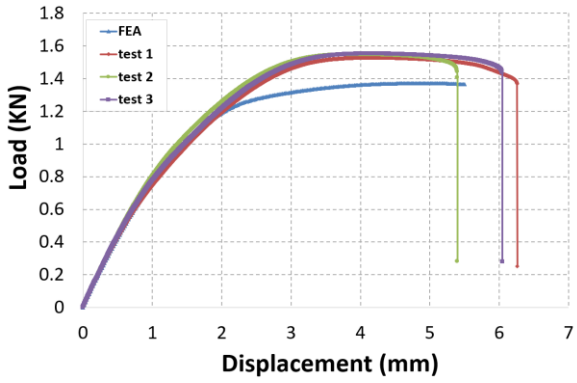
NIDA 20%



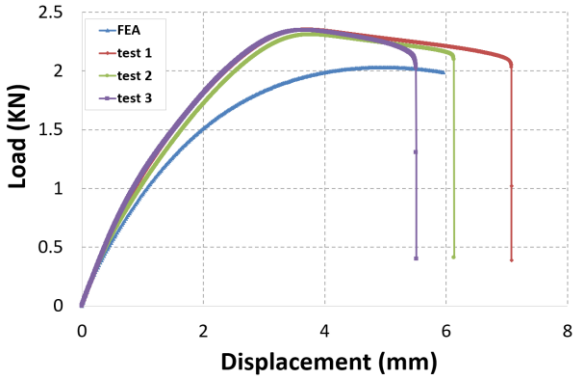
RECT 50%



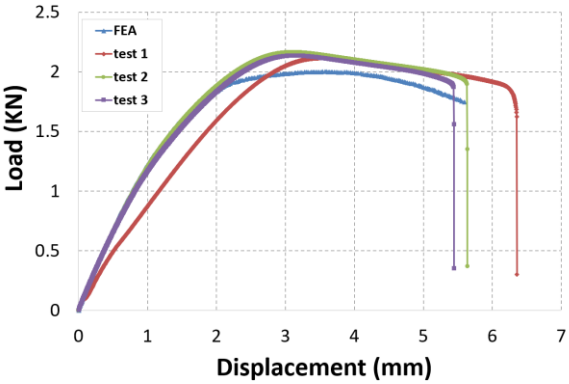
NIDA 50%



RECT 75%



NIDA 75%



Filling 100%

Figure 4. 29: Force versus displacement for different filling patterns.

4.3.3 3D printing modeling

It is crucial to thoroughly comprehend the effect of the issues that govern the 3D printing process; this allows us to understand how the input parameters affect the mechanical behavior of the part. This section will give the results of the Digimat-AM simulation of 3D-printed components. Digimat's efforts in additive manufacturing are all about correctly simulating the 3D printing process, considering parameters like the printing chamber, the material, the shape of the part, and more. We will select the filament printing option because we use FFF 3D printing technology. DIGIMAT sets the element size for the mesh, which is excessively fine with a Voxel size of 0.3 mm, as seen in ***Figure 4. 30***. ***Table 4. 4*** and ***Table 4. 5*** list the settings used to print the specimens.

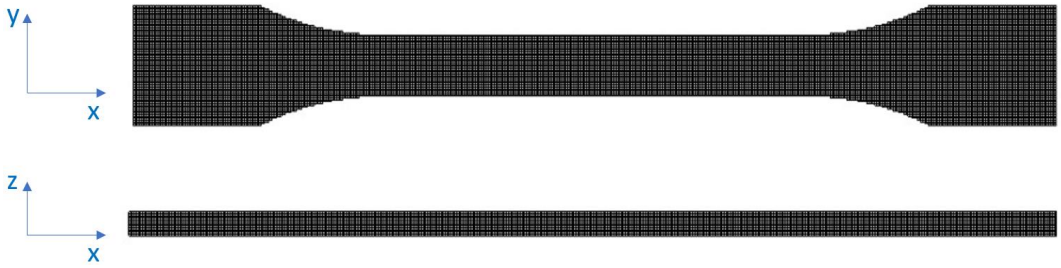


Figure 4. 30: Meshing of the specimen in Digimat.

Table 4. 4: Printing parameters.

Temperature of the room	23°C
Extrusion temperature	220°C
Temperature of the tray	80°C
Layer thickness	0.3 mm
Final temperature	23°C

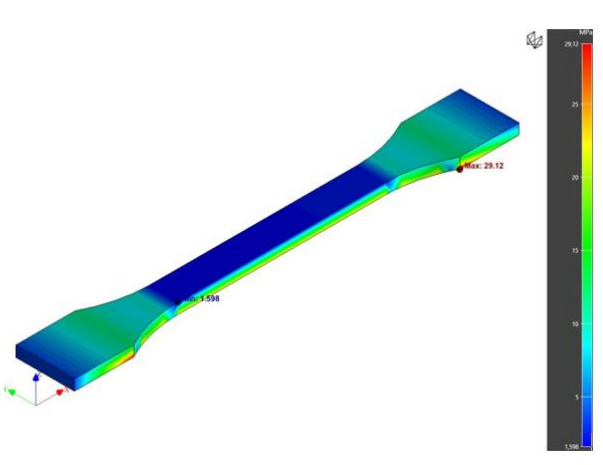
Table 4. 5: Information on printed test specimens.

Type of filling	Printing time	Filaments needed	Number of layers
NIDA 20%	40mn31s	876 mm	13
NIDA 50%	53mn23s	1277 mm	13
NIDA 75%	56mn00s	1300 mm	13
RECT 20%	39mn40s	859 mm	13
RECT 50%	46mn15s	1094 mm	13
RECT 75%	48mn00s	1294 mm	13
100 %	1h2mn26s	1416 mm	13

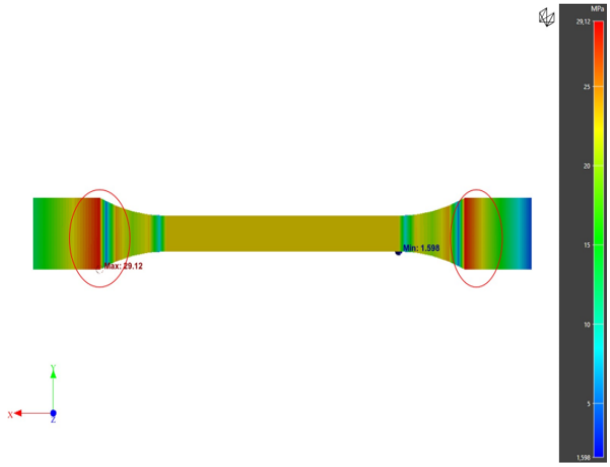
4.3.3.1 Effect of 3D printing on the geometry of the part

The 3D printing thermomechanical simulation results for the specimen with 100% density are displayed below. ***Figure 4. 31*** (a) shows the residual stress results. The maximum stress appears between the first and second layers (***Figure 4. 31*** (b)) and gradually reduces with composite thickness. This concentration does not exceed 30 MPa, generated by the part's deformation due to the difference between the bed temperature (165°C) and the heated polymer (220°C). It also depends on the thermal stresses due to thermal conduction from the last layer deposited.

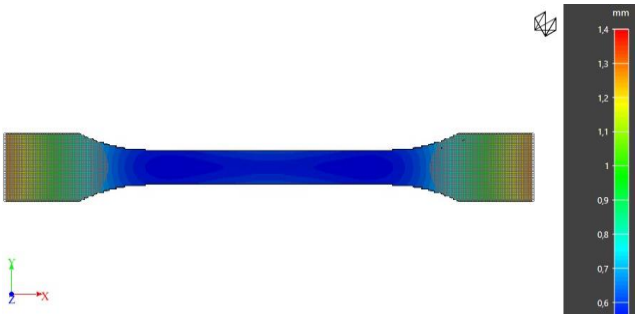
Figure 4. 31 (c) and (d) show the warpage of the part after printing; it is the most important phenomenon that occurs after the piece is printed. It occurs when thermoplastics such as the PETG expand slightly and then, during cooling, retract. Due to the higher extrusion temperature, a thermal reaction occurs, resulting in the plastic shrinking during cooling. The sample's sharp corners have a large amount of warpage. The conclusion is that the corners are more prone to warping than the center portion. The mechanical properties of the solid parts are influenced by the manufacturing defects generated during the deposition of successive layers using non-optimal manufacturing parameters. Porosity is a defect related to the filamentary nature of the FFF process, **Figure 4.** ***31*** (e). Indeed, poor adhesion between adjacent wefts of successive layers would result in a dense part with pores inside.



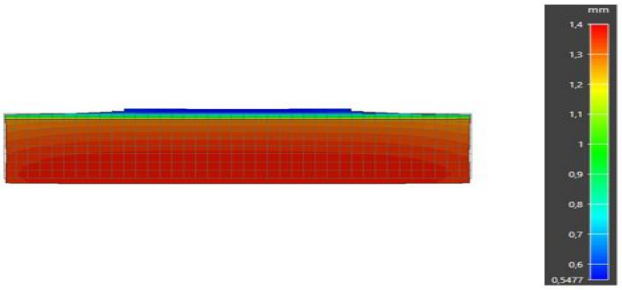
(a) Residual stress on the whole part



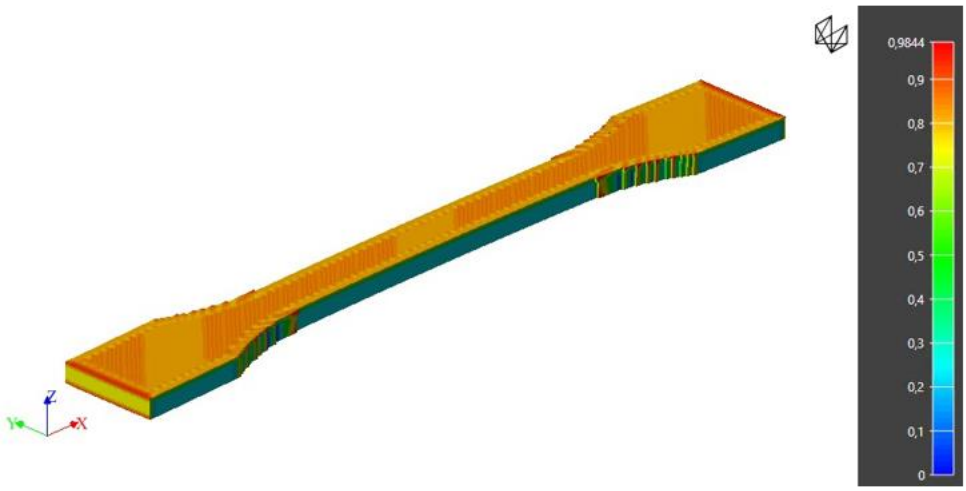
(b) Residual stress on the first layer



(c) Evolution of warpage in the XY plane



(d) Evolution of warpage in the YZ plane



(e) Evolution of the porosity

Figure 4. 31: Effect of 3D printing on the part's geometry, 100% filling.

4.3.4 Parametric study of 3D printing

Sample temperature, Von Mises stress changes, and deflection were measured at various points across the sample, ***Figure 4. 32*** . Most previous research has been on the design of industrial

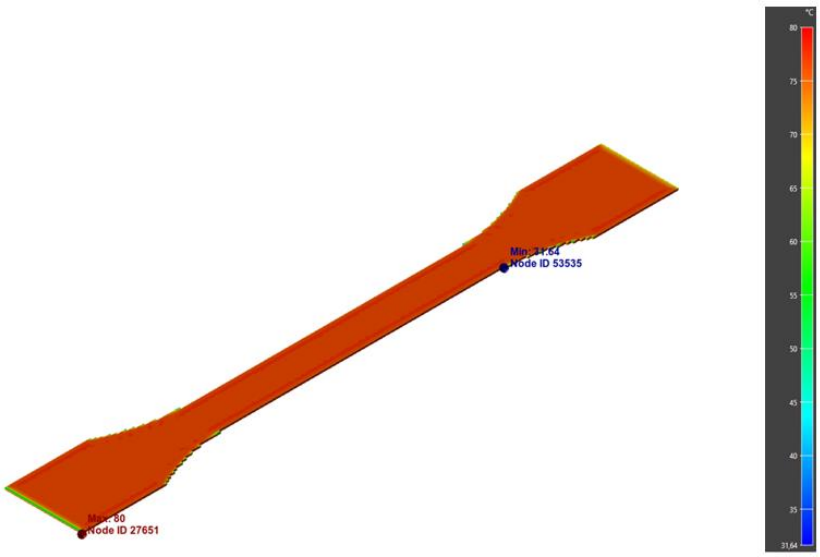
products during the additive manufacturing process, despite the temperature being the most crucial element influencing the mechanical behavior of polymer composites.



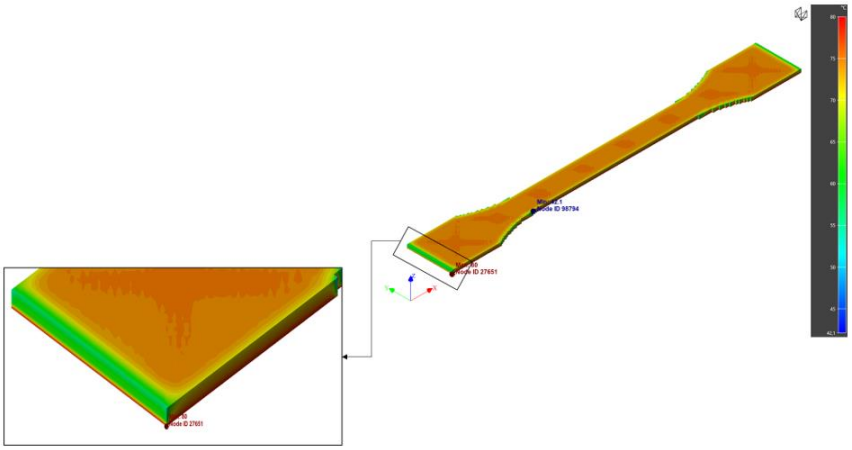
Figure 4. 32: Reference points for the study of temperature distribution.

Figure 4. 33 depicts the structure of the various printed layers and how the temperature varies for different CF-PETG thicknesses. During the 3D printing process, there can be a temperature gradient within the printed object. This is because the printing process involves heating the filament to a high temperature and then rapidly cooling it to solidify it into the desired shape. The outer surface of the printed object cools more quickly than the inner layers, creating a temperature gradient from the outer surface to the inner layers. This temperature gradient can affect the properties of the printed object, such as its strength and dimensional accuracy. It is vital to use appropriate printing parameters such as printing speed, layer height, and cooling settings to minimize the temperature gradient. A heated build plate can also help maintain a consistent temperature throughout printing.

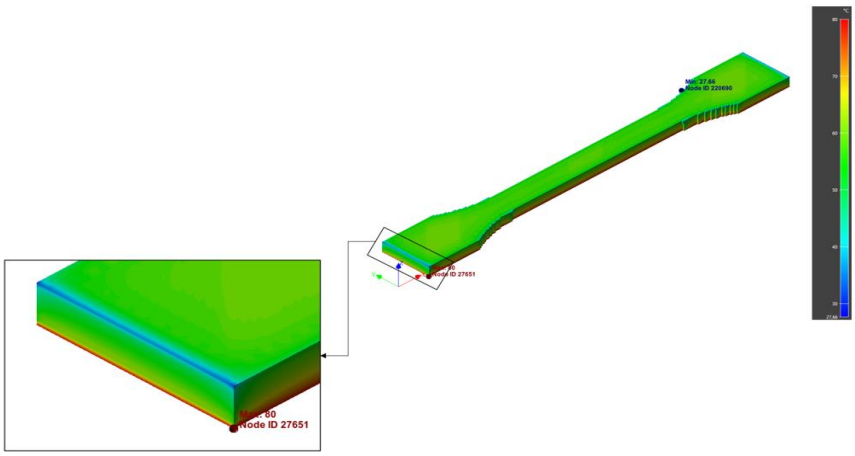
The hottest zone is located on the top surface of the first layer, with maximum temperatures of around 80°C. However, the temperature of the bottom surface drops to that of the bed. In the case of the first layer, the composite material (CF-PETG) thickness investigation showed a temperature variation between 32 and 80°C. When the top layer is printed, the adjacent layer is reheated, which assumes layer adhesion and affects the temperature gradient. During the printing process, the specimen's thermal distribution analysis shows a significant thermal gradient; the temperature of the 1st printed layer is 30°C, while for the 4th, it is 73°C.



(a) 1st layer



(b) 4th layer



(c) 13th layer

Figure 4. 33: Temperature variation at different layers of the specimen.

During the 3D printing of dumbbell-shaped specimens using a composite material (carbon fiber + PETG matrix) with FFF (Fused Filament Fabrication) technology, the material's behavior will vary at different points in the printing process.

1st layer:

The composite material will be extruded onto the print bed during the first layer. As the material cools and solidifies, it will adhere to the bed and form the foundation of the printed object. The PETG matrix will provide the adhesion and hold the carbon fiber in place. The first layer is crucial to ensure a strong base for the rest of the print, so the extrusion and bed leveling must be carefully calibrated to ensure a good first layer.

Mid layer:

The central layer of the dumbbell-shaped specimen is where the material will experience the most stress. The carbon fiber in the composite material will provide high strength and stiffness to resist the applied loads, while the PETG matrix will provide flexibility and durability. It is essential to ensure that the carbon fiber is aligned in the direction of the applied load to maximize the strength and stiffness of the printed dumbbell.

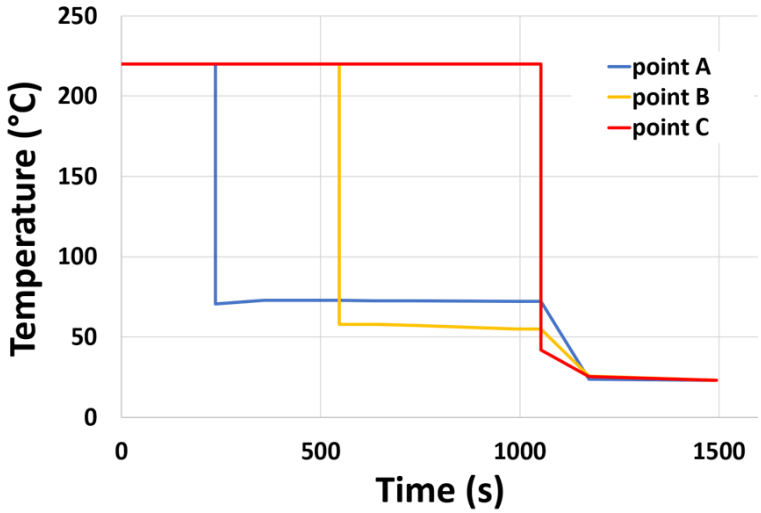
Last layer:

The composite material will be extruded onto the top surface of the printed dumbbell during the last layer. This layer must be carefully calibrated to ensure the printed object has a smooth surface. The PETG matrix will again provide adhesion, and the carbon fiber will provide strength and stiffness to resist applied loads. The last layer must be carefully printed to ensure the final printed object has the desired mechanical properties and aesthetics.

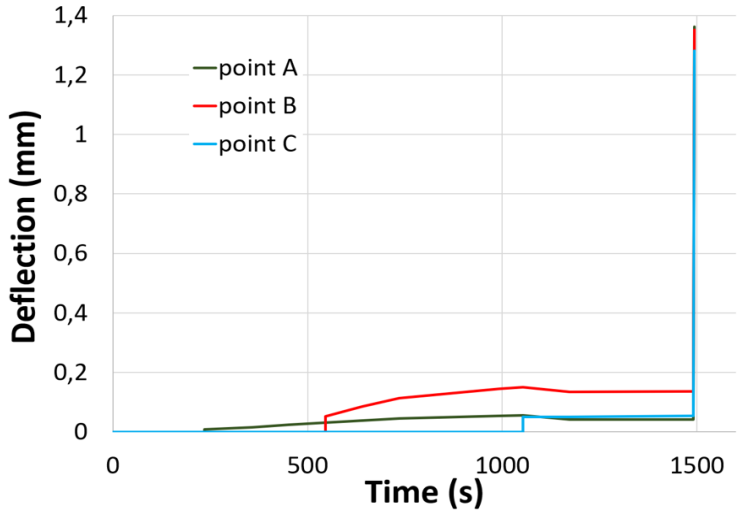
Overall, the behavior of the composite material during 3D printing will depend on factors such as the extrusion temperature, the speed of the printing process, and the layer height. It is important to carefully calibrate these variables to ensure a high-quality print with the desired mechanical properties.

Figure 4. 34 (a) shows this example: the temperature initially declines fast from the extrusion temperature of 220°C. It tends to stabilize after 1300 seconds at the final temperature of the part 23°C, representing the absolute cooling temperature.

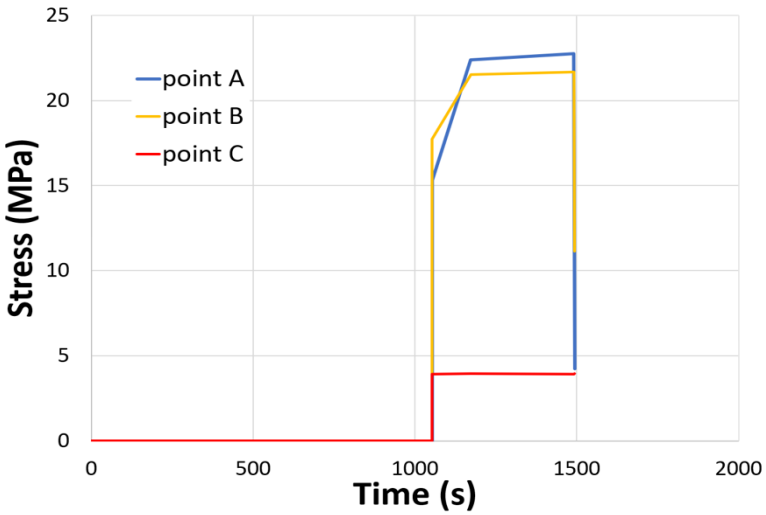
Figure 4. 34 (b) shows the variation of the deflection during the printing process in three different points of the composite thickness: A (1st layer, with 0.3 mm thickness), B (4th layer, with 1.2 mm thickness), and C (13th layer, with 3.9 mm thickness). The deflection increases and reaches its maximum when the part cools down. Moreover, the deflection at point A (in the first layer) is higher than the deflection value at points B and C.



(a) Temperature Vs. Time curve in different layers of the composite.



(b) Deflection Vs. Time curve in different layers of the composite.



(c) Stress Vs. Time curve in different layers of the composite.

Figure 4. 34: Variation of temperature, deflection, and stress in different layers of the 3D-printed composite.

Material properties, layer thickness, build speed, and surface quality are among the variables that might change during 3D printing. Certain limitations may be modified depending on the 3D printer and the printed material to reach the desired result. For example, layer thickness may be changed to get a more detailed or smoother finish on a print, while build speed can be raised to save total printing time. Some materials may require various temperatures or cooling durations to achieve the final result. All of these limits can influence the overall quality of a 3D-printed object. Thus, they must be considered when setting up a 3D printing job. ***Figure 4. 34*** (c) depicts the variation of the Von Mises stress during the printing process in the three different areas of the composite thickness. When the solidification phase of the part begins, the stress concentration increases and reaches its maximum at t = 1500 s.

Figure 4. 35 shows the temperature and deflection curve demonstrating all the steps of 3D printing for a specimen with a 20% honeycomb filler. These steps can be divided into three zones: printing, heat holding, and cooling. The room temperature (T=220°C) decreases gradually until the cooling temperature (T=23°C). The variation of the temperature as a function of the Von Mises stress is presented in ***Figure 4. 36*** . At t=444s, the layer temperature stabilizes around 55°C while the stress increases. However, when the solidification phase of the part begins, the stress concentration increases and reaches its maximum at t=925s. This concentration does not exceed 32 MPa for a specimen with a 20% honeycomb filling and is generated by thermal stresses due to heat conduction from the last deposited layer. The fused filament fabrication (FFF) process relies on the rapid melting and cooling of the plastic filament to consolidate the designed geometry.

Some shrinkage is inevitable as polymers must cool from extrusion temperature (T=220°C) to room temperature (T=23°C). This effect is more pronounced for high-performance polymers such as PEEK, PEKK, and ULTEM. As these polymers cool below their glass transition temperature, their stiffness increases, leading to residual stresses. The layers below the newly deposited layer cool down from the extrusion temperature, and heat is transferred from the top layer in three ways: conductive heat transfer to the cooled layer below, convective heat transfer to the air around the part, and radiative heat transfer to the rest of the part and the manufacturing chamber.

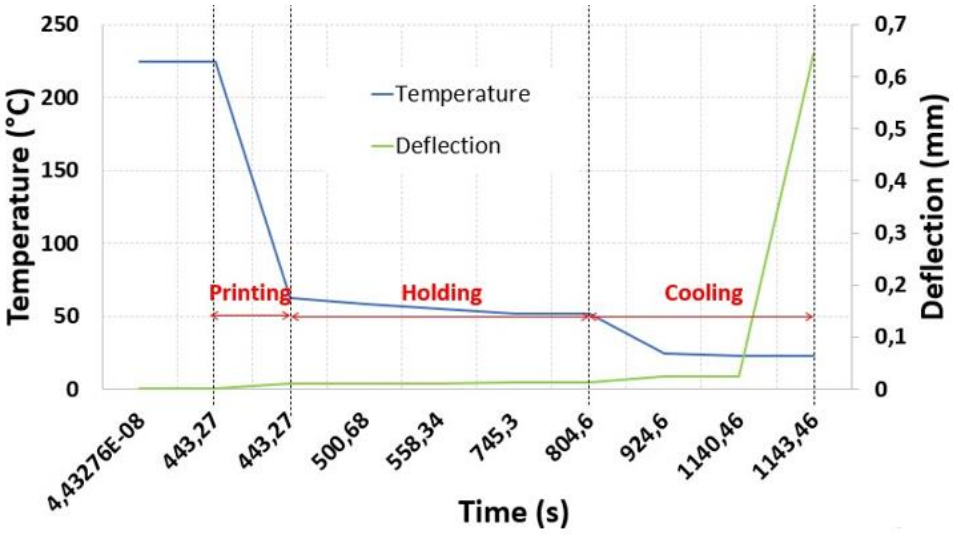


Figure 4. 35: Variation of the temperature and deflection vs. Printing time.

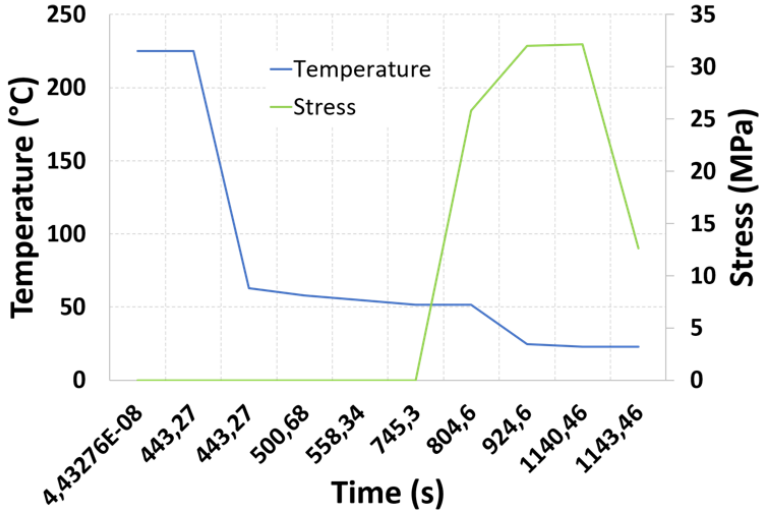


Figure 4. 36: Variation of the temperature and Von Mises stress vs. Printing time.

4.3.5 Abaqus/Digimat coupling for efficient numerical modeling

Abaqus/Digimat coupling is a powerful multi-scale analysis tool, allowing us to connect the material behavior described by Digimat with the structural behavior described by Abaqus in a single integrated analysis. The Digimat material model allows for the simulation of complex material behavior, including nonlinear and anisotropic behavior, considering microstructure effects. Connecting the two, we can accurately simulate the behavior of structures with materials having a complex microstructure. In this part, and to get closer to natural conditions, we applied the Abaqus/Digimat coupling to simulate the honeycomb-type specimen with a

filling rate of 75%. %. Indeed, this approach allows for the taking into account of the effect of the 3D printing process on the behavior of the part.

After starting the calculation and following a sequence of work alternating between the two software, Abaqus and Digimat (***Figure 4. 37***), we found the results displayed in ***Figure 4. 38***. In general, various factors can cause the failure of 3D-printed composite specimens. Some of the most common causes of failure include inadequate layer adhesion, weak bonding between layers, incorrect curing parameters, inadequate material properties, and an overall lack of strength. Insufficient layer adhesion occurs when the 3D printing process does not properly bind the individual layers of the composite together. Weak bonding between layers can occur when the 3D printing process does not properly disperse the matrix material, resulting in soft interfaces between the layers. Incorrect curing parameters can cause the composite material to be under or over-cured, resulting in inadequate material properties. Inadequate material properties can cause the specimen to fail due to a lack of strength or stiffness. Finally, sample failure can be caused by a combination of factors that add up to a lack of strength. ***Figure 4. 38*** shows the Force-Displacement curves for the experimental tests, the Abaqus, and the Abaqus/Digimat coupling calculations. It can be seen that the results found in the Abaqus/Digimat coupling are very close to the experimental ones, so it can be concluded that the effect of 3D printing influences the behavior of the material, and this can be explained more by the difference between the FEA and Digimat-RP curves.

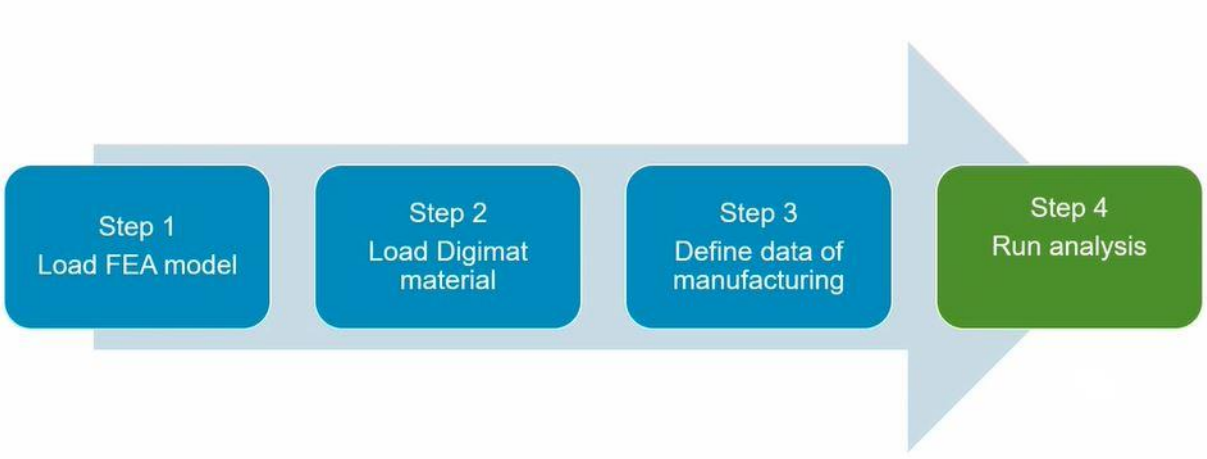


Figure 4. 37: Coupling procedure between Abaqus and Digimat.

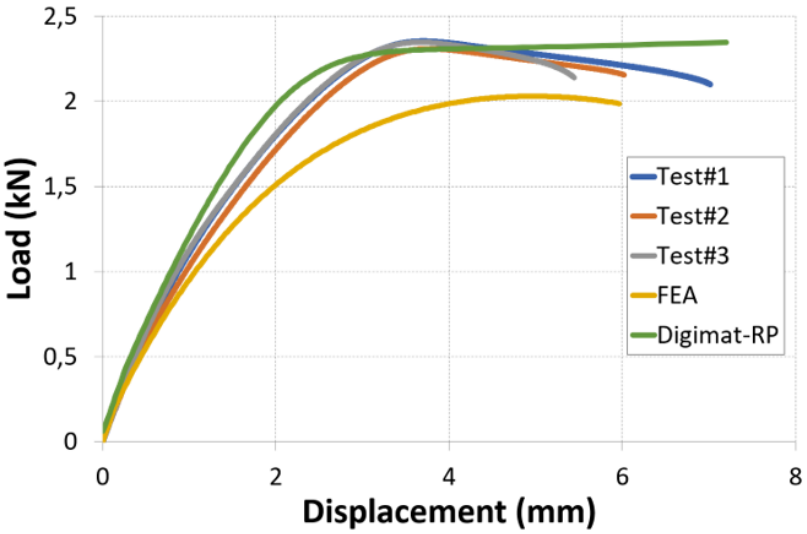


Figure 4. 38: Force vs. Displacement curve, NIDA-75%.

4. 4 Dynamic compression behavior of 3D-printed CF-PETG composites

4.4.1 Finite element model

Split Hopkinson Pressure Bar tests were modeled with ABAQUS software to examine stress wave propagation and dynamic deformation of the composite materials (CF-PETG). The incidence and transmitted bar models had a 20 mm diameter and 1985 mm and 1948 mm length. The striker was 400 mm in size and had the same diameter. A material with isotropic elastic properties was used to mimic the incident and transmitted bars, as well as the striker. The specimen had a typical size of $13mm^3$ and was modeled using an orthotropic material. The honeycomb samples were produced using specifically created Python code, which was then incorporated into the Abaqus program. With this integration's help, we could build models with honeycomb structures and fill ratios of 20, 50, 75, and 100%. ***Figure 4. 39*** provides a practical illustration of this process by displaying a sample with a 20% fill ratio produced using Python code. It was necessary to use this integrated modeling and simulation methodology to examine various sample configurations and assess how well they performed under particular circumstances.

A critical step was taken regarding the property modulus of the CF-PETG material in Abaqus to guarantee the accuracy of the simulations. The curve obtained from actual tests was carefully calibrated and integrated. The variable effects of printing parameters enabled us to incorporate precise material properties. This method strengthened the validity and reliability of our studies, allowing us to make a more rigorous comparison between numerical results and experimental data.

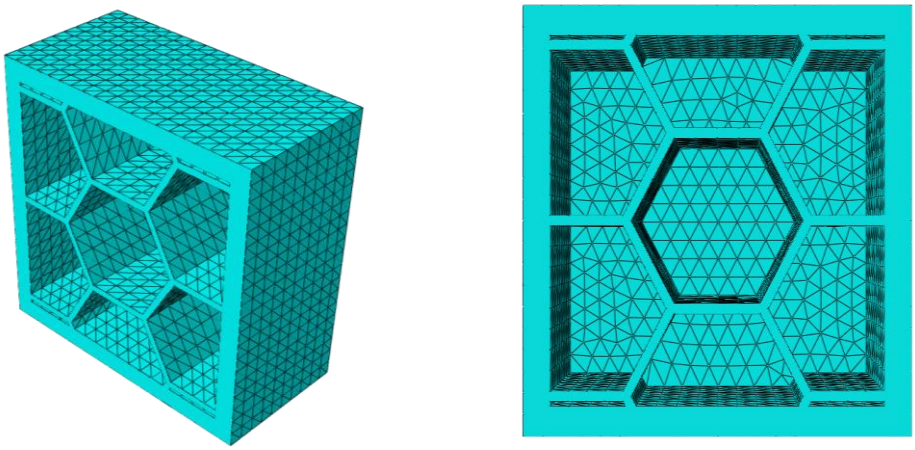


Figure 4. 39: Example of a honeycomb test specimen with 20% fill (13×13×13 mm^3).

4.4.2 Meshing and limit condition

The number of nodes, the total number of elements, and the mesh type are presented in ***Table 4. 6***, while ***Figure 4. 40*** shows a detail of the overall model. When simulating intricate structures like the honeycomb filling pattern, the choice of mesh type is crucial. For this situation, we used a mesh of linear tetrahedral (C3D4) pieces. This choice was made because of the filler pattern's intricate geometrical makeup, which includes wavy lines and interlocking patterns reminiscent of a honeycomb structure. While providing adequate accuracy for describing complicated geometries, linear tetrahedral elements help capture fine details and local deformations. This meshing strategy will make it possible to model interactions within the honeycomb structure more accurately and realistically, which will help us understand its mechanical behavior [134].

To determine the incident, transmitted, and reflected waves, thin gauge skins were positioned on the incident and transmitted bars. These skins were modeled using M3D4R's mesh with membrane elements.

Table 4. 6: Mesh information on each fill rate.

Fill rate	Total number of nodes	Total number of elements	Type meshing
20%-HON	8185	30667	C3D4
50%-HON	11577	51308	C3D4
75%-HON	24427	111875	C3D4
100%-HON	19683	17576	C3D4

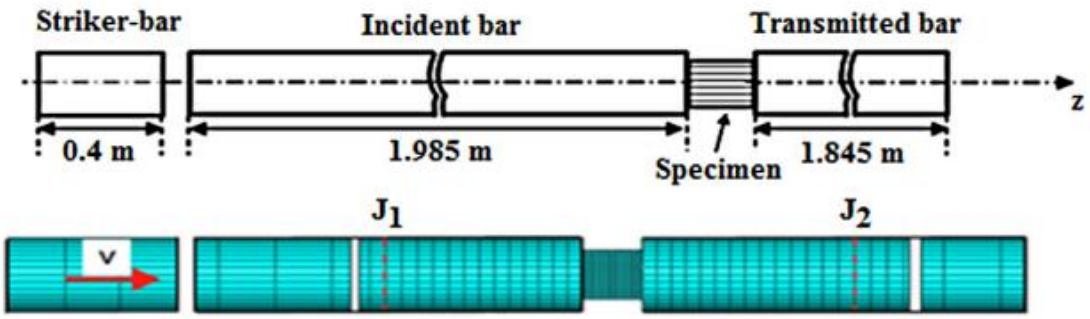
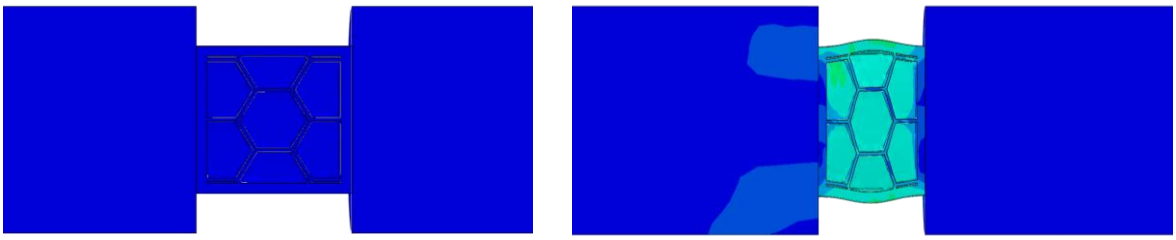


Figure 4. 40: Numerical model of the SHPB system.

A compelling example of the carefully considered positioning of honeycombs in relation to the direction of compression is seen in ***Figure 4. 41***. This figure demonstrates the bees' inherent inventiveness in strategically positioning their nests to increase their resistance to compressive stresses. This ingenious modification highlights how intricate honeycomb architecture is, where every angle and placement have a specific function.

Table 4. 7 provides crucial information regarding the structural analysis of a bars model in Abaqus. It outlines three distinct types of bars within the structure: Incidental bars, Transmitted bars, and Strikers. Each class specifies the number of nodes and elements involved in the meshing process. Incidental bars comprise 28,543 nodes and 23,424 elements, utilizing the C3D8R element type. Transmitted bars involve 27,010 nodes and 22,188 elements using the C3D8R element type. Lastly, Strikers comprise 7,081 nodes and 5,760 elements, meshed with the C3D8R element type. This data is vital for understanding the complexity and scale of the structural analysis being performed, which can have significant implications for the overall design and performance of the system.

At various points on the SHPB assembly's interfaces, a surface-to-surface contact is defined to simulate the interaction at these interfaces, allowing compressive loads to be transferred between the agent nodes and the master segments. ***Table 4. 8*** presents the boundary conditions applied to the striker.



(a) *(b)*

Figure 4. 41: The honeycombs' orientation about the direction of compression.

Table 4. 7: Mesh information on each bar.

Bars	Total number of nodes	Total number of elements	Type meshing
Incidental bar	28543	23424	C3D8R
Transmitted bar	27010	22188	C3D8R
Striker	7081	5760	C3D8R

Table 4. 8: Limit condition applied to the striker.

Impact Pressure (bar)	1.4	1.7	2.0	2.4
Striker velocity (m/s)	3800	6300	8200	9800

4.4.3 Results and Discussion

4.4.3.1 Results of variations in Von Mises stresses, plasticity, and displacements

Several important conclusions can be drawn from the simulation of the dynamic compression of the honeycomb filling pattern performed in Abaqus at different pressures (1.4 bar, 1.7 bar, 2 bar, and 2.4 bar) and filling ratios (20%, 50%, 75%, and 100%). First, the numerical outcomes show a clear relationship between the rise in applied pressure and several significant parameters, including Von Mises stress, plasticity, and displacements. For the 20%-filled honeycomb design sample, ***Figure 4. 42*** and ***Figure 4. 43*** analysis reveals that the Von Mises stress for the 1.7 bar pressure exhibits a broader range and a more significant value than the 1.4 bar pressure.

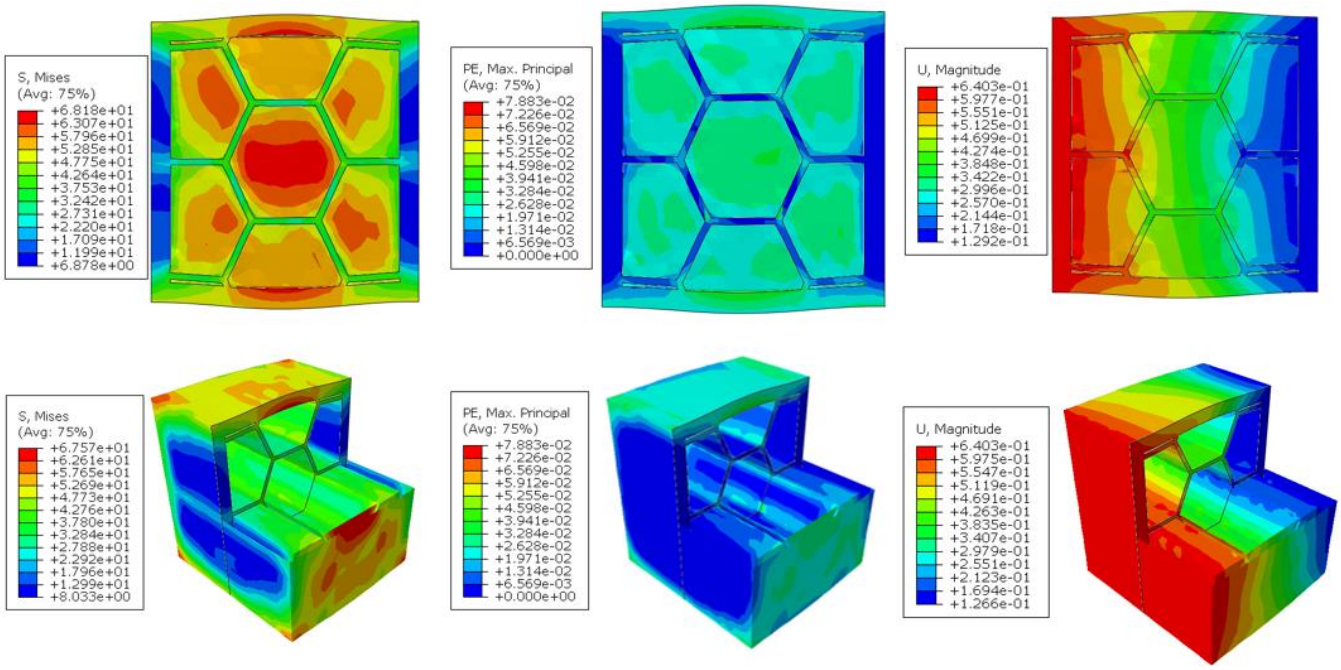


Figure 4. 42: Maximum Von Mises stress, plasticity, and displacement values for the honeycomb pattern with a 20% fill ratio, 1.4 bar.

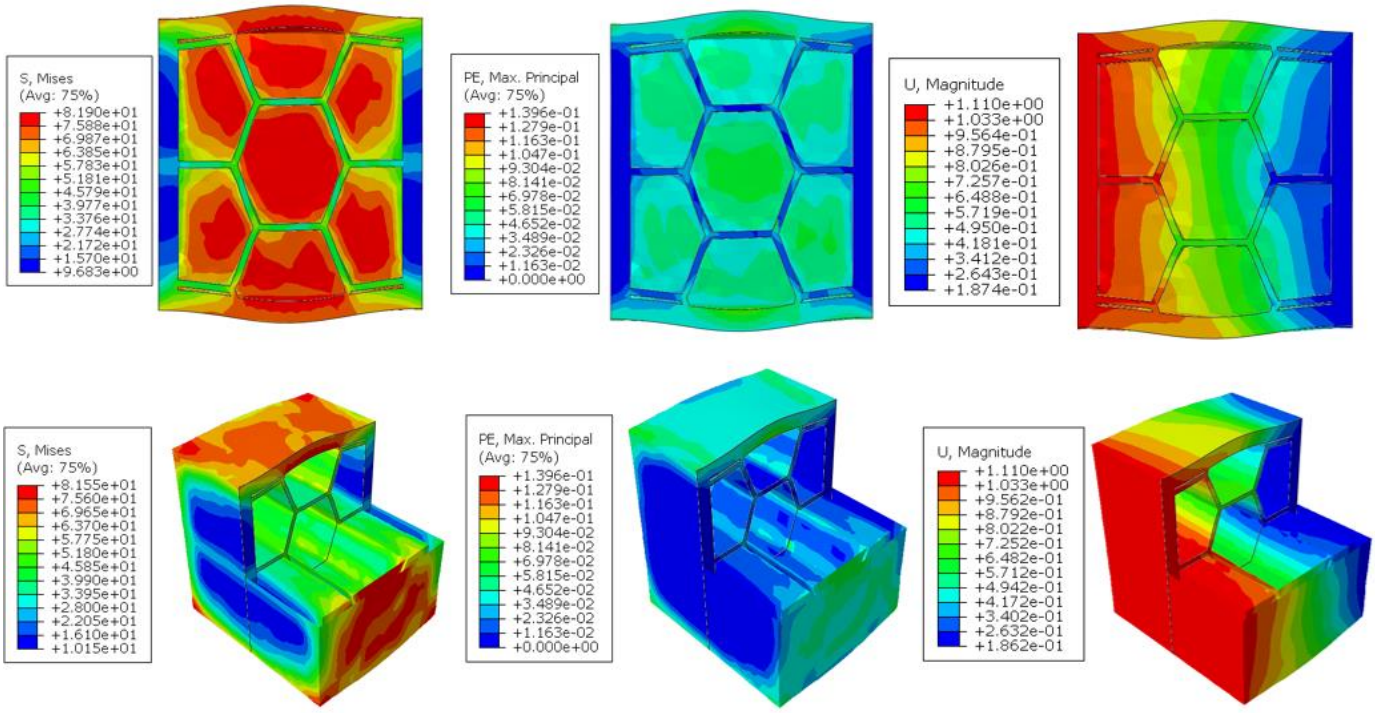


Figure 4. 43: Maximum Von Mises stress, plasticity, and displacement values for the honeycomb pattern with a 20% fill ratio, 1.7 bar.

Additionally, ***Figure 4. 43*** and ***Figure 4. 44***, which show how stresses, plasticity, and displacements changed for two different filling ratios (20% and 75%) under the same pressure of 1.7 bar, show that the structure with a filling ratio of 75% is more resilient than the one with a ratio of 20%. Additionally, flexibility and displacement are more severe in the event of a 20% filling ratio than a 75% filling ratio.

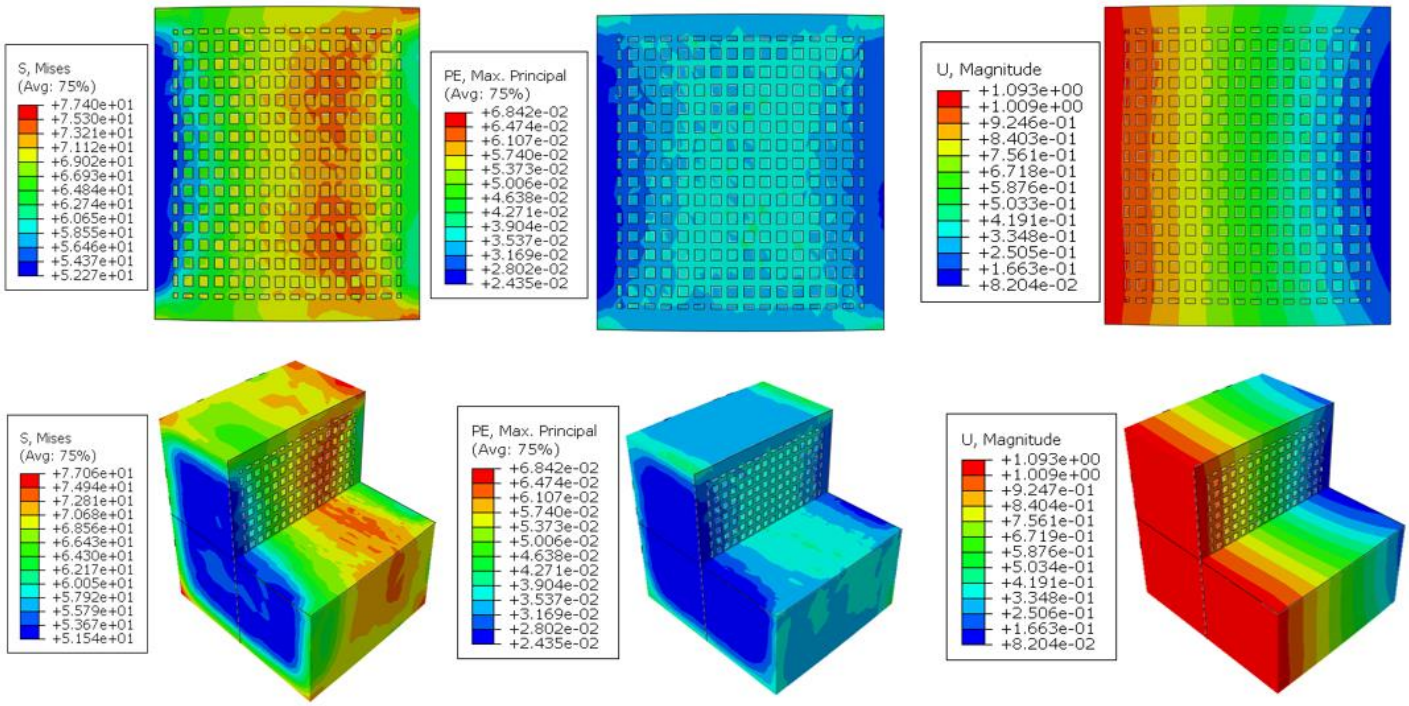
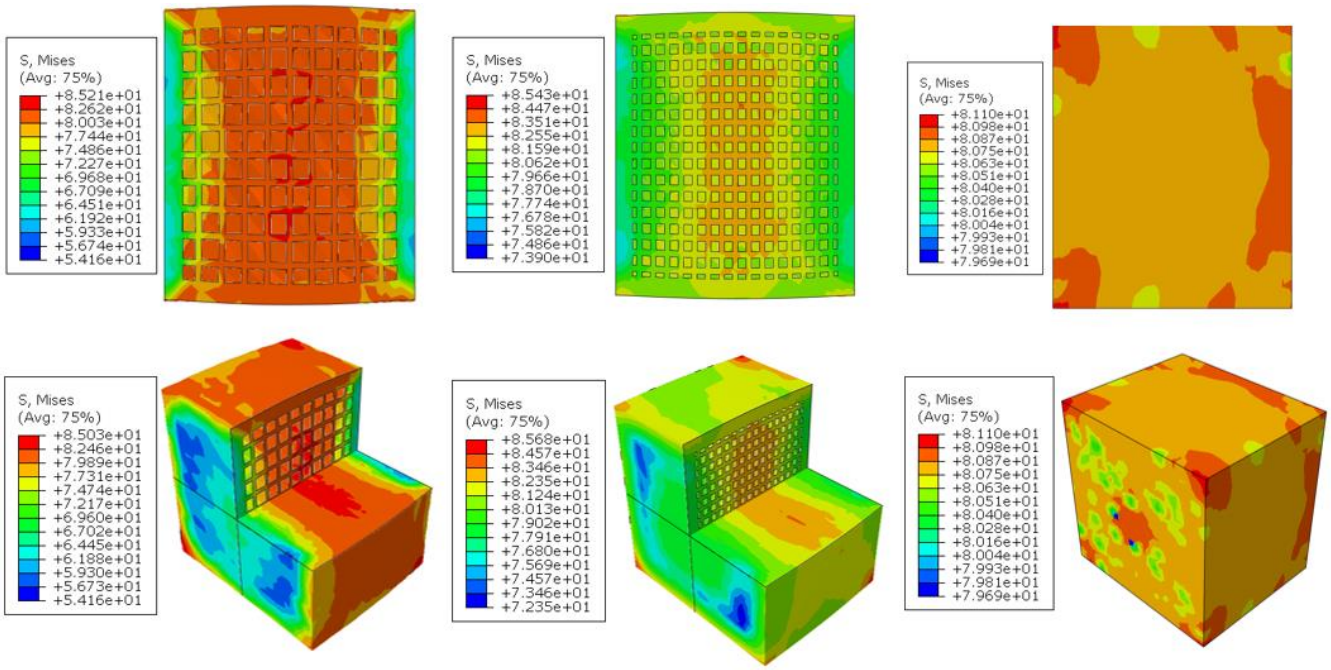


Figure 4. 44: Maximum Von Mises stress, plasticity, and displacement values for the honeycomb pattern with a 75% fill ratio, 1.7 bar.

Assuming a pressure of 2.4 bar, ***Figure 4. 45*** shows the difference in Von Mises stresses for three different filling ratios: 50%, 75%, and 100%. The performance of the honeycomb structure can be understood in great detail by carefully analyzing the Von Mises stress fluctuations. It is evident that, compared to the systems with fill ratios of 100% and 50%, the structure with a fill ratio of 75% exhibits greater strength and better coherence. This observation supports the honeycomb structure's inherent benefits. It is conceivable, for instance, to rationalize material use and optimize production costs by using a fill ratio of 75% rather than 100%. In light of these findings, a fill ratio of 75% balances mechanical performance and resource efficiency, making it a potentially better option in several engineering applications.

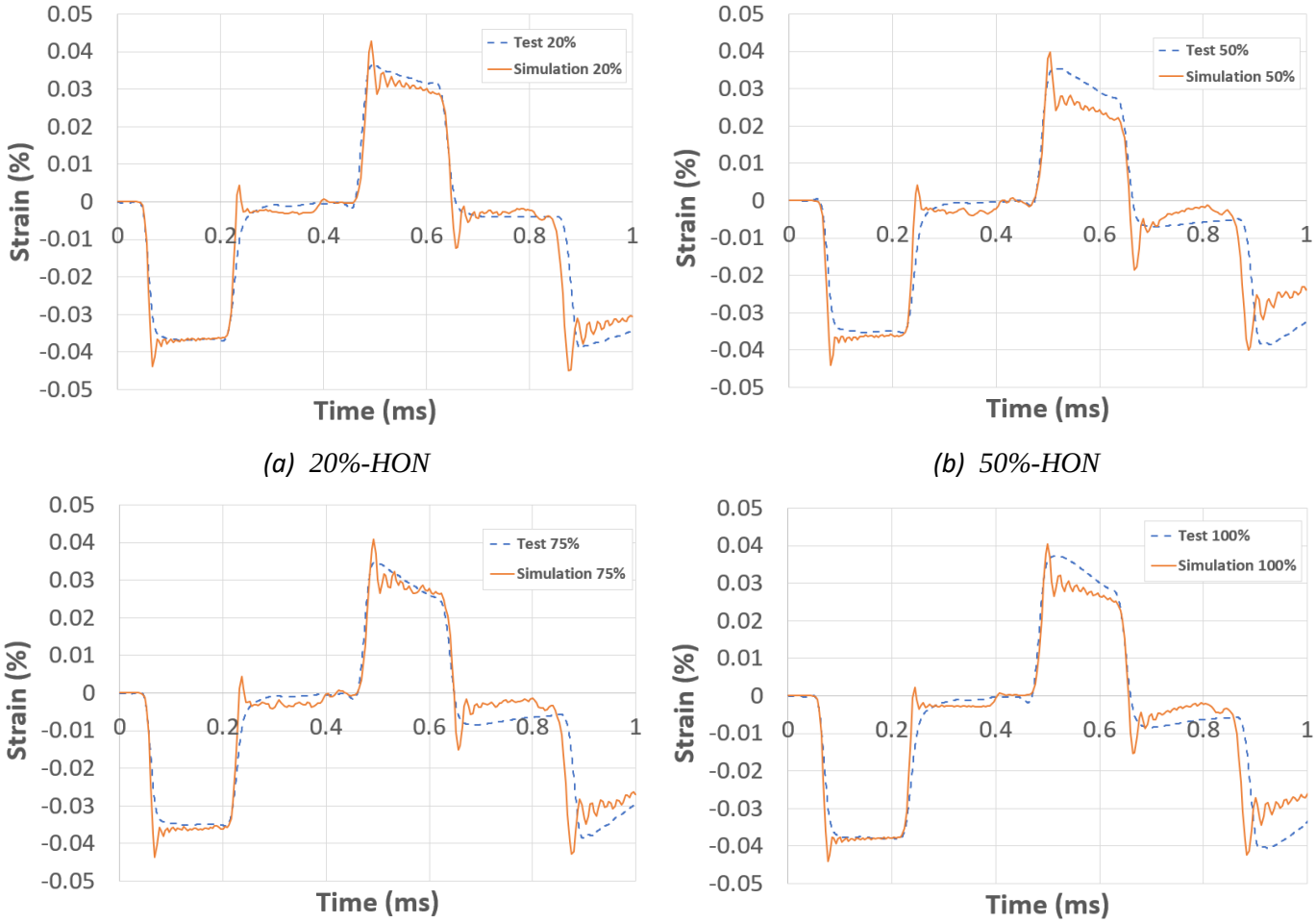


(a) 50% (b) 75% (c) 100%

Figure 4. 45: Variation of Von Mises stresses for different filling ratios 50%, 75%, and 100%, 2.4 bar.

4.4.3.2 Comparison and validation: test vs. simulation

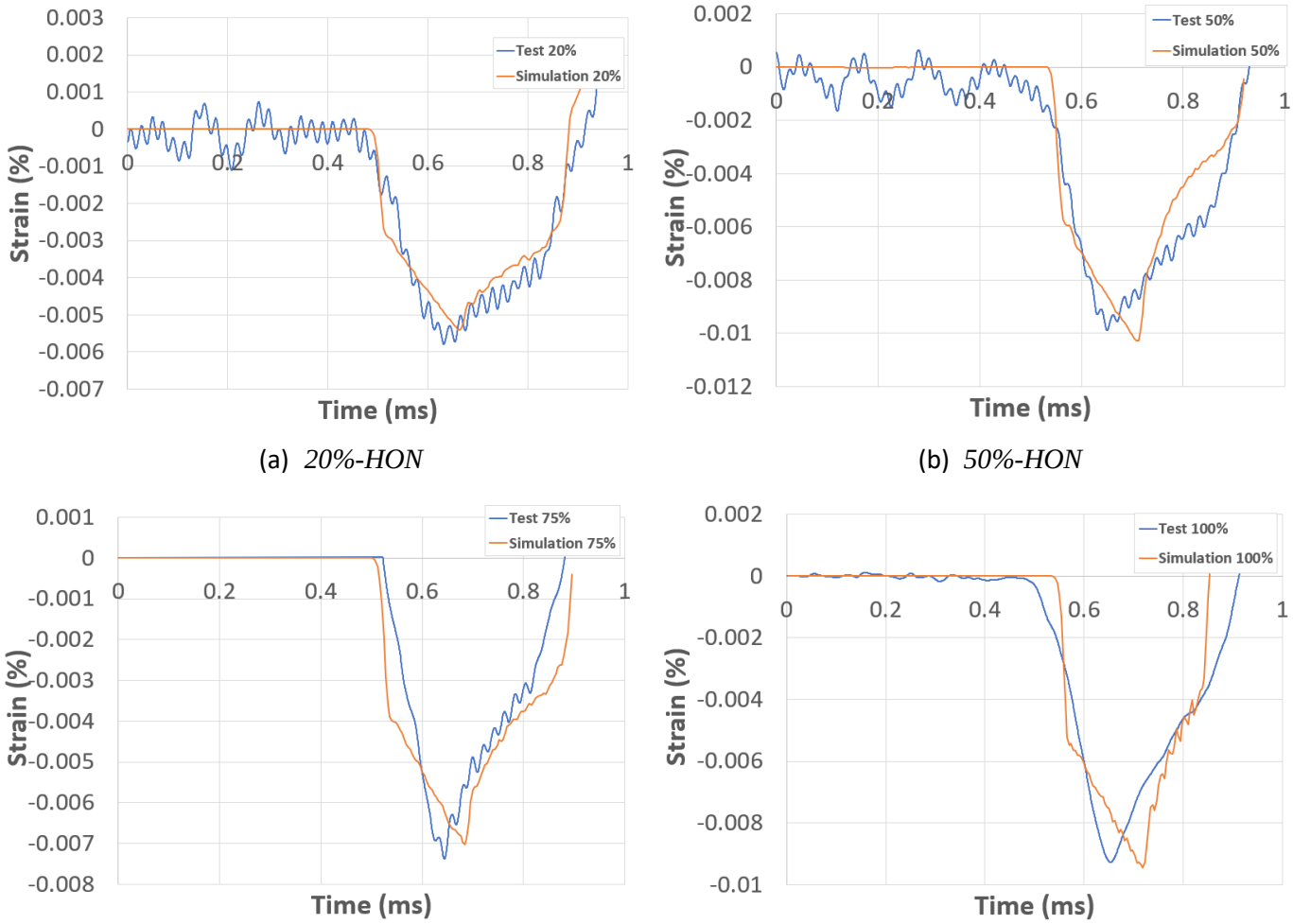
Figure 4. 46 to ***Figure 4. 50*** illustrate the validation between numerical and experimental data for different filling ratios (20, 50, 75, and 100%) at a pressure of 1.4 bar. The excellent correlation between the various parameters examined is remarkable. Upon scrutinizing the data illustrated in ***Figure 4. 47***, several intriguing patterns emerge. First, the curves are similar, indicating a consistent relationship between the sent signal and the fill rate. These parallels shouldn't, however, cause us to ignore the minor but essential variations between the curves. One of these variations can be found in the curves' maximum points. These points change with the fill rate. In particular, the fill rate at 50% shows the steepest curve, indicating that the transmitted signal grows noticeably with each fill rate increment. On the other hand, the fill rate of 20% exhibits the least steep curve, suggesting that an increase in fill rate has a less significant effect on an increase in the transmitted signal. This finding could significantly impact how systems that depend on fill rate for signal transmission efficiency are designed and optimized.



(a) 20%-HON *(b) 50%-HON*

(c) 75%-HON *(d) 100%-HON*

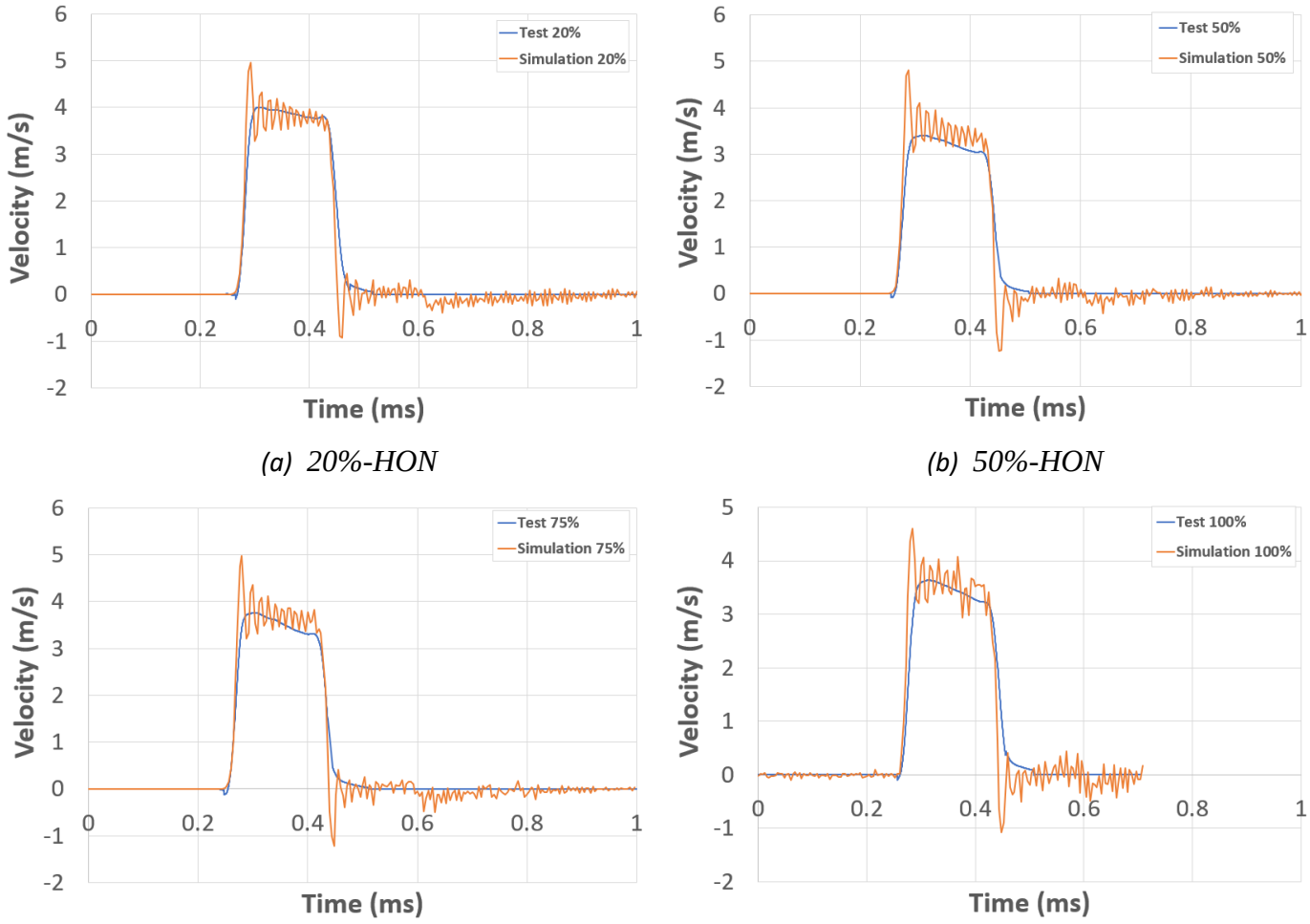
Figure 4. 46: Variation of the incident signal for filling rates from 20% to 100% at 1.4 bar pressure: test vs. simulation.



(a) *20%-HON* (b) *50%-HON*

(c) *75%-HON* (d) *100%-HON*

Figure 4. 47: Variation of the transmitted signal for filling rates from 20% to 100% at 1.4 bar pressure: test vs. simulation.

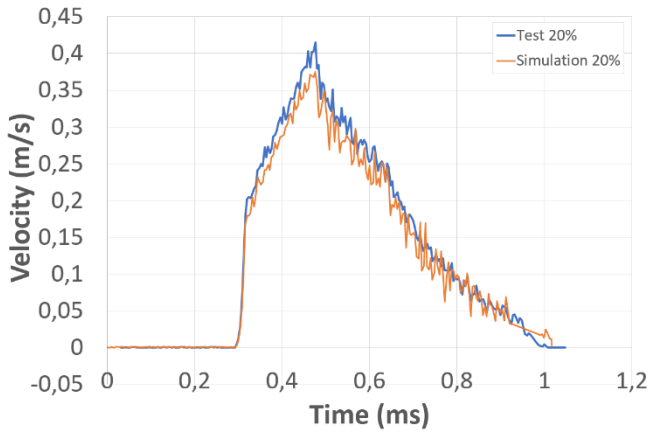


(a) 20%-HON *(b) 50%-HON*

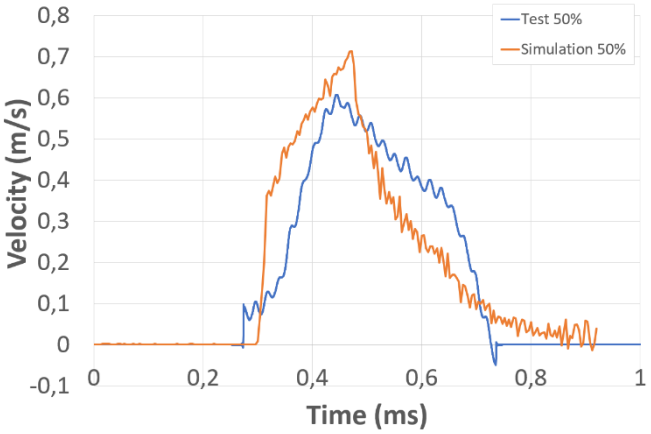
(c) 75%-HON *(d) 100%-HON*

Figure 4. 48: Variation of the incident velocity for filling rates from 20% to 100% at 1.4 bar pressure: test vs. simulation.

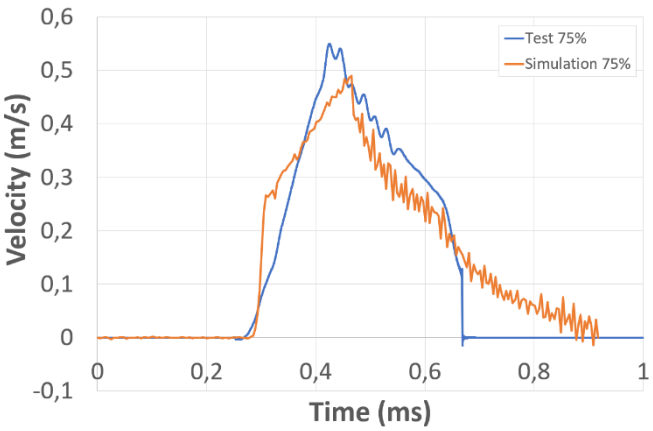
Figure 4. 49 displays variations in transmission velocities concerning fill rate. The transmitted velocity is 0.4 m/s at a filling ratio of 20 percent, the lowest, and 0.6 m/s at a filling ratio of 50 percent, the greatest. These findings highlight how the filling ratio significantly affects the system's characteristics being studied. They show how changes in the quantity of material directly impact the behavior and functioning of the system.



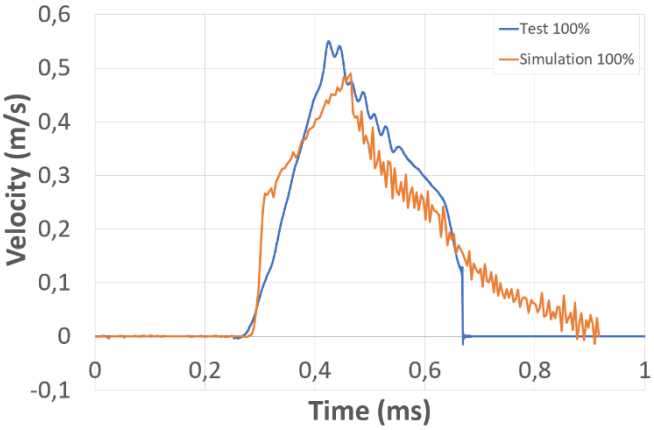
(a) 20%-HON



(b) 50%-HON

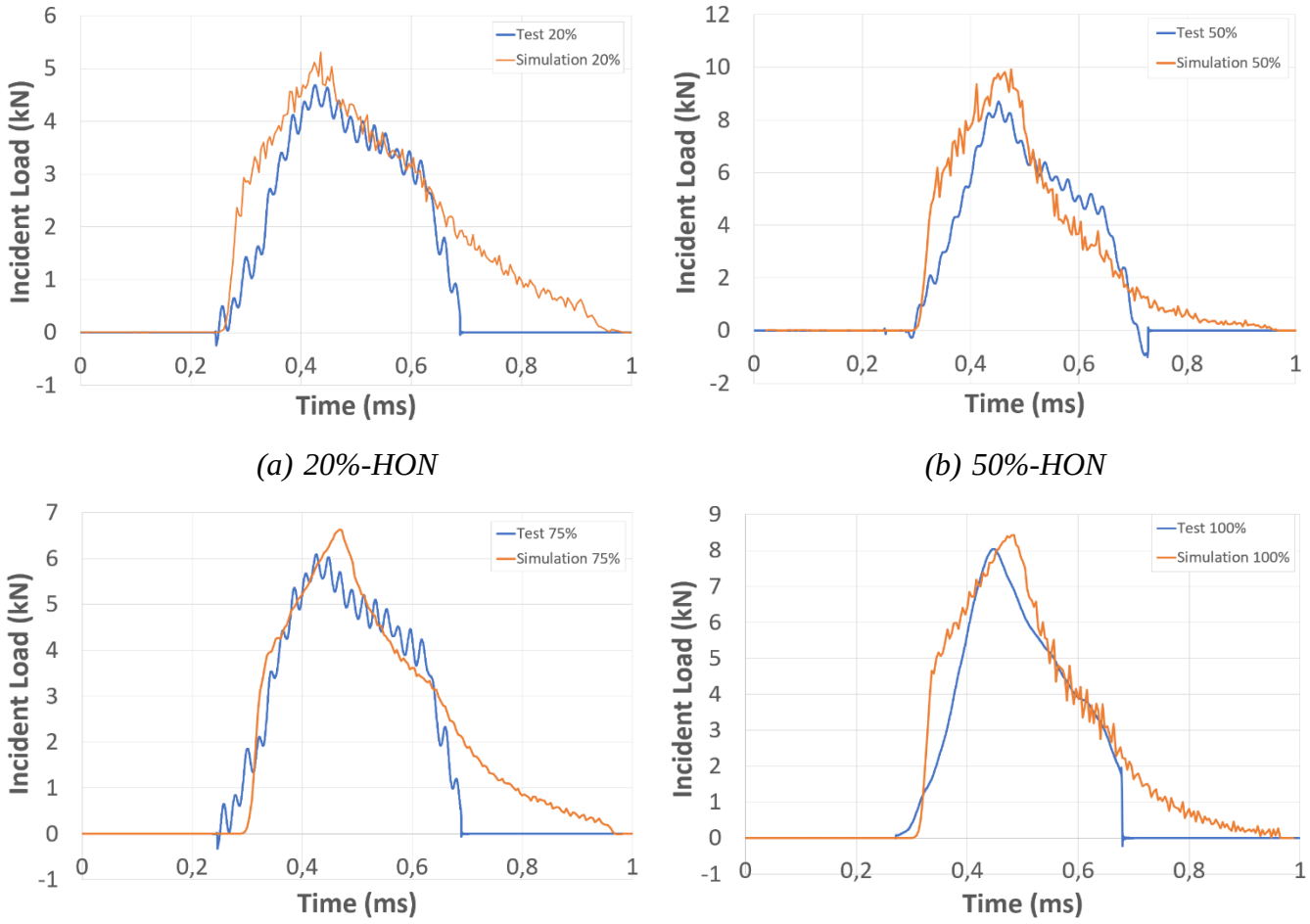


(c) 75%-HON



(d) 100%-HON

Figure 4. 49: Variation of the transmitted velocity for filling rates from 20% to 100% at 1.4 bar pressure: test vs. simulation.



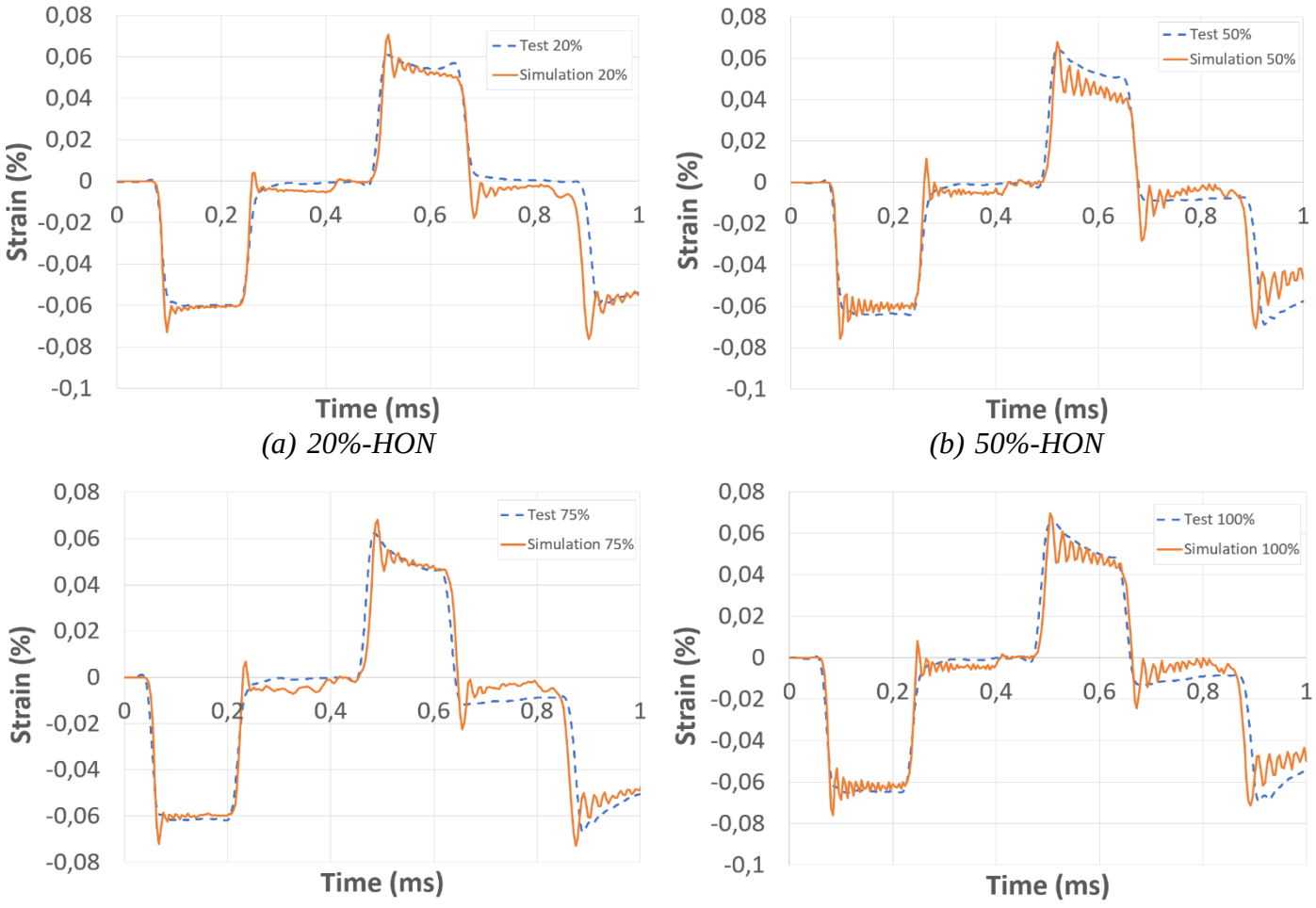
(a) 20%-HON *(b) 50%-HON*

(c) 75%-HON *(d) 100%-HON*

Figure 4. 50: Variation of the incident load for filling rates from 20% to 100% at 1.4 bar pressure: test vs. simulation.

Figure 4. 51 shows the variation in the incident signal for filling ratios ranging from 20% to 100% at a constant pressure of 1.7 bar. To assess the impact of pressure on material behavior, we can compare the curve corresponding to a filling ratio of 20% at two different pressures, 1.4 bar (as shown in ***Figure 4. 46*** (a)) and 1.7 bar (as shown in ***Figure 4. 51*** (a)). Noticeably, the reflected signal at 1.7 bar is higher than that at 1.4 bar. The transition between the incident bar, the sample, and the transmitted bar at higher pressures can explain this observation. ***Figure 4. 50*** depicts the incident load fluctuation for filling ratios of 20% to 100% at 1.4 bar of pressure. The curve has a maximum value of 6 KN for a 50% fill rate, the highest curve compared to the other filling ratios. Due to the restriction imposed by the 50 percent filling ratio, the incident force curve during this test will demonstrate a sharp rise in force during the load build-up phase. The holding phase, which follows, is characterized by a time of steady load during which the

force is generally stable because of the material's strength. As the load is removed, the tension reduces, which causes a sudden fall in force, which can be seen during the unloading phase. Finally, the force during the relaxation phase may gradually decrease until it reaches zero, demonstrating reversibility.



(a) 20%-HON *(b) 50%-HON*

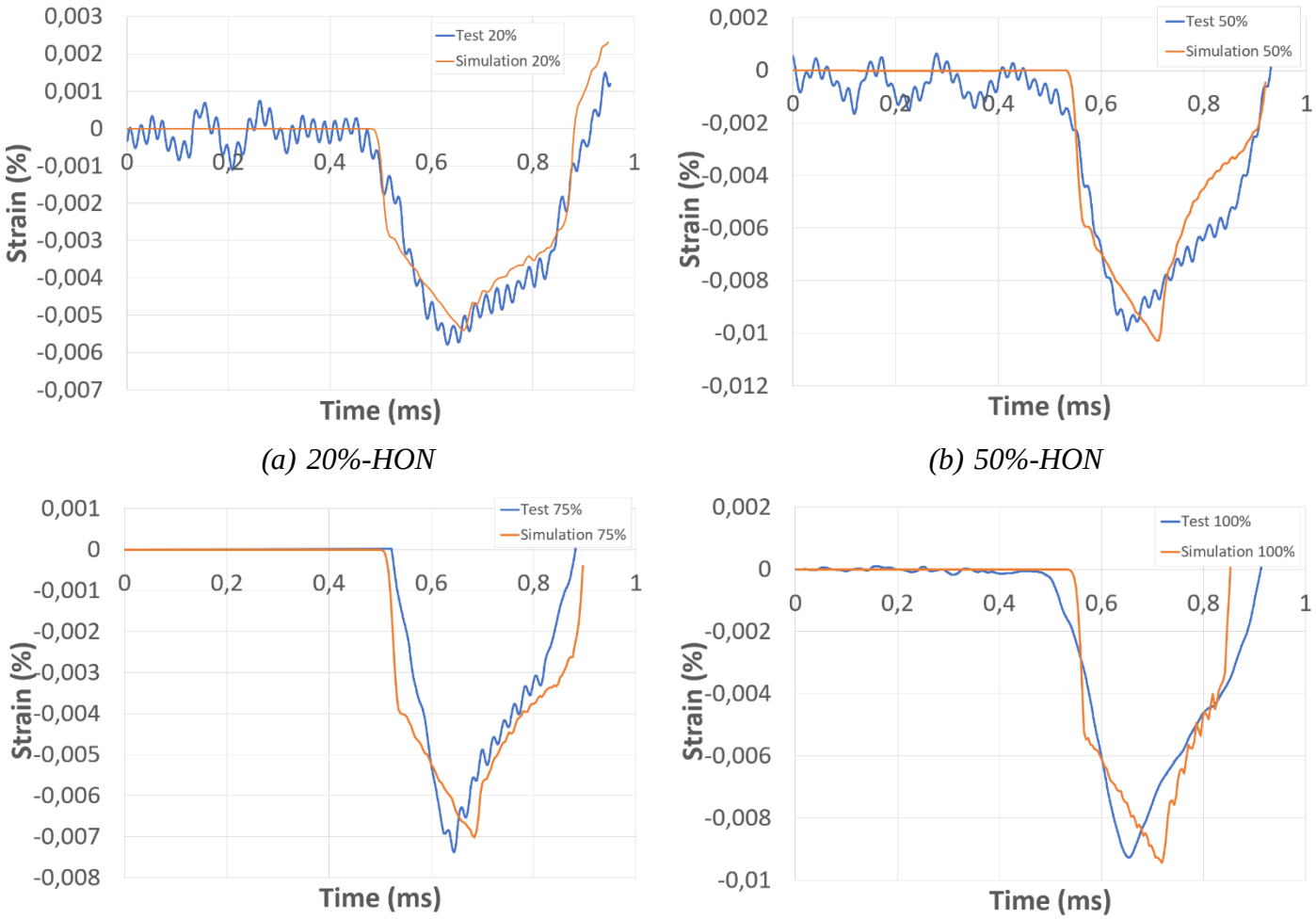
(c) 75%-HON *(d) 100%-HON*

Figure 4. 51: Variation of the incident signal for filling rates from 20% to 100% at 1.7 bar pressure: test vs. simulation.

Figure 4. 52 presents the validation of deformation signals transmitted at different filling rates (20%, 50%, 75%, and 100%) during dynamic compression testing at a pressure of 1.7 bar. A similar trend is observed among the various filling rates but with different peak points. For the 20% filling rate, the deformation signal is 0.6%, indicating the lowest deformation signal. Conversely, the 100% filling rate exhibits the highest deformation signal at 0.9%.

Figure 4. 53 illustrates the fluctuation of incident velocity at different filling ratio values, ranging from 20% to 100%, at a constant pressure of 1.7 bar. Immediate observation reveals

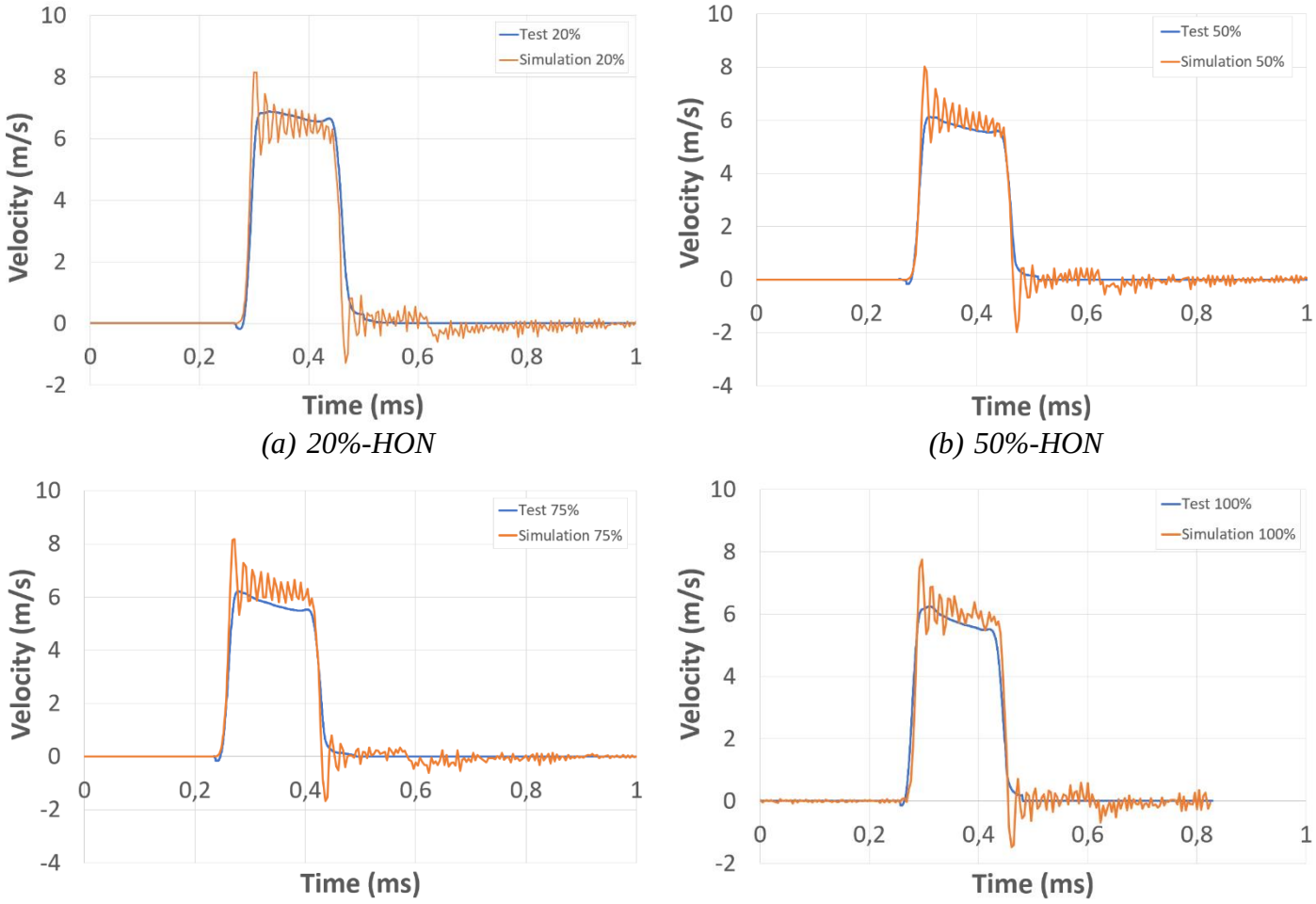
that there are no significant variations between the maximum points. Moreover, a notable trend emerges: the highest incident velocity is associated with a strain rate of 20%, reaching its minimum when the strain rate is 100%.



(a) 20%-HON *(b) 50%-HON*

(c) 75%-HON *(d) 100%-HON*

Figure 4. 52: Variation of the transmitted signal for filling rates from 20% to 100% at 1.7 bar pressure: test vs. simulation.

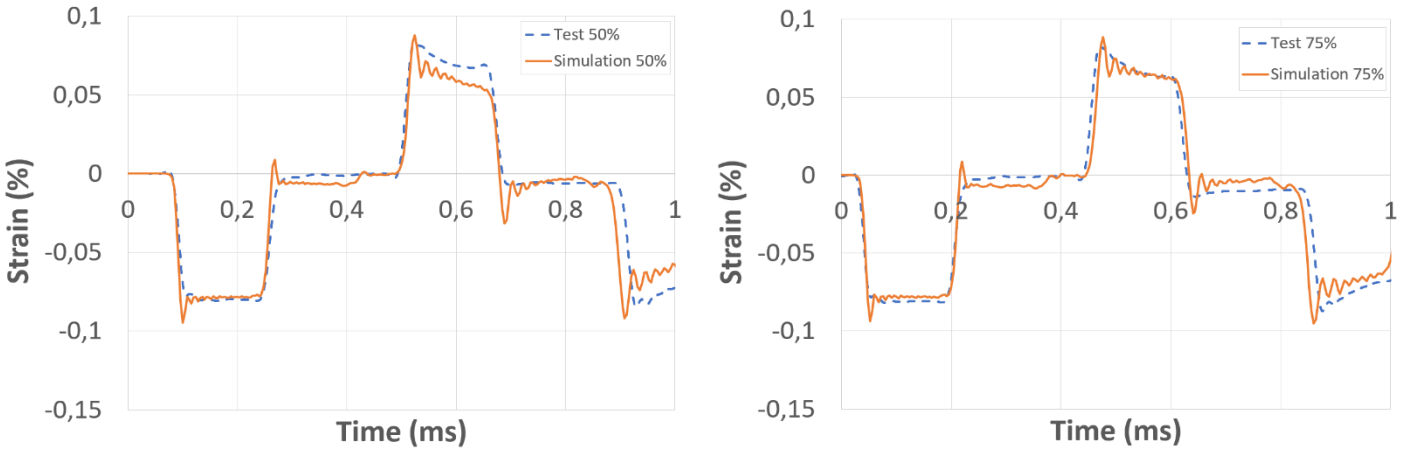


(a) 20%-HON *(b) 50%-HON*

(c) 75%-HON *(d) 100%-HON*

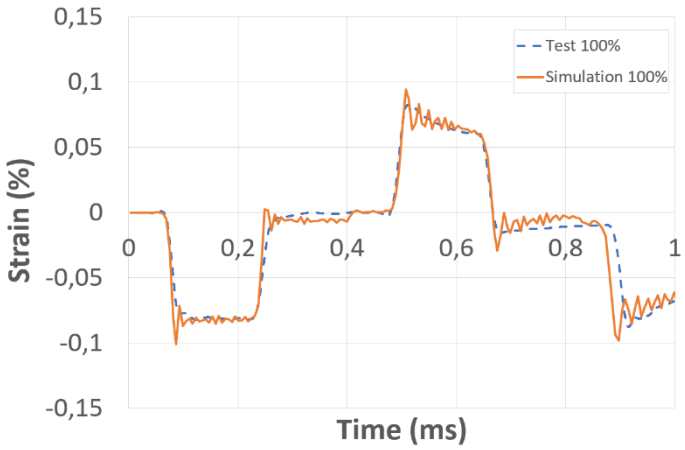
Figure 4. 53: Variation of the incident velocity for filling rates from 20% to 100% at 1.7 bar pressure: test vs. simulation.

The validation of the parameters for our study's two different pressure levels, 2.0 bar, and 2.4 bar, is shown in detail in ***Figure 4. 54*** to ***Figure 4. 57***. This validation phase's primary goal was to evaluate the consistency between the numerical values produced by our models and the field experiment findings. The graphs represent the curves from the experimental data and those created by our numerical simulations. The results of this visual comparison were quite encouraging, showing a strong correlation between the experimental and numerical curves. This agreement between numerical predictions and actual data supports the validity of our model and attests to its capacity to accurately mimic system behavior at 2.0 bar and 2.4 bar pressures.



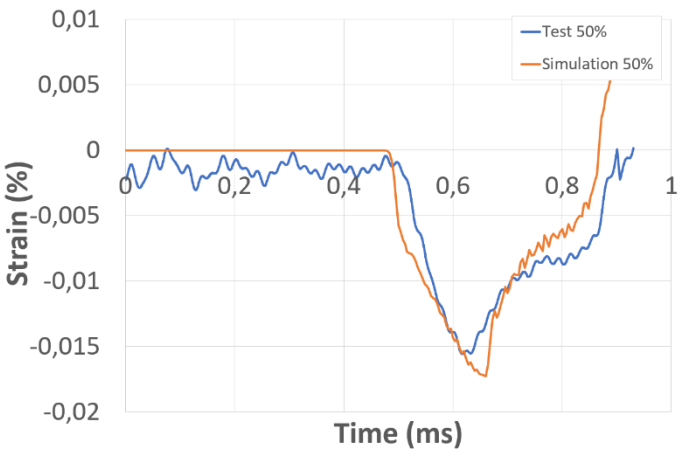
(a) 50%-HON

(b) 75%-HON

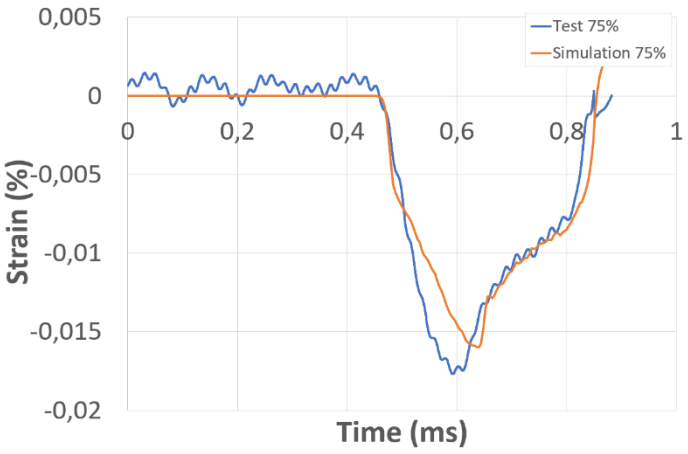


(c) 100%-HON

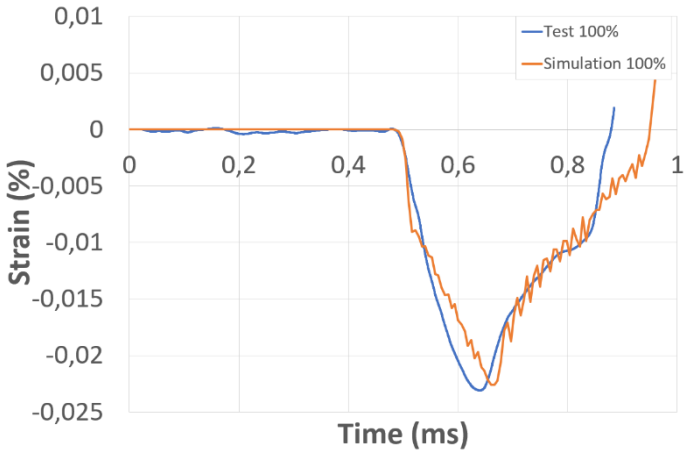
Figure 4. 54: Variation of the incident signal for filling rates from 50% to 100% at 2.0 bar pressure: test vs. simulation.



(a) 50%-HON

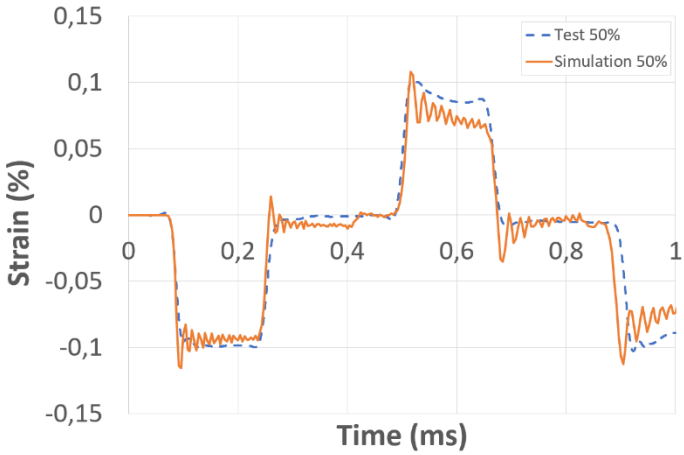


(b) 75%-HON

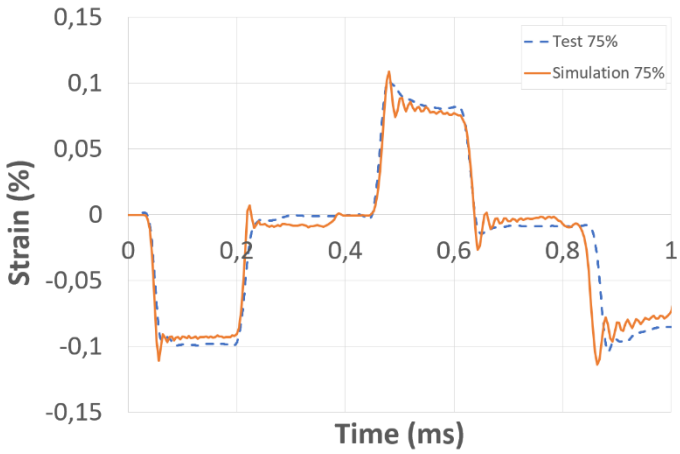


(c) 100%-HON

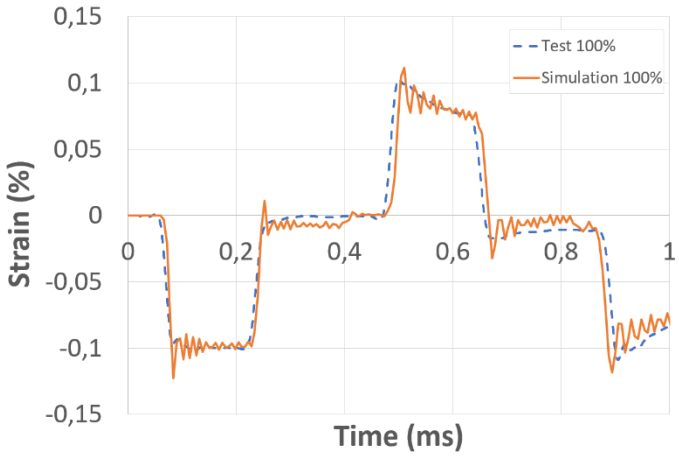
Figure 4. 55: Variation of the transmitted signal for filling rates from 50% to 100% at 2.0 bar pressure: test vs. simulation.



(a) 50%-HON

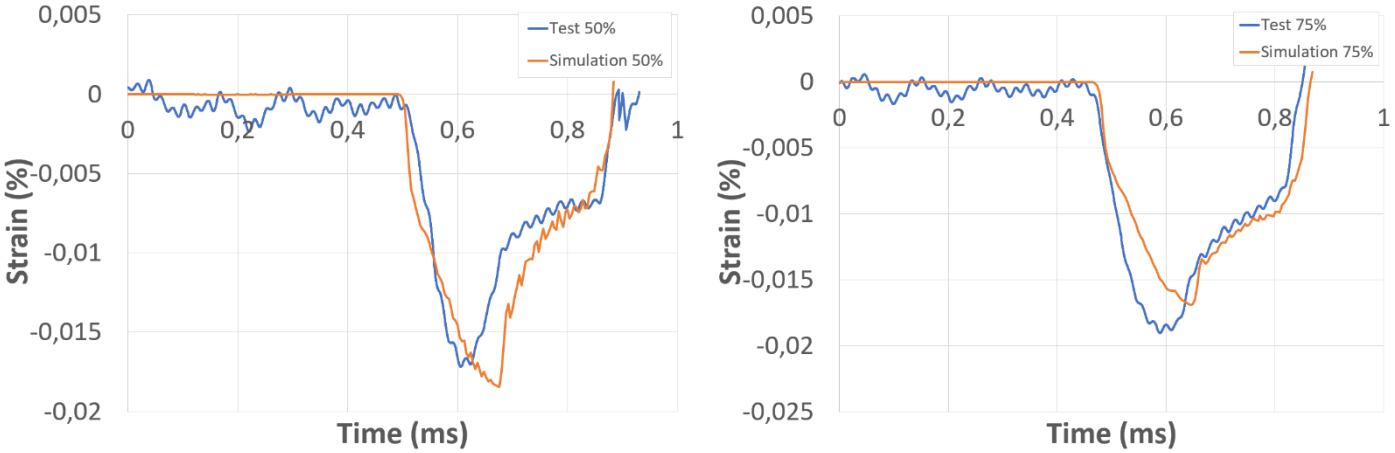


(b) 75%-HON



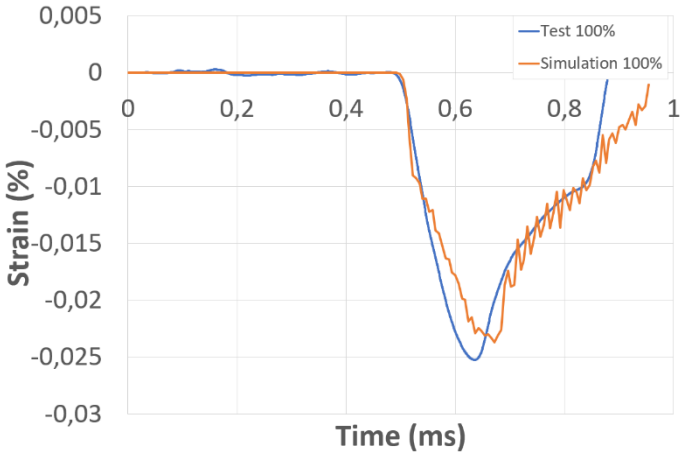
(c) 100%-HON

Figure 4. 56: Variation of the incident signal for filling rates from 50% to 100% at 2.4 bar pressure: test vs. simulation.



(a) 50%-HON

(b) 75%-HON



(c) 100%-HON

Figure 4. 57: Variation of the transmitted signal for filling rates for Nida filler from 50% to 100% at 2.4 bar pressure: test vs. simulation.

4. 5 Static compression modeling of Aerosil/polycarbonate composites

4.5.1 Homogenization cycle

The significance of homogeneity between the nanofiller (Aerosil) and matrix (polycarbonate) is highlighted by Digimat MF, a valuable tool for composite material design and analysis. Particularly in the case of Aerosol/polycarbonate, this homogeneity becomes essential. Digimat MF allows for accurately evaluating these intricate materials' mechanical, thermal, and electrical properties because of its sophisticated modeling and simulation capabilities. Digimat MF provides a comprehensive understanding of material behavior under various loads and situations by integrating multi-scale models. With this method, the interactions between the matrix and the nanofiller and how they affect the composite's overall performance are better understood. Efficient homogenization guarantees that the nanofiller is distributed uniformly

throughout the matrix, which can significantly enhance the final material's strength, electrical or thermal conductivity, and longevity.

Figure 4. 58 illustrates the loop and operation within Digimat MF to homogenize the matrix and the reinforcement, commonly referred to as "mean field Homogenization." This method relies on three essential steps. Firstly, in step 1, known as localization, the macro deformation at the composite level is locally calculated. This step allows for the deformation in each constituent phase to be determined. Subsequently, in step 2, the stresses are calculated in each phase and then averaged to obtain the macro stress at the composite level. This calculation loop is automated within Digimat MF, ensuring an effective and precise homogenization of the matrix and the reinforcement.

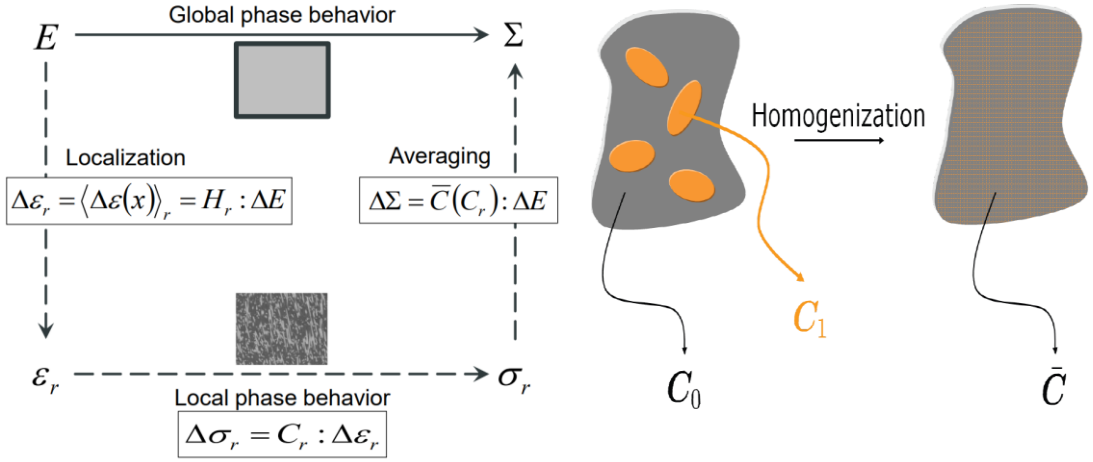
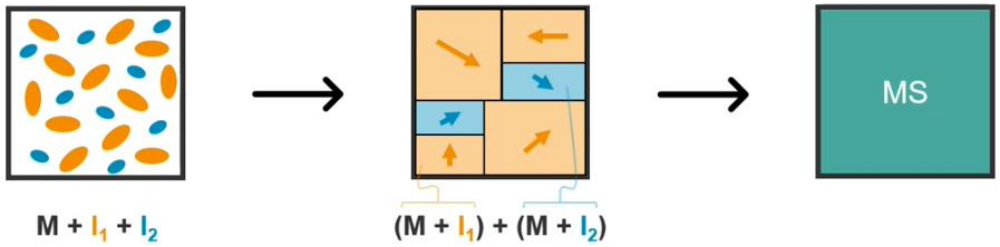
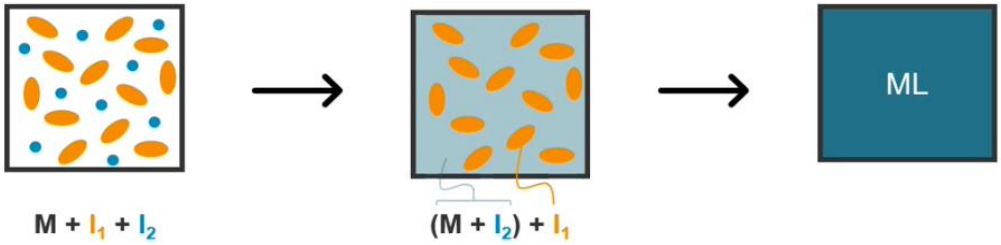


Figure 4. 58: Mean-field homogenization cycle.

In multiphase materials, when dealing with multiple orientations of nanofibers, two types of homogenization are prominent: multistep and multilevel, ***Figure 4. 59***. Multistep involves separate homogenization of different phases: initially, each type of fiber undergoes individual homogenization without mixing, followed by a second homogenization combining all phases. Conversely, multilevel is more suited for spherical fibers and voids. Initial homogenization involves mixing the matrix with the blue fibers and introducing orange inclusions before a second homogenization phase.



(a) *Multistep homogenization*



(b) Multilevel homogenization

Figure 4. 59: Multistep & Multilevel homogenization for multiphase inclusions

4.5.2 Nanocharge effect after Aerosil/ Polycarbonate homogenization

A simulation using Digimat-MF software was conducted to homogenize the composite material. We initially inserted both materials (polycarbonate and Aerosil) and identified their behaviors by inputting their mechanical properties. Subsequently, we characterized the microstructure and varied the matrix's nanocharge (Aerosil) content. Following this, we applied a small uniaxial deformation of 6% (***Figure 4. 60***) to observe the effect of the nanocharge on the material behavior. With the help of this technology, it is possible to analyze in-depth the effects of nanofillers on the mechanical characteristics of the composite material, which offers insightful information for improving its performance.

After running the calculation in Digimat MF, the results show that the nanocharge content affects the mechanical behavior, ***Figure 4. 61***. Increasing the nanocharge content leads to higher Young's modulus and maximum strength (Rm), even when dealing with deficient nanocharge levels (0wt.%, 1wt.%, 2wt.%, and 4wt.%). Nanoparticles have a high specific surface area per unit mass, enhancing materials' mechanical properties when incorporated. As the nanocharge content increases, these nanoparticles dispersed in the matrix strengthen the interatomic bonds, thereby increasing Young's modulus, which measures the material's stiffness and maximum strength, indicating the material's ability to withstand a maximum load before failure.

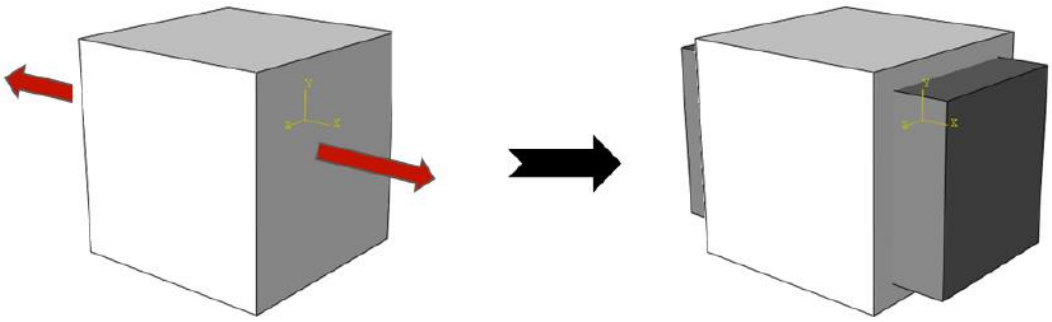


Figure 4. 60: Illustration of the Uniaxial_1 loading.

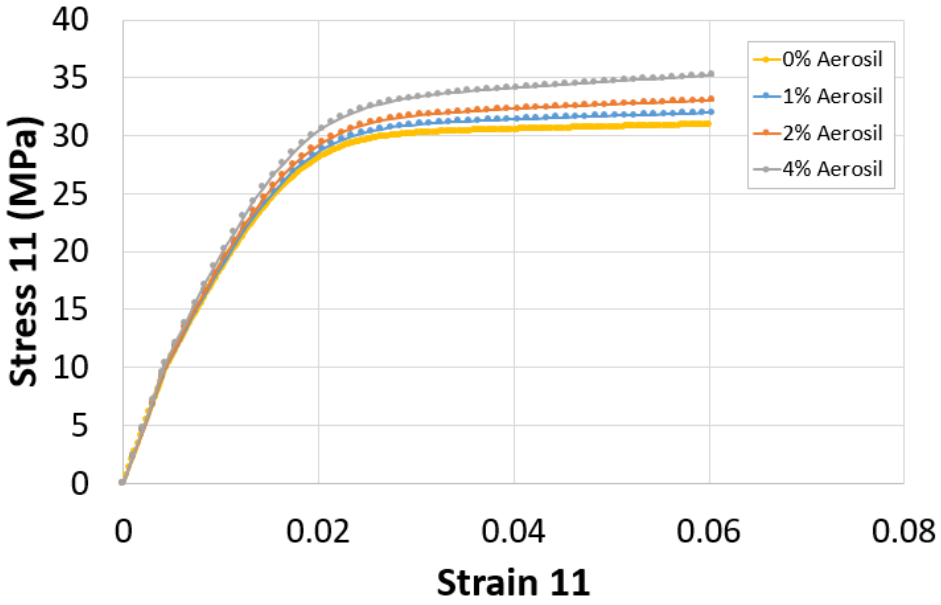


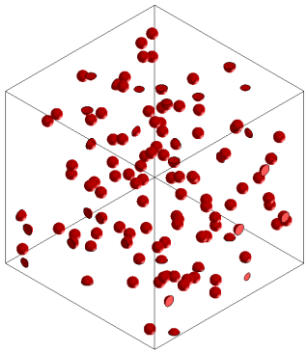
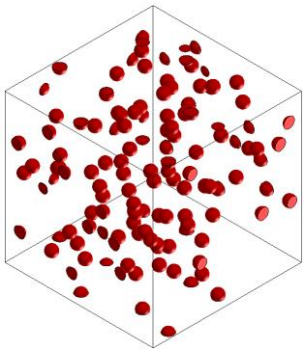
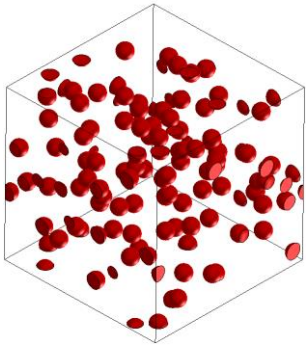
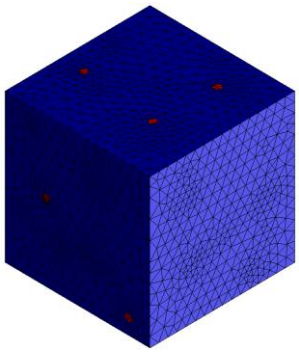
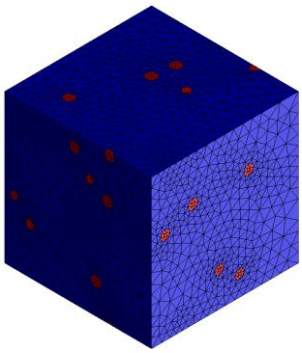
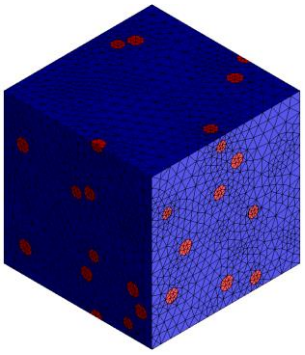
Figure 4. 61: Nanocharge effect after Polycarbonate/Aerosil homogenization for 6% loading, uniaxial deformation in direction 11

4.5.3 Representation of the elementary volume of the composite

Digimat FE makes it possible to correctly forecast how the composite material (Aerosil/polycarbonate) would react to various load circumstances, facilitating the creation of more robust, safe, and effective products. Digimat FE expedites product development and saves money and time by eliminating the need for expensive physical prototypes and experimental testing. ***Table 4. 9*** shows the elemental volume of the composite (Aerosil/polycarbonate) with mesh for different levels of nanofiller, clearly showing the homogenization and incorporation of nanoparticles into the matrix. The Aerosil 300 reinforcement, incorporating nanoparticles, is combined with a polycarbonate matrix. The proportions of Aerosil in the composite vary between 1%, 2%, and 4%, with a uniform spatial distribution of the constituent phases. Phase interactions are defined by a continuum material model with a perfectly bonded interface. In

terms of behavior, the nanoparticles (Aerosil) follow a linear elastic model, while the polycarbonate exhibits elastoplastic behavior.

Table 4. 9: The representation of the elementary volume of the composite (Aerosil/polycarbonate) with meshing for various nanoceramic levels.

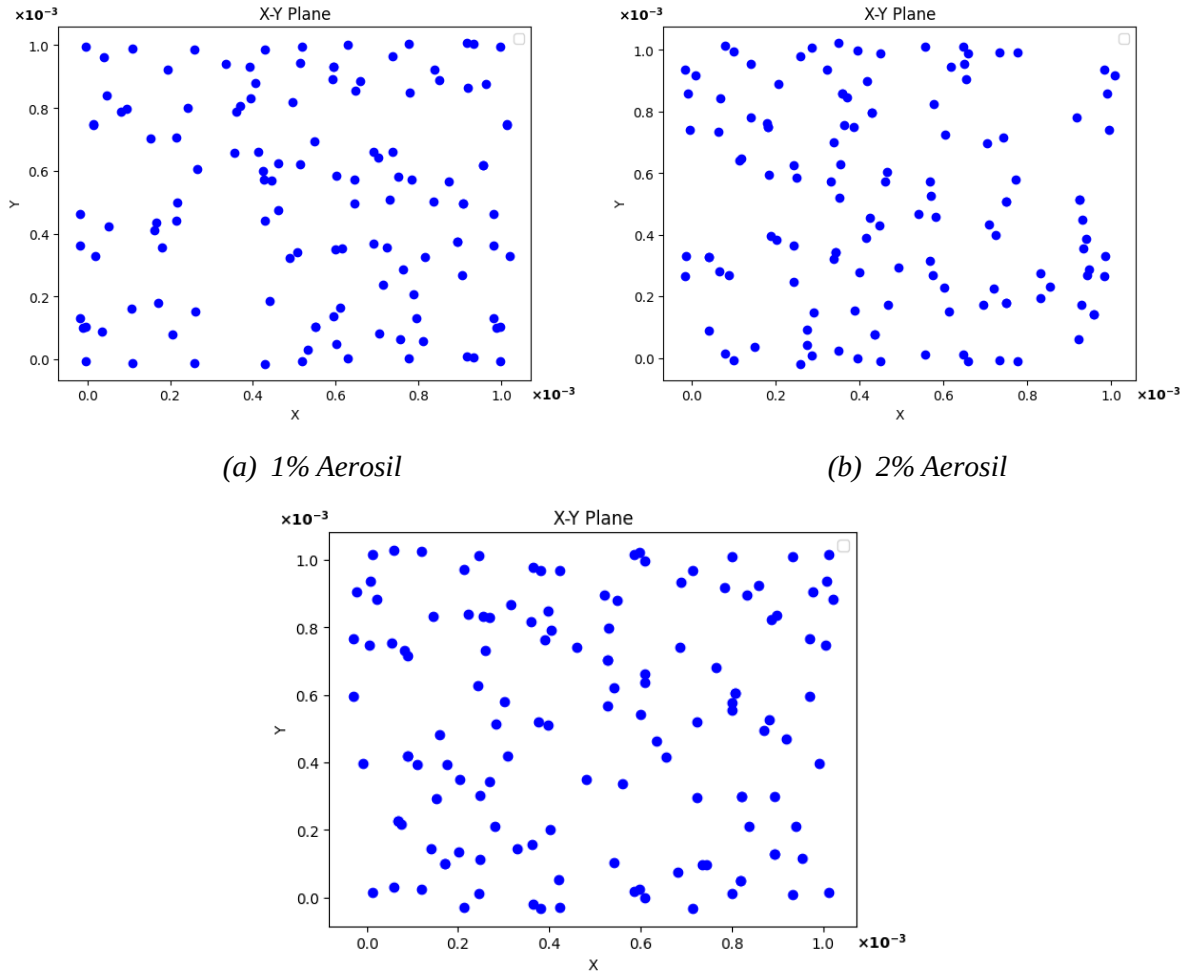
	Nanoceramic wt.%		
	1%	**2%**	**4%**
3D homogenization			
Mesh			

4.5.4 Position of the nanoceramic relative to the matrix

Figure 4. 62 depicts the disappearance and location of nanofillers in the matrix in the XY plane, including concentrations of 1wt.%, 2wt.%, and 4wt.%. One important finding is that the nanofillers are arranged randomly inside the matrix. Upon closer inspection, it becomes evident that the nanofillers' locations differ considerably between percentages, indicating an inherent dynamic in the dispersion as a function of concentration.

A gamma diagram as a function of relative weight is displayed in ***Figure 4. 63*** . In tetrahedral mesh production, the "Gamma" parameter is associated with the ratio between the radii of inscribed and circumscribed spheres. This option manages the quality of the tetrahedral mesh elements. The "Gamma" parameter is scaled to equal 1 for a regular tetrahedron and is used to modify the ratios of the spheres connected to the tetrahedrons. ***Figure 4. 63***'s significant

interval, which ranges from 0.27 to 1 Gamma, shows how the control parameter varies and affects the mesh tetrahedrons' geometry. Specifically, a relative weight of 0.185 and a gamma of 0.88 indicate a minor decline in mesh quality. However, the relative weight decreases to 0.05 at a gamma of 0.95, demonstrating a discernible improvement in mesh quality and convergence towards a more accurate depiction of the intended geometry. These findings demonstrate how critical the Gamma parameter is to creating tetrahedral meshes, emphasizing the need to select this value with care to guarantee a high-quality mesh and precise simulation of the characteristics of the composite material under investigation.



(a) 1% Aerosil

(b) 2% Aerosil

(c) 4% Aerosil

Figure 4. 62: Position of the nanoceramic relative to the matrix in the XY plane.

Figure 4. 63 depicts Rho's fluctuation with relative weight. One of the influencing factors is the parameter Rho, which is the ratio of the mesh element's longest edge to its most petite edge length. Interestingly, a maximum relative weight of 0.15 is associated with a Rho of 0.63,

indicating that this particular Rho number provides an ideal mesh geometric representation. This finding emphasizes Rho's substantial impact on mesh quality and the parameter's significance in producing appropriate mesh pieces.

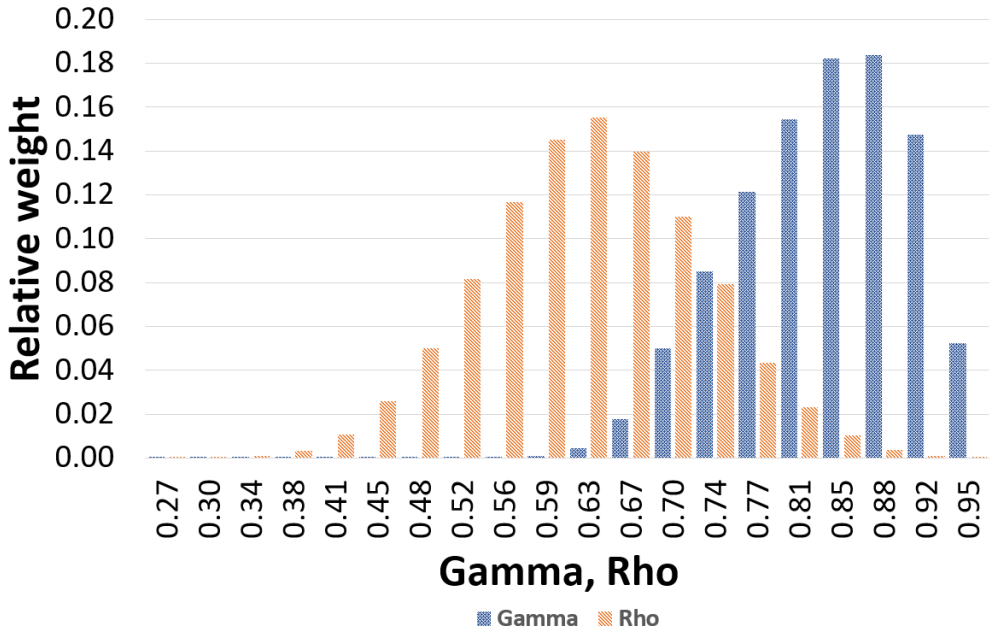
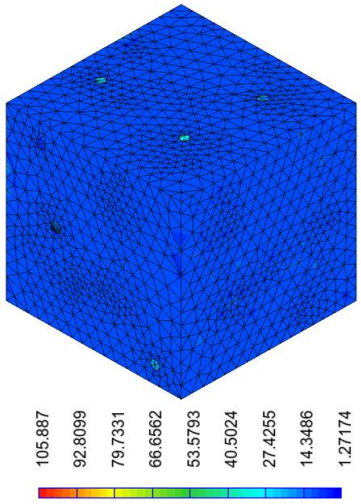
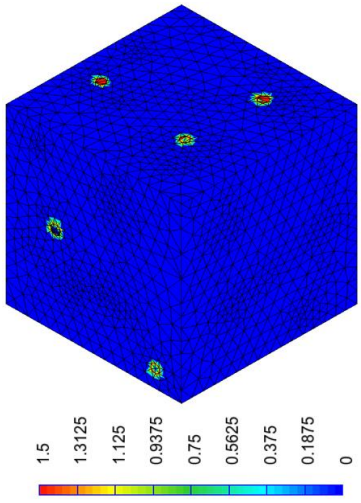
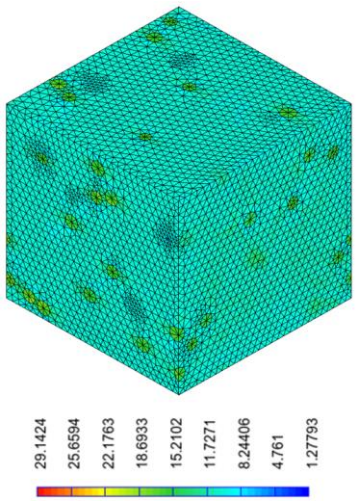
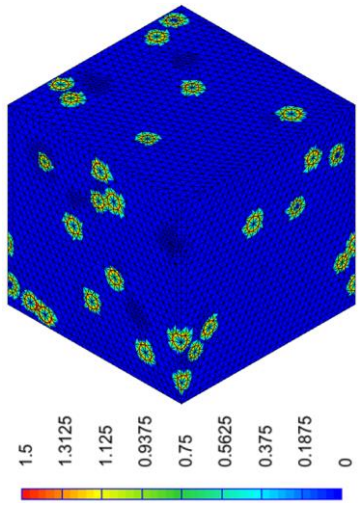
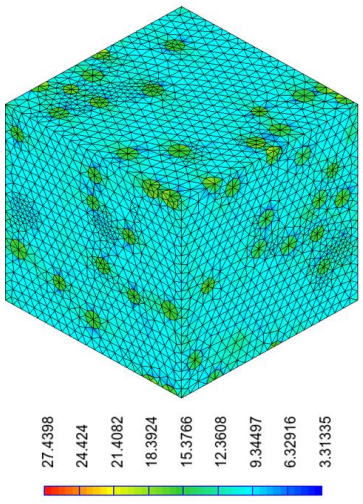
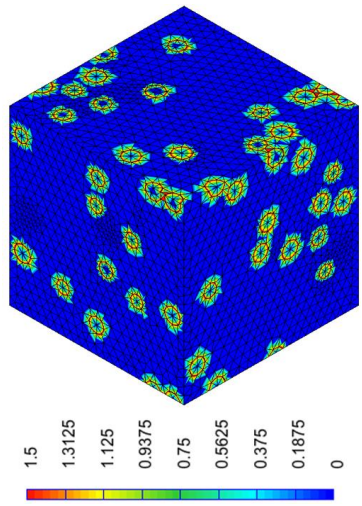


Figure 4. 63: Gamma and Rho variation as a function of relative weight for Aerosil 1%.

The analysis results in Digimat FE allow us to make several pertinent observations concerning the representation of the elementary volume for each nano-filler wt.%. A low load (stress) of 10 MPa is applied to observe the variations and effects of nanofillers and variations in Von Mises stresses and contact at the nanoparticles and matrix level, as shown in **Table 4. *10***. After calculation, it is notable that Von Mises stresses are maximal at the Aerosil nanofiller installation position for 1wt.%, 2wt.%, and 4wt.%. This specific zone reveals a significant concentration of pressure at this precise location.

More precisely, Von Mises stresses reach a maximum value of 27.42 MPa for a nano-filler wt.% of 1%, while for a wt.% of 2%, these stresses are minimal, reaching a value of 15.21 MPa. The term "contact status" refers to the state of contact between the various constituent phases of the composite. In other words, it indicates whether the nanofillers are in contact with each other or the polycarbonate matrix.

Table 4. 10: Variation of Von Mises stresses and elastic Strain as a function of nanofiller ratio.

Nanofiber wt.%	Equivalent von Mises Stress	Contact Status
1wt.%		
2wt.%		
4wt.%		

4. 6 Conclusion

For the first part, a 3D numerical model was created to examine the effects of printing speed (10, 30, 50, and 70 mm/s) and printing parameters on the ABS specimen's tensile ASTM D638 behaviour. The objective was to replicate temperature and residual stress changes during the FDM process. The following is a summary of the study's findings:

- Development and validation of the numerical model using Abaqus/Digimat coupling with experimental results.
- The availability and accuracy of numerical tools can facilitate understanding the impact of process factors on 3D-printed parts.
- The residual stress and deflection are reduced by accelerating the printing speed.
- The most significant temperature gradient was observed for the printing discretization while filaments were deposited. While varied values were observed on the surface of the printed part with filament deposit, the temperature was constant across the part surface when layers were deposited.
- Due to the temperature difference between the platform plate and the part layers, high residual stresses were projected between the first and the sixth layers. With each passing minute of printing, the part solidifies, and the temperature drops, increasing the stress's magnitude. The Von Mises stress reaches its maximum value during the cooling phase; for the layer deposit process and the filament deposit process, this value is 37.08 MPa.
- The temperature was found to vary significantly over the thickness of the polymer. Therefore, if the printed item's temperatures changed drastically, the concentration of stresses was higher. These residual stresses can lead to the development of cracks in the material and delamination between the layers of the printed part.

The second part is dedicated to studying the static (tensile) behavior of CF-PETG material. The results of exploratory testing and numerical analysis are closely correlated, demonstrating that the new material suits various applications.

- Development and validation of the numerical model using Abaqus/Digimat coupling with experimental results.
- The availability and quality of numerical tools can make understanding how process variables affect 3D-printed components easier.

The third part is devoted to studying the dynamic behavior of CF-PETG. This study investigated the dynamic characteristics of components 3D printed from CF-PETG with different fill densities using the Split Hopkinson Pressure Bar (SHPB) technique. The study demonstrated low and high fill densities were more cost-effective than solid samples. In addition, the material's dynamic behavior showed significant changes under different impact loads, leading to cumulative damage and, ultimately, catastrophic failure.
A good correlation between numerical and experimental results demonstrates the robustness and accuracy of our modeling approach.

The final section explored the successful development of a new class of additively manufactured composites using Aerosil 300 as the reinforcing agent and polycarbonate as the matrix. The thermal and mechanical properties of the material were exhaustively characterized by incorporating different compositions with varying weight percentages of Aerosil reinforcement, ranging from 1wt.% to 4wt.%. A numerical model developed by Digimat software to simulate Aerosil/polycarbonate homogenization shows the disappearance of nanofillers from the matrix and the representation of the elementary volume of the composite.

General conclusion

The main objective of this thesis is to work on 3D-printed composite and nanocomposite materials, specifically by developing numerical and experimental tools to model various materials digitally and experimentally. Our laboratory's numerical and experimental tools, including innovative software, machines, and equipment for physicochemical analysis, greatly facilitate this modeling process.

Based on the first chapter, the bibliographic chapter, we observe that many studies have been conducted by previous researchers on 3D printing, both experimentally and numerically. However, most researchers who modeled printed parts did not consider the impact of printing parameters. They often worked in Abaqus, which assumes perfect parts, which is not true. Therefore, one of this thesis's objectives is to numerically model printed parts by considering printing defects and parameters to validate experimental results and get as close to reality as possible.

Based on the literature and previous studies, we also noticed that few researchers have worked on nanocomposites either experimentally or numerically. This is why we have focused on developing and working on a new composite material, "nanocomposites," to study the effect of nanoparticles on the behavior of thermoplastic-based materials. Using numerical tools, we demonstrated the distribution of nanofillers within the matrix.

We began the thesis by working on the thermoplastic material ABS to familiarize ourselves with the numerical tools, such as 3D printing modeling, and the coupling between the Abaqus and Digimat software to account for printing effects in finite element calculations. After gaining familiarity with these numerical tools, we conducted tensile tests on CF-PETG material. We developed a numerical model, explicitly using the Abaqus/Digimat coupling to correctly validate our model, being among the first researchers to work on this topic. We successfully validated the results with different fill rates and types of infill.

Next, by the progression of the work and the tasks outlined in the thesis plan, we conducted dynamic tests using Hopkinson bars on cubic CF-PETG samples with varying fill rates for honeycomb infill. We developed a finite element numerical model to validate the experimental

results at different impact speeds. We demonstrated the effect of impact speed on the dynamic behavior of the material and fill rates.

For the final part, we developed a new composite material, a thermoplastic (polycarbonate) reinforced with ceramic nanoparticles. We conducted static compression tests under temperatures ranging from -90°C to 80°C, an interval chosen because many industries, especially aerospace, require materials to withstand very low temperatures. Various nanoparticle concentrations (1%, 2%, and 4%) were produced to demonstrate nanofillers' effect on the composite material's behavior. Additionally, a Digimat model was developed to observe the distribution of nanofillers and the homogenization between the reinforcement and the matrix.

References

[1] M. Touri, F. Kabirian, M. Saadati, S. Ramakrishna, et M. Mozafari, « Additive manufacturing of biomaterials− the evolution of rapid prototyping », *Advanced Engineering Materials*, vol. 21, nº 2, p. 1800511, 2019.

[2] M. Daly, M. Tarfaoui, M. Chihi, et C. Bouraoui, « FDM technology and the effect of printing parameters on the tensile strength of ABS parts », *The International Journal of Advanced Manufacturing Technology*, vol. 126, nº 11, p. 5307-5323, 2023.

[3] X. Wang, M. Jiang, Z. Zhou, J. Gou, et D. Hui, « 3D printing of polymer matrix composites: A review and prospective », *Composites Part B: Engineering*, vol. 110, p. 442-458, 2017.

[4] I. Goda, M. Nachtane, Y. Qureshi, H. Benyahia, et M. Tarfaoui, « COVID-19: Current challenges regarding medical healthcare supplies and their implications on the global additive manufacturing industry », *Proceedings of the Institution of Mechanical Engineers, Part H: Journal of Engineering in Medicine*, vol. 236, nº 5, p. 613-627, 2022.

[5] I. Akbar, M. El Hadrouz, M. El Mansori, et M. Tarfaoui, « Investigation of thermo-mechanical shape memory signatures of 3D printed and Injection molded polymers », *CIRP Journal of Manufacturing Science and Technology*, vol. 41, p. 277-291, 2023.

[6] A. El Moumen, M. Tarfaoui, et K. Lafdi, « Modelling of the temperature and residual stress fields during 3D printing of polymer composites », *The International Journal of Advanced Manufacturing Technology*, vol. 104, p. 1661-1676, 2019.

[7] M. Tarfaoui, M. Nachtane, I. Goda, Y. Qureshi, et H. Benyahia, « Additive manufacturing in fighting against novel coronavirus COVID-19 », *The International Journal of Advanced Manufacturing Technology*, vol. 110, nº 11, p. 2913-2927, 2020.

[8] M. Rouway *et al.*, « 3D printing: Rapid manufacturing of a new small-scale tidal turbine blade », *The International Journal of Advanced Manufacturing Technology*, vol. 115, nº 1, p. 61-76, 2021.

[9] A. El Moumen, M. Tarfaoui, et K. Lafdi, « Additive manufacturing of polymer composites: Processing and modeling approaches », *Composites Part B: Engineering*, vol. 171, p. 166-182, 2019.

[10] S. Khan, K. Joshi, et S. Deshmukh, « A comprehensive review on effect of printing parameters on mechanical properties of FDM printed parts », *Materials Today: Proceedings*, vol. 50, p. 2119-2127, 2022.

[11] Y. Y. Tanoto, J. Anggono, W. Budiman, et K. V. Philbert, « Strength and dimension accuracy in fused deposition modeling: A comparative study on parts making using ABS and PLA polymers », *Rekayasa Mesin*, vol. 11, nº 1, p. 69-76, 2020.

[12] L. Santana, J. L. Alves, A. da C. Sabino Netto, et C. Merlini, « A comparative study between PETG and PLA for 3D printing through thermal, chemical and mechanical characterization », *Matéria (Rio de Janeiro)*, vol. 23, p. e12267, 2018.

[13] M. Nachtane, M. Tarfaoui, Y. Ledoux, S. Khammassi, E. Leneveu, et J. Pelleter, « Experimental investigation on the dynamic behavior of 3D printed CF-PEKK composite under cyclic uniaxial compression », *Composite structures*, vol. 247, p. 112474, 2020.

[14] P. Latko-Durałek, K. Dydek, et A. Boczkowska, « Thermal, rheological and mechanical properties of PETG/rPETG blends », *Journal of Polymers and the Environment*, vol. 27, p. 2600-2606, 2019.

[15] P. Latko-Durałek, K. Dydek, E. Golonko, et A. Boczkowska, « Mechanical properties of PETG fibres and their usage in carbon fibres/epoxy composite laminates », *Fibres & Textiles in Eastern Europe*, n° 2 (128, p. 61-65, 2018.

[16] J. M. Barrios et P. E. Romero, « Improvement of surface roughness and hydrophobicity in PETG parts manufactured via fused deposition modeling (FDM): An application in 3D printed self–cleaning parts », *Materials*, vol. 12, n° 15, p. 2499, 2019.

[17] R. Srinivasan, K. N. Kumar, A. J. Ibrahim, K. Anandu, et R. Gurudhevan, « Impact of fused deposition process parameter (infill pattern) on the strength of PETG part », *Materials Today: Proceedings*, vol. 27, p. 1801-1805, 2020.

[18] K. Szykiedans, W. Credo, et D. Osiński, « Selected mechanical properties of PETG 3-D prints », *Procedia Engineering*, vol. 177, p. 455-461, 2017.

[19] H. G. Hosseinabadi, R. Bagheri, L. A. Gray, V. Altstädt, et K. Drechsler, « Plasticity in polymeric honeycombs made by photo-polymerization and nozzle based 3D-printing », *Polymer Testing*, vol. 63, p. 163-167, 2017.

[20] X. Tian, T. Liu, C. Yang, Q. Wang, et D. Li, « Interface and performance of 3D printed continuous carbon fiber reinforced PLA composites », *Composites Part A: Applied Science and Manufacturing*, vol. 88, p. 198-205, 2016.

[21] W. Zhong, F. Li, Z. Zhang, L. Song, et Z. Li, « Short fiber reinforced composites for fused deposition modeling », *Materials Science and Engineering: A*, vol. 301, n° 2, p. 125-130, 2001.

[22] S. Dul, L. Fambri, et A. Pegoretti, « Filaments production and fused deposition modelling of ABS/carbon nanotubes composites », *Nanomaterials*, vol. 8, n° 1, p. 49, 2018.

[23] D. Singh, A. R. Reddy, et S. Arjula, « Characterization of additive manufactured PETG and carbon fiber—PETG », *Int. J. Res. Eng. Appl. Manag*, vol. 4, p. 152-156, 2018.

[24] S. Valvez, A. P. Silva, et P. N. Reis, « Compressive behaviour of 3D-printed PETG composites », *Aerospace*, vol. 9, n° 3, p. 124, 2022.

[25] O. S. Es-Said, J. Foyos, R. Noorani, M. Mendelson, R. Marloth, et B. A. Pregger, « Effect of layer orientation on mechanical properties of rapid prototyped samples », *Materials and Manufacturing Processes*, vol. 15, n° 1, p. 107-122, 2000.

[26] S. Ahn, M. Montero, D. Odell, S. Roundy, et P. K. Wright, « Anisotropic material properties of fused deposition modeling ABS », *Rapid prototyping journal*, vol. 8, n° 4, p. 248-257, 2002.

[27] N. Kang, Y. Fu, P. Coddet, B. Guelorget, H. Liao, et C. Coddet, « On the microstructure, hardness and wear behavior of Al-Fe-Cr quasicrystal reinforced Al matrix composite prepared by selective laser melting », *Materials & Design*, vol. 132, p. 105-111, 2017.

[28] C. Pavon, M. Aldas, J. López-Martínez, et S. Ferrándiz, « New materials for 3D-printing based on polycaprolactone with gum rosin and beeswax as additives », *Polymers*, vol. 12, n° 2, p. 334, 2020.

[29] M. Quanjin, M. Rejab, M. Idris, B. Zhang, et N. M. Kumar, « Filament winding technique: SWOT analysis and applied favorable factors », *SCIREA Journal of Mechanical Engineering*, vol. 3, n° 1, p. 1-25, 2019.

[30] B. Singh, R. Kumar, et J. S. Chohan, « Polymer matrix composites in 3D printing: A state of art review », *Materials Today: Proceedings*, vol. 33, p. 1562-1567, 2020.

[31] G. C. Onwubolu et F. Rayegani, « Characterization and optimization of mechanical properties of ABS parts manufactured by the fused deposition modelling process », *International Journal of Manufacturing Engineering*, vol. 2014, n° 1, p. 598531, 2014.

[32] M. Tarfaoui, M. Daly, R. Kbaier, et M. Chihi, « Investigation of 3D printed CF-PETG composites' tensile behaviors: Synergizing simulative and real-world explorations », *Composites Science and Technology*, vol. 247, p. 110385, 2024.

[33] M. Nachtane, M. Tarfaoui, Y. Ledoux, S. Khammassi, E. Leneveu, et J. Pelleter, « Experimental investigation on the dynamic behavior of 3D printed CF-PEKK composite under cyclic uniaxial compression », *Composite structures*, vol. 247, p. 112474, 2020.

[34] M. Rouway *et al.*, « 3D printing: Rapid manufacturing of a new small-scale tidal turbine blade », *The International Journal of Advanced Manufacturing Technology*, vol. 115, n° 1, p. 61-76, 2021.

[35] M. Rouway, M. Tarfaoui, N. Chakhchaoui, L. E. H. Omari, F. Fraija, et O. Cherkaoui, « Additive manufacturing and composite materials for marine energy: case of tidal turbine », *3D Printing and Additive Manufacturing*, vol. 10, n° 6, p. 1309-1319, 2023.

[36] H. Zou *et al.*, « The out-of-plane compression behavior of cross-ply AS4/PEEK thermoplastic composite laminates at high strain rates », *Materials*, vol. 11, n° 11, p. 2312, 2018.

[37] H. Ye, X. Y. Liu, et H. Hong, « Fabrication of metal matrix composites by metal injection molding—A review », *Journal of materials processing technology*, vol. 200, n° 1-3, p. 12-24, 2008.

[38] T. G. Spears et S. A. Gold, « In-process sensing in selective laser melting (SLM) additive manufacturing », *Integrating Materials and Manufacturing Innovation*, vol. 5, n° 1, p. 16-40, 2016.

[39] R. Balokhonov, V. Romanova, et A. Kulkov, « Microstructure-based analysis of deformation and fracture in metal-matrix composite materials », *Engineering Failure Analysis*, vol. 110, p. 104412, 2020.

[40] Ü. A. Usca *et al.*, « Estimation, optimization and analysis based investigation of the energy consumption in machinability of ceramic-based metal matrix composite materials », *journal of materials research and technology*, vol. 17, p. 2987-2998, 2022.

[41] A. Nirala *et al.*, « Comprehensive study of magnesium based metal matrix composite », *Materials Today: Proceedings*, vol. 46, p. 6587-6591, 2021.

[42] S. Mileiko *et al.*, « Oxide-fibre/nickel-based matrix composites—part I: fabrication and microstructure », *Composites science and technology*, vol. 62, n° 2, p. 167-179, 2002.

[43] L. C. Hwa, S. Rajoo, A. M. Noor, N. Ahmad, et M. Uday, « Recent advances in 3D printing of porous ceramics: A review », *Current Opinion in Solid State and Materials Science*, vol. 21, n° 6, p. 323-347, 2017.

[44] S. A. Brinckmann, N. Patra, J. Yao, T. H. Ware, C. P. Frick, et R. S. Fertig III, « Stereolithography of SiOC polymer-derived ceramics filled with SiC micronwhiskers », *Advanced Engineering Materials*, vol. 20, n° 11, p. 1800593, 2018.

[45] S. Li *et al.*, « Additive manufacturing of SiBCN/Si 3 N 4 w composites from preceramic polymers by digital light processing », *RSC advances*, vol. 10, n° 10, p. 5681-5689, 2020.

[46] H. Xiong, L. Zhao, H. Chen, X. Wang, K. Zhou, et D. Zhang, « 3D SiC containing uniformly dispersed, aligned SiC whiskers: Printability, microstructure and mechanical properties », *Journal of Alloys and Compounds*, vol. 809, p. 151824, 2019.

[47] P. Feng, P. Wei, P. Li, C. Gao, C. Shuai, et S. Peng, « Calcium silicate ceramic scaffolds toughened with hydroxyapatite whiskers for bone tissue engineering », *Materials characterization*, vol. 97, p. 47-56, 2014.

[48] X. Tian *et al.*, « 3D printing of continuous fiber reinforced polymer composites: development, application, and prospective », *Chinese Journal of Mechanical Engineering: Additive Manufacturing Frontiers*, vol. 1, n° 1, p. 100016, 2022.

[49] Y. Ming, Z. Xin, J. Zhang, Y. Duan, et B. Wang, « Fabrication of continuous glass fiber-reinforced dual-cure epoxy composites via UV-assisted fused deposition modeling », *Composites Communications*, vol. 21, p. 100401, 2020.

[50] G. W. Melenka, B. K. Cheung, J. S. Schofield, M. R. Dawson, et J. P. Carey, « Evaluation and prediction of the tensile properties of continuous fiber-reinforced 3D printed structures », *Composite Structures*, vol. 153, p. 866-875, 2016.

[51] C. Yang, X. Tian, T. Liu, Y. Cao, et D. Li, « 3D printing for continuous fiber reinforced thermoplastic composites: mechanism and performance », *Rapid Prototyping Journal*, vol. 23, n° 1, p. 209-215, 2017.

[52] D.-J. Kwon *et al.*, « Impacts of thermoplastics content on mechanical properties of continuous fiber-reinforced thermoplastic composites », *Composites Part B: Engineering*, vol. 216, p. 108859, 2021.

[53] J. Bijelic-Donova, S. Garoushi, L. V. Lassila, F. Keulemans, et P. K. Vallittu, « Mechanical and structural characterization of discontinuous fiber-reinforced dental resin composite », *Journal of dentistry*, vol. 52, p. 70-78, 2016.

[54] S. Ko, J. Davey, S. Douglass, J. Yang, M. E. Tuttle, et M. Salviato, « Effect of the thickness on the fracturing behavior of discontinuous fiber composite structures », *Composites Part A: Applied Science and Manufacturing*, vol. 125, p. 105520, 2019.

[55] L. J. Tomlin, T. A. Cender, S. Sauerbrunn, et S. G. Advani, « Methodology to establish a forming process window for thermoset aligned discontinuous fiber composites », *Composites Part A: Applied Science and Manufacturing*, vol. 180, p. 108064, 2024.

[56] D. Kumlutaş, I. H. Tavman, et M. T. Çoban, « Thermal conductivity of particle filled polyethylene composite materials », *Composites science and technology*, vol. 63, nº 1, p. 113-117, 2003.

[57] Y. Flom et R. Arsenault, « Effect of particle size on fracture toughness of SiC/Al composite material », *Acta metallurgica*, vol. 37, nº 9, p. 2413-2423, 1989.

[58] G. Jagadeesh et S. Gangi Setti, « A review on micromechanical methods for evaluation of mechanical behavior of particulate reinforced metal matrix composites », *Journal of Materials Science*, vol. 55, p. 9848-9882, 2020.

[59] S. Goutianos, T. Peijs, B. Nystrom, et M. Skrifvars, « Development of flax fibre based textile reinforcements for composite applications », *Applied composite materials*, vol. 13, p. 199-215, 2006.

[60] Y. Li *et al.*, « A review of the electrical and mechanical properties of carbon nanofiller-reinforced polymer composites », *Journal of Materials Science*, vol. 54, p. 1036-1076, 2019.

[61] R. Rafiee et R. M. Moghadam, « On the modeling of carbon nanotubes: a critical review », *Composites Part B: Engineering*, vol. 56, p. 435-449, 2014.

[62] A. M. Esawi, K. Morsi, A. Sayed, M. Taher, et S. Lanka, « Effect of carbon nanotube (CNT) content on the mechanical properties of CNT-reinforced aluminium composites », *Composites Science and Technology*, vol. 70, nº 16, p. 2237-2241, 2010.

[63] G.-M. Vallet, M. Dunand, et J.-F. Silvain, « Influence of carbon nanotubes dispersion on thermal properties of copper-carbon nanotubes (CNTs) composite materials », *Universal Journal of Materials Science*, vol. 3, nº 4, p. 55-61, 2015.

[64] S. Roy, R. S. Petrova, et S. Mitra, « Effect of carbon nanotube (CNT) functionalization in epoxy-CNT composites », *Nanotechnology reviews*, vol. 7, nº 6, p. 475-485, 2018.

[65] M. Tarfaoui, A. El Moumen, M. Boehle, O. Shah, et K. Lafdi, « Self-heating and deicing epoxy/glass fiber based carbon nanotubes buckypaper composite », *Journal of materials science*, vol. 54, p. 1351-1362, 2019.

[66] D. Rezzig, M. Tarfaoui, et S. Abdeslam, « The effect of interphase and agglomeration on the mechanical properties of aluminum matrix nanocomposites reinforced with carbon nanotubes », *Materials Today Communications*, vol. 37, p. 107103, 2023.

[67] S. Maity, J. R. Bochinski, et L. I. Clarke, « Metal Nanoparticles Acting as Light-Activated Heating Elements within Composite Materials », *Advanced Functional Materials*, vol. 22, nº 24, p. 5259-5270, 2012.

[68] A. A. Yaqoob *et al.*, « Recent advances in metal decorated nanomaterials and their various biological applications: a review », *Frontiers in chemistry*, vol. 8, p. 341, 2020.

[69] C. Sciancalepore, F. Moroni, M. Messori, et F. Bondioli, « Acrylate-based silver nanocomposite by simultaneous polymerization–reduction approach via 3D stereolithography », *Composites Communications*, vol. 6, p. 11-16, 2017.

[70] E. Saleh *et al.*, « 3D inkjet-printed UV-curable inks for multi-functional electromagnetic applications », *Additive Manufacturing*, vol. 13, p. 143-148, 2017.

[71] R. Nonato, L. Mei, B. Bonse, E. Chinaglia, et A. Morales, « Nanocomposites of PLA containing ZnO nanofibers made by solvent cast 3D printing: Production and characterization », *European Polymer Journal*, vol. 114, p. 271-278, 2019.

[72] T. Siripongpreda, V. P. Hoven, B. Narupai, et N. Rodthongkum, « Emerging 3D printing based on polymers and nanomaterial additives: Enhancement of properties and potential applications », *European Polymer Journal*, vol. 184, p. 111806, 2023.

[73] G. Alberti, C. Zanoni, L. R. Magnaghi, et R. Biesuz, « Disposable and low-cost colorimetric sensors for environmental analysis », *International Journal of Environmental Research and Public Health*, vol. 17, n° 22, p. 8331, 2020.

[74] P. Kunchala et K. Kappagantula, « 3D printing high density ceramics using binder jetting with nanoparticle densifiers », *Materials & Design*, vol. 155, p. 443-450, 2018.

[75] R. Kumar, M. Kumar, et J. S. Chohan, « The role of additive manufacturing for biomedical applications: A critical review », *Journal of Manufacturing Processes*, vol. 64, p. 828-850, 2021.

[76] H. Algzlan et S. Varada, « Three-dimensional printing of the skin », *JAMA dermatology*, vol. 151, n° 2, p. 207-207, 2015.

[77] Y. W. D. Tay, B. Panda, S. C. Paul, N. A. Noor Mohamed, M. J. Tan, et K. F. Leong, « 3D printing trends in building and construction industry: a review », *Virtual and physical prototyping*, vol. 12, n° 3, p. 261-276, 2017.

[78] C. M. Thakar, S. S. Parkhe, A. Jain, K. Phasinam, G. Murugesan, et R. J. M. Ventayen, « 3d Printing: Basic principles and applications », *Materials Today: Proceedings*, vol. 51, p. 842-849, 2022.

[79] C. W. J. Lim, K. Q. Le, Q. Lu, et C. H. Wong, « An overview of 3-D printing in manufacturing, aerospace, and automotive industries », *IEEE potentials*, vol. 35, n° 4, p. 18-22, 2016.

[80] J. C. Najmon, S. Raeisi, et A. Tovar, « Review of additive manufacturing technologies and applications in the aerospace industry », *Additive manufacturing for the aerospace industry*, p. 7-31, 2019.

[81] G. Atakok, M. Kam, et H. B. Koc, « Tensile, three-point bending and impact strength of 3D printed parts using PLA and recycled PLA filaments: A statistical investigation », *Journal of Materials Research and Technology*, vol. 18, p. 1542-1554, 2022.

[82] B. Ergene, G. Atlıhan, et A. Pınar, « Investigation of the effect of taper angle and boundary condition on natural frequency of the 3D printed PET-G beams », *International Journal of 3D Printing Technologies and Digital Industry*, vol. 6, n° 1, p. 31-39, 2022.

[83] S. Lekurwale, T. Karanwad, et S. Banerjee, « Selective laser sintering (SLS) of 3D printlets using a 3D printer comprised of IR/red-diode laser », *Annals of 3D Printed Medicine*, vol. 6, p. 100054, 2022.

[84] M. B. Kumar, P. Sathiya, et M. Varatharajulu, « Selective laser sintering », *Advances in Additive Manufacturing Processes; China Bentham Books: Beijing, China*, p. 28, 2021.

[85] B. Gao, H. Zhao, L. Peng, et Z. Sun, « A review of research progress in selective laser melting (SLM) », *Micromachines*, vol. 14, nº 1, p. 57, 2022.

[86] A. Kafle, E. Luis, R. Silwal, H. M. Pan, P. L. Shrestha, et A. K. Bastola, « 3D/4D printing of polymers: fused deposition modelling (FDM), selective laser sintering (SLS), and stereolithography (SLA) », *Polymers*, vol. 13, nº 18, p. 3101, 2021.

[87] J. Fei *et al.*, « Progress in photocurable 3D printing of photosensitive polyurethane: a review », *Macromolecular Rapid Communications*, vol. 44, nº 18, p. 2300211, 2023.

[88] V. M. Vaz et L. Kumar, « 3D printing as a promising tool in personalized medicine », *Aaps Pharmscitech*, vol. 22, p. 1-20, 2021.

[89] N. Arora, S. Dua, V. K. Singh, S. K. Singh, et T. Senthilkumar, « A Comprehensive Review on Fillers and Mechanical Properties of 3D Printed Polymer Composites », *Materials Today Communications*, p. 109617, 2024.

[90] S. G. Sarvankar et S. N. Yewale, « Additive manufacturing in automobile industry », *Int. J. Res. Aeronaut. Mech. Eng*, vol. 7, nº 4, p. 1-10, 2019.

[91] I. Gibson, D. Rosen, B. Stucker, I. Gibson, D. Rosen, et B. Stucker, « Design for additive manufacturing », *Additive manufacturing technologies: 3D printing, rapid prototyping, and direct digital manufacturing*, p. 399-435, 2015.

[92] K. V. Wong et A. Hernandez, « A review of additive manufacturing », *International scholarly research notices*, vol. 2012, nº 1, p. 208760, 2012.

[93] M. Javaid, A. Haleem, R. P. Singh, R. Suman, et S. Rab, « Role of additive manufacturing applications towards environmental sustainability », *Advanced Industrial and Engineering Polymer Research*, vol. 4, nº 4, p. 312-322, 2021.

[94] J. Li, Z. Huang, G. Liu, Q. An, et M. Chen, « Topology optimization design and research of lightweight biomimetic three-dimensional lattice structures based on laser powder bed fusion », *Journal of Manufacturing Processes*, vol. 74, p. 220-232, 2022.

[95] D. Srinivasan *et al.*, « 3D printing manufacturing techniques, materials, and applications: an overview », *Advances in Materials Science and Engineering*, vol. 2021, nº 1, p. 5756563, 2021.

[96] M. S. Karkun et S. Dharmalingam, « 3D printing technology in aerospace industry–a review », *International Journal of Aviation, Aeronautics, and Aerospace*, vol. 9, nº 2, p. 4, 2022.

[97] G. Schiller, « Additive manufacturing for Aerospace », présenté à 2015 IEEE Aerospace Conference, IEEE, 2015, p. 1-8.

[98] M. Revilla-León, M. Sadeghpour, et M. Özcan, « An update on applications of 3D printing technologies used for processing polymers used in implant dentistry », *Odontology*, vol. 108, nº 3, p. 331-338, 2020.

[99] M. van der Stelt *et al.*, « Pioneering low-cost 3D-printed transtibial prosthetics to serve a rural population in Sierra Leone–an observational cohort study », *EClinicalMedicine*, vol. 35, 2021.

[100] I. Papa, E. Manco, G. Epasto, V. Lopresto, et A. Squillace, « Impact behaviour and non destructive evaluation of 3D printed reinforced composites », *Composite Structures*, vol. 281, p. 115112, 2022.

[101] N. Maqsood et M. Rimašauskas, « Delamination observation occurred during the flexural bending in additively manufactured PLA-short carbon fiber filament reinforced with continuous carbon fiber composite », *Results in Engineering*, vol. 11, p. 100246, 2021.

[102] B. D. Le, F. Dau, J.-L. Charles, et I. Iordanoff, « Modeling damages and cracks growth in composite with a 3D discrete element method », *Composites Part B: Engineering*, vol. 91, p. 615-630, 2016.

[103] R. Sepe, F. Bollino, L. Boccarusso, et F. Caputo, « Influence of chemical treatments on mechanical properties of hemp fiber reinforced composites », *Composites Part B: Engineering*, vol. 133, p. 210-217, 2018.

[104] M. Akbari, P. Asadi, P. Zolghadr, et A. Khalkhali, « Multicriteria optimization of mechanical properties of aluminum composites reinforced with different reinforcing particles type », *Proceedings of the Institution of Mechanical Engineers, Part E: Journal of Process Mechanical Engineering*, vol. 232, nº 3, p. 323-337, 2018.

[105] S. Ozden, R. Ekici, et F. Nair, « Investigation of impact behaviour of aluminium based SiC particle reinforced metal–matrix composites », *Composites Part A: Applied Science and Manufacturing*, vol. 38, nº 2, p. 484-494, 2007.

[106] Y. Shi, C. Pinna, et C. Soutis, « Modelling impact damage in composite laminates: a simulation of intra-and inter-laminar cracking », *Composite Structures*, vol. 114, p. 10-19, 2014.

[107] H. Bakhtiari, M. Aamir, et M. Tolouei-Rad, « Effect of 3D printing parameters on the fatigue properties of parts manufactured by fused filament fabrication: a review », *Applied Sciences*, vol. 13, nº 2, p. 904, 2023.

[108] E. J. Ekoi, A. N. Dickson, et D. P. Dowling, « Investigating the fatigue and mechanical behaviour of 3D printed woven and nonwoven continuous carbon fibre reinforced polymer (CFRP) composites », *Composites Part B: Engineering*, vol. 212, p. 108704, 2021.

[109] V. Shanmugam *et al.*, « Fatigue behaviour of FDM-3D printed polymers, polymeric composites and architected cellular materials », *International Journal of Fatigue*, vol. 143, p. 106007, 2021.

[110] P. Rezaeian, M. R. Ayatollahi, A. Nabavi-Kivi, et N. Razavi, « Effect of printing speed on tensile and fracture behavior of ABS specimens produced by fused deposition modeling », *Engineering Fracture Mechanics*, vol. 266, p. 108393, 2022.

[111] J. Vallejo, E. García-Plaza, P. Núñez, J. Chacón, M. Caminero, et A. Romero, « Machinability analysis of carbon fibre reinforced PET-Glycol composites processed by additive manufacturing », *Composites Part A: Applied Science and Manufacturing*, vol. 172, p. 107561, 2023.

[112] E. Cuninková *et al.*, « Numerical and experimental design of the former for TORT cables », *IEEE Transactions on Applied Superconductivity*, vol. 33, nº 5, p. 1-5, 2023.

[113] E. García, P. Núñez, M. Caminero, J. Chacón, et S. Kamarthi, « Effects of carbon fibre reinforcement on the geometric properties of PETG-based filament using FFF additive manufacturing », *Composites Part B: Engineering*, vol. 235, p. 109766, 2022.

[114] C. Yan *et al.*, « PETG: applications in modern medicine », *Engineered Regeneration*, 2023.

[115] M. Kováčová *et al.*, « Novel hybrid PETG composites for 3D printing », *Applied Sciences*, vol. 10, nº 9, p. 3062, 2020.

[116] G. Holcomb, E. B. Caldona, X. Cheng, et R. C. Advincula, « On the optimized 3D printing and post-processing of PETG materials », *MRS communications*, vol. 12, nº 3, p. 381-387, 2022.

[117] W. Li *et al.*, « Hygrothermal aging behavior and flexural property of carbon fiber-reinforced polyethylene terephthalate glycol composites », *Textile Research Journal*, vol. 93, nº 5-6, p. 1005-1018, 2023.

[118] M. A. Mustafa, S. Raja, L. A. A. Asadi, N. H. Jamadon, N. Rajeswari, et A. P. Kumar, « A Decision-Making Carbon Reinforced Material Selection Model for Composite Polymers in Pipeline Applications », *Advances in Polymer Technology*, vol. 2023, nº 1, p. 6344193, 2023.

[119] H. Isakhani, S. Yue, C. Xiong, W. Chen, X. Sun, et T. Liu, « Fabrication and mechanical analysis of bioinspired gliding-optimized wing prototypes for micro aerial vehicles », présenté à 2020 5th International Conference on Advanced Robotics and Mechatronics (ICARM), IEEE, 2020, p. 602-608.

[120] M. Tarfaoui, Y. Qureshi, M. Chihi, et M. Daly, « Mechanical characterisation of Aerosil-polycarbonate-based ceramic nanocomposites: 3D printing versus injection moulding technology », *Journal of Composite Materials*, vol. 57, nº 29, p. 4615-4634, 2023.

[121] F. Han *et al.*, « Analysis of ballistic performance and penetration damage mechanisms of aramid woven fabric reinforced polycarbonate composites with different matrix content », *Chemical Engineering Journal*, vol. 453, p. 139470, 2023.

[122] Y. Guo, M. Yuan, X. Qian, Y. Wei, et Y. Liu, « Rapid prediction of polymer stab resistance performance », *Materials & Design*, vol. 192, p. 108721, 2020.

[123] T. K. Mulenga, A. U. Ude, et V. Chinnasamy, « Mechanical analysis of sisal fiber/bio-epoxy/fly-ash reinforced hybrid composites », *Journal of Composite Materials*, vol. 57, nº 28, p. 4463-4477, 2023.

[124] S. Siraj, A. H. Al-Marzouqi, M. Z. Iqbal, et W. Ahmed, « Impact of micro silica filler particle size on mechanical properties of polymeric based composite material », *Polymers*, vol. 14, nº 22, p. 4830, 2022.

[125] M. Kawaguchi, « Dispersion stabilities and rheological properties of fumed silica suspensions », *Journal of Dispersion Science and Technology*, vol. 38, n° 5, p. 642-660, 2017.

[126] M. M. Karabela et I. D. Sideridou, « Synthesis and study of properties of dental resin composites with different nanosilica particles size », *Dental materials*, vol. 27, n° 8, p. 825-835, 2011.

[127] P. Alaee Faradonbeh, « Rheological behavior of silica based suspensions for shear thickening applications », 2022.

[128] W. Zhang *et al.*, « Characterization of residual stress and deformation in additively manufactured ABS polymer and composite specimens », *Composites Science and Technology*, vol. 150, p. 102-110, 2017.

[129] D. Popescu, A. Zapciu, C. Amza, F. Baciu, et R. Marinescu, « FDM process parameters influence over the mechanical properties of polymer specimens: A review », *Polymer Testing*, vol. 69, p. 157-166, 2018.

[130] S. Dwiyati, A. Kholil, R. Riyadi, et S. Putra, « Influence of layer thickness and 3D printing direction on tensile properties of ABS material », présenté à Journal of Physics: Conference Series, IOP Publishing, 2019, p. 066014.

[131] T. Hada, M. Kanazawa, M. Iwaki, T. Arakida, et S. Minakuchi, « Effect of printing direction on stress distortion of three-dimensional printed dentures using stereolithography technology », *Journal of the Mechanical Behavior of Biomedical Materials*, vol. 110, p. 103949, 2020.

[132] C. Vălean, L. Marșavina, M. Mărghitaș, E. Linul, N. Razavi, et F. Berto, « Effect of manufacturing parameters on tensile properties of FDM printed specimens », *Procedia Structural Integrity*, vol. 26, p. 313-320, 2020.

[133] B. N. Turner et S. A. Gold, « A review of melt extrusion additive manufacturing processes: II. Materials, dimensional accuracy, and surface roughness », *Rapid Prototyping Journal*, vol. 21, n° 3, p. 250-261, 2015.

[134] M. Daly, M. Tarfaoui, M. Chihi, et C. Bouraoui, « Dynamic analysis of 3D-printed CF-PETG composites with different infill densities », *Progress in Additive Manufacturing*, p. 1-29, 2024.

Publications

M. Daly, M. Tarfaoui, M. Chihi, et C. Bouraoui, « FDM technology and the effect of printing parameters on the tensile strength of ABS parts », The International Journal of Advanced Manufacturing Technology, vol. 126, no 11, p. 5307-5323, 2023.

M. Daly, M. Tarfaoui, M. Bouali, et A. Bendarma, « Effects of Infill Density and Pattern on the Tensile Mechanical Behavior of 3D-Printed Glycolyzed Polyethylene Terephthalate Reinforced with Carbon-Fiber Composites by the FDM Process », Journal of Composites Science, vol. 8, no 4, p. 115, 2024.

M. Daly, M. Tarfaoui, M. Chihi, et C. Bouraoui, « Dynamic analysis of 3D-printed CF-PETG composites with different infill densities », Progress in Additive Manufacturing, p. 1-29, 2024.

M. Daly, M. Chihi, C. Bouraoui, et M. Tarfaoui, « Advancing composite materials: Exploring thermomechanical properties of Aerosil/polycarbonate composites via additive manufacturing », Journal of Manufacturing Processes, vol. 131, p. 1770-1783, 2024.

M. Tarfaoui, **M. Daly**, R. Kbaier, et M. Chihi, « Investigation of 3D printed CF-PETG composites' tensile behaviors: Synergizing simulative and real-world explorations », Composites Science and Technology, vol. 247, p. 110385, 2024.

M. Chihi, M. Tarfaoui, Y. Qureshi, **M. Daly**, et C. Bouraoui, « Experimental investigation of the effect of infill parameters on dynamic compressive performance of 3D-Printed carbon fiber reinforced polyethylene terephthalate glycol composites », Journal of Thermoplastic Composite Materials, p. 08927057231222805, 2023.

H. I. Beloufa, M. Tarfaoui, K. Lafdi, **M. Daly**, et A. Bendarma, « Graphene nanosheets as novel nanofillers in an epoxy matrix for improved mechanical properties », in Advances in Nanosheets-Preparation, Properties and Applications, IntechOpen, 2023.

H. I. Beloufa, M. Tarfaoui, K. Lafdi, **M. Daly**, et A. Bendarma, « Graphene Sheets as Novel Nanofillers in Epoxy Matrix for Improved Mechanical Properties », 2023.

M. Tarfaoui, Y. Qureshi, M. Chihi, et **M. Daly**, « Mechanical characterisation of Aerosil-polycarbonate-based ceramic nanocomposites: 3D printing versus injection moulding technology », Journal of Composite Materials, vol. 57, no 29, p. 4615-4634, 2023.

S. Tamayo-Vegas, K. Lafdi, M. Tarfaoui, K. K. Lafdi, et **M. Daly**, « Analysis of Acid Diffusion Effects on Physical Properties of Polymer Composites: A Combined Study of Mechanical and Electrical Characterization », Applied Mechanics, vol. 4, no 3, p. 974-989, 2023.

S. Tamayo-Vegas, K. Lafdi, M. Tarfaoui, K. K. Lafdi, et **M. Daly**, « Use of In-situ and Ex-situ Characterization Techniques to Study the Effects of Acid Diffusion on Physical Properties of Polymer Composites. », 2023.

COLLEGES BRETAGNE LOIRE | SCIENCES POUR L'INGENIEUR ET LE NUMERIQUE

ENSTA BRETAGNE

Titre : Conception et optimisation de Matériaux Composites de Nouvelle Génération par Fabrication Additive : Vers des Performances Mécaniques Révolutionnaires.

Mots clés : Impression 3D, Matériaux composites, Modélisation numérique, Thermoplastiques

Résumé : Cette thèse examine le comportement des matériaux composites imprimés en 3D dans des conditions environnementales variées, avec un focus sur les effets de la température, les essais dynamiques, statiques, et la modélisation numérique. L'impression 3D transforme des secteurs comme l'aéronautique, l'automobile et le médical, en permettant de produire rapidement des formes complexes. Cependant, des défis subsistent, tels que la déformation des pièces et une cadence de production inférieure aux méthodes classiques. L'objectif est d'améliorer les performances mécaniques des thermoplastiques et composites en optimisant les paramètres d'impression pour limiter les défauts comme le gauchissement et les contraintes résiduelles. Le travail se concentre sur le développement de nouveaux matériaux, tels que des polymères thermoplastiques renforcés de fibres de carbone et de nanocéramiques, destinés à la fabrication de composants multi-matériaux. Les matériaux étudiés incluent l'ABS, le CF-PETG et le polycarbonate renforcé d'Aerosil. L'influence du type de renfort, des motifs de remplissage (rectilignes, nid d'abeilles) et des taux de remplissage (20 %, 50 %, 75 % et 100 %) a été analysée à travers des méthodes expérimentales et numériques. Des techniques comme la microscopie électronique à balayage (MEB) et la modélisation par éléments finis (MEF) ont permis d'explorer la microstructure et les propriétés mécaniques.

Title: Design and Optimization of Next-Generation Composite Materials through Additive Manufacturing: Towards Revolutionary Mechanical Performance.

Keywords: 3D printing, Composite materials, Numerical modeling, Thermoplastics.

Abstract: This thesis examines the behavior of 3D-printed composite materials under various environmental conditions, focusing on the effects of temperature, dynamic and static testing, and numerical modeling. 3D printing is transforming industries such as aerospace, automotive, and medical by enabling the rapid production of complex shapes. However, challenges remain, such as part deformation and lower production rates compared to traditional methods. The goal is to enhance the mechanical performance of thermoplastics and composites by optimizing printing parameters to reduce defects like warping and residual stresses. The research focuses on developing new materials, such as carbon fiber and nanoceramic-reinforced thermoplastic polymers, to produce multi-material components. The materials studied include ABS, CF-PETG, and polycarbonate reinforced with Aerosil. The influence of reinforcement type, infill patterns (rectilinear, honeycomb), and infill percentages (20%, 50%, 75%, and 100%) were analyzed through experimental and numerical methods. Techniques such as scanning electron microscopy (SEM) and finite element modeling (FEM) were used to explore the microstructure and mechanical properties.